universität wien

DISSERTATION / DOCTORAL THESIS

Titel der Dissertation /Title of the Doctoral Thesis

„Emulsion-templated macroporous polyepoxides“

verfasst von / submitted by

Patrick Georg Steindl, BSc MSc

angestrebter akademischer Grad / in partial fulfilment of the requirements for the degree of

Doktor der Naturwissenschaften (Dr.rer.nat)

Wien, 2022/ Vienna 2022

Studienkennzahl lt. Studienblatt / degree programme code as it appears on the student record sheet:	A 796 605 419
Dissertationsgebiet lt. Studienblatt / field of study as it appears on the student record sheet:	Chemie
Betreut von / Supervisor:	Univ.-Prof. Dr. Dipl.-Chem. Alexander Bismarck
Mitbetreut von / Co-Supervisor:	Dr. Angelika Menner

Abstract

This work explores the preparation of porous poly(epoxide) foams using the method of emulsion templating and describes the thorough characterisation thereof. Furthermore, special focus was placed on the development of a custom-designed apparatus for gas permeability testing.

Our integrated gaseous transport device, based on the pressure rise technique, does not only allow to determine gas permeability, but is also suitable for both steady state and transient diffusion (oxygen in nitrogen) measurements. The combination of both working modes allows to deduce effective porosity and effective pore length. Pure diffusion measurements provide information on the ratio of the diffusion coefficient in a medium compared to free space. The apparatus accurately determines viscous permeabilities and slip coefficients over a wide permeability range and can even be used for flow exceeding the laminar range. Validity and accuracy of the measurements were established through tests performed on Berea sandstones and open-porous epoxy foams.

Porous polyepoxide foams based on the commercial epoxy adhesive Araldite®2020 were prepared from surfactant-stabilised W/O emulsions, employing an aqueous electrolyte solution as template phase. Materials with porosities ranged between 45-60%, thus classified as polymerised medium internal phase emulsions (polyMIPEs), were produced by altering the internal phase volume ratio, resulting in materials with elastic moduli between 60 and 200 MPa and compressive strengths in the range of 2 to 6.5 MPa. Changes in the surfactant concentration mainly influenced the pore structure, enabling the tailored fabrication of closed-cell as well as open-porous, interconnected foams with permeabilities up to 200 mD. Evaluation of the swelling behaviour of the Araldite®2020 polyMIPEs, studied by immersing foam samples in a series of solvents of different polarities for eleven days, proved the excellent chemical stability of our porous polyepoxides.

Progressing from the low viscosity model system Araldite®2020 to the epoxy system EF80, flexible porous polyepoxide foams were prepared from MIPEs with an external organic phase containing resin, hardener, emulsifier and carbon nanotubes. Curing at ambient conditions

resulted in polyepoxide foams with interconnected pore morphology with an average pore size of about 10 µm, while pores from MIPEs solidified at 50°C and with the addition of carbon nanotubes as thickening agent were on average one magnitude larger. EF80 foams did not fracture when being compressed to 30% of their original height. Energy loss coefficients determined from the energy uptake during cyclic compression tests ranged between 40-60% and thus showed the resiliency of our flexible poly(epoxide)MIPEs.

Zusammenfassung

Diese Arbeit beschäftigt sich mit der Herstellung von porösen Polyepoxidschäumen mittels *Emulsion Templating* und deren umfangreicher Charakterisierung. Ein weiterer Schwerpunkt wurde auf Entwurf und Entwicklung eines anwendungsspezifischen Geräts zur Bestimmung der Durchlässigkeit gegenüber Gasen, i.e. Gaspermeabilität, gesetzt.

Unser ganzheitliches Gastransportinstrument, basierend auf einer Druckanstiegstechnologie, erlaubt nicht nur die Bestimmung der Gaspermeabilität, sondern eignet sich auch für Messungen sowohl im Fließgleichgewicht als auch bei transienter Diffusion (z.B. Sauerstoff in Stickstoff). Durch Kombination beider Betriebsarten, kann auf die effektive Porosität und den effektiven Porendurchmesser geschlossen werden. Reine Diffusionsmessungen liefern Informationen über das Verhältnis der Diffusionskoeffizienten in einem Medium relativ zum freien Raum. Das Gerät bestimmt präzise über einen großen Permeabilitätsbereich viskose Permeabilitäten und Slip-Koeffizienten und kann sogar für Gasfluss außerhalb des laminaren Bereichs verwendet werden. Aussagekraft und Genauigkeit der Messungen wurden durch Tests an Berea-Sandsteinen und offenporigen Epoxidschäumen nachgewiesen.

Poröse Polyepoxidschäume, basierend auf dem kommerziellen Epoxidkleber Araldite®2020, wurden aus Tensid-stabilisierten Wasser-in-Öl Emulsionen, unter der Verwendungen einer wässrigen Elektrolytlösung als Templat-Phase, hergestellt. Materialien mit Porositäten zwischen 45-60%, deshalb klassifiziert als *polymerised medium internal phase emulsions* (*polyMIPEs*), wurden durch Variation des Verhältnisses von interner zu kontinuierlicher Phase hergestellt. Die resultierenden Schäume wiesen Elastizitätsmodule zwischen 60 und 200 MPa und Druckfestigkeiten in Bereich von 2 bis 6.5 MPa auf. Eine Veränderung der Tensidkonzentration beeinflusste vorwiegend die Porenstruktur. Dies ermöglicht die gezielte Herstellung von sowohl geschlossen-porigen als auch offen-porigen, verbundenen Schäumen mit Permeabilitäten bis zu 200 mD. Zur Untersuchung des Quellverhaltens von Araldite®2020 polyMIPEs wurden gleich dimensionierte Schaumstücke für elf Tage in eine Reihe von Lösungsmitteln unterschiedlicher Polarität getaucht. Die Tests bewiesen die ausgezeichnete chemische Beständigkeit unserer porösen Polyepoxide.

Aufbauend auf den Erkenntnissen gewonnen von der Verwendung des niedrigviskosen Modellsystems Araldite®2020 wurden unter der Verwendung des Epoxids EF80 elastische poröse Polyepoxidschäume ausgehend von Emulsionen mit externer organischer Phase, welche Monomere, Härter, Emulgator und Kohlenstoffnanoröhrchen (CNTs) enthielt, produziert. Aushärtung unter normalen Umgebungsbedingungen lieferte Epoxidschäume mit ineinandergreifender Porenstruktur mit einer durchschnittlichen Porengröße von etwa 10 µm, während Aushärtung bei 50°C und der Zusatz von CNTs als Verdickungsmittel, im Mittel um eine Größenordnung größere Poren lieferte. Die EF80-Schäume hielten einer Kompression auf 30% ihrer ursprünglichen Höhe stand, ohne zu zerbrechen. Die Energieverlustkoeffizienten, ermittelt aus der Energieaufnahme während zyklischer Kompressionsmessungen, lagen zwischen 40 und 60%, was sowohl auf Elastizität als auch Belastbarkeit unserer flexiblen Epoxid-polyMIPEs hinweist.

Acknowledgements

I am truly grateful that I was given by Prof Alexander Bismarck and Dr Angelika Menner, my supervisors, the opportunity to do a PhD in the PaCE group. Without their trust, motivation and expertise, I would not have been able to finalise this project. I deeply appreciate all the time you invested in helping me, even at weekends or holidays, and for demonstrating that community, teamwork and social skills are at least as important as intellect.

In the same breath, I would like to thank Dr Qixiang Jiang, John for his support and his often so valuable input, which helped me overcome not just one obstacle. I highly appreciate him sharing his experiences with emulsion templating and his broad knowledge on this topic and foams in general with me.

Dmitri Rusakov and I started around the same time with our PhDs and worked on the same project. It was always nice having him around, exchanging experiences and information, sharing concerns and we had a great time attending a conference in Portugal.

I would like to thank Dr Shu San Manley for her initial work on the gas permeability apparatus and everything related to it.

I could not have wished for a better group than PaCE. Throughout the years and despite the constant come and go of group members, I have always felt welcome, respected and comfortable. I enjoyed the internationality of the group, being surrounded over the years by people from almost all parts of the world, with different languages and cultures. I am grateful for all the fun, interesting conversations and the good company when we went out after work or just gathered somewhere for a couple of drinks. A special thank you goes to Olivier Hubert and Neptun Yousefi for making the awful first lockdowns slightly more bearable with our weekly get-togethers. I am incredibly thankful for having been a member of this group, for all the people I have met and for all the friends I have made.

Last but not least, I am incredibly thankful for having such a supportive family. They always stand behind me, no matter what. I know that I can always rely on them, come to them whenever I need something, even though I have never told them much about my studies. I might not show it enough, but I am extremely grateful for having grown up in an intact family

environment, being surrounded by people who care about me, who I can always turn to, knowing that their home will always be a safe space for me. THANK YOU

Table of contents

Abstract III
Zusammenfassung V
Acknowledgements VII
Table of contents IX
List of figures XI
List of tables XIV
List of symbols XV
List of abbreviations XVIII
List of publications XX
1. Introduction 1
2. Aims & Objectives 4
3. Literature review 6
3.1. Common methods for producing porous polymers 6
3.2. Emulsion templating 8
3.3. Emulsions 12
3.3.1. Stabilisation of emulsions 20
3.3.2. Factors affecting the morphology of emulsion-templated porous materials 24
3.4. Epoxy resins 27
3.5. Epoxy foams 30
3.6. Compressive behaviour of cellular solids 32
3.6.1. Factors affecting the mechanical properties of cellular solids 35
4. Experimental 36
4.1. Materials 36
4.1.1. Sandstone 36
4.1.2. Porous polyepoxides 36
4.1.3. Gas permeability & diffusivity measurements 37
4.1.4. Surfactant screening and swelling tests 38
4.2. Methods 38
4.2.1. Emulsion preparation 38
4.2.2. Scanning Electron Microscopy (SEM) - Structure and pore morphology 39
4.2.3. Pycnometry – Density and porosity 39
4.2.4. Dynamic Scanning Calorimetry (DSC) - Thermal stability 40
4.2.5. Uniaxial single and cyclic compression tests - Mechanical properties 40
4.2.6. Equilibrium swelling tests 42
4.3. Gas permeability & diffusivity measurements 42
4.3.1. Introduction to gas permeability 43
4.3.2. Theoretical background 44
4.3.1. Setup and measurement procedure 50
4.3.1. Gas permeability of porous polyepoxides 51
4.3.2. Diffusivity *(Paper I)* 62

5. Results & Discussion 64

5.1. Araldite®2020 poly(epoxide)MIPEs *(Paper II)*.....64

5.2. Flexible poly(epoxide)MIPEs *(Paper III)* 67

5.2.1. MWCNTs-stabilised poly(epoxide)MIPEs..... 68

5.2.2. Si-NP-stabilised poly(epoxide)MIPEs *(Paper III)*..... 72

5.2.3. Surfactant-free poly(epoxide)MIPEs *(Paper III)* 73

6. Conclusions 74

7. Outlook – suggestions for future work 76

8. References..... 77

Appendices: Papers I-III

List of figures

Figure 1: left: classification of porous materials according to their pore size; right: pore throats are the channels the connect pores..... 1

Figure 2: Number of publications between 1990 and 2021 (data obtained on 19 January 2022) for search concepts, emulsion templating‘ and ‚polyLIPE/polyMIPE/polyHIPE’. SciFinder® (classic) was used as search platform. 9

Figure 3: Illustration of the emulsion templating process, supported by real images (right hand side). Addition of an aqueous internal phase leads first to a diluted and then a concentrated emulsion. After curing of the organic matrix phase, the internal phase is removed, leaving a porous material behind. 10

Figure 4: Schematic representation of the different kinds of materials that can be produced from emulsions containing a polymerizable species either in the internal (dispersed) phase (IP), the external (continuous) phase (EP) or both. 11

Figure 5: Energetic relations in emulsion formation/break-up. 13

Figure 6: Illustration of the most important phenomena leading to emulsion destabilisation and ultimately phase separation. 14

Figure 7: Scheme of the potential energy as described by the DLVO – theory. 16

Figure 8: Electrostatic and steric repulsion are the two main mechanisms preventing droplet aggregation. The interaction potential, although completely different, both heavily depend on the distance *x* of two droplet centres. 20

Figure 9: Stabilization of water or oil droplets in the respective opposite environment. 23

Figure 10: The versatility of epoxy resins is one of their biggest assets. 27

Figure 11: Primary curing reaction between amine and glycidyl/epoxy group. 28

Figure 12: Structure-property relationship for Bisphenol-A epoxy resin 29

Figure 13: Epoxies offer a good price-performance ratio 30

Figure 14: Schematic illustration of the mechanical response of a typical polyMIPE/HIPE undergoing compression. 33

Figure 15: Structures of the constituents of the epoxy systems Araldite®2020 and EF80.....37

Figure 16: Illustration of a typical hysteresis loop as obtained from cyclic compression tests. An energy loss coefficient (ELC) can be calculated from the areas under the loading and unloading curve, respectively. 41

Figure 17: Illustration of pipe flow and its most influential parameters as described by Darcy’s equation 43

Figure 18: At low pressure, molecule-wall collisions dominate. Slip causes an artificial increase in permeability. At high pressure, viscous and slip flow coexist → linear relationship between p_m and K.....47

Figure 19: Negative (dp/dx) indicates decrease of fluid pressure in direction of flow; flow work on the body has to compensate frictional resistance. 48

Figure 20: Schematic representation of a gas permeability measurement. The pressure gradient (dp_2/dt) is determined by plotting the recorded pressure over time. The results of the left part (1) of the equation are inserted into the right part. Consequently, the viscous permeability k and the slip coefficient K_0 are evaluated from slope and intercept. 50

Figure 21: Gas permeability setup 51

Figure 22: a) Stepwise illustration of the sealing of the porous polyepoxides; b) graphical representation of a specimen and its different layers; c) test results of one piece of foam are afflicted with only a small error, while averaging over several specimen leads to a significant increase in the error of the evaluated parameters.....52

Figure 23: Permeability coefficient as function of mean pressure p_m (a) and of C as function of mass flow rate G (b) for polyMIPE 2.S3.....52

Figure 24: Dependence of the gas permeability on the limiting pore throat diameter. One can see a trend to higher permeabilities for samples with a higher surfactant ratio. 54

Figure 25: Permeability coefficient at various mean pressures for polyMIPEs 2.S1-2.S5.....54

Figure 26: SEM micrographs of 2.S2 (a) and 2.S5 (b): entire cross sections of samples prepared for gas permeability tests were analysed. 55

Figure 27: Pore size distribution of polyepoxide 2.S1 illustrated as histogram of relative frequencies (left axis) and in terms of the cumulative number and volume frequencies 57

Figure 28: Friction factor vs. pore Reynolds number plot as graphical indicator for the prevailing flow regimes.. 59

Figure 29: Linear plot of C vs. G for poly(epoxide)MIPEs 2.S1-2.S5.....61

Figure 30: Comparison of the setups for gas permeability (a) and diffusivity (b) testing. 62

Figure 31: a-e) SEM images of epoxy polyMIPEs 2.S1-2.S5; f) compressive performance of the same foams.....65

Figure 32: Average swelling ratios of Araldite®2020 polyMIPEs 2.S1-2.S5. 67

Figure 33: (a)-(f): SEM-images of flexible polyMIPEs 3.S1-3.S6 and their elastic moduli E_c (g) and crush strengths σ_c (h) as function of their foam density ρ_f. 69

Figure 34: a-d) Cyclic compression tests performed on polyMIPE 3.S6 for different limiting strains; e+f) development of residual strain and energy loss coefficient with increasing cycle numbers. 70

Figure 35: SEM images of epoxy polyMIPEs 3.S9 (a) and 3.S10 (b), prepared from emulsion templates with 0.4 and 1.2 wt% silica nanoparticles, respectively. 72

Figure 36: SEM images of epoxy polyMIPEs 3.S3, 3.S6, 3.S7 and 3.S8, prepared from emulsion templates with 60% IPR (a,b) and 70% IPR (c,d). 73

Figure 37: E-modulus and crush-strength of poly(epoxide)MIPEs prepared by us in comparison with results from literature. 74

List of tables

Table 1: List of reviews about emulsion templating and related topics 11

Table 2: Average pore diameters: arithmetic mean d[1,0], Sauter diameter d[3,2], median pore diameter d_{50}, and d_{v10}, average pore throat sizes d_{pt}, porosity ε, Knudsen Diffusion coefficients K_0 and viscous permeabilities k for porous polyepoxides 2.S1-2.S5. 53

Table 3: Permeabilities k_{DF} and Forchheimer factors *b* determined from *C* vs. *G* plots.....62

Table 4: Summary of emulsion formulations and properties of epoxy polyMIPEs 2.S1-2.S5 64

Table 5: Formulation and morph. and mech. properties of the prepared epoxy foams 68

List of symbols

Latin letters

A	sample cross-section area	$[m^2]$
ΔA	difference in surface area	$[m^2]$
a	represents viscous flow (=μ/k)	$[kg\ m^{-3}\ s^{-1}]$
b	Forchheimer factor, measure of inertial effects	$[m^{-1}]$
C	$=\frac{(p_1^2-p_2^2)M}{2RTLG}$	$[kg\ m\ s^{-1}]$
C1, C2	proportionality constants (≈1)	[-]
c_p	specific heat capacity	$[J\ kg^{-1}\ K^{-1}]$
c_O	concentration of O_2	$[mol\ m^{-3}]$
$c_{O\text{-}N}$	oxygen concentration in N_2 - efflux stream	[ppm by V]
Δc_O	oxygen concentration difference across the sample	$[mol\ m^{-3}]$
D	diffusion coefficient	$[m^2\ s^{-1}]$
D_{eff}	effective diffusion coefficient	$[m^2\ s^{-1}]$
D_{AB}	free diffusion coefficient of O_2 in N_2	$[m^2\ s^{-1}]$
$\left(\frac{dp_2}{dt}\right)$	rate of pressure rise	$[Pa\ s^{-1}]$
d_p	capillary/pore/droplet diameter	[m]
d_{pt}	pore throat size	[m]
d[1,0]	arithmetic mean pore diameter	[m]
d[3,2]	volume/surface mean diameter (Sauter diameter)	[m]
d_{50}	median pore diameter (50% of all drops are smaller)	[m]
d_{90}	drop diameter such that 90% of all drops are of smaller diameter	[m]
d_{v10}	10% of the total liquid volume is in smaller drops	[m]
E_c	elastic/Young's/compression modulus	[Pa]
$E_{f/p/w}$	foam/plateau/wall modulus	[Pa]
E_{kin}	kinetic energy	[J]
f	friction factor	[-]
G	total mass flux	$[kg\ m^{-2}\ s^{-1}]$
G_1, G_2	mass fluxes through two groups of pores	$[kg\ m^{-2}\ s^{-1}]$
ΔG^{form}	free energy of emulsion formation	[J]
g	gravitational acceleration	$[m\ s^{-2}]$
K	permeability coefficient	$[m^2\ s^{-1}]$
K	curvature of a spherical droplet (=2/r)	$[m^{-1}]$
K_0	slip coefficient	[m]
Kn	Knudsen number	[-]

k	viscous permeability	[m^2]
k_{DF}	Darcy-Forchheimer permeability	[m^2]
k_B	Boltzmann constant	[$J\ K^{-1}$]
L	sample length	[m]
L_{eff}	effective pore length	[m]
M	molecular weight (of transporting species)	[$g\ mol^{-1}$]
m_{dry}	mass of the dried polymer after swelling tests	[kg]
m_0	mass of initial dry polymer	[kg]
n_O	molar transport rate of oxygen	[$mol\ s^{-1}$]
p	pressure	[Pa]
p_0	pressure at which Q is measured	[Pa]
p_1	N_2-pressure applied in permeability tests	[Pa]
p_2	N_2-pressure after passing the sample (chamber)	[Pa]
p_{IO}	partial pressure of O_2 at the O_2 end	[Pa]
p_m	mean pressure	[Pa]
Δp_L	Laplace/capillary pressure across a curved interface	[Pa]
Δp	total pressure drop across sample	[Pa]
P	porosity	[%]
Q	swelling ratio	[-]
Q	volumetric flow rate	[$m^3\ s^{-1}$]
Q_N	N_2 flow rate	[$m^3\ s^{-1}$]
R (in RT)	universal gas constant = 8.3145	[$J\ mol^{-1}\ K^{-1}$]
R	droplet radius	[m]
Re	Reynolds number	[-]
Re_p	pore Reynolds number	[-]
Re_{crit}	critical Reynolds number	[-]
r_D	$= D_{eff}/D_{AB}$	[-]
S_∞	solubility of solute in ext. phase for a droplet of infinite curvature	[-]
$S(r)$	solubility of the solute when contained in a spherical droplet	[-]
ΔS^{conf}	configurational entropy of emulsion formation	[$J\ K^{-1}$]
T_g	glass transition temperature	[°C]
T	absolute temperature	[K]
t	time	[s]
u	fluid superficial velocity	[$m\ s^{-1}$]
$\bar{u}$	mean gas velocity	[$m\ s^{-1}$]
$\bar{u}_v$	viscous flow contribution	[$m\ s^{-1}$]
$\bar{u}_s$ ($\bar{u}_0$ in *Paper I*)	slip flow contribution / slip effect	[$m\ s^{-1}$]

u_p	pore/interstitial velocity	[m s^{-1}]
u_r	relative velocity between gas and liquid	[m s^{-1}]
u_{lO}	superficial velocity of O_2 entering the sample	[m s^{-1}]
V	volume	[m^3]
V_{sw}	volume of swollen polyMIPE	[m^3]
V_m	molar volume of the solute	[m^3 mol^{-1}]
V_0	volume of initial dry polyMIPE	[m^3]
$\bar{v}$	mean molecular gas velocity	[m s^{-1}]
v_0	droplet (or Stokes') velocity	[m s^{-1}]
We	Weber number	[ ]

Greek letters

γ_{ij}	interfacial tension between phases i and j	[N m^{-1}]
γ_l	surface tension of liquid	[N m^{-1}]
Γ	correction factor for D_{eff}/D_{AB}	[-]
ε_{eff}	effective porosity	[%]
ε	strain	[-]
ε	porosity	[%]
η	dynamic viscosity of the continuous phase	[Pa s]
θ	contact angle (o…oil, w…water, p…polymer)	[°]
λ	mean free path length	[m]
μ	gas viscosity	[Pa s]
μ(r)	chemical potential in a droplet	[J mol^{-1}]
μ_∞	chemical potential in bulk liquid	[J mol^{-1}]
ρ	density	[g cm^{-3}]
ρ_{abs}, ρ_s	absolute/skeletal density	[g cm^{-3}]
ρ_{bulk}, ρ_f	bulk/foam density	[g cm^{-3}]
ρ_g	gas mass density	[kg m^{-3}]
ρ_w	wall density	[g cm^{-3}]
σ_c	compressive stress	[Pa]
τ	tortuosity	[-]
ϕ	openness	[-]
ϕ_p	polymer volume fraction at swelling equilibrium	[-]
ω_{sol}	ratio of extracted material	[-]

List of abbreviations

AC	azodicarbonamide
AIBN	azobisisobutyronitrile
CER	cohesive energy ratio
CIPS	chemically induced phase separation
CTBN	carboxyl-terminated butadiene-acrylonitrile rubber
DGEBA	diglycidyl ether of bisphenol-A
DGEBF	diglycidyl ether of bisphenol-F
DLVO	Derjaguin – Landau – Verwey – Overbeek
DMF	(N,N)-dimethyl formamide
DMSO	dimethyl sulfoxide
DSC	differential scanning calorimetry
DVB	divinyl benzene
EDL	electrochemical double layer
EIPS	evaporation induced phase separation
ELC	energy loss coefficient
EMT	epoxidized mangosteen tannin
ESO	epoxidized soybean oil
ET	emulsion templating
fcc	face-centred cubic
GA	Gibson-Ashby
hcp	hexagonal close-packed
HLB	hydrophilic lipophilic balance
HLD	hydrophilic – lipophilic deviation
IP	internal phase
IPDA	isophorone diamine
IPR	internal phase ratio
ISP	integrated surfactant potency
IUPAC	International Union of Pure and Applied Chemistry
KPS	potassium persulfate (Kaliumpersulfat)
LIPE/MIPE/HIPE	low/medium/high internal phase emulsion
LSW-Theory	Lifshitz – Slyozov – Wagner theory
MTHPA	methyltetrahydrophtalic anhydride
MWCNT	multi-walled carbon nanotubes
NIPS	non-solvent induced phase separation
PEG	polyethylene glycol

PEO	polyethylene oxide
PIPS	polymerisation induced phase separation
PIT	phase inversion temperature
PSD	pore size distribution
RIPS	reaction induced phase separation
SEM	scanning electron microscopy
THF	tetrahydrofuran
TIPS	thermally induced phase separation
VIPS	vapour induced phase separation
W/O – O/W	water-in-oil / oil-in-water

List of publications

This thesis is a summary of the following articles and manuscripts, which are referred to in the text by Roman numerals and appended at the end of the thesis:

Paper I (*published*)

An integrated method for measuring gas permeability and diffusivity of porous solids. Manley, S. S.; **Steindl, P.**; Hewitt, G. F.; Bismarck, A. Chemical Engineering Science, 2020, 223, article 115725

Manley, S. S.: conceptualisation, methodology, investigation, formal analysis, writing - original draft. Steindl, P.: validation, software, formal analysis, investigation, writing – revision & editing, visualisation. Hewitt, G. F.: conceptualisation, methodology. Bismarck, A.: supervision, resources, writing – revision & editing.

Paper II (*published*)

Permeable emulsion-templated porous polyepoxides. **Steindl, P.**; Menner, A.; Bismarck, A. Polymer, 2022, 240, article 124476

Steindl, P.: methodology, software, formal analysis, investigation, visualisation, writing – original draft. Menner, A.: conceptualization, funding acquisition, project administration, supervision, writing – review & editing. Bismarck, A.: conceptualization, methodology, funding acquisition, supervision, resources, writing – review & editing.

Paper III (*published*)

Emulsion-templated flexible epoxy foams. **Steindl, P.**; Decker, H.; Retzl, B.; Jiang, Q.; Menner, A.; Bismarck, A. Polymer, 2021, 215, article 123380

Steindl, P.: formal analysis, investigation, visualisation, writing – original draft. Decker, H.: methodology, formal analysis. Retzl, B.: methodology, formal analysis. Jiang, Q.: conceptualization, methodology, supervision, writing – review & editing. Bismarck, A.: supervision, funding acquisition, resources, writing – review & editing.

1. Introduction

Throughout evolution, when people - scientists, engineers - were looking for solutions to difficult problems, they seeked inspiration in nature, the seemingly inexhaustible source of inspiration. For most of the time, pure observation was the only possible way to study nature. One person, undeniably one the most brilliant brains of mankind, who was already in his lifetime known for his meticulous studies of nature and its mechanics, was Leonardo da Vinci. What set him apart from many others is that he was not satisfied with pure observation, he aspired to imitate nature and provide mankind not only knowledge but also new technologies. Nowadays, a whole scientific branch, bionics (biology and electronics) is dedicated to the exploration and investigation of biological systems and methods, aiming at applying and transferring them to engineering and modern technology (e.g. lotus effect, radar). While this thesis is certainly not about bionics, its underlying idea is the same – learning from nature:

"When modern man builds large load-bearing structures, he uses dense solids: steel, concrete, glass. When nature does the same, she generally uses cellular materials: wood, bone, coral. There must be a reason for it." (M.F. Ashby, 1983)[1]

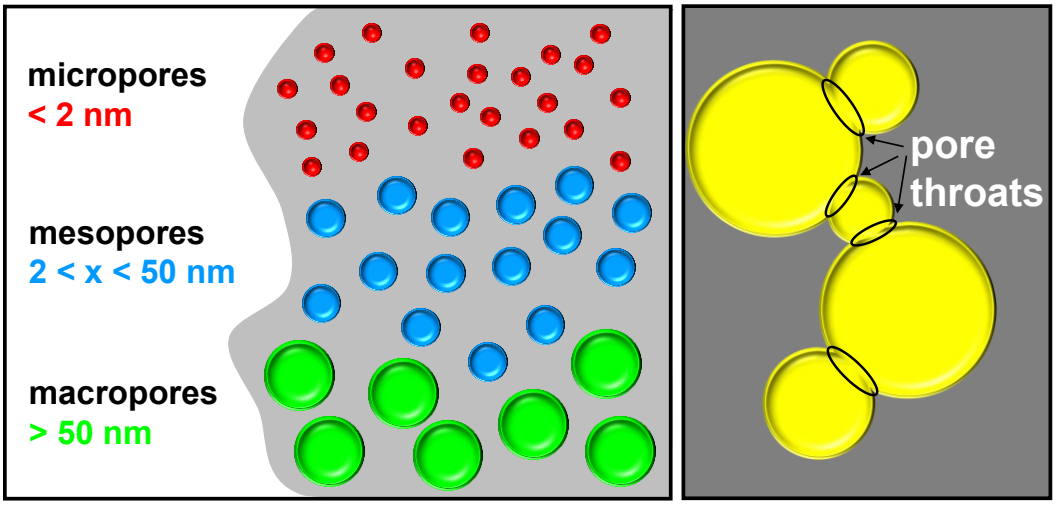

Figure 1: left: classification of porous materials according to their pore size; right: pore throats are the channels the connect pores

A porous material can be imagined as a biphasic-system, with one phase being a solid and the other air (void space). If spherically shaped, the void cells are termed pores and the windows connecting two pores are referred to as pore throats. According to their pore size,

porous materials are commonly classified as microporous (< 2 nm), mesoporous (2 < x < 50 nm) or macroporous (> 50 nm) (**Figure 1**).

In the last few decades, the interest in and demand for porous materials has skyrocketed, not least because of increasingly concerning global environmental problems. Porous polymers have the potential to be equivalent substitutes for metals or other solids from a structural and load bearing point of view, due to their excellent weight-to-performance ratio. A reduction in weight results in a decrease in energy input required to move an object. The lighter an aircraft is for example, the lower is its fuel consumption. Macroporous polymers are further used as insulation materials and in packaging, as cores for composite sandwich structures, in filters, chromatography columns and catalysis for example, making use of their large surface area.

Polymer foams are a subset of porous materials. Besides methods such as chemical and physical blowing, salt leaching, sintering or phase separation, polymer foams can also be prepared from emulsion templates. Emulsion templating was first reported in 1962 but has been established only in the last two decades as a reliable and highly reproducible method for synthesising polymer foams. High or medium internal phase emulsions (HIPEs/MIPEs) are prepared by dispersing a major internal phase as discrete droplets in a minor, monomer containing, external (or continuous) phase. The latter is polymerised and the internal phase, serving as template, subsequently removed again, leaving behind a porous material termed poly(merised)HIPE/MIPE. Emulsion templating outperforms conventional foaming techniques with regard to the ability to tailor morphology and properties of the final materials. Adjustment of emulsion formulation and emulsification as well as polymerisation conditions give control over the properties of polymer foams.

The best explored and most common emulsion-templated porous polymers are based on styrene (St) and divinylbenzene (DVB); investigating this specific system has significantly contributed to the progress of emulsion templating in the last decades. However, their inherent brittleness limits the applications of poly(St-co-DVB) based foams. Each polymer system is characterised by a unique set of properties and each application requires certain properties. Therefore, it is crucial to choose a suitable polymer system that suits one's needs. However,

out of the huge pool of polymers that are on the market, only a small fraction has been utilised for the manufacture of porous materials by now. Epoxy resins possess a wide range of advantageous properties, such as high mechanical and thermal stability, excellent chemical (corrosion) resistance and insulating properties, good adhesion to a variety of substrates and versatile processing, while still being relatively cost-friendly, compared to high-performance polymers such as polyimides or PEEK. Compared to other monomer systems which show distinct shrinkage after polymerisation, polyepoxides maintain size and shape on curing. Nevertheless, despite all these beneficial attributes of epoxy systems, curing of epoxy resins in presence of water is a challenge that has to be dealt with. We believe that the liaison of epoxides and emulsion templating is not only very reasonable, but also potentially very powerful and is therefore worth to be further explored.

2. Aims & Objectives

The goal of this work is to prepare macroporous polyepoxides using emulsion templating and thereby show that the pool of monomer systems applicable for this method is far from exhausted. Moreover, the superiority of emulsion templating over commonly used methods, such as chemical or physical blowing, should be demonstrated.

In a first step, the aim is to prepare solid epoxy foams from surfactant-stabilised water-in-oil (W/O) emulsions using an easily processable (low viscosity) commercial epoxy system, as a proof of concept. The influence of alterations in formulation and emulsification conditions on a final material's morphology and properties will be investigated. Due to their different applications, synthesis of polymer foams with open-porous as well as closed-cell pore structure is aspired. For a thorough characterisation of materials with interconnected pore morphology, determination of their permeability is indispensable. Therefore, gas permeability measurements will be carried out using a purpose-built apparatus, whose working principle is based on a pressure-rise technique.

Building on the gained insights and findings, a more specific, flexible, epoxy system will be employed to prepare flexible porous polyepoxides with tuneable, spring-like properties. These foams will be subjected to cyclic compression tests in order to investigate their ability to retrieve their initial shape after release of the applied compressive load.

Thus, to achieve the set/aspired objectives of this PhD project, the following challenges had to be overcome:

1 Proof of concept: emulsion templated macroporous polyepoxides

- 1.1 Performing a surfactant screening to identify a non-ionic emulsifier capable to stabilise W/O emulsions based on the chosen commercial epoxy model system
- 1.2 Selective variation of formulation and emulsification parameters – surfactant amount, agitation speed, internal phase ratio – to explore the limits of this particular monomer/hardener/surfactant system.

1.3 Characterisation of the prepared porous polyepoxides: morphology/pore structure, density & porosity, thermal stability, compression properties, gas permeability, swelling behaviour

2 Setting up the gas permeability apparatus and testing its reliability

3 Flexible epoxy polyHIPEs

3.1 Preparation of polyHIPEs using a flexible epoxy system

3.2 Characterisation of the polymer foams, including cyclic compression tests

Subsequent to this short introductory section, outlining principal ideas, aims and experimental tasks of this project, a literature review will give information about the theoretical background and summarise relevant previous research. Porous polymers and their applications are briefly introduced, prior to a more detailed description of emulsions, including different types, formation as well as (de)stabilisation. Afterwards, the most common and popular methods to produce macroporous polymers are presented, with special focus on emulsion templating and its capability to influence a material's morphological as well as mechanical properties. Following a general introduction to epoxy resins, recent progress in the preparation of epoxy foams is reported. Explanations about the measurement of gas permeability and the fluid flow through porous media in general conclude the literature review.

3. Literature review

3.1. Common methods for producing porous polymers

Macroporous polymers can be prepared using a range of methods.[2-4] The choice of the method depends primarily on the polymer system and the required properties for potential applications. Simplicity/complexity of a process, effort and costs have to be considered as well. With increasing importance and popularity of green chemistry, environmental benignity became one of the principal factors to consider when deciding upon a preparation method for porous polymers.

The most common processes to manufacture macroporous polymers include gas foaming, phase separation and templating.

In **chemical blowing**, the reaction of a so-called blowing agent with a functional group of another compound (in epoxy systems mostly the amine or anhydride hardener) of the formulation generates gas and introduces porosity.[5,6] The gaseous compound can also be the side product of the polymerisation reaction (or released during the decomposition of additives (e.g. azo-compounds → N_2).[7,8] While the process is highly effective and easy to implement, control over exact shape and dimensions of the final porous material is limited, compared to templating methods.

Physical blowing techniques mainly employ low-boiling aliphatic compounds (e.g. hexane, cyclohexane) as blowing agents, which are mixed with monomers, hardener and any additives.[6,9] Heat, produced in the exothermic curing reaction or applied externally, commonly triggers the liquid-vapour phase transition and leads to the creation of a porous structure. Supercritical fluids, such as supercritical carbon dioxide ($scCO_2$), are of interest as 'green' blowing agents.[10-12] However, they can only be used in pressurised environments when CO_2 is not gaseous. A sudden pressure drop induces the expansion of the $scCO_2$ accompanied with a phase transition. Pore size, pore size distribution (PSD) and pore structure can be influenced to a certain degree by the choice of the blowing agent (its properties) and the pressure conditions. Traditionally used halogenated compounds, such as chlorofluorocarbons

and perfluorinated compounds, are only rarely employed because of environmental concerns, high diffusivity and considerable expenses.

Rather uncommon are approaches of **biological blowing**, for example the formation of gas by yeast. A major drawback of all blowing techniques is the lack of interconnectivity in the final pore structure.

Furthermore, it is possible to prepare porous polymers, in particular membranes, by means of **phase separation** (PS).[2,13] The process is based on creating a homogenous polymer-solvent solution and then forcing the system to phase separate by tuning the polymer-solvent miscibility, yielding a polymer-rich and a solvent-rich phase. The phase separated structure is locked in place by freeze drying, followed by removal of the solvent. There are several ways to trigger phase separation. The most common and best explored methodologies are thermally induced phase separation (TIPS),[14-18] non-solvent induced PS (NIPS),[18-23] also known as immersion precipitation, and chemically induced PS (CIPS), [24-30] also referred to as polymerisation induced (PIPS)[31,32] or reaction induced PS (RIPS).[33] Further processes and terms used in literature include solvent induced PS (SIPS),[34,35] vapour induced PS (VIPS),[18,36-38] evaporation induced PS (EIPS),[38,39] photo induced PS (as sub category of PIPS)[40] and pressure induced PS.[41,42]

Syntactic foams can be prepared by adding hollow or expandable spheres to a resin formulation.[43-46] These spheres remain in the material and are thus primarily responsible for introducing porosity. Moreover, they substantially contribute to the properties of the final porous polymer which is characterised by a well-defined closed-cell pore structure with pores of uniform size, controllable through the size of the additives.

Colloidal templating[47] is the umbrella term for particle templating, foam templating, emulsion templating and methods derived therefrom, e.g. foamed emulsion templating[48-54]. All templating methods make use of porogens which are defined as substances “that can be used as a template and then removed to generate pores.[22] Solids, liquids, gases and even supercritical fluids are employed as porogens.[55] They are integrated as external compounds

into a resin formulation and removed again after curing of the polymer matrix, leaving a porous structure behind.

Particle templating (also called particle leaching) employs organic or inorganic solid particles which are eventually washed out (e.g. for salt crystals[56]) or dissolved to produce porous polymers.[55] This method allows for the preparation of porous materials with a well-defined pore morphology and a narrow pore size distribution, similar to syntactic foams. **Salt leaching**, as subset of particle templating, describes the addition of micron-sized salt crystals to a monomer-based solution.[10] Salt is initially integrated in the polymer matrix, but after curing again washed out.

Foam templating uses gaseous templating phases, air in the special case of **air templating**, also referred to as frothing.[48,57] In air templating, a monomer containing mixture is frothed by mechanically beating air into it.[58-60] Stabilisers are often needed to prevent collapse of the foam before curing can sufficiently stabilise the fragile framework. Foam templates can further be generated by injecting gas (e.g. argon[61,62]) through membranes into a liquid solution, followed by immediate fixation of the foam by freezing with liquid nitrogen or the use of pressurised carbon dioxide or nitrogen.[12,63] The major advantage of foam templating is that the template phase does not require removal since it is air or another gas. While this saves time and money, the method generally suffers from a lack of control over pore structure determining properties/parameters, such as the pore/bubble size.

Emulsion templating, detailed in the following, describes the formation of an emulsion from a monomer-hardener-emulsifier formulation and a liquid templating phase, which is removed after curing.

3.2. Emulsion templating

Knowledge about emulsion science (e.g. formation and stability) is the base of emulsion templating and thus indispensable for understanding the method and for purposefully utilising all its assets. Pioneer work in the field of emulsion templating was done by Bartl and von Bonin already at the beginning of the 1960s.64 They synthesised divinylbenzene - styrene and methacrylic acid methyl ester polymers from O/W emulsions with monomers of either

substance forming part of the external organic phase. In 1966, Lissant defined the terms ‘low/medium/high internal phase (ratio) emulsion’ and introduced their catchy abbreviations LIPE/MIPE/HIPE.65 The term ‘polyHIPE’, as description for low-density polymers prepared from emulsion templates, was first used in a patent filed by Unilever in 1982.66 However, about twenty more years passed until around the turn of the millennium the unstoppable and still ongoing rise of emulsion templating started.

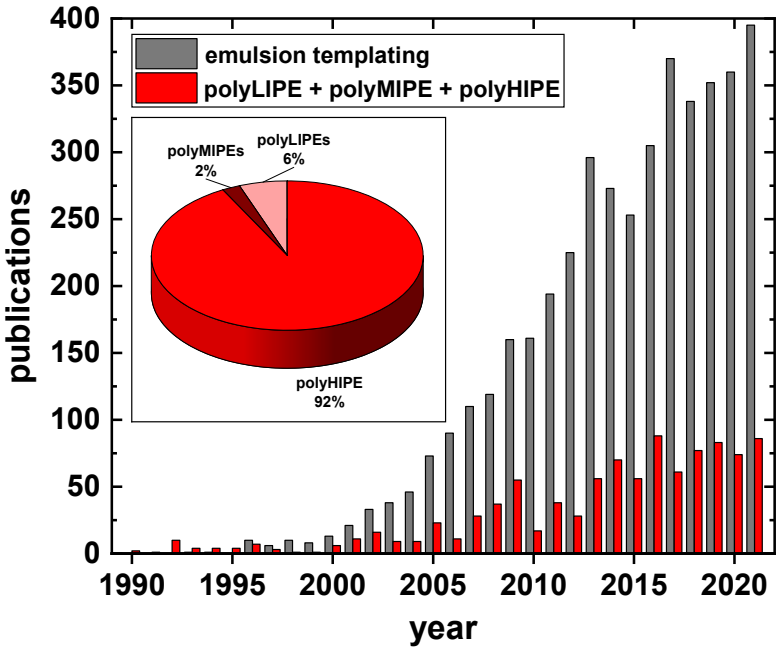

Figure 2: Number of publications between 1990 and 2021 (data obtained on 19 January 2022) for search concepts, emulsion templating‘ and ‚polyLIPE/polyMIPE/polyHIPE’. SciFinder® (classic) was used as search platform.

The increasing interest in emulsion templating is also reflected in the number of publications containing the concept ‘emulsion templating’, as illustrated in **Figure 2**: from 2000 to 2020 the annual number of publications related to emulsion templating increased from 13 to 360. Consequently, also the number of articles related to polyLIPEs/MIPEs/HIPEs increased, with polyHIPEs accounting for more than 90% (inset **Figure 2**).

Porous scaffolds can be prepared from emulsions, if the external phase contains monomers/hardener and an initiator, often also an emulsifying agent (**Figure 3**). The internal phase is dispersed as small droplets in the organic phase, eventually yielding an emulsion with characteristic creamy texture. The droplet phase performs the task of a liquid template, essentially determining the porosity and defining the morphology of the final material.

Solidification of the external matrix, followed by removal of the internal phase, results in porous polymers termed poly(merised)LIPEs/MIPEs/HIPEs, in analogy to the classification of emulsions as LIPEs/MIPEs/HIPEs according to their internal phase ratios of lower than 30%, 30 - 74% and higher than 74%, respectively.

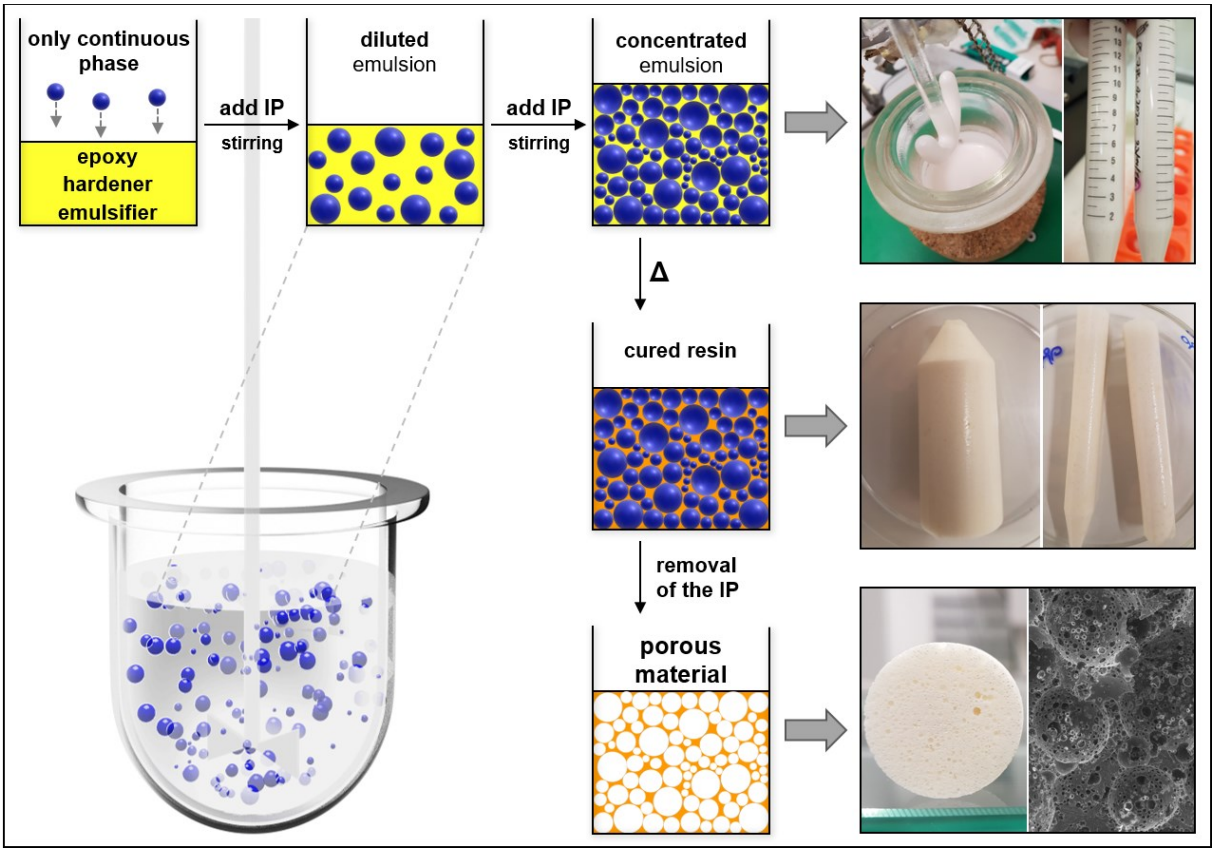

Figure 3: Illustration of the emulsion templating process, supported by real images (right hand side). Addition of an aqueous internal phase leads first to a diluted and then a concentrated emulsion. After curing of the organic matrix phase, the internal phase is removed, leaving a porous material behind.

Polymerizable emulsions can not only be used to prepare porous scaffolds. Addition of monomers to the internal phase and subsequent polymerisation yields polymer beads,[67-72] whereas solidification of both phases can be used to produce composites (**Figure 4**).[73,74] A number of comprehensive reviews about emulsion templating and emulsion-templated porous materials, written by some of the leading scientists in this field, is presented in **Table 1**.

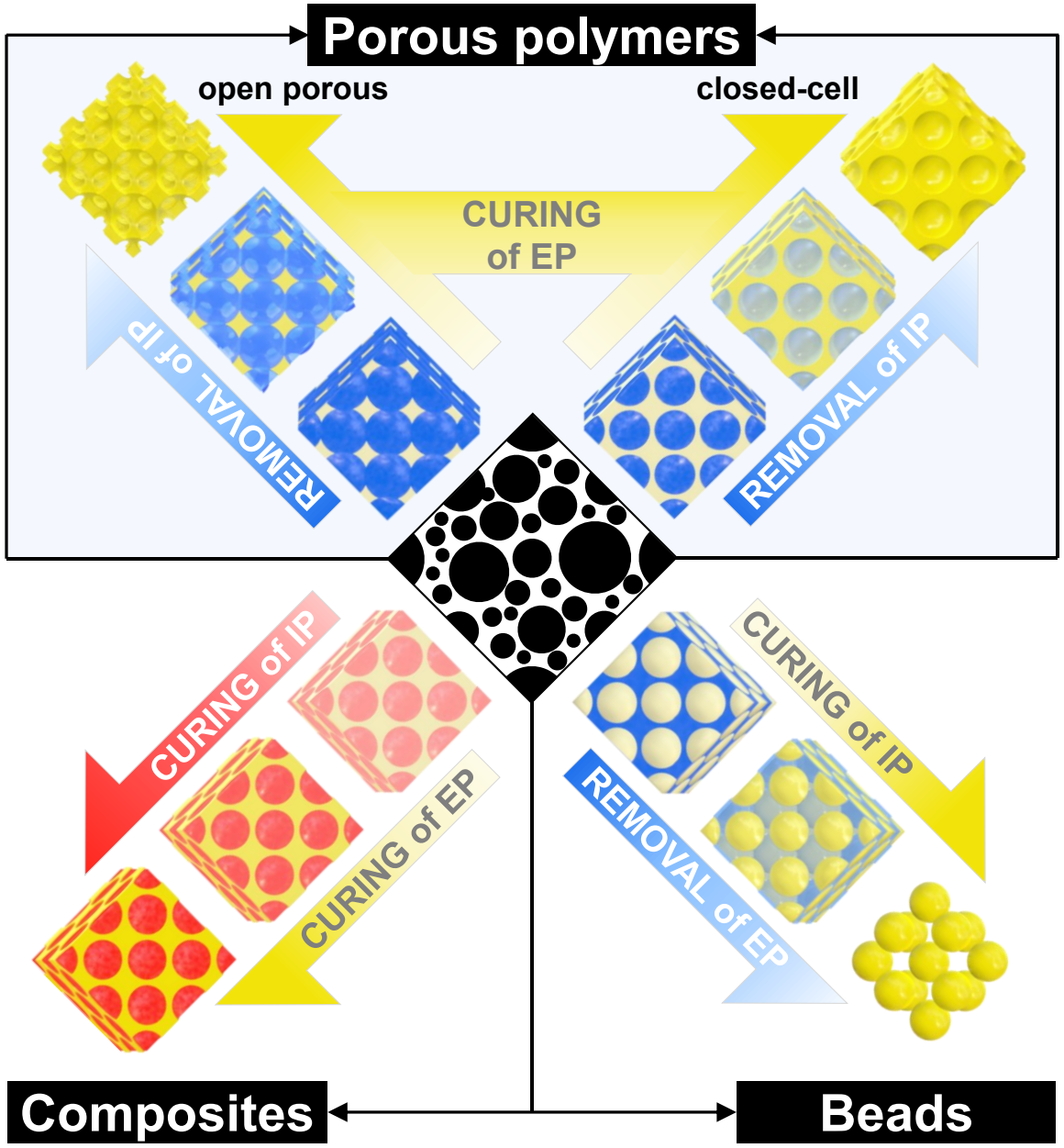

Figure 4: Schematic representation of the different kinds of materials that can be produced from emulsions containing a polymerizable species either in the internal (dispersed) phase (IP), the external (continuous) phase (EP) or both.

Table 1: List of reviews about emulsion templating and related topics (in chronological order)

Author(s)	Title	Year
Cameron N.R.[75]	High internal phase emulsion templating as a route to well-defined porous polymers	2005
Zhang H., Cooper A.I.[76]	Synthesis and applications of emulsion-templated porous materials	2005
Kimmins S.D., Cameron N.R.[77]	Functional Porous Polymers by Emulsion Templating: Recent Advances	2011
Pulko I., Krajnc P.[78]	High Internal Phase Emulsion Templating - A Path to Hierarchically Porous Functional Polymers	2012

Cameron N.R., Krajnc P., Silverstein M.S.[47]	Colloidal Templating	2012
Silverstein M.S.[79]	Emulsion-templated porous polymers: A retrospective perspective	2013
Silverstein M.S.[80]	PolyHIPEs: Recent advances in emulsion-templated porous polymers	2014
Tebboth M., Menner A., Kogelbauer A., Bismarck A.[81]	Polymerised high internal phase emulsions for fluid separation applications	2014
Silverstein M.S.[82]	Emulsion-templated polymers: Contemporary contemplations	2017
Stubenrauch C., Menner A., Bismarck A., Drenckham W.[48]	Emulsion and Foam Templating - Promising Routes to Tailor-Made Porous Polymers	2018
Zhang T., Sanguramath R.A., Israel S., Silverstein M.S.[83]	Emulsion Templating: Porous Polymers and Beyond	2019
Dikici B.A., Claeyssens F.[84]	Basic Principles of Emulsion Templating and Its Use as an Emerging Manufacturing Method of Tissue Engineering Scaffolds	2020
Kramer S., Cameron N.R., Krajnc P.[85]	Porous Polymers from High Internal Phase Emulsions as Scaffolds for Biological Applications	2021
Foudazi R.[86]	HIPEs to PolyHIPEs	2021

3.3. Emulsions

An emulsion is by definition of the IUPAC (International Union of Pure and Applied Chemistry) ‘a fluid colloidal system in which liquid droplets…are *dispersed* in a liquid’. More commonly, emulsions are described as systems of two immiscible liquids forming a homogenous dispersion. One classification system uses nature and spatial distribution of the two phases. Based on the classical example of an oil/water system, the lipophilic substance is termed oil phase and the hydrophilic one aqueous phase. Successful homogenization yields water-in-oil (W/O) or oil-in-water (O/W) emulsions, whereupon the nature of the droplet phase is named first by convention. The substance forming the droplets is called dispersed, discontinuous or internal phase; the bulk/matrix is referred to as continuous or external phase.

Volume and viscosity ratios, temperature and type and concentration of emulsifier prevailingly determine which phase is the dispersed and continuous phase. The internal phase volume ratio (IPR), the volume fraction of the internal phase relative to the total emulsion volume, is the base of another classification system. Emulsions are categorised as low, medium or high internal phase emulsions (LIPEs/MIPEs/HIPEs), with IPR below 30 %, between 30 % and 74

%, and above 74 %, respectively. The threshold for HIPEs is related to the space occupied by rigid equal sized spheres in a hexagonal close-packed (hcp) or face-centred cubic (fcc) lattice.

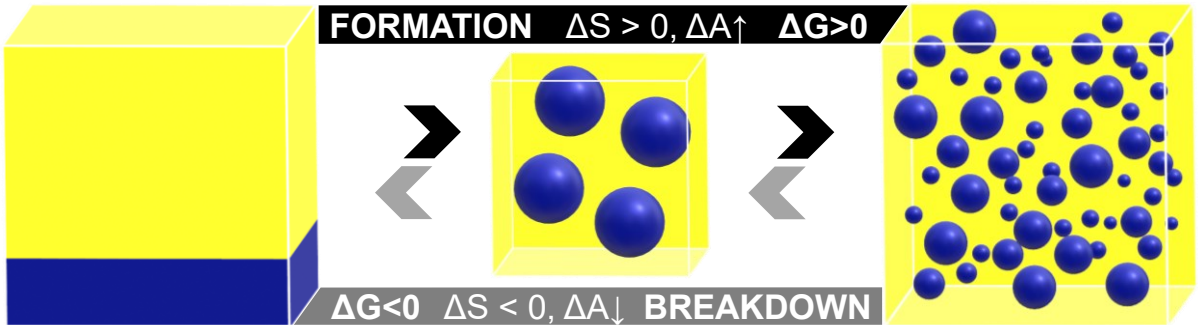

Figure 5: Energetic relations in emulsion formation/break-up. Left-to-right: droplet break-up leads to increases in interface area *ΔA* and configurational entropy *ΔS*, resulting in a positive Gibbs free energy *ΔG*, thus, emulsion formation usually requires energy input. Right-to-left: emulsion breakdown occurs spontaneously, because it is energetically favoured due to decreases in interface area.

$$\Delta G^{form} = \gamma_{12}\Delta A - T\Delta S^{conf} \quad (1)$$

The free energy of emulsion formation ΔG^{form}, derived from the second law of thermodynamics (**Eq.(1)**), is mainly comprised by three components: an interfacial energy term $\gamma_{12}\Delta A$, an entropy term $T\Delta S^{conf}$ and a composition term $\Sigma n_i d\mu_i$, which can be omitted for emulsions because of constant composition, if assumed that surfactant migration from continuous into droplet phase is negligible.

An increase in droplet number is inevitably connected with an increase in configurational entropy. However, ΔS^{conf} and/or an increase in temperature are rarely able to compensate the high gain in interface area $\Delta A = A_2 - A_1$. Thus, in most cases $\gamma_{12}\Delta A >> T\Delta S^{conf}$ and as a direct consequence $\Delta G^{form} > 0$, which means that emulsion formation is nonspontaneous.[87,88] Spontaneous emulsification rarely happens and only in case of sufficiently low interfacial tension ($\gamma_{12} \approx 0$!). Therefore, due to its inherent thermal instability, energy input is required to facilitate emulsification and push a two-phase system towards kinetic stability.

Energy is commonly introduced by stirring, shaking, blending, ultrasonication or shear, all leading to a significant increase in surface area because of droplet break-up and thus favouring emulsion formation. This suggests that in fact it is the surface/interfacial area that plays a key role in emulsion formation, more than merely the number of droplets. On the other end,

reduction of the interfacial area is the driving force for emulsion destabilisation and break-down. The main mechanisms promoting emulsion destabilisation are depicted in **Figure 6.**

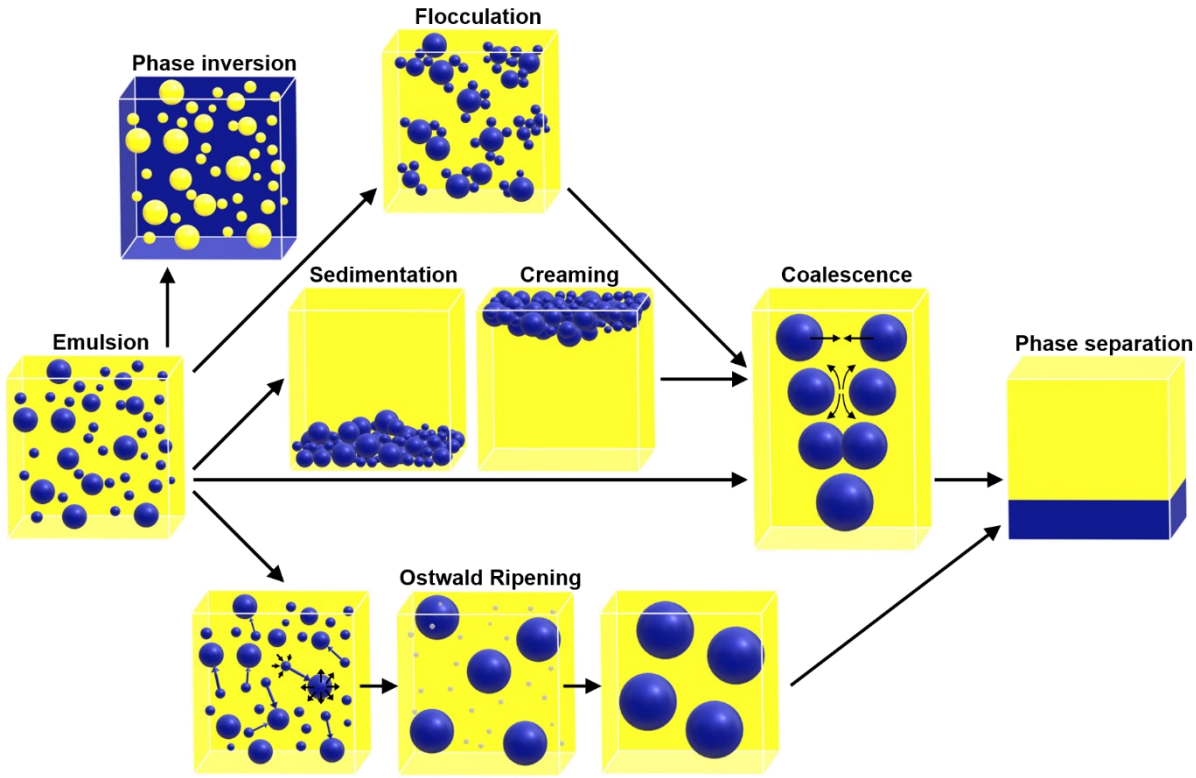

Figure 6: Illustration of the most important phenomena leading to emulsion destabilisation and ultimately phase separation.

Stoke's law (**Eq.(2)**) relates some important parameters involved in emulsion formation and stability (such as droplet size and viscosity) by balancing hydrodynamic $6\pi\eta r v$ and gravitational force $\frac{4}{3}\pi r^3 \Delta\rho g$. It states that the droplet (or Stokes) velocity v_0 [m s^{-1}] is directly proportional to the droplet radius r, mainly determined by the energy input during emulsification, the density difference between dispersed and continuous phase $\Delta\rho = |\rho_2 - \rho_1|$ [g cm^{-3}] and the gravitational acceleration g (≈9.8 m s^{-2}), whereas it is indirectly proportional to the viscosity of the continuous phase η [Pa s].

$$v_0 = \frac{dx}{dt} = \frac{2r^2 \Delta\rho g}{9\eta} \quad (2)$$

The higher the velocity of droplets moving in the external phase, the faster emulsion destabilisation due to creaming and sedimentation progresses. A density difference between the two phases causes a net gravitational force acting on the dispersed droplets. If the density of the dispersed phase exceeds the density of the external one, droplets precipitate and

sediment.[89-91] The opposite case of ascending droplets (or bubbles) due to lower density of the internal phase is called creaming.[91] Both processes, sedimentation and creaming, result in a concentration gradient along the vertical axis, with droplets accumulating at the bottom or the liquid-air interface, respectively. The sedimentation/creaming rate of a single droplet is described by Stoke's law (**Eq.(2)**). Emulsion destabilisation due to sedimentation and creaming can be kept low by minimisation of the density difference, reduction of the droplet size or by using a continuous phase of higher viscosity. Strictly, Stoke's law is only valid for droplets with monodispersed size distribution.

The Weber number *We* is another important parameter related to emulsion formation.[92] It is defined as the ratio between inertial forces and surface tension and provides information about droplet break-up for Newtonian liquids in subsonic gas flows (**Eq.(3)**).

$$\mathrm{We} = \frac{\rho_g u_r^2 d_p}{\gamma_l} \qquad \textbf{(3)}$$

where is ρ_g is the gas mass density [kg m^{-3}] , u_r the relative velocity between gas and liquid [m s^{-1}], d_p the drop or liquid jet diameter [m] and γ_l the surface tension of the liquid [N m^{-1}].

Flocculation refers to the aggregation of droplets into larger units ('flocs') stimulated by van der Waals attractions.[93,94] After sedimentation and creaming, flocculation is another destabilisation mechanism in which droplets maintain their size. DLVO – theory predicts the tendency of droplets to aggregate, by mainly combining attractive van der Waals and repulsive electrostatic forces into one total potential energy function (Figure 7). A colloidal system is considered stable when repulsive forces prevail.

When two droplets approach from infinity, at a certain droplet distance the total potential energy function reaches a local minimum and flocculation occurs. The formed droplet network is only loose and droplets can easily be redispersed. On further reducing the droplet distance, the primary minimum of the potential energy curve is reached and droplets coalesce.

Coalescence occurs when two or more droplets merge to form a larger one.[91,93,95] It strongly depends on short-range forces (**Figure 7**) and thus requires droplet collision or at least close contact between the droplets. Therefore, coalescence often occurs as consequence or in

combination with sedimentation, creaming, flocculation or aggregation. Emulsion destabilisation proceeds in different stages: drainage and thinning of the film of continuous phase between two droplets, film rupture and ultimately collapse of the droplets.

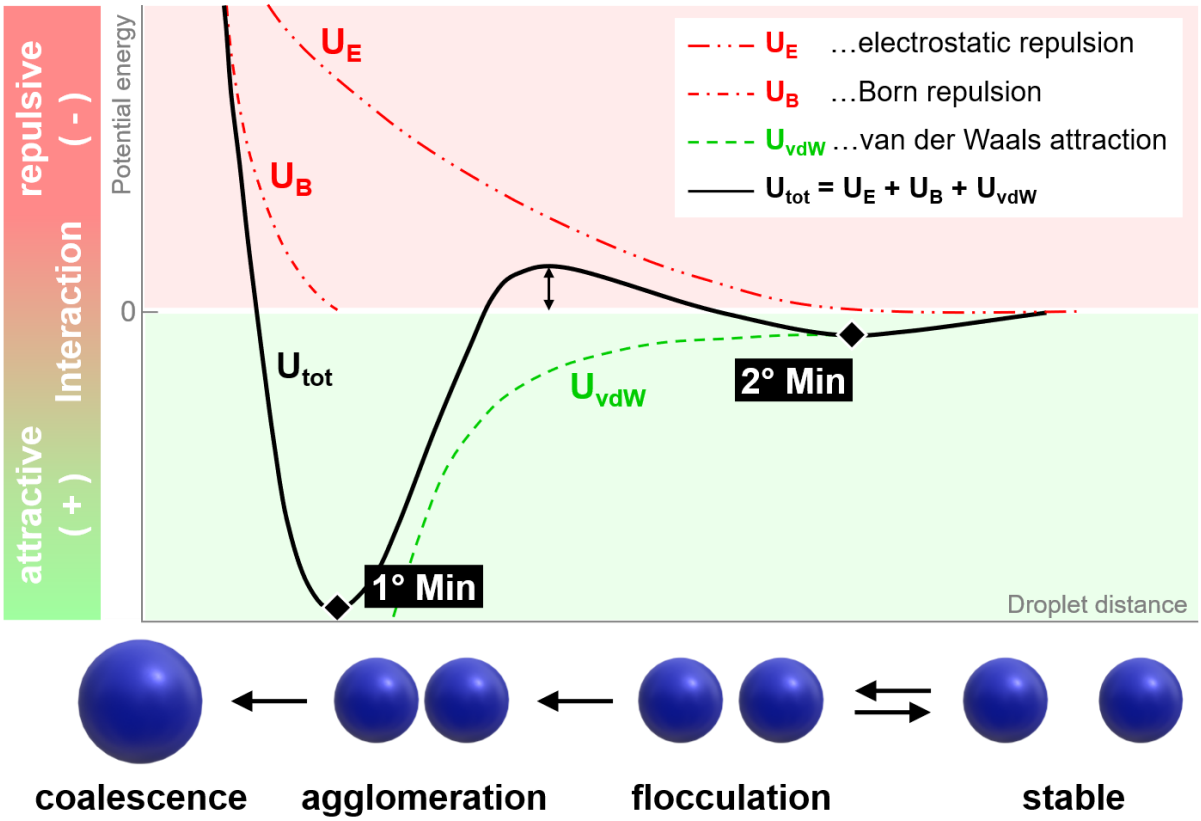

Figure 7: Scheme of the potential energy as described by the DLVO – theory. The interaction potential between two droplets changes with distance and determines the stability of emulsions towards flocculation, agglomeration and coalescence. It is mainly the sum of attractive van der Waals forces (U_{vdW}), electrostatic (U_E) and Born repulsion (U_B). (adopted from Graeber N., PhD thesis)[96]

This results in a reduction of interfacial area and therefore acts as the main driving force. A highly viscous continuous phase, for example, can retard the drainage rate by reducing the mobility/movement within the continuous phase, as described by the Stokes – Einstein equation (**Eq.(4)**). This leads to a reduction in droplet collision and thus lowers coalescence:

$$D = \frac{k_B T}{6\pi\eta r} \tag{4}$$

where D [m^2 s^{-1}] is the diffusion coefficient, η [Pa s] the dynamic viscosity of the continuous phase, r [m] the droplet radius, k_B [J K^{-1}] the Boltzmann constant and T [K] the absolute temperature.

However, the addition of an emulsifier is often more effective in preventing droplet fusion. Emulsifiers adsorb at the interface of dispersed droplets and can hereby increase film stability

by altering interfacial tension and increasing the elasticity of the interface and/or add charges to droplets.

Phase inversion describes the phenomenon of identity switch of the two phases, i.e. the internal phase becomes the external and vice versa.[93,95,97-101] It can be stimulated or inhibited by the choice of the internal phase ratio (IPR), the addition of a surfactant or other additives, the viscosities of the two phases or the energy input (agitation speed, type of impeller, etc) during emulsification.

Ostwald Ripening (OR), also called coarsening or disproportionation, is a direct consequence of poly-dispersity and manifests itself as growth of large droplets at the expense of smaller ones.[93,102,103] The process is driven by the curvature dependence of the chemical potential (**Eq.(5)**) and thus the solubility of droplets of different sizes.[104] The curvature κ, on the other hand, is inevitably related to the droplet radius. The capillary pressure across a curved interface Δp_L [Pa] can be calculated as function of droplet radius r [m] and interfacial tension between droplet and continuous phase γ_{12} [mN/m] using the Young-Laplace equation:[105,106]

$$\mu(r) = \mu_\infty + V_m \gamma \kappa \xrightarrow[\text{Young-Laplace eq.}]{\Delta p_L = \frac{2\gamma}{r} = \gamma\kappa} \mu(r) = \mu_\infty + \frac{2\gamma}{r} V_m \tag{5}$$

with $\mu(r)$ and μ_∞ being the chemical potential in droplet and bulk liquid, respectively, V_m the molar volume of the dispersed phase, $\kappa = \frac{2}{r}$ the curvature of a spherical droplet and Δp_L the Laplace pressure.

According to **Eq.(5)**, capillary pressure and thus chemical potential increase with decreasing droplet size. Originating from the increased solubility, as described by the Kelvin equation (**Eq.(6)**),[107-110] derived from the equilibrium potentials of both phases, molecules diffuse from small droplets of the dispersed phase into the bulk and eventually deposit on larger droplets.[111] The then even higher capillary pressure of small droplets promotes further shrinkage and at the same time larger droplets continue to grow.

$$S(r) = S_\infty \exp\left(\frac{2\gamma}{r}\frac{V_m}{RT}\right) = S_\infty \exp\left(\Delta p_L \frac{M}{\rho RT}\right) \tag{6}$$

where S_∞ denotes the solubility of the dispersed phase in the external phase for a droplet of infinite curvature and $S(r)$ the solubility of the solute when contained in a spherical droplet of radius r. The rate of Ostwald ripening can be calculated using the Lifshitz – Slyozov – Wagner (LSW) theory.[112-116]

Ostwald ripening can hardly be completely suppressed (this would only apply for a perfectly monodispersed system or for an internal phase with no solubility in the external phase at all), but it is possible to reduce the rate of OR, for example through a narrow droplet size distribution, low solubility of the dispersed phase in the continuous one, the addition of electrolytes (e.g. sodium chloride, calcium chloride, sodium sulphate)[117-121] to the aqueous phase or influencing interfacial tension and the stability of the interfacial layer by adding a suitable emulsifier.[88,122,123]

In addition to the distinct classifications of emulsions according to the combination of chemical nature and spatial distribution in O/W or W/O and according to their IPR, liquid-liquid dispersions can further be labelled as macroemulsions, nanoemulsions or microemulsions. The principal characteristics used hereby are droplet size, as suggest by the prefixes macro/nano/micro, appearance and emulsion stability, in terms of the time frame until substantial degradation occurs. Confusingly, the boundaries of the subgroups and the terminology used in literature are not consistent.[124] Macroemulsions typically have droplets larger than 1 µm and therefore scatter light, which makes them appear milky white. They are kinetically stable but thermodynamically unstable, which means external energy input is required to overcome the energy barrier for increasing the interfacial area related to droplet break-up.

Nanoemulsions have droplets in a size range between about 20 nm and a few hundred nanometres. Depending on the droplet size they can be either transparent (or at least translucent) or blue-white.[125,126] Typically, the dispersed phase of nanoemulsions consists of a combination of ionic surfactant and co-stabiliser. The latter can either be a water insoluble compound such as a long-chain alkane (hexadecane) or a short aliphatic chain alcohol.[127] Similar to macroemulsions, emulsification does not happen spontaneously. Nanoemulsions

are also only kinetically stable, but nevertheless show significant differences in long-term physical stability. Due to their small droplet sizes, Brownian motion exceeds the vertically acting gravitational force and thus prevents sedimentation, creaming. Steric stabilisation (**Figure 8**), induced by adsorption of surfactant molecules at the droplet surfaces, results in layers with thicknesses comparable to the droplet size, which protects nanoemulsions from flocculation and coalescence. The Laplace pressure of droplets in nanoemulsions can take on values up to several hundred thousand Pascal, which explains why Ostwald ripening is the main destabilisation mechanism in nanoemulsions.[128] Furthermore, nanoemulsions are relatively insensitive towards temperature or pH changes.[129]

Widely spread synonyms include 'submicrometer emulsion', 'ultrafine emulsion', 'finely dispersed emulsion' and most notably 'miniemulsion'.[130-132] Although the term 'nanoemulsion' prevailed (mainly because the droplets are in the nanometre range) and most publications indicate the equality of the two words, few authors still treat nano- and miniemulsions as separate species.[133] Moreover, IUPAC has only an entry for 'mini-emulsion'.[134]

Microemulsions have a characteristic average droplet size in the range of 1 – 100 nm, which is significantly smaller than the wavelength of visible light and thus the reason for optical transparency. It is crucial for the formation of a microemulsion that the two liquids exhibit very low interfacial tensions (γ_{12}=0). Commonly a mixture of surfactants or a combination of surfactant and co-stabilizer is used.[126]

Unlike macro- and nanoemulsions, microemulsions are thermodynamically stable and subsequently exhibit substantially different properties. Considering the size range, the term 'microemulsion' is a misnomer. One possible explanation for the misleading naming is that the droplets in conventional emulsions are often assumed to have an average diameter of about 1 mm (10^{-3} m). The prefix 'micro' stands for 10^{-6} and the combination with 10^{-3} m yields 10^{-9} m which equals 1 nm.[134] Unlike nanoemulsions, which require low to moderate emulsifier concentrations in the range of 1 – 3 wt.%, high concentrations in the range of 15 – 30 wt.% are typically needed to prepare microemulsions.[126,135]

Differences as well as similarities between nanoemulsions and microemulsions have been thoroughly reviewed and summarised by McClements.[124]

3.3.1. Stabilisation of emulsions

Emulsion stability refers to the timescale until destabilisation mechanisms have caused a substantial change in emulsion properties. Dispersed colloidal systems exhibit a natural tendency to attract each other, which, in the absence of repulsive forces or an energy barrier, can quickly culminate in phase separation. Generally, there are two strategies/approaches/mechanisms to retard emulsion breakdown: electrostatic and steric stabilisation.[136] This can be achieved by adding either molecular or particulate emulsifying agents. Each species features a distinct set of advantages, which make them suitable/appropriate for certain applications.

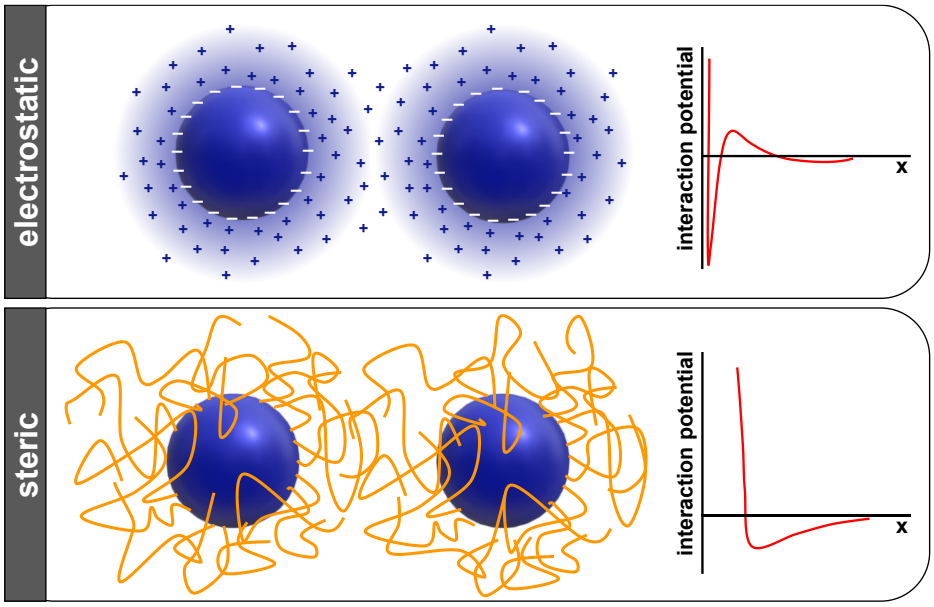

Figure 8: Electrostatic and steric repulsion are the two main mechanisms preventing droplet aggregation. The interaction potential, although completely different, both heavily depend on the distance *x* of two droplet centres.

In electrostatically stabilised emulsions an ionic charge is imparted to the interface of droplets, which induces the formation of an electrochemical double layer (EDL) causing mutual repulsion of droplets. Steric stabilisation, on the other hand, is achieved through a structure-mechanical barrier, created by immobilising non-ionic surfactant or polymer molecules on the droplet interfaces. Both approaches aim at screening the attractive forces and thus preventing

droplet collisions, which are prerequisite for coalescence. The DLVO-theory (**Figure 7**) is therefore widely used to describe or even predict colloidal stability.

The predominant types of emulsifying agents employed in emulsion/dispersion stabilisation are surface active agents, called surfactants and particles. Emulsifiers adsorb at the liquid-liquid interface and form an interfacial film, which not only reduce the interfacial tension but reduce the overall thermal instability. The interfacial film either acts directly as steric or mechanical barrier (polymers, non-ionic surfactants and particles, respectively) or induces an electrical barrier (ionic surfactants), thus effectively reducing the rate of coalescence.

Surfactants are amphiphilic molecules with a polar or ionic hydrophilic head group and a non-polar lipophilic long-chain hydrocarbon tail. They are commonly classified according to the nature of the head group as non-ionic, cationic, anionic or zwitter-ionic/amphoteric. Additionally, surfactants can be categorised as polymeric surfactants. Cationic surfactants (e.g. amine salts, NH_4^+ salts) have positively charged head groups after dissociating from their counterions and, therefore, readily adsorb on negatively charged sur- and interfaces, while anionic surfactants (e.g. SDS, alkane sulfonic salts) carry a negative charge and thus deliberately adsorb at positively charged sur- and interfaces. Interestingly, about half of the annual worldwide produced surfactants are cationic, while anionic surfactants account only for a single-digit percentage. Zwitter-ionic surfactants (e.g. fatty acid esters, amides) can take on either charge, depending on the solution pH. Non-ionic compounds (e.g. polyethylene oxides (PEO), sorbitan esters, polyoxyethylene sorbitan esters) adsorb on surfaces in a way so that the hydrophilic moiety of the surfactant molecule is oriented towards the aqueous/hydrophilic phase of the emulsion. In W/O emulsions, for instance, non-ionic surfactants with highly polar head groups will adsorb with their heads on the interface of the water phase. The long hydrophobic tails extend into the oil phase and stabilise the droplets sterically by forming a firm interfacial film. The mechanical strength of the film is particularly of importance for W/O emulsions, because the (nearly) uncharged water droplets have no electrical barrier which could contribute to the stabilisation. Bancroft's rule gives a first indicator which type of emulsion

to expect. It states that the phase with a higher solubility for the surfactant becomes the continuous phase.

Polymeric surfactants have gained popularity only in the last few decades. Block-copolymers are employed because of their structure, constituting of several amphipathic units. Properties of can be tuned through adjustment of the lengths of the hydrophilic and hydrophobic parts by alteration of the polymerisation procedure.[137] Finding a suitable surfactant for a given emulsion system can be time-consuming and tedious. Therefore, several guidelines were developed to provide assistance in selecting the most suitable/effective surfactant for any system and application. The oldest yet still most popular concept is the HLB (hydrophilic lipophilic balance) approach.[138-142] The HLB value of a surfactant is governed by the size of the polar moiety. It was initially simply calculated as one fifth of the molecular weight percentage of the hydrophilic portion, leading to an empirical scale ranging from 0 to 20. The more hydrophilic a compound, the higher its HLB. Surfactants with an HLB > 10 are considered water soluble, while surfactants with an HLB < 10 show a higher solubility in the oil phase. Griffin proposed the HLB method in 1949 originally only for POE-based non-ionic surfactants,[143,144] but since then it was adopted also for the use with ionic compounds on an extended scale up to 40. This approach unfolds its real power when the required HLB of an oil phase, determined experimentally, is matched with the HLB of a surfactant or a blend of surfactants with different HLB values.

Several approaches of calculating HLB values have been developed. Davies developed a methodology especially applicable for ionic surfactants applicable methodology to determine the HLB according to a group contribution theory.[141,145,146] However, neither the influence of temperature nor phase ratio on the emulsion type were accounted for. Numerous other researchers attempted to relate the HLB to diverse molecular properties, such as cloud point or critical micelle concentration, with limited success though.[126,139] Even though the HLB concept is widely used, it has serious limitations. What the method can do is, is indicating which type of emulsion can be expected from a surfactant with certain HLB value. Neither emulsification conditions (temperature, energy input) are considered, nor the proportion of oil and water phase nor the amount of surfactant employed.

Aiming at accounting for the major shortcomings of the HLB concept, other systematic methods providing assistance in the selection of a suitable emulsifier were developed. This includes the PIT (phase inversion temperature),[126,147-150] HLD (hydrophilic – lipophilic deviation) methods,[126,151-154] CER (cohesive energy ratio) concept,[142,155,156] critical packing parameter (CPP)[142,157] and integrated surfactant potency (ISP).[140]

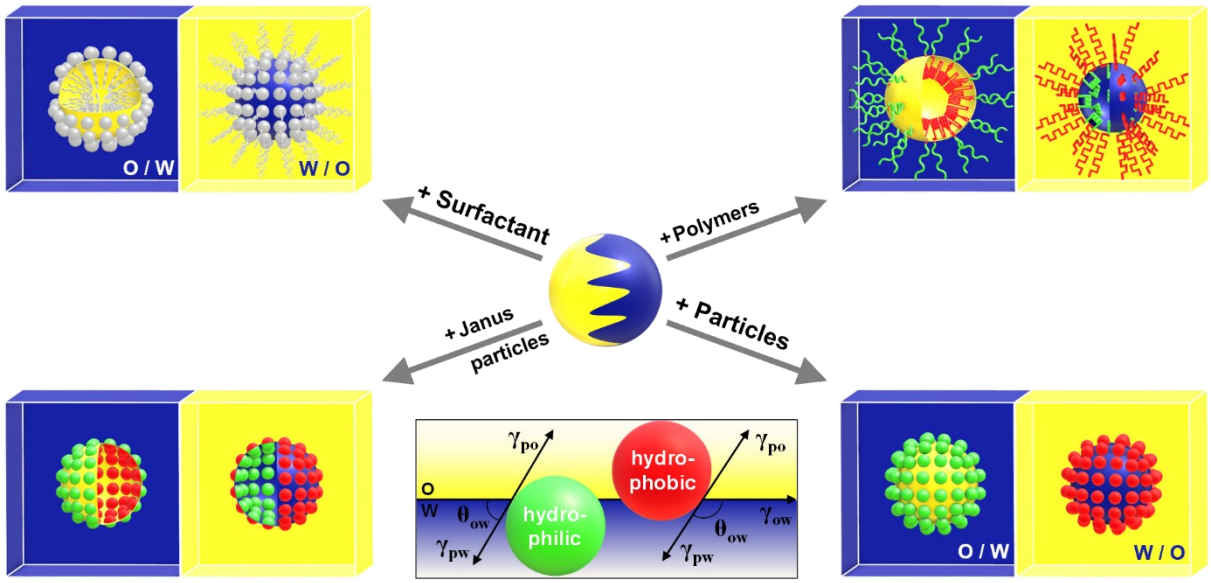

Figure 9: Stabilization of water or oil droplets in the respective opposite environment.

When particles are used to stabilise liquid-liquid dispersions, the resulting emulsions are termed Pickering emulsions.[158-169] Compared to surfactants, particles are generally not amphiphilic, but still surface-active. Driven by the gain in free energy due to the reduction of liquid-liquid interfacial area, particles deliberately adsorb at the interface between oil and water phase and form a robust interfacial film which protects droplets from coalescence. The energy gained through the adsorption of particles exceeds the energy gained through adsorption of surfactant molecules by manyfold. Wettability (and thus contact angle), size, shape and concentration of the particles heavily impact emulsion stability. Hydrophilic particles with contact angles $\theta < 90°$ (always measured into the water phase) are known to effectively stabilise O/W emulsions, while hydrophobic particles with $\theta > 90°$ tend to stabilise W/O emulsions. Particle-stabilised emulsions are in many aspects superior to surfactant-stabilised emulsions. Besides the mechanically highly robust interfacial film, Pickering emulsions are much less sensitive to change in the environment, i.e. temperature and pH, which facilitates

stabilisation over a much wider temperature range. The costs for surfactants are usually higher than for particles and moreover, much higher amounts are commonly necessary. However, destabilisation of Pickering emulsions is difficult due to their thermodynamic stability, while surfactant-stabilised emulsions are only kinetically stable and can therefore relatively easy be destabilised.

Janus particles are particles which combine two distinctly different properties in one particle (e.g. hydrophilic and hydrophobic, conductive and insulating). Due to their bivalent character, they are not only surface-active but also amphiphilic, which predestines them as emulsifiers. Indeed, they were found to be highly effective in stabilising emulsions, exhibiting higher interfacial activity and desorption energy than uniform particles.[161,170-175]

3.3.2. Factors affecting the morphology of emulsion-templated porous materials

Morphology describes the shape and structure of a material on macroscopic as well as on microscopic scale. Discussing the structural properties of a porous material prepared by emulsion templating requires an emulsion whose stability endures or exceeds the time until polymerisation has progressed to the stage at which the polymerizable phase is immobilised. This frequently coincides with the gel point, which is characterised by an abrupt increase in viscosity of the monomer-containing phase. The morphology of an emulsion-templated porous material heavily depends on (a) the emulsion formulation, (b) the energy input during emulsification as well as (c) the emulsification and curing temperature.

Porosity can be tuned by adjusting the internal phase ratio, while type and concentration of emulsifier strongly influence the pore structure (open-porous/closed-cell, pore diameter, pore throat size). Polymerisation of molecular surfactant stabilised W/O emulsions mostly result in materials with spherical pores. At high internal phase ratios, pore deformation can also lead to polyhedral-shaped pores. Pores can be completely surrounded by bulk material (closed cells) or connected with other pores through small pore throats (open pores), thus forming a pore network. The formation of a pore network is facilitated if the droplet phase constitutes less than 26 vol.% of the total emulsion volume, hence exceeding the threshold value of 74 vol.% of a

close-packed arrangement of the droplets, in analogy to crystal structures, and also if higher amounts of emulsifier are used.

Type and amount of emulsifier play a crucial role in determining a material's pore structure. Suitable surfactants are able to promote the formation of an interconnected pore system. Commonly, a minimum of 7 vol.% surfactant is required to achieve a notable change in pore morphology from closed-cell towards open-porous. A surfactant content of around 20 vol.% was suggested as point of reference to obtain highly interconnected open porous scaffolds.[176] In particle-stabilised (Pickering) emulsions, the energy gain caused by the decrease in fluid-fluid interfacial area drives the irreversible adsorption of surface-active particles at the interface of the droplets. The particles form a dense monolayer around the droplets and thereby act as steric barrier against coalescence, leading to a morphology dominated by closed pores. The particle contact angle is the decisive factor that determines whether certain particles are appropriate for stabilising a given emulsion or not. Generally, hydrophilic particles are chosen to stabilise O/W emulsions, hydrophobic ones for the stabilisation of W/O emulsions. Opposing the general rule, solid foams with interconnected pore structure were successfully prepared from Pickering emulsions to which small amounts of molecular surfactant were added after emulsification.[177,178] Wong et al. added the aqueous phase and a non-ionic surfactant simultaneously to an organic phase containing titania nanoparticles.[179] The combination of both types of stabilisers led to a material with bimodal pore size distribution, the larger particle-stabilised pores being surrounded by smaller interconnected surfactant-stabilised pores. In his perspective article 'HIPEs to PolyHIPEs',[86] Foudazi discusses in depth the different mechanisms influencing pore size, pore size distribution and also pore throat formation and thus pore structure by relating to reported experimental evidence.

In packed beds, typically found in a reactor, and in absence of any stabilising agents, droplets are separated from each other only by a very thin monomer film, prone to rupture upon application of mechanical forces during solvent extraction or vacuum evaporation for instance. This leads to the creation of pore throats at the small areas of contact between droplets. Cameron et al. investigated the formation of interconnected structures by studying density

differences between polymer gel phase and monomer phase during polymerisation of a DVB-styrene HIPE using cryo-SEM.[180] They observed shrinking of the continuous phase during polymerisation, followed by rupture of the thin polymer layer where adjacent droplets get into contact with each other. Menner et al., on the other hand, introduced the following hypothesis after examining the internal structure of polyHIPEs: advancing polymerisation is accompanied by a decrease in surfactant solubility, thus inducing migration of surfactant molecules to the O/W interface.[181] This leads to the formation of surfactant-rich polymer-poor regions in the contact area between two droplets. Upon drying, the thin emulsifier films between the pores rupture, resulting in a higher degree of interconnectivity due to the creation and enlargement of pore throats. This demonstrates the influence of the surfactant not only on emulsion stability, but also the final morphology of a material. Furthermore, Williams et al. studied the effect of varying surfactant concentration in a DVB/styrene-based emulsion template on the pore characteristics of the resulting rigid foam.[182] They reported an inverse relationship between surfactant concentration and pore size, i.e. the more surfactant, the smaller the pores. However, too large amounts of emulsifier negatively impacted the polymer walls' continuity, thus yielding polymer foams with bi-continuous or non-droplet-shaped morphology. However, these foams suffered from fairly poor mechanical properties due to excess surfactant in the emulsion.[176]

Alternative methods to tune the pore structure of polyMIPEs/HIPEs prepared from surfactant-stabilised templates include (i) employment of electrolyte solutions ($CaCl_2$, K_2SO_4) as dispersed phase (→ smaller pores with increasing concentration),[182-184] (ii) dilution of the organic phase using non-reactive compounds (i.e. polymer, solvent, non-solvent) (→ increased porosity and surface area),[185,186] (iii) controlled stimulation of Ostwald ripening (→ larger pores and pore throats),[187] (iv) the use of different initiator systems (→ control of pore diameter and pore throat size),[188,189] (v) the use of aromatic solvents such as toluene or chlorobenzene in the continuous phase of emulsion templates (→ smaller pores, larger pore throats, higher surface area)[190] and also the spatial distribution of the phases.[176]

Varying the energy input is another tool to control a porous material's morphology. Commonly, the influence of thermal energy, by means of emulsification and curing temperature, and energy input during emulsification, i.e. stirring speed, are discussed. It was shown that if the emulsion template contained an initiator, a temperature increase led to polyHIPEs/MIPEs with smaller pores, due to the faster decomposition of the initiator.[179] However, higher temperatures also promote emulsion destabilisation. Together with other emulsification parameters, controlling the temperature and thus coalescence, facilitated tailoring of the pore size between a few micrometres and 100 µm.[191] Carnachan et al. successfully demonstrated the effectiveness of heating the aqueous phase prior to adding it to the organic phase and emulsification. By tuning the temperature of the aqueous phase between 23°C and 80°C, they were able to triple the pore size.[187]

Controlling the energy input during emulsification, often represented by the agitation speed, offers another way to influence pore and pore throat sizes and is thus closely connected to the mechanical behaviour of a macroporous material.[188,192] Higher energy input leads to a finer dispersion of the internal phase due to additional droplet break-up, resulting in smaller pores.[193]

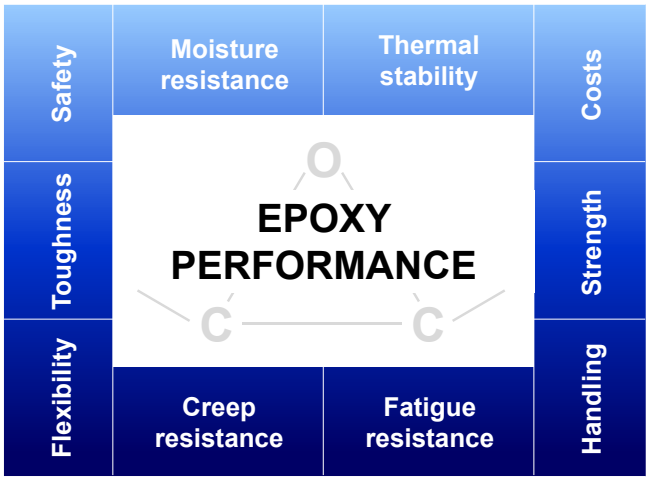

Figure 10: The versatility of epoxy resins is one of their biggest assets.

3.4. Epoxy resins

As stated above, commonly used monomer systems for emulsion templating are vinyl and meth/acrylates that can be polymerised by free radical polymerisation, while other monomer systems relying on polycondensation or polyaddition are much less explored; despite the fact

that such monomer systems would provide porous polymers with much better mechanical and physical properties. Epoxy resins are molecules with more than one epoxide group which can irreversibly react with a curing agent to form an insoluble cross-linked polymer network. Rooted in the epoxy ring's ability to react with a range of compounds (e.g. amines, anhydrides), polyepoxide networks can possess a wide range of properties, depending on the initial reactants, their ratio and the reaction conditions. Surfactants, fillers or any other additives, frequently employed in the production of composites and porous polymers, further impact a material's properties. Thus, by the choice of the formulation, it is possible to tailor the properties of epoxy polymers with regard to thermal stability, chemical resistance, flexibility or toughness for instance. Their versatility makes epoxies superior to many other systems (**Figure 10**).

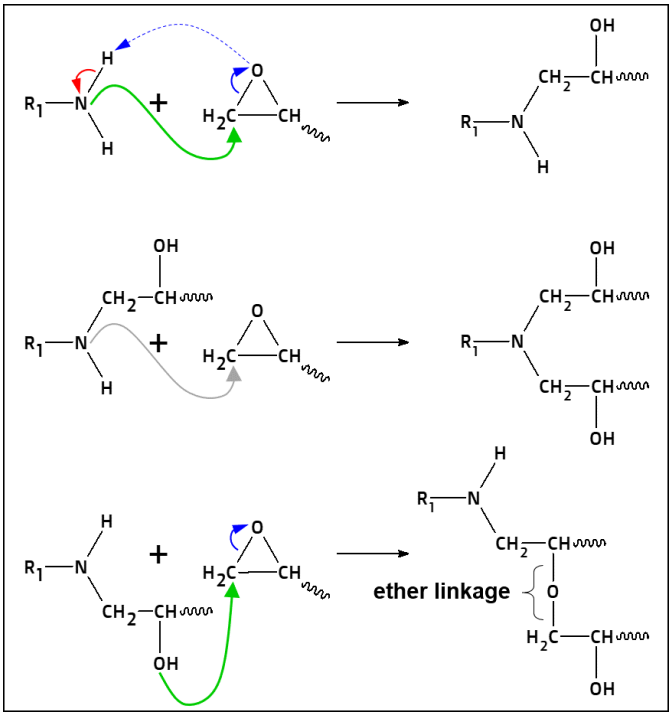

Figure 11: Primary curing reaction between amine and glycidyl/epoxy group. The electron lone-pair of the amine-nitrogen attacks the lower substituted carbon atom of the glycidyl group.

Produced from a condensation reaction between bisphenol A and epichlorohydrin, bisphenol A diglycidylethers contribute about 75% to the worldwide use of epoxy resins. Epoxides are cured through polyaddition, most commonly in the presence of polyamines or anhydrides as hardeners. The reaction of an epoxy group with an amine, initiated by a nucleophilic attack of the amine nitrogen at the terminal carbon atom of the epoxide, is schematically illustrated in Figure 11. Even though reactions between epoxides and amines are dominating, hydroxyl

groups can also react with glycidyl groups and form ether bonds. Polyadditions have the advantage that no volatiles or other by-products are released during the reaction, compared to, for example, the production of H_2O in poly-condensations. Consequently, epoxies are dimensionally very stable and show only very low shrinkage during curing.

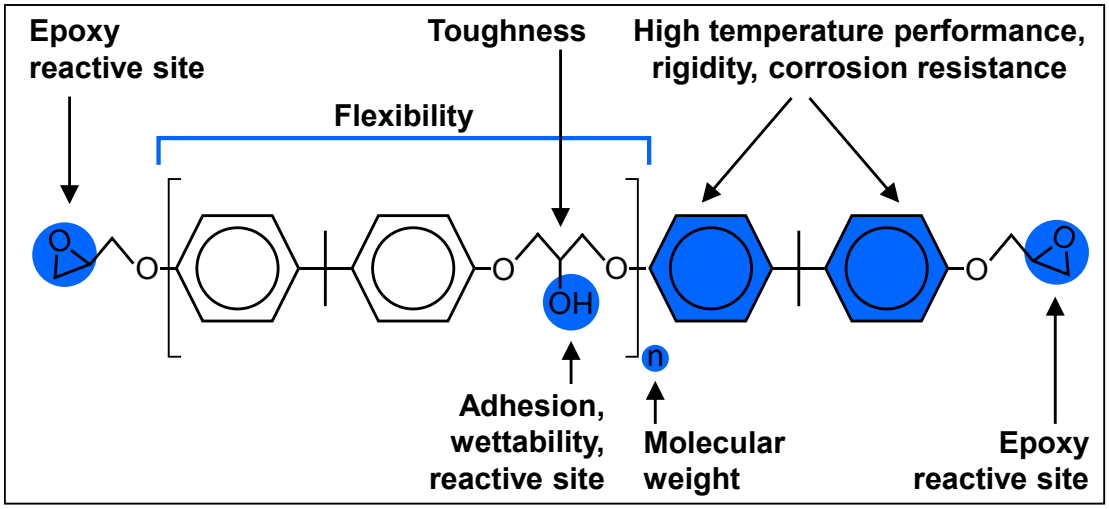

Figure 12: Structure-property relationship for Bisphenol-A epoxy resin

Many properties of bisphenol-A based epoxy resins are rooted in the structure of the epoxy monomers (**Figure 12**). Such a structure-property relationship is very helpful in choosing or even designing molecules for certain applications. The aromatic rings give these resins a hydrophobic character, superior to competing systems, such as polyurethanes or acrylics, making them an excellent choice for adhesives or sealants for instance. Moreover, they aromatic rings also responsible for pronounced corrosion resistance and good thermal properties.

Epoxies are known for their good adhesive performance, which can be attributed to the high number of polar groups. Epoxide groups are the reactive sites that are targeted by hardeners. Monomers with only one or two molecular units of Bisphenol-A ($n=1,2$) are liquid, of low viscosity, and transparent at ambient conditions, while a higher number ($n>2$) results in RT solid epoxy resins. Additionally, epoxies are a good choice, because they offer a good price-performance ratio. This means they provide good (mechanical) properties at a reasonable price (**Figure 13**).

3.5. Epoxy foams

Epoxy foams enjoy high popularity,[194] mainly driven by their excellent weight-to-performance ratio and their versatility, combining the wide range of properties of epoxies with the advantages of porous materials.[195-198] The porous structure holds responsible for low density and low weight of epoxy foams. Depending on the pore morphology, low moisture uptake, thermal and acoustic insulation and shock absorption can be added to the list of beneficial properties.[44,199] This makes epoxy foams attractive for applications in packaging, sealing, filtration and as cores in composite sandwich structures.[200,201]

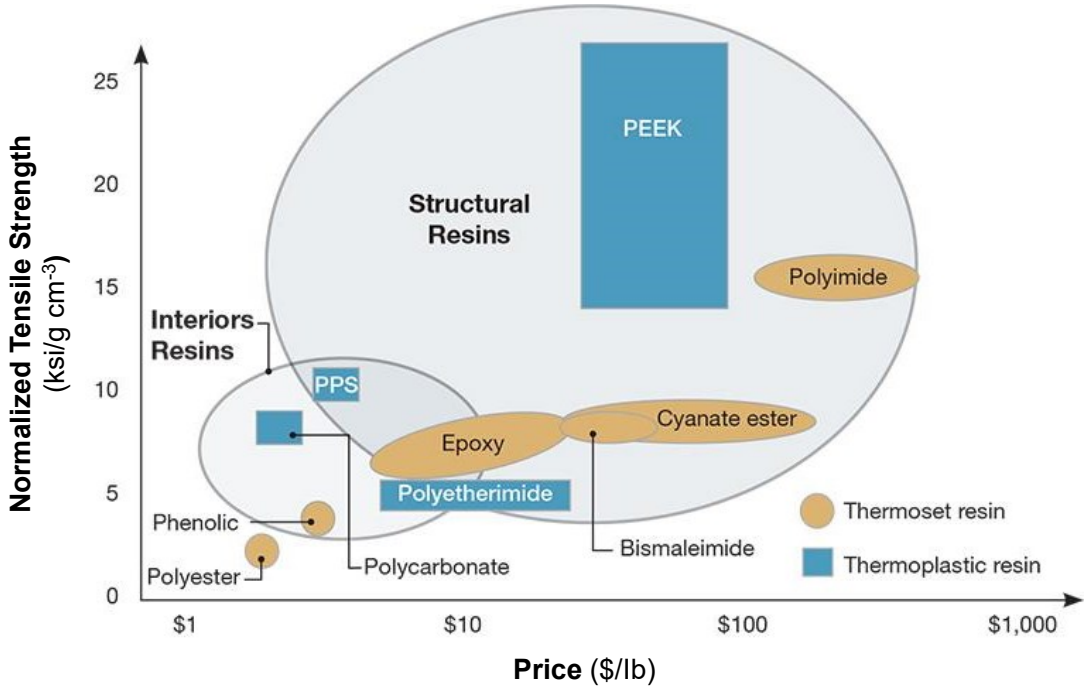

Figure 13: Epoxies offer a good price-performance ratio (http://www.compositesworld.com/articles/the-outlook-for-thermoplastics-in-aerospace-composites-2014-2023)

Epoxy foams are conventionally prepared by chemical and physical blowing.[202] Chemical or physical blowing agents are mixed with an epoxy formulation, including resin and hardener, as well as other additives. Chemical blowing agents (e.g. azo-compounds) generate gas upon chemical reaction,[203-211] while physical blowing agents[212-215] (usually low boiling point chemicals, such as hexane) gasify upon heating; the gas froths the epoxy formulations into stable liquid foams, which result after curing in solid epoxy foams. The addition of hollow or expandable spheres to an epoxy resin formulation has been used in particular to prepare syntactic foams. Foam templating (or mechanical frothing)[48,58,59,216-220] has also been used to

produce macroporous epoxy resins. Air is mechanically beaten in preferably highly viscous mixtures of monomers and hardener, which are subsequently cured. The dispersed air bubbles serve as templates for controlling the pore size and shapes as well as the porosity of the cured epoxy foam.

Khundamri et al.[221] employed epoxidized mangosteen tannin (EMT) as reinforcing material in the preparation of epoxy foams based on epoxidized soybean oil (ESO) and methyltetrahydrophtalic anhydride (MTHPA), with azodicarbonamide (AC) as chemical blowing agent. The use of EMT led to an increase in compressive strength, a decrease in compression set and it also raised glass transition and degradation temperature. Even though porosities were not explicitly reported, SEM images clearly indicate the porous nature of the material. Gu et al.[222] synthesised flexible epoxy foams from a mixture containing carboxyl-terminated butadiene-acrylonitrile rubber (CTBN), a bisphenol A epoxy resin and starch. They focused on investigating the influence of the CTBN:epoxy ratio and the amounts of curing (dicyandiamide) and blowing agent (AC) on the foam performance. Hashimoto et al.[223] reacted a polyepoxy compound with a carbonate oligomer with terminal phenolic hydroxyl groups, in presence of a catalyst. The carbonate served as crosslinker and due to the release of CO_2 simultaneously also as foaming agent, resulting in a uniform pore structure. The foams showed excellent mechanical durability, good heat resistance and high flexibility against compression, bending and warp. Wang et al.[45] have produced syntactic epoxy foams with significantly improved flexibility and higher thermal stability by incorporating a combination of 0.5-2 mm sized fillers. Buddhacosa et al.[224] added amorphous sodium borosilicate hollow microspheres and waste tyre-derived elastomeric fillers to a blend of bisphenol A and F epoxy. Syntactic epoxy foams with 70% higher vibration damping were manufactured, but at the cost of lower compression properties. Song et al.[46] used mechanical frothing to fabricate epoxy foams with improved mechanical properties. The addition of 0.5 and 1 wt% hollow elastomeric microspheres significantly enhanced fracture resistance and impact toughness, compared to an unfilled epoxy foam, without sacrificing the compressive properties.

Wang et al.[225] were among the first ones to use emulsion templating with epoxies. The continuous phase contained one of two epoxy systems, a bisphenol-A diglycidyl ether (DGEBA) or glycidyl amino epoxy,[226] together with a low molecular weight polyamide resin as curing agent, nonyl phenol polyoxyethylene as surfactant and 4-methyl-2-pentanon as solvent. An aqueous suspension of colloidal silica was in both cases used as internal phase. Among others, the influence of the volume fraction of the dispersed phase, the amount of silica in the internal phase and the optimal hydrophile-lipophile balance (HLB) of the surfactant and were investigated. Tu et al.[227] prepared epoxy foams in a similar way as Wang et al.[226] and subsequently hydrophilized the surface of porous epoxy monoliths by swelling the porous monolith in an acetone solution containing 10 wt% azobisisobutyronitrile (AIBN), immersing the dried foam into an acrylic acid solution and finally grafting acrylic acid molecules to the surface by initiating the radical polymerisation through heat. The surface modification caused a significant improvement of wettability and water absorption of the porous epoxy monolith. Anusha et al.[228] succeeded to prepare emulsion-templated conductive epoxy foams by adding carbon black to the resin formulation.

Emulsion templates typically show a higher stability than foam templates due to the similar densities of internal and external phase.[48,229] For certain applications, such as encapsulation, it is desirable to have the target liquid as the internal phase of the emulsion templates, which, after curing, have the liquid encapsulated in the porous materials.[230-232]

3.6. Compressive behaviour of cellular solids

The mechanical properties of cellular materials, e.g. polyLIPEs/MIPEs/HIPEs, are most commonly determined by compression tests. Stress - strain (σ - ε) curves, illustrating the variation of the compressive load as function of applied strain, are recorded while samples of defined shape and known dimensions are compressed between two metal plates. They primarily describe the nature of a material (e.g. brittle, tough, elastic), but also contain information about the pore structure, which is of interest for applications involving energy absorption or pressure changes for instance.

Typically, the compressive response of polymer foams can be divided in three distinct regions (**Figure 14**):[233] (i) elastic deformation, (ii) plastic deformation and (iii) failure/rupture. The linear elastic region is characterised by a sharp initial increase of the σ - ε curve at very low strains, recognisable by the direct proportionality of loading stress and displacement. It commonly extends to a strain of maximum 5-10% and represents reversible deformation. The narrower the linear elastic region, the higher is a material's brittleness. The slope of the linear elastic region, termed elastic/Young's/compression modulus, is an important parameter for describing the stiffness of a material. Subsequently, the curves level off and transition into the plasma deformation, which is characterised by compression of cells and buckling of cell walls.

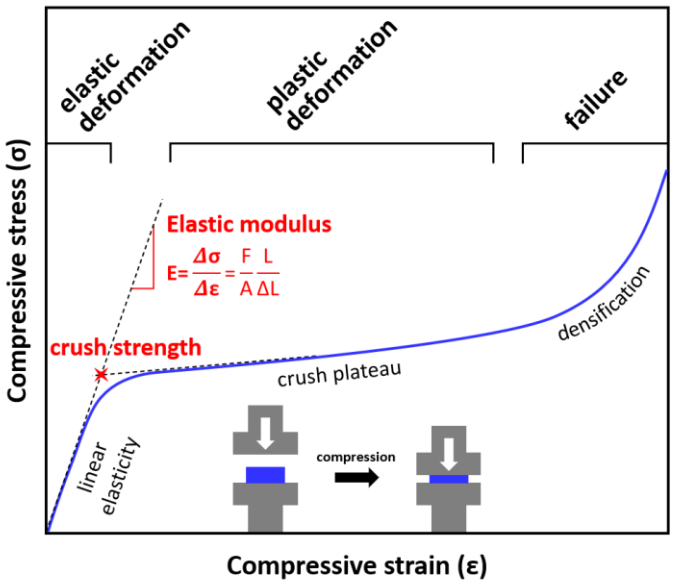

Figure 14: Schematic illustration of the mechanical response of a typical polyMIPE/HIPE undergoing compression.

While in the elastic region, the energy absorbed due to internal friction, is used to restore the original shape of the test specimen when the load is released, mechanical energy is irretrievably lost when cellular solids are compressed beyond their elastic limits, i.e. plastically deformed. A slightly positive profile in this region indicates an elastomeric nature and moreover suggests a certain contribution of closed cells to the compressive behaviour. On deformation, the gas in closed cells is compressed, the cell gas pressure increasingly contributes to the stiffness of a material and causes a positive slope in the plastic region. In fully open porous materials, on the contrary, compression induces an airflow out of the material, creating viscous

forces, which contribute substantially less than the gas pressure and hence leads to almost horizontal plateaus. A rapid increase in stress indicates the onset of densification, going along with cell walls crushing into each other and total compaction.

Although general qualitative trends how various formulation and processing parameters affect the mechanical properties of polymer foams have been reported, not all links and relations are fully understood yet. This makes the establishment of equations for quantitative predictions of mechanical properties very challenging. Gibson and Ashby (GA) have started their studies about mechanics of cellular solids and their theoretical description at the beginning of the 1980s and have since then coined this field like no others.[1,234,235] They first proposed a simple equation correlating relative Young's modulus (quotient of foam E_f and wall modulus E_w) to relative density (quotient of foam ρ_f and wall density ρ_w) and pore dimensions (length and thickness of edges and struts), which, however, only yields good results for linear elastic deformation, i.e. at very small strains. Building on their simplified initial expression, GA suggested to include a term taking account for elastic buckling and to introduce the openness ϕ into the equation (**Eq.(7)**):[236]

$$\frac{E_f}{E_w} = \underbrace{C_1 \phi^2 \left(\frac{\rho_f}{\rho_w}\right)^n}_{\text{pore edge/strut bending}} + \underbrace{C_2 (1-\phi)\left(\frac{\rho_f}{\rho_w}\right)}_{\text{pore wall stretching}} \tag{7}$$

where C_1 and C_2 are proportionality constants with a value of approximately 1. The openness ϕ denotes the fraction of bulk material found in the edges of the cells surrounding the voids, whereas $(1-\phi)$ refers to the wall material surrounding voids. In closed-cell foams, ϕ is typically in the range of 0.6 – 0.8,[236] while ϕ is close to 1 for fully open-porous structures due to the negligibility or even absence of pore walls. The first term, $\phi^2 \left(\frac{\rho_f}{\rho_w}\right)^n$, describes pore edge/strut bending, predominant in open porous foams, whereas the exponent n is often 2, but can generally vary between 1 and 3; the second term, $(1-\phi)\left(\frac{\rho_f}{\rho_w}\right)$, represents membrane (pore face/wall) stretching, rooted in the flexure of struts. GA also developed an equation for entirely

closed-cell foams, considering a third term the pressure build-up in closed pores upon compression, which, however, reduces to **Eq.(7)** at small pressures. GA themselves and numerous other researchers proposed and developed modifications and refinements for better suitability for certain types of materials and morphologies.[237-239]

3.6.1. Factors affecting the mechanical properties of cellular solids

For many applications, the mechanical behaviour of a material is of interest if not of outmost importance. Emulsion templating offers a broad range of tools that can be used to tailor a material to one's needs. It is needless to say that this topic is strongly interrelated to emulsion stabilisation and morphology of polyMIPEs/HIPEs.[240-242] The mechanical properties of porous emulsion-templated materials depend significantly on the modulus of the resin and the foam density of the material.[243-247] Substitution of bulk polymer for air leads to a reduction in density and thus lowers the stiffness. Inversely, increasing the monomer fraction in an emulsion (template) commonly leads to a material with higher density and thus also significantly higher modulus, hence, E(polyLIPE) > E(polyMIPE) > E(polyHIPE). This behaviour is also reflected in stress-strain curves by a decrease of modulus and crush plateau with increasing porosity.

Copolymerisation with a bulky, rigid monomer presents another way to increase the elastic modulus, however, often at the expense of toughness and elasticity. Toughness, combining strength and ductility, describes a material's ability to absorb energy during deformation before fracturing. It is quantified by the area under the stress – strain curve, which can easily be evaluated using integration. Elastic materials, on the other hand, are characterised by their ability to recover their original size and shape after removal of any deforming load.

4. Experimental

4.1. Materials

4.1.1. Sandstone

Sandstone cores 1.S1 – 1.S8 (*Paper I*) with porosities in the range of 3 - 40% were provided by Berea® Sandstone (Petroleum Cores, Ohio, USA).

4.1.2. Porous polyepoxides

For the preparation of the polyMIPEs described in *Papers II* & *III*, two different two-component epoxy systems (resin (A) and hardener (B)) were used (**Figure 15**):

(1) Low viscosity epoxy resin Araldite® 2020 (*Paper II*) was purchased from Huntsman (Huntsman Corporation, Switzerland). Component A consists of a mixture of diglycidyl ether of bisphenol A (DGEBA) (M_n < 700) and 1,4-butanediol diglycidyl ether as reactive diluent. Component B is formed by the cycloaliphatic isophorone diamine (IPDA) and trimethylhexane-1,6-diamine.

(2) Flexible epoxy system EF80 (*Paper III*), with the main components of the resin being DGEBA and 1,6-hexanediol diglycidyl ether, was purchased from Easy Composites (Staffordshire, United Kingdom). The hardener is a mixture of nonylphenol, trimethylhexane-1,6-diamine, coco alkyl amines (C12-C18) and 2,4,6-tris(dimethyl-aminomethyl)phenol.

As stabilising agents, the non-ionic surfactant sorbitan monolaurate (Span®20, HLB 8.6) (*Paper II*) and poly(ethylene glycol)-block-poly(propylene glycol)-block-poly(ethylene glycol) (PEG-PPG-PEG) (Pluronic L-81) (*Paper III*). Calcium chloride dihydrate ($CaCl_2 \cdot 2H_2O$) was added in both cases as electrolyte to the internal aqueous phase.as Salt and surfactants were purchased from Sigma-Aldrich (Vienna, Austria). Multi-walled carbon nanotubes (MWCNTs) and modified silica nanoparticles (HDK H18), used for producing flexible poly(epoxide)MIPEs (*Paper III*), were kindly provided by Arkema (Lacq, France) and Wacker Chemie AG (Germany), respectively. All chemicals were used as received, unless stated otherwise.

4.1.3. Gas permeability & diffusivity measurements

Nitrogen (>99.999% purity) and oxygen (99.5% purity), used for permeability and diffusivity tests of sandstones (*Paper I*), were obtained from BOC Edwards Ltd., Crawley, UK, while nitrogen (5.0) consumed during gas permeability measurements performed on poly(epoxide)MIPEs (*Paper II*) was purchased from Messer Austria GmbH (Gumpoldskirchen, Austria).

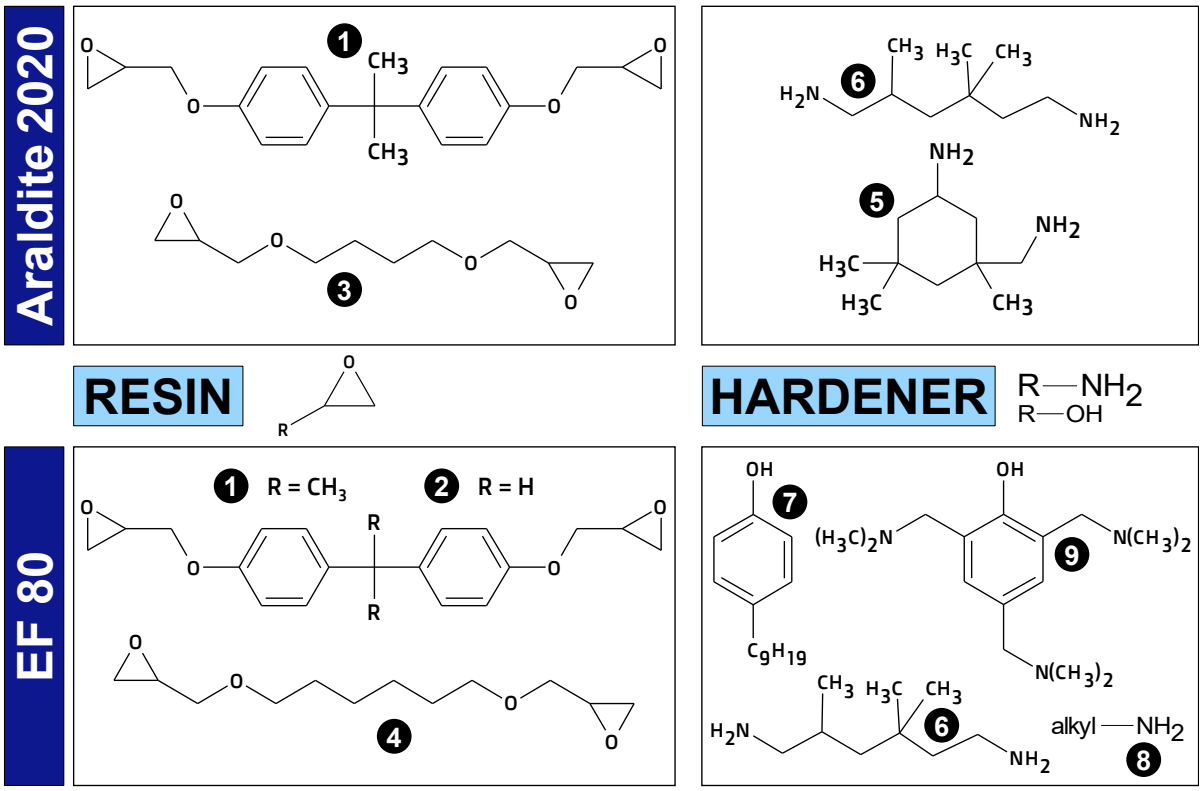

	Chemical compound	CAS
1	Diglycidylether of Bisphenol A (DGEBA)	25068-38-6
2	Diglycidylether of Bisphenol F (DGEBF)	28064-14-4
3	1,4-Butanediol diglycidyl ether	2425-79-8
4	1,6-Hexanediol diglycidyl ether	16096-31-4
5	Isophorone diamine (IPDA)	2855-13-2
6	Trimethylhexane-1,6-diamine	25620-58-0
7	Nonylphenol	25154-52-3
8	Amines, coco alkyl (mainly C12-C18)	61788-46-3
9	2,4,6-Tris(dimethyl-aminomethyl)phenol	90-72-2

Figure 15: Structures of the main constituents of the epoxy systems Araldite®2020 and EF80.

Sandstone as well as porous polyepoxide samples were sealed with the highly viscous epoxy adhesive Araldite® Rapid (Araldite® Precision Adhesive RS Components Ltd., Corby, UK) to prevent fluid leakage. A silicon-based release agent (Silicone mould release spray, Electrolube, RS Components Ltd., Corby UK) was applied to the inner surface of the PTFE

moulds to facilitate removal of the samples from the mould after embedding in the epoxy resin Araldite®2020 (RS Components Ltd., Corby UK).

4.1.4. Surfactant screening and swelling tests

All emulsifiers tested for their suitability to stabilise water-in-Araldite®2020 emulsions (*Paper II*) – i.e. Pluronic®L-81 (PEG-PPG-PEG) (HLB 2), Span®80 (sorbitan monooleate) (4.3), Hypermer®2296 (based on polyisobutylene succinic anhydride and the copolymer of PEG) (4.9), Hypermer®1083 (mixture of sorbitan oleate and block copolymeric ester of a hydroxy stearic acid and ethylene glycol) (4-6), Hypermer®B246 (block copolymeric ester of a hydroxy stearic acid and ethylene glycol) (6), Span®20 (sorbitan monolaurate) (8.6), Brij®O10 (PEG (10) oleyl ether) (12.4), Triton®X-100 (PEG *tert*-octylphenyl ether) (13.4), Tween®80 (PEG sorbitan monooleate) (15), Tween®20 (PEG sorbitan monolaurate) (16.7) and Triton® X-405 (PEG *tert*-octylphenyl ether) (17.6) – were purchased from Sigma-Aldrich (Vienna, Austria).
The solvents isopropanol, acetone, dimethyl formamide (DMF), dimethyl sulfoxide (DMSO), tetrahydrofuran (THF) and benzene, employed in the swelling experiments (*Paper II*), were also purchased from Sigma-Aldrich, Diesel oil from Shell.

4.2. Methods

4.2.1. Emulsion preparation

Throughout *Papers II* & *III*, emulsion templating was used to produce porous poly(epoxide)MIPEs. An aqueous calcium chloride solution (10 g/l), serving as internal phase, was added dropwise under constant stirring to homogenised mixtures of EF80 (resin+hardener)/Pluronic L-81/MWCNTs and Araldite®2020 (resin+hardener)/Span®20, respectively. *Paper II* focused on investigating possible relations between surfactant ratio (13 - 20 vol%) and internal phase ratio (49 – 60 vol%) on a range of morphological, physical and mechanical properties, while *Paper III* studied the influence of internal phase ratio (60/70 vol%), curing temperature (RT (23°C)/50°C) and CNT-content (0 - 1.2 wt%). The cured MIPEs were washed with distilled water prior to being dried at 50-60°C until constant weight. Exact formulations and emulsification procedures are detailed in the respective papers.

4.2.2. Scanning Electron Microscopy (SEM) - Structure and pore morphology

Through *Papers II* & *III*, a JCM-6000 Neoscope bench-top scanning electron microscope (JEOL Ltd., Eching, Germany) was used to study internal structure and pore morphology of the prepared porous polyepoxides. Thin foam pieces were mounted on SEM stubs using conductive carbon stickers and then sputter gold coated (JFC-1200 Fine Coater, JEOL Ltd., Eching, Germany) to achieve sufficient electrical conductivity. The electron microscope was operated in secondary electron mode at an acceleration voltage of 15 kV.

Pore diameters d_p and pore throat sizes d_{pt} were measured from the micrographs using the software package ImageJ, statistical analysis was done using Microsoft Excel.

4.2.3. Pycnometry – Density and porosity

Generally, pycnometry is based on repeatedly determining a samples volume, which is inaccessible for a certain displacement medium. Skeletal (absolute) densities ρ_s were determined using gas displacement pycnometry (AccuPyc II 1340, Micromeritics Ltd., Aachen, Germany) by detecting a pressure change resulting from the displacement of gas by a solid. Helium is commonly preferred because of its inert character, its negligibly small adsorption tendency at ambient conditions and its ability to penetrate into pores. Small foam fragments were pestled (*Paper II* & *III*), sandstones (*Paper I*) crushed using a hammer, then the pulverised material was transferred into a sample cup for weighing. After inserting the cup into the pycnometer, the loaded sample chamber was pressurised with helium to a pre-set value, before allowing the gas to expand into a reference chamber of known volume. The sample volume was accessible from the pressure difference in the sample chamber before and after the expansion and the known volumes of both chambers by applying Boyle's law. Finally, skeletal densities were obtained as the quotient of sample mass and skeletal volume.

Measurements of foam (bulk) densities ρ_f were based on graphite powder displacement pycnometry (GeoPyc 1360 V1.03, Micromeritics Ltd., Aachen, Germany). DryFlo, showing a high degree of flowability and quasi-fluid characteristics in addition to being non-penetrating, acted as displacement medium. A zero-volume baseline was established by measuring the

volume of DryFlo in the sample chamber (blank data), before immersing several small polyMIPE pieces (*Paper II* & *III*) in the displacement medium and repeating the measurement (sample run). Under constant agitation, a plunger compacted the DryFlo in the cylindrical sample chamber and consolidated it around the foam fragments. The difference in penetration of the piston between blank and sample run was used to evaluate the foam volume. Knowing the mass of the polymer pieces, calculation of the corresponding foam densities was straight forward. Foam (or bulk) densities of Berea sandstones *Paper I* were obtained by simply measuring mass and dimensions of sandstone fractures.

The percentage porosity *P* (*ε* in *Paper I*) could then be calculated from **Eq.**(8):

$$\mathrm{P} = \left(1 - \frac{\rho_f}{\rho_s}\right) \cdot 100\% \qquad \textbf{(8)}$$

4.2.4. Dynamic Scanning Calorimetry (DSC) - Thermal stability

Glass transition temperatures T_g were determined using dynamic scanning calorimetry (Discovery DSC, TA Instruments, Eschborn, Germany) in order to study the possible influence of the surfactant amount used in the emulsion formulation on Araldite®2020 polyMIPEs (*Paper II*). Small foam fragments were powdered and subsequently subjected to two cycles of a predefined temperature program: after equilibration at -30°C, the samples were heated to 150°C at a rate of 5°C/min and after five minutes of equilibration cooled down again to -30°C at the same rate. The glass transition temperature is seen in a typical DSC curve (temperature vs. heat flow) as step-shaped endothermic change in specific heat capacity c_p.

4.2.5. Uniaxial single and cyclic compression tests - Mechanical properties

Mechanical properties of the polyepoxide foams were tested under compression using a universal mechanical testing machine (Instron Series 5969, Instron Ltd., UK). In *Paper III*, a 1 kN load cell was employed to compress cuboid samples (10 mm x 15 mm x 15 mm) by 70% of their initial height, while in *Paper II* measurements were performed on foam disks (diameter 25 mm, height 10 mm) using a 50 kN load cell. The maximum strain thereby was 60%. All tests

were carried out at room temperature and with a compression speed of 1 mm/min. For every polyMIPE with the same composition at least five specimens were tested.

The elastic (compression) modulus E_c, a measure for stiffness and proportionality constant between stress σ and strain ε, was determined from the slope of the initial linear region of the stress-strain curves, the plateau modulus E_p from the slope of the rubber plateau. The compressive (or crush) strength σ_c, defined as the maximum stress at the end of the initial linear elastic section, was obtained from the intercept of the extensions of linear regressions to the initial linear region and the second linear (plateau) region.

4.2.5.1. Cyclic compression tests

In *Paper III*, porous poly(epoxide)MIPEs were additionally subjected to cyclic compression tests at predefined strain amplitudes of 10%, 20%, 50% and 70% for 200 cycles in order to study their durability and the reversibility of mechanical properties. These strains were selected because they represented the polyMIPEs' mechanical behaviour at the end of the first linear region, beginning of the linear plateau region, the end of the plateau region and the densification. Loading and unloading rate of the crosshead were set to 5 mm/min.

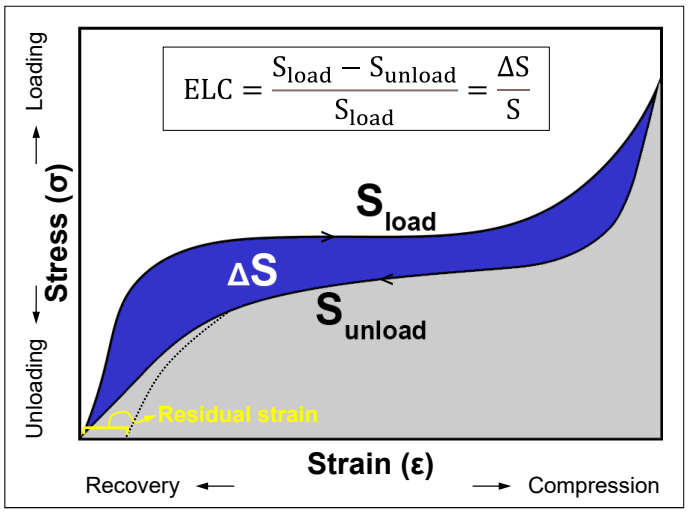

Figure 16: Illustration of a typical hysteresis loop as obtained from cyclic compression tests. An energy loss coefficient (ELC) can be calculated from the areas under the loading and unloading curve, respectively.

The area ΔS enclosed by the loading and unloading curves S_{load} and S_{unload} (**Figure 16**), respectively, was obtained by integration using software (OriginPro 2019b). The energy loss coefficient *ELC*, sometimes also referred to as loss ratio or hysteresis ratio, quantifies a

material's ability to absorb kinetic energy during cyclic loading. Residual strains were determined as the strains of the unloading curves when the stresses reached zero.

4.2.6. Equilibrium swelling tests

Produced polyepoxide foams (*Paper II)* were immersed in a series of solvents of different polarity (isopropanol, dimethyl sulfoxide (DMSO), (N,N)-dimethylformamide (DMF), tetrahydrofuran (THF), acetone, benzene and diesel oil) to study their swelling behaviour and chemical resistance. Epoxy foams S1-S5 were cut into cuboids (5 mm x 5 mm x 10 mm) using a bandsaw. Weight and dimensions of the polyMIPEs were recorded before placement in vials and solvent addition (10 ml) and then after 1h, 2h, 4h, 8h, 1d, 2d, 4d, 6d, 8d and 11d. Finally, all specimens were dried in a vacuum oven for 24h at 60°C, prior to weighing them again, to determine the mass of the dry network after extraction of soluble materials.

Swelling ratio Q and the inversely proportional polymer volume fraction at swelling equilibrium ϕ_p were calculated from the volumina of the swollen V_{sw} and initial dry polyMIPEs V_0:

$$Q = \frac{V_{sw}}{V_0} = \frac{1}{\phi_p} \tag{9}$$

Lose and unattached molecules, e.g. excess surfactant, are extracted during the swelling process, leading to a reduction in weight. The ratio of extracted material ω_{sol} was quantified by comparing the weight of the dry polyMIPEs before immersion into a solvent and after solvent removal at the end of the swelling test after eleven days, m_0 and m_{dry} respectively:

$$\omega_{sol} = \frac{m_{dry} - m_0}{m_0} \tag{10}$$

4.3. Gas permeability & diffusivity measurements - method development and validation

This chapter bridges *Paper I* and *Paper II*. On one hand, it contains more detailed information about several aspects of the underlying theory of the gas permeability measurements. On the other hand, it describes the preparation of porous samples for permeability measurements and discusses the results of tests performed on Araldite®2020 epoxy polyMIPEs. Most of the information given here is not included in any of the publications. However, few paragraphs

from the published manuscript (*Paper I*) were also used in this chapter in order to establish or maintain connection between different topics.

4.3.1. Introduction to gas permeability

Permeability characterises the ease of a fluid flowing through a porous solid, thus it is often described as fluid conductivity.[248] Results of permeability measurements allow to draw conclusions about a material's pore morphology.[249] Despite the broad range of available test methods, such as mercury porosimetry,[250,251] image analysis[252] or NMR,[253-256] permeability measurements based on the application of a pressure gradient across a porous sample are most common.

The French civil engineer Henry Darcy investigated the flow of water through sandstone and other porous media.[257] Based on his observations, he formulated in 1856 a basic equation, relating the volumetric flow rate Q [m^3 s^{-1}] to the pressure gradient *(dp/dx)* driving the flow, which is commonly known as Darcy's law* (**Eq.(11)**):

$$Q = \frac{dV}{dt} = -\frac{k}{\mu} A \left(\frac{dp}{dx}\right) \tag{11}$$

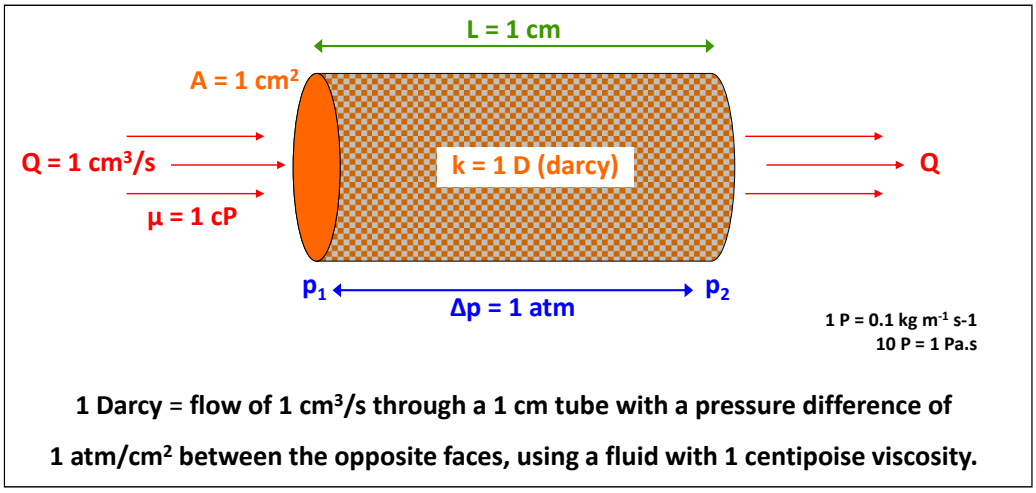

Figure 17: Illustration of pipe flow and its most influential parameters as described by Darcy's equation where A [m^2] is the sample cross-sectional area, μ [Pa s] the dynamic viscosity of the fluid and k [m^2] the permeability. The ratio of flow rate and cross-section area, Q/A, is termed fluid superficial (also filter or empty tube) velocity u [m s^{-1}]. By measuring the volumetric fluid flow rate through the material, the permeability k can be calculated.[258-260]

We reported the development of an integrated apparatus, which can be used for the determination of both permeability and diffusivity, including transient diffusion and diffusion under the influence of a pressure gradient.[261] The main advantage and novelty about an integrated apparatus is that it encompasses several characterisation techniques and allows the simultaneous measurement of multiple independent properties, thus being highly efficient. It can be used for the characterisation of a wide range of porous media, ranging from sandstone to porous polymers. This chapter first elaborates the development of the working equation for determining gas permeability in porous media and then focuses on permeability measurements carried out on open porous Araldite®2020 epoxy polyMIPEs.

4.3.2. Theoretical background

Darcy's law (**Eq.(11)**) states that the rate of fluid flow through a porous medium is directly proportional to the applied pressure gradient. Therefore, it can be used to determine the permeability of porous materials by means of a pressure-rise method. In order to assure its validity, a number of conditions has to be fulfilled: the fluid flow must be laminar, it is assumed that the resistance to flow is entirely due to viscous drag and the porous material needs to be inert to the fluid.[260]

Reynolds number *Re* and friction factor *f*, both dimensionless, are among the most common parameters used to characterise fluid flow through porous media. *Re* is defined as the ratio of inertial to viscous forces and can thus provide information about the flow regime, e.g. predicting whether a flow is laminar or turbulent. Its general form is commonly written as:

$$\mathrm{Re} = \frac{\text{inertial forces}}{\text{viscous forces}} = \frac{\rho u L}{\mu} \qquad (12)$$

where ρ [kg m^{-3}] is the fluid density, u [m s^{-1}] the fluid velocity, L [m] a characteristic linear dimension of the medium (e.g. pipe diameter, grain size, pore size) and μ [Pa s] the dynamic viscosity of the fluid.

Assuming Darcy's law is valid, low *Re* are obtained for viscous drag-dominated flow (viscous forces >> inertial forces). Viscous forces lead to a pressure drop in the fluid and thus energy loss. The pressure drop increases linearly with volume flow rate and/or fluid velocity ($Q = A \cdot u$).

High resistance can also be rooted in high viscosity of the fluid or low permeability of the medium. Consequently, *k=0* is equivalent to infinite resistance. In porous media, not only viscous but also form drag, i.e. inertial forces, contribute to resistance against fluid flow. When their contribution becomes significant (e.g. at high flow rates), the linear relationship between flow rate and pressure drop, as given by Darcy's law, becomes inaccurate and is thus replaced by a nonlinear expression, such as the Forchheimer equation (**Eq.(21)**).

Due to the broad variety of porous materials, several conceptionally equivalent, but slightly modified *Re* were defined.[262,263] More precisely, modifications concerned the terms for the velocity *u* and the characteristic linear dimension *L*. Comiti et al. (2000) stated that the pore Reynolds number Re_p **(Eq.(13))** should be preferentially used for open porous systems:[264]

$$\mathrm{Re_p} = \frac{\rho \mathrm{u_p} \mathrm{d_p}}{\mu} \xrightarrow{\mathrm{u_p}=\frac{\mathrm{u}}{\varepsilon}} \mathrm{Re_p} = \frac{\rho \mathrm{u} \mathrm{d_p}}{\varepsilon \mu} \tag{13}$$

The characteristic linear dimension in Re_p is the average pore diameter d_p, determined in this publication from analysis of SEM images. The pore velocity u_p [m s^{-1}] accounts for the reduced area available for fluid flow, compared to the flow through a single capillary. Bulk material reduces the volume that is accessible for fluid flow. Conservation of mass in fluid flow is described by the continuity equation, which requires a continuous and steady flow. This can only be achieved if the fluid velocity within a porous material is higher than the superficial velocity. Porosity *ε* connects superficial velocity *u* and pore velocity u_p (equivalent to interstitial velocity in packed beds) through the Dupuis-Forchheimer relation $u_p = \frac{u}{\varepsilon}$. Accordingly, $\varepsilon = 0$ is tantamount to infinite resistance and $u_p = u$ for the limiting case of $\varepsilon = 1$. Moreover, not only the porosity, but a material's pore structure in general affects flow characteristics. Important parameters in this context are surface area, surface roughness, pore size, pore throat size and tortuosity. The larger the contact area between fluid and solid surface of the porous medium (relative to flow volume), the higher the resistance to flow. Accordingly, the resistance to flow decreases with increasing diameter. Flow between two points in a porous medium rarely takes the shortest way. It is dictated by a material's pore distribution and thus follows a tortuous path, which exceeds the length of the direct linear connection. The ratio of effective path length L_{eff}

to the shortest distance between two points L is termed tortuosity τ ($=L_{eff}/L$). Tortuosity is commonly determined by gas diffusion measurements[265-268] or electrical conductivity of a non-conducting porous material when saturated with brine.[269]

The friction factor (**Eq.(14)**) was introduced to adequately represent the region of flow in which the influence of form drag cannot be neglected any longer, i.e. when Darcy's law does not provide a sufficient description anymore.[264,270] Based on the analogy of pipes and pores, Carman adopted the concepts originally developed for pipe flow to porous media:[271]

$$\mathrm{f} = \frac{16}{\mathrm{Re_p}} + 0.1936. \tag{14}$$

There are major differences between gas and liquid flow in porous media, which as a consequence leads to higher gas permeabilities than liquid permeabilities for a given porous material.[260,272] The lower viscosity of gases facilitates higher flow rates in porous media and thus results in an increased probability of flow in the non-Darcy regime (higher Re_p). Moreover, the compressibility of the gas needs to be considered. As such, Darcy's law can be applied locally to relate fluid velocity and pressure gradient, but the velocity will actually change along the flow path according to a parabolic profile.[273,274]

Most commonly, description of fluid flow is based on the assumption that the fluid behaves like a continuum, which allows for the use of averaged parameters, such as the mean velocity. This approach is only viable as long as the pressure of a gas or liquid is in its respective typical range. At very low gas pressure (or density), however, the continuum approach breaks down, because the requirement of gas molecules to collide more frequently with other gas molecules than the (pore) walls is not fulfilled anymore (**Figure 18**). In this case, gas flow through a porous medium resembles more the passage of individual molecules than a fluid continuum. A parameter often consulted in this context is the mean free path length λ, which is defined as the mean distance travelled by a molecule between subsequent collisions with other molecules. When the tube diameter approaches λ, gas flow is faster than predicted by Poiseuille's law; the same applies for low pressure gas flow through porous media. Slippage increases the flow rate (i.e. higher velocity at constant cross section) over and above

predictions following Darcy's law, which consequently leads to overestimated permeabilities.[275] This phenomenon, occurring particularly at low gas pressures between the flowing gas and the wall, is referred to as *slip effect* and the corresponding flow as *slip flow, Knudsen flow* or *free molecular flow*.

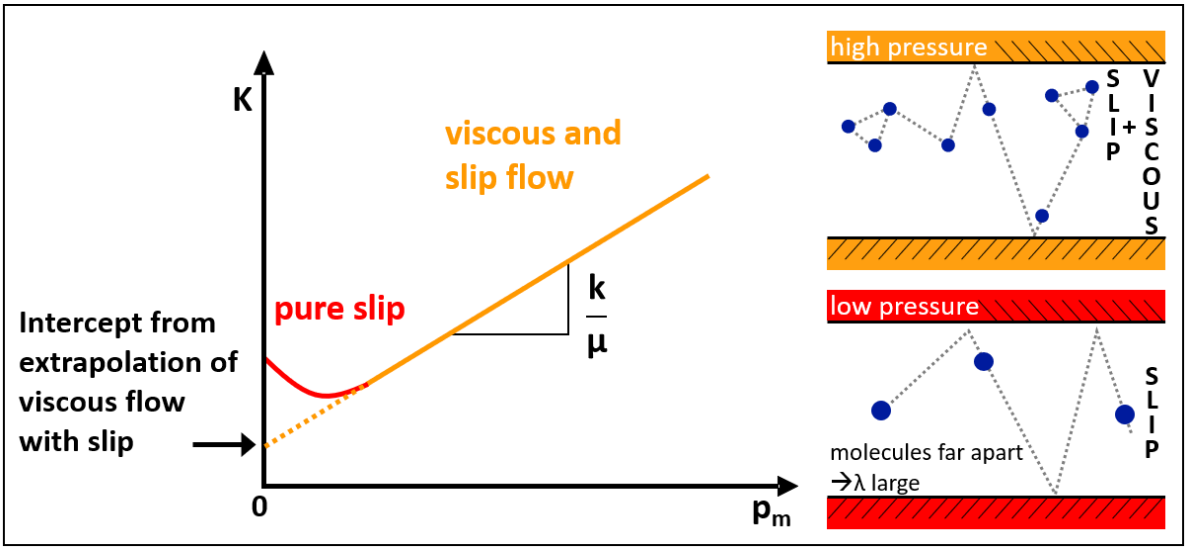

Figure 18: At low pressure, molecule-wall collisions dominate. Slip causes an artificial increase in permeability. At high pressure, viscous and slip flow coexist → linear relationship between p_m and K.

The slip effect was described by Milikan (1923);[276] its application to porous media was reported, among others by Hewitt (1967).[277,278] More recent work on this topic has been performed by Biloé (2003),[279] Lin (2004),[280] Tanikawa (2006),[272] Jannot (2012),[281] Ziarani (2011),[282] Berg (2014),[283] Kawagoe (2016)[284] and Liu (2016).[285] Klinkenberg (1951)[286] was the first to recognise that the difference in permeabilities to gases and liquids was caused by the slip effect. Therefore, this phenomenon is often also often referred to as 'Klinkenberg effect'. His idea was to model gas flow through porous media as Knudsen flow through a capillary tube (or a set thereof).

The parabolic flow velocity profile of laminar flow theory assumes no movement ($u=0$) of fluid molecules at the solid wall. However, the velocity at the interface between wall and fluid has a finite value. Neglecting slip would lead to underestimation of the rate of transport of momentum to the wall (i.e. the wall shear stress), particularly when a gas is employed as fluid. One approach to describe gas flow through porous media is to consider first the case of single component flow through a single capillary of diameter d. Here, the mean gas velocity $\bar{u}$ at a

position along the capillary can be calculated as the sum of viscous flow $\bar{u}_v$ and slip flow $\bar{u}_s$ (identical to u_0 used in *Paper I*):[277,278]

$$\bar{u} = \bar{u}_v + \bar{u}_s \tag{15}$$

$$\bar{u} = -\frac{d^2}{32\mu}\left(\frac{dp}{dx}\right) - \frac{\pi d}{16}\frac{\bar{v}}{p}\left(\frac{dp}{dx}\right) \tag{16}$$

$$\bar{v} = \sqrt{\frac{8RT}{\pi M}} \tag{17}$$

where $\bar{v}$ [m s^{-1}] is the mean molecular velocity of the gas as derived by the *kinetic theory of gases*, R [J mol^{-1} K^{-1}] the universal gas constant, T [K] the absolute temperature and M [g mol^{-1}] the molecular weight of the transported species.

Friction between fluid and capillary wall opposes the flow, thus the flow work on the body has to compensate the frictional resistance. This leads to a decrease of fluid pressure in the direction of flow (**Figure 19**), which is represented by the negative pressure gradient (*-dp/dx*) in **Eq.(11)** and **(16)**.

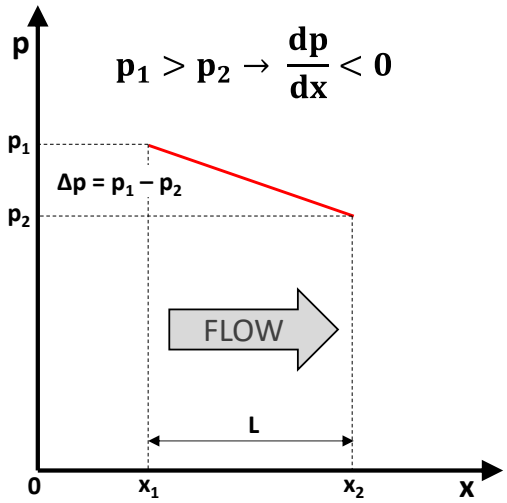

Figure 19: Negative (*dp/dx*) indicates decrease of fluid pressure in direction of flow; flow work on the body has to compensate frictional resistance.

When slip is negligible, i.e. when molecule-molecule collisions are dominant (as is usually the case for liquid flow), the slip flow term in **Eq.(16)** can be omitted and the equation reduces to the Hagen-Poiseuille equation:

$$u = \frac{Q}{A} = -\frac{d^2}{32\mu}\left(\frac{dp}{dx}\right) \quad \xrightarrow{d=2R,\ A=R^2\pi} \quad Q = \frac{dV}{dt} = -\frac{\pi R^4}{8\mu}\left(\frac{dp}{dx}\right) \tag{18a,b}$$

The mass flux of a gas, the product of velocity *u (ū)* and density *ρ,* remains unaffected from changes in pressure and flow velocity. After considering assumptions such as constant temperature and using relationships like the density-pressure proportionality (described in more detail in *Paper I*), one arrives at **Eq.(19)**:

$$\frac{\bar{u}_1 p_1 L}{\Delta p} = \frac{d^2}{32\mu} p_m + \frac{\pi d}{16}\bar{v} \tag{19}$$

Carman (1956) eventually derived an expression applicable to porous media, considering the porous material as network of capillaries:[271]

$$K = \frac{Q_2 p_2 L}{\Delta p A} = \frac{V\left(dp_2/dt\right)L}{p_1 A} = \frac{k}{\mu} p_m + \frac{4}{3} K_0 \sqrt{\frac{8RT}{\pi M}} \tag{20}$$

where Q_2 is the volumetric flow rate downstream (low pressure side) [$m^3\ s^{-1}$], p_1 the gas inlet pressure [Pa], p_2 the downstream pressure [Pa], Δp the pressure difference across the sample [Pa], *L* the sample length [m], *A* the sample cross section area [m^2], *V* the vessel volume [m^3], *t* the time [s], *μ* the gas viscosity [Pa s] (*μ* for N_2 at 293K = 1.76×10^{-5} Pa s), *M* the molar mass of gas [g mol^{-1}], *R* the gas constant [J $mol^{-1}\ K^{-1}$] and *T* the temperature [K]; *K* [$m^2\ s^{-1}$] is the permeability coefficient, p_0 [Pa] the pressure at which *Q* is measured, *k* [m^2] the viscous permeability (analogous to $d^2/32$ for a single capillary – see **Eq.(19)**), $(4/3)K_0$ [m] the slip coefficient (analogous to $\pi d/16$ for the single capillary case). The factor *4/3* has its origin in the resistance of a flow channel to molecular flow, applied specifically to cylindrical tubes with circular cross section area. Knudsen (1909) extensively described and discussed its derivation and its application in the calculation of gas flow outside the linear Darcy flow regime.[287] Thus, and also for consistency with other publications[271,288,289] this factor is retained here.

After evacuating the apparatus, a nitrogen stream of constant pressure was applied to the upper side of the sample, inducing a gas flow from the high- to the low-pressure side, where the gas was collected in a vessel of known volume (V_{large}=1.9696 dm^3, V_{small}=0.24 dm^3). The rate of pressure rise Q_2 was evaluated as slope of a plot of the pressure at the low-pressure side p_2 vs. time *t* and the permeability coefficient *K* [$m^2\ s^{-1}$] calculated. *K* was plotted against

the mean pressure $p_m = \frac{p_1}{2}$, assuming p_2 to be negligibly small (p_2~0 Pa). A linear fit to the experimental data of a K vs. p_m plot has the gradient $\frac{k}{\mu}$. Thus, extracting the viscous permeability k from the slope is straight forward (**Figure 20**). The Knudsen flow coefficient (or slip flow coefficient) K_0 is determined from the extrapolation of the intercept ($\frac{4}{3}K_0\sqrt{\frac{8RT}{\pi M}}$) of the linear fit with the y-axis of the plot $K = f(p_m)$ (**Figure 18**).

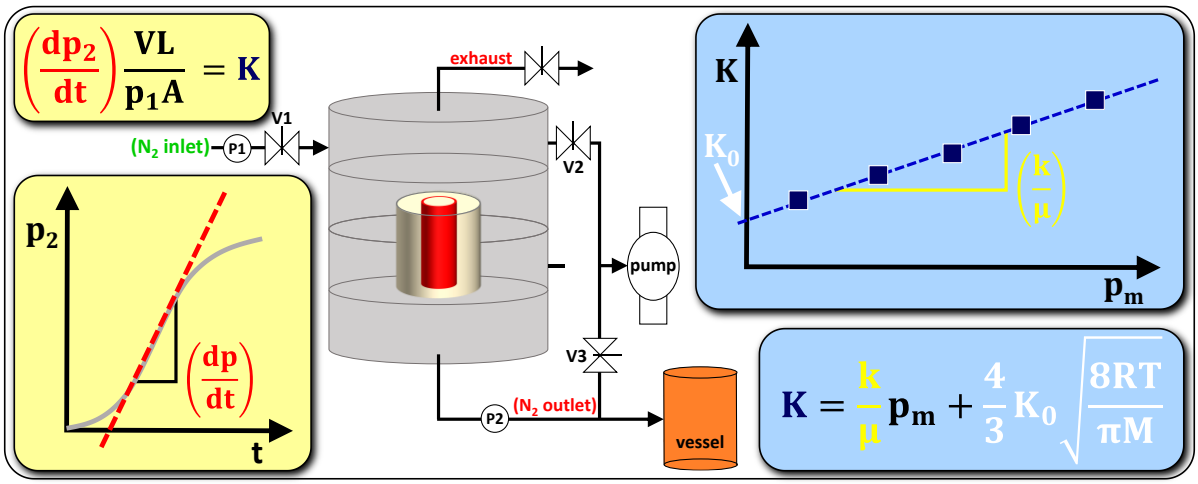

Figure 20: Schematic representation of a gas permeability measurement. The pressure gradient (dp_2/dt) is determined by plotting the recorded pressure over time. The results of the left part (1) of the equation are inserted into the right part. Consequently, the viscous permeability k and the slip coefficient K_0 are evaluated from slope and intercept.

4.3.1. Setup and measurement procedure

Gas permeability was measured using a purpose-built apparatus, which is shown in (**Figure 21**). The device is presented in more detail with measures and as CAD drawing in Manley et al. (2020) (*Paper I*),[261] where also the measurement procedure is described. Sample preparation is described extensively in *Paper I* and illustrated in (**Figure 22a**).

In brief, sandstones (*Paper I*) and poly(epoxide)MIPEs (*Paper II*), 13 mm and 15 mm in diameter, respectively, were sealed with the high viscosity epoxy system Araldite®Rapid to avoid unwanted gas leakage. PTFE moulds, impregnated with a thin film of release agent (WD-40 or a silicon-based equivalent), were used to embed the coated samples in Araldite®2020. Once the epoxy was cured (mostly overnight at ambient conditions), the cylindrical specimen was cut to a height of 25 mm and inserted into the sample chamber, followed by evacuation to a pressure of about 10 Pa. Measurements were performed on at least two epoxy polyMIPEs

per formulation, two samples each which were always tested from both sides (**Figure 22b,c**). Accordingly, 2.S*1-1-1.1* refers to epoxy polyMIPE 2.S1, sample 1, piece 1 measured from 1 side, while 2.S1-1 corresponds to the average over all measurements of 2.S1 sample 1.

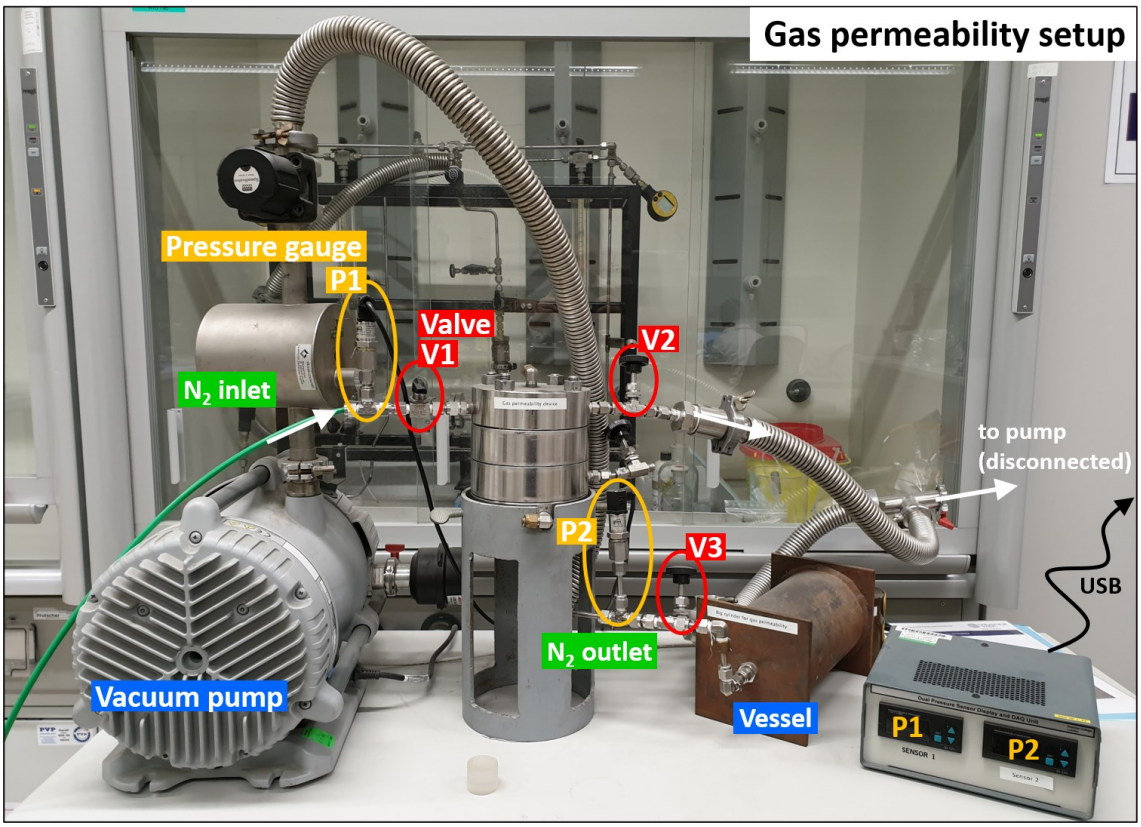

Figure 21: Gas permeability setup

4.3.1. Gas permeability of porous polyepoxides

The linear relationship between the mean pressure p_m and the permeability coefficients K is shown exemplary for polyMIPE 1.S3 in **Figure 23 (left)**. **Table 2** summarises porosities, pore and pore throat size and lists the determined viscous permeabilities k and Knudsen diffusion coefficients K_0. PolyMIPE 2.S5 exhibited with 147 ± 42 mD (1.47 ± 0.42 ×10^{-13} m^2) the highest permeability, followed by 2.S1, 2.S3 and 2.S4 with very similar permeabilities of 93 ± 29 mD, 94 ± 19 mD and 85 ± 21 mD, respectively. 2.S2 was the least permeable polyepoxide foam with 37 ± 12 mD. Contrary to the permeabilities, 2.S5 showed the lowest Knudsen flow coefficient, 7.3×10^{-6} ± 2.6 ×10^{-6} m, only slightly lower than the result for 2.S2. Similar values were again found for the other three polyMIPEs.

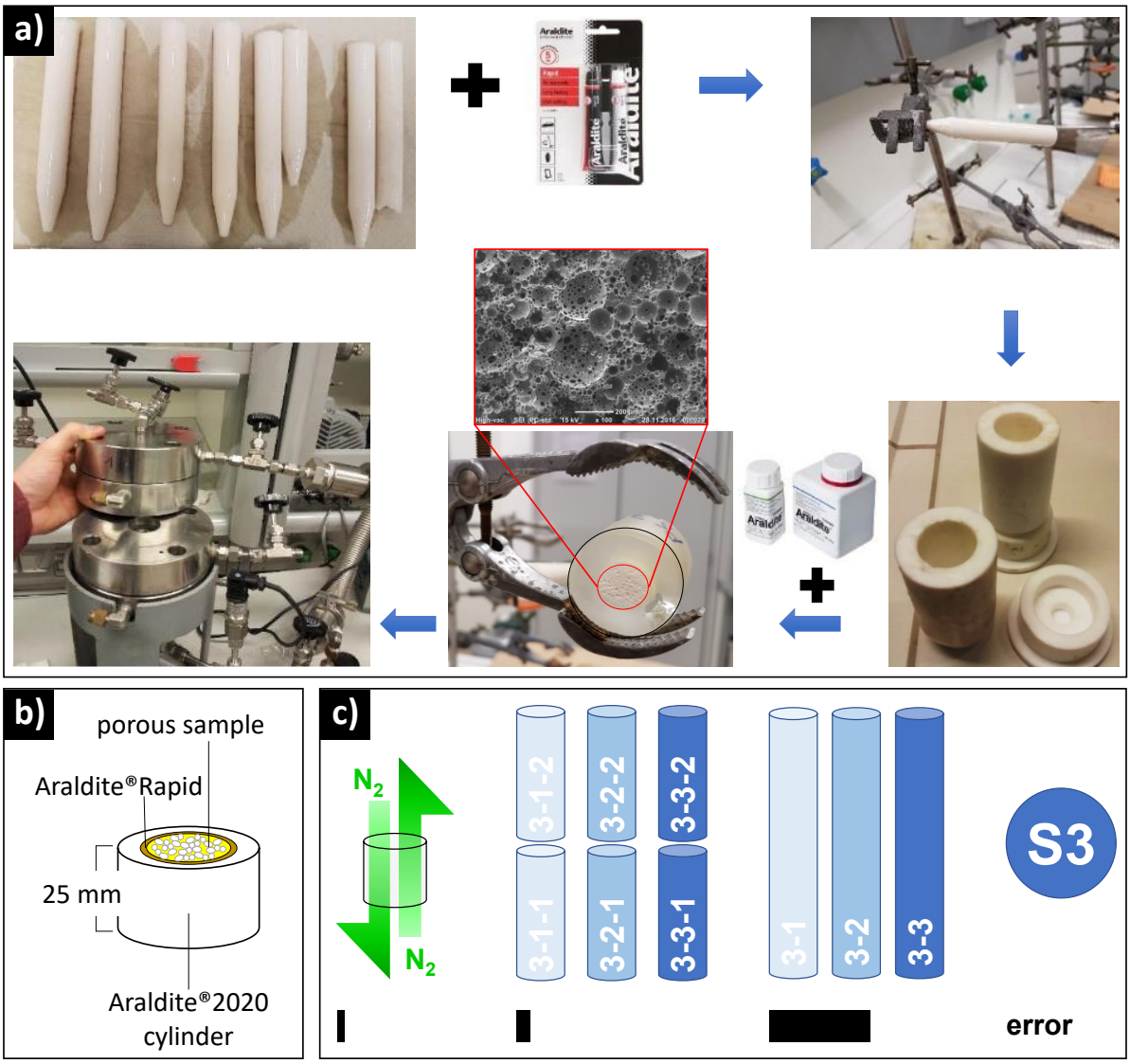

Figure 22: a) Stepwise illustration of the sealing of the porous polyepoxides; b) graphical representation of a specimen and its different layers; c) test results of one piece of foam are afflicted with only a small error, while averaging over several specimen leads to a significant increase in the error of the evaluated parameters.

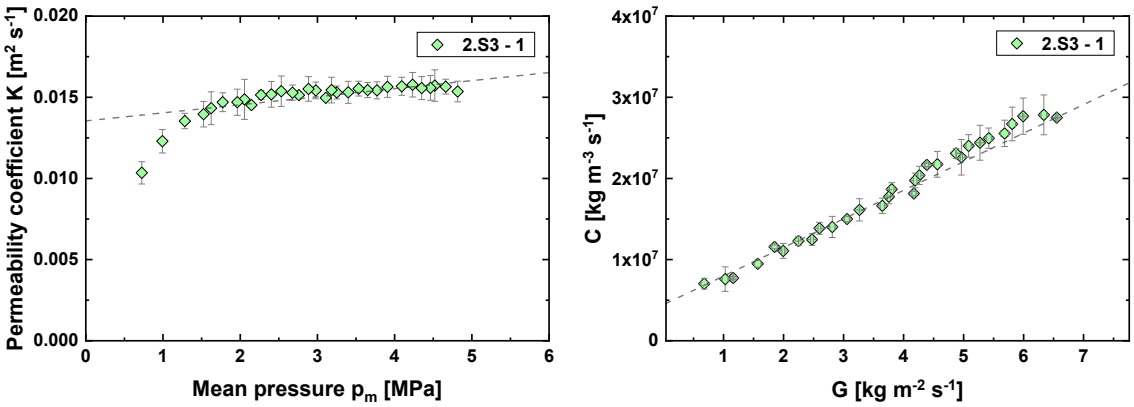

Figure 23: Permeability coefficient as function of mean pressure p_m (a) and of $C = \frac{p_1}{2K} = \frac{p_m}{K}$ as function mass flow rate G (b) for polyMIPE 2.S3

Comparison of the results of all epoxy foams yielded no systematic and fully coherent dependency of the permeability on neither porosity nor pore size, although certain results, detailed below, do suggest a correlation between some of the parameters. 2.S5 exhibited the largest pores (arithmetic mean d[1,0]) and the highest porosity, thus justifying the higher permeability compared to the other foam cores. Consequently, the less porous polyMIPEs 2.S3 and 2.S4, with smaller average pore diameters d[1,0], were also less permeable.

Table 2: Data taken from *Paper II*. Average pore diameters: arithmetic mean d[1,0], Sauter diameter d[3,2], median pore diameter d_{50}, and d_{v10}, average pore throat sizes d_{pt}, porosity ε, Knudsen Diffusion coefficients K_0 and viscous permeabilities k for porous polyepoxides 2.S1-2.S5.

	Pores (in [µm])					**Pore throats**	**ε**	**K_0**	**k**
	d[1,0]	**d_{50}**	**d_{90}**	**d[3,2]**	**d_{v10}**	**d_{pt}** / [µm]	[%]	[m]	[mD]
2.S1	28.3	15.0	39.5	518.8	400.5	9.7 ± 12.2	43 ± 3	1.1E-05 ± 3.8E-06	93 ± 29
2.S2	31.3	19.2	56.5	426.8	290.5	6.5 ± 8.6	58 ± 3	8.3E-06 ± 1.8E-06	37 ± 12
2.S3	34.6	15.7	86.1	211.4	135.8	7.0 ± 7.1	54 ± 3	2.1E-05 ± 3.5E-06	94 ± 19
2.S4	37.6	17.8	144.7	210.8	134.4	8.0 ± 8.1	54 ± 4	2.1E-05 ± 2.8E-06	85 ± 21
2.S5	48.3	19.8	137.8	303.9	193.5	10.1 ± 8.5	62 ± 2	7.3E-06 ± 2.6E-06	147 ± 42

Slip flow is expected to have more impact on gaseous transport in materials with smaller pores. This agrees with the lowest Knudsen diffusion coefficient found for 2.S5 and the higher values for 2.S3 and 2.S4. However, permeabilities of epoxy foams 2.S1 and 2.S2, prepared with 16 vol% surfactant, cannot be related to their porosities, likely due to a significant fraction of closed or dead-end pores. Evaluation of the experimental data yielded a significantly lower permeability for 2.S2, even though it exhibited one of the highest porosities. 2.S1 displays the opposite relation, lowest porosity but intermediate permeability, relative to analysed foam cores.

Fluid flow is primarily determined by the dimensions of the flow channel. Accordingly, pore throats connecting the larger pores creating the flow path, play a crucial role for gaseous transport through porous media and hence permeability. A d_{pt} vs. k plot (**Figure 24**) indicated increased permeabilities for samples prepared with 20 vol% surfactant, i.e. 2.S3-2.S5, and thus a higher degree of interconnectivity.

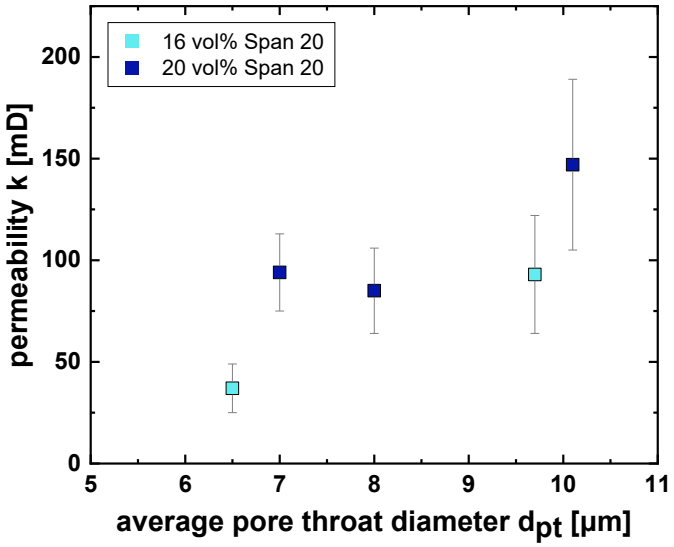

Figure 24: Dependence of the gas permeability on the limiting pore throat diameter. One can see a trend to higher permeabilities for samples with a higher surfactant ratio.

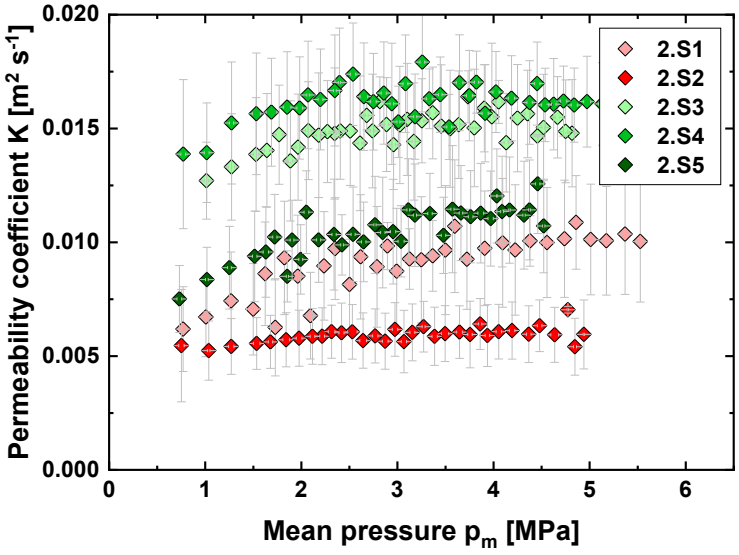

Figure 25: Permeability coefficient at various mean pressures for polyMIPEs 2.S1-2.S5

Figure 25 shows a graphical comparison of the p_m *vs. K* plots of all five polyMIPEs. The large error bars of the permeability coefficients instantaneously attract attention. However, this is by no means an indicator for the quality or reproducibility of the measurements, but rather suggests differences in the fine pore structure between sample batches of the same formulation, resulting in slightly varying results evaluated from the permeability tests. **Figure 20c** visualises schematically the development of the error in *K*, starting from one single

foam specimen, tested from both sides, over all specimens from one polyMIPE to the average of all analysed specimens of one formulation (e.g. 2.S3).

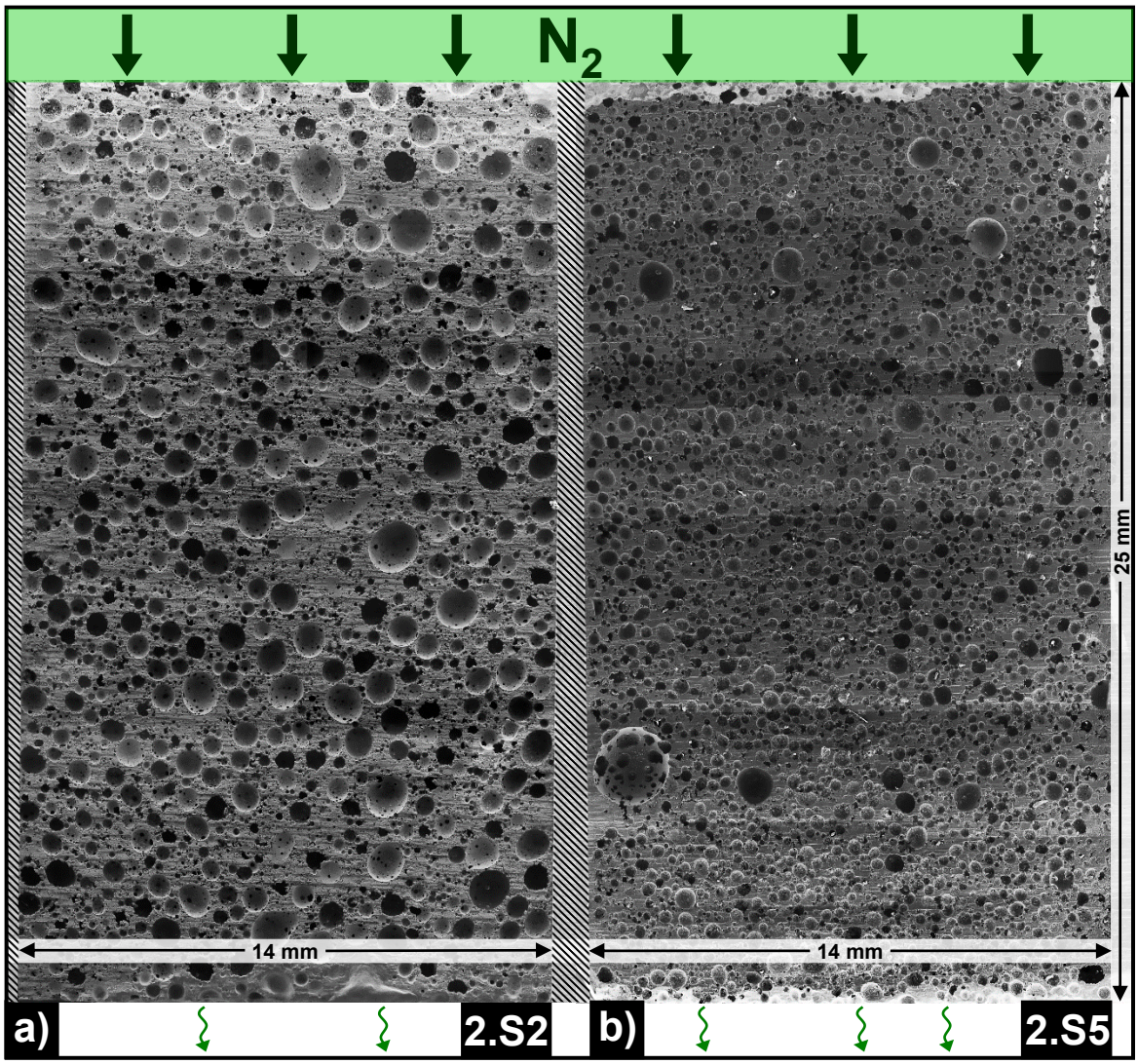

Figure 26: SEM micrographs of 2.S2 (a) and 2.S5 (b): entire cross sections of samples prepared for gas permeability tests were analysed.

The sum of measurements performed on one foam core was mostly associated only with small errors, indicating the homogeneity of that individual polyMIPE and the absence of a pore size gradient. The large error bars, on the other hand, revealed differences in independently prepared polyMIPEs from the same formulation. All specimens were tested roughly at the same mean pressures and pressure intervals, an exact adjustment of the input pressure was not possible. This has to be improved to develop the method further. Hence, permeabilities were averaged over a very narrow pressure range, which probably also contributed to a minor degree to the large y-errors. To shine more light onto the measured gas permeabilities, two

poly(epoxide)MIPE monoliths analysed by gas permeability measurements, were bisected vertically in order to examine their entire cross-sections. More than 300 scanning electron micrographs per piece were stitched together (using ImageJ) (**Figure 26**) with the aim of gaining a better understanding of the results obtained from the gas permeability measurements.

On a first glance, the patchwork cross-sections were consistent with the corresponding SEM images from *Paper II*. Pores, sized several hundred micrometres, dominated the image of 2.S2 (**Figure 26a**). A top-to-bottom gradient of the pore sizes was not observed which indicated the stability of the emulsion (see *Literature review – Emulsions*). A vast number of very small pores < 5 µm, observed on images with higher magnifications (*Paper II*) and reflected in their pore size distributions, were not visible in **Figure 26** because of the necessary down-scaling. It is noticeable that there are fairly large areas of bulk material in between the pores which clearly hinder gas passing through the polyMIPE. Pore sizes in 2.S5 (**Figure 26b**) were more uniformly distributed and the bigger pores were much smaller than in 2.S2. The small pores that filled the space between the larger ones could not be observed here either. Compared to 2.S2, there was clearly less bulk material present. However, already thin layers of bulk polymer block any fluid flow through a sample.

The moderate internal phase ratios (49 - 60 vol%) and the wide pore size distributions, indicating that a small number of large pores occupied disproportionately more volume than the much higher count of small pores, left enough space for the accumulation of bulk material. Overall, the pore throats were too small to compensate for the only sparsely existent continuous interconnected pore system. The combination and contribution of all these factors explained, why the gas permeabilities of all epoxy polyMIPEs 2.S1-2.S5 showed similar low permeabilities. This demonstrates the importance of a thorough characterisation of polymer foams.

4.3.1.1. Flow regimes – deviation from Darcy flow

Logarithmic *Re* vs friction factor plots, referred to as Moody diagrams if the influence of the relative roughness is also displayed,[290] are a popular tool to identify the regime(s) of fluid flow

present. The *Re* ranges associated with the different flow regimes vary for all modifications of *Re*, such as pore or interstitial *Re*, etc. A graphical representation allows for a quick assessment of the flow regime(s) independent of the *Re* used, because the curve, formed by connecting all data points, takes on the same shape for all *Re* modifications. In pipe flow, the change from laminar to turbulent flow happens abruptly and can, therefore, be indicated by a critical Reynolds number Re_{crit}. For porous materials, however, transitions between flow regimes are rather gradual due to the presence of a distribution of pore sizes (**Figure 27**).

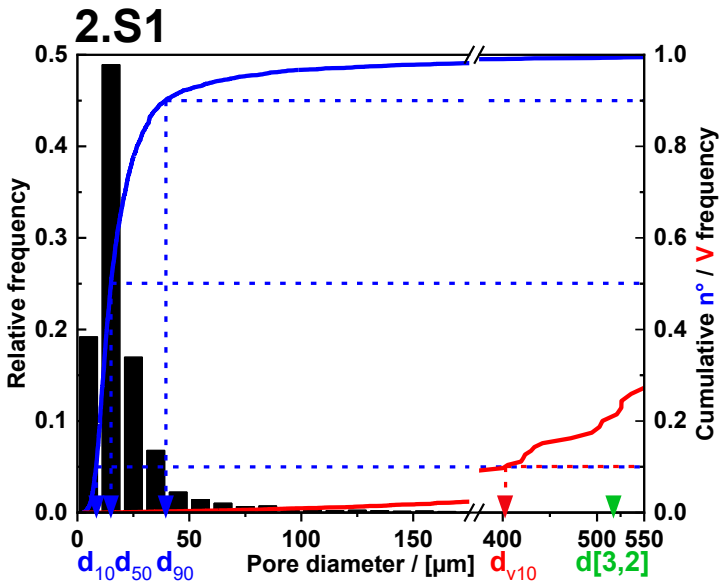

Figure 27: Pore size distribution of polyepoxide 2.S1 illustrated as histogram of relative frequencies (left axis) and in terms of the cumulative number and volume frequencies (right axis).

Dybbs et al. (1975) first identified three different *Re* regimes for flow in porous media: 1) Darcy flow (Re_p < 1-10), 2) Forchheimer flow (Re_p 10 < 200), 3) turbulent flow (Re_p > 350).[291] Later, Dybbs and Edwards (1984)[263,292] refined their classification and proposed to divide the flow into four parts (from low to high *Re*): 1) Darcy or creeping flow, 2) inertia flow, 3) unsteady laminar flow, 4) highly unsteady and chaotic flow (resembling turbulence in pipe flow). Skjetne et al.[293] introduced a modified and extended classification system for flow regimes in geometrically complex porous media: Darcy flow, weak inertia, transition from weak to strong inertia, strong inertia (Forchheimer), turbulence. Jolls and Hanratty (1966) reported the onset of turbulence at Re_p between 110 and 150.[294] Hall & Hiatt (1996) found that the transition to

fully developed turbulent flow happened around Re_p=150,[295] while Seguin et al. (1998) reported substantial fluctuations starting from about Re_p=180.[296]

Viscous flow is characterised by a linear relationship between *Re* and friction factor. At low *Re*, Darcy's law is expected to be valid and should satisfactorily describe fluid flow in the linear region, in which flow is assumed to be of purely viscous nature. With increasing *Re*, the linear relationship breaks down and the curve truncates, indicating the onset of inertial effects. Comiti et al. (2000) presented data collected from several publications in a pore friction factor vs. Re_p number plot.[264] They reported that the transition from viscous towards turbulent flow in porous materials can be expressed conveniently by the general expression $f = (\alpha/Re_p) + \beta$,[264] which results in **Eq.(14)** for α=16 and β=0.194.

It is evident from **Eq.(13)** that Re_p is proportional to the mean pore diameter, which means that fluid flow is substantially influenced by the pore size of a material or more precisely the pore size distribution. It is debatable, if one single parameter is or can be enough to describe the pore size distribution within porous media. Despite that or perhaps exactly because of that, there is an extensive number of different mean values used to state an average pore diameter, either related to number or volume distribution (defined in ASTM E799-03(2020)e1). Among the most commonly used parameters are d_{10}, d_{50} (=median) and d_{90}, where the subscripted numbers state the percentage of pores falling below these values; d_{v10} specifies that 10% of the total pore volume is occupied by pores with smaller diameters than this value; *d[1,0]* is the ordinary arithmetic mean and *d[3,2]* is the Sauter-mean or volume-to-surface mean diameter, which puts more weight on larger pores. While the choice of parameter is of less concern for strictly monodispersed media, it becomes highly relevant for materials with broad pore size distributions. Literature is inconclusive about the choice of a parameter describing the average characteristic length scale of either pores or particles.[297] Among others, one can find publications using the number averages d_{10},[298,299] d_{15},[300] d_{50}[297] or the Sauter mean diameter d[3,2].[301] Some researchers tried more complex approaches, such as using two pore sizes or even pore size distributions,[302-304] with moderate success though.

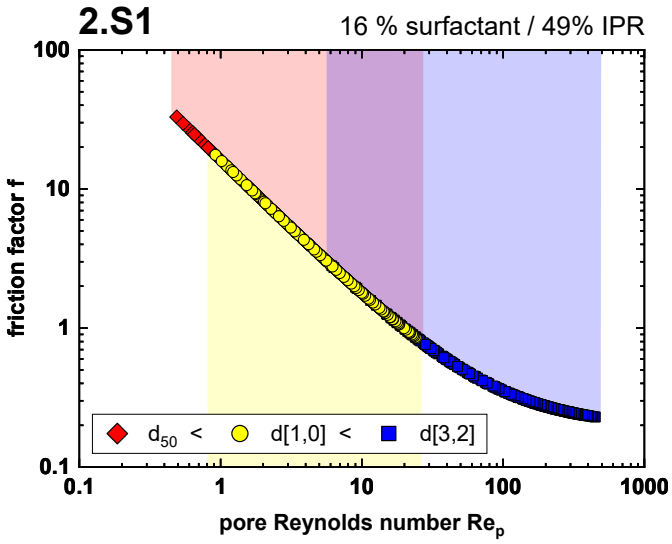

Figure 28: Friction factor vs. pore Reynolds number plot as graphical indicator for the prevailing flow regimes. The choice of the statistical parameters describing the average pore size substantially affects the assessment of the flow regime (as suggested by a *f* vs Re_p plot).

Based on analysis of SEM images, various mean diameters were calculated for poly(epoxide)MIPEs 2.S1-2.S5 (*Paper II ESI*). The impact of the pore size on the perceived flow behaviour is exemplified for sample 2.S1 in a plot Re_p vs *f* in **Figure 28**, containing Re_p calculated using *d[1,0]*, *d[3,2]* and d_{50} as characteristic length. Datapoints related to d_{50} and *d[1,0]* were located in the linear regime and thus the flow was expected to be predominantly viscous, i.e. laminar, while the plot suggested already significant non-linear inertial contributions when *d[3,2]* was used to calculate Re_p. These contributions have to be considered and accounted for in further calculations. Due to the linear relationship between Re_p and *f* of d_{50} and *d[1,0]*, it is assumed that Darcy's law should adequately describe the gas flow through poly(epoxide)MIPEs. The datapoints related to *d[3,2]*, however, indicate that the use of a Forchheimer type equation (**Eq.(21)**) is required.

4.3.1.2. Non-Darcy flow through open porous poly(epoxide)MIPEs

At higher flowrates, i.e. Re_p > 100-150, the fluid flow behaviour through porous media is not purely dictated by Darcy (viscous) flow anymore, because contributions of the bulk form drag effect start to become significant. To take these contributions into account, Dupuit and Forchheimer extended Darcy's equation by a quadratic term, which expresses not only the proportionality of inertial forces to the square of the mean velocity, but also their independence of viscosity (**Eq. (21)**):[305]

$$\frac{\mathrm{dp}}{\mathrm{dx}} = \mathrm{au} + \mathrm{b}\rho\mathrm{u}^2 \tag{21}$$

where coefficient a $\left(=\frac{\mu}{k}\right)$ [kg m^{-3} s^{-1}] represents the viscous flow and coefficient b [m^{-1}] the form factor or Forchheimer coefficient. Coefficients a and b are in literature often also denoted as α and β. The form drag force, described by the quadratic term, stems from the porous medium obstructing the fluid flow. The ρu^2 term in Forchheimer's equation can be explained through its connection to kinetic energy ($E_{kin}=\frac{1}{2}mu^2$) per unit volume of fluid, which cannot be neglected at higher flow rates. According to **Eq.(21)**, inertial effects result in an increased pressure drop for a given flow rate, $\left(\frac{dp}{dx}\right)_{\text{Forchheimer}} > \left(\frac{dp}{dx}\right)_{\text{Darcy}}$, hence, Darcy's law underestimates the pressure drop at high flow rates. From another point of view, if the pressure drop is held constant, the 'Forchheimer flow rate' will be lower than predicted by Darcy's law, $Q_{\text{Forchheimer}} < Q_{\text{Darcy}}$. Dividing the nonlinear by the linear term essentially gives a Re with characteristic length scale $\sqrt{k}$.[306] For $Re << 1$, contributions of the Forchheimer term can be neglected and Darcy's law is recovered. Generally, the Forchheimer coefficient decreases with increasing permeability and porosity. One of the main reasons for the occurrence of non-Darcy flow is the tortuous flow path that fluids tend to follow in porous media. Accordingly, the Forchheimer coefficient is larger for materials with higher tortuosity. It is commonly accepted that the quadratic term in the Forchheimer equation is related to inertia effects in the laminar regime, which is substantially different from the quadratic velocity dependence for turbulent flow.[307]

Based on **Eq.(21)**, a methodology for describing such flows was developed.[308] The mass flux G can be estimated directly from measurements since:

$$\mathrm{G} = \rho\mathrm{u} \rightarrow \rho_2 \frac{\mathrm{Q}_2}{\mathrm{A}} = \mathrm{Q}_2\mathrm{p}_2 \frac{\mathrm{M}}{\mathrm{RTA}} \xrightarrow{\mathrm{Q}_2\mathrm{p}_2=\mathrm{V}\frac{\mathrm{dp}_2}{\mathrm{dt}}} = \mathrm{V}\left(\frac{\mathrm{dp}_2}{\mathrm{dt}}\right)\frac{\mathrm{M}}{\mathrm{RTA}} \tag{22}$$

In case of isothermal flow of gases, the superficial velocity $u = \frac{G}{\rho}$ can be inserted into **Eq.(22)**, where $\rho = \frac{pM}{RT}$. After integration and rearrangements, the following equation is obtained:

$$\frac{\mu}{k} + bG = \frac{(p_1^2 - p_2^2)M}{2RTLG} = C \tag{23}$$

Using $K = \frac{V\left(\frac{dp_2}{dt}\right)L}{p_1 A}$ from Eq.(20), *C* can first be simplified to Eq.(24) and in a next step to Eq.(25), by assuming that $(p_1^2 - p_2^2) \cong p_1^2$.

$$C = \frac{(p_1^2 - p_2^2)}{2Kp_1} \tag{24}$$

$$C = \frac{p_1}{2K} = \frac{p_m}{K} \tag{25}$$

Plotting *C* vs. total mass flux *G* (**Figure 29**), which is proportional to $V\left(\frac{dp_2}{dt}\right)$, is expected to give a straight line that intersects the ordinate at $a\left(=\frac{\mu}{k}\right)$; the slope provides the Forchheimer coefficient *b*.

The data obtained from permeability measurements was used to investigate non-Darcy flow. As exemplified in **Figure 23 (right)** for one specimen of polyMIPE 2.S3 set, the plot of *G* vs. *C* is indeed linear, which is an indicator for the contribution of form drag exerted on the gas by the porous polyepoxide. The averaged results of 2.S1-2.S5 fortify this finding (**Figure 29**). From the intercept $a\left(=\frac{\mu}{k}\right)$ it is straightforward to calculate the permeability *k*. The derived permeabilities k_{DF} and Forchheimer factors *b* are summarised in **Table 3**.

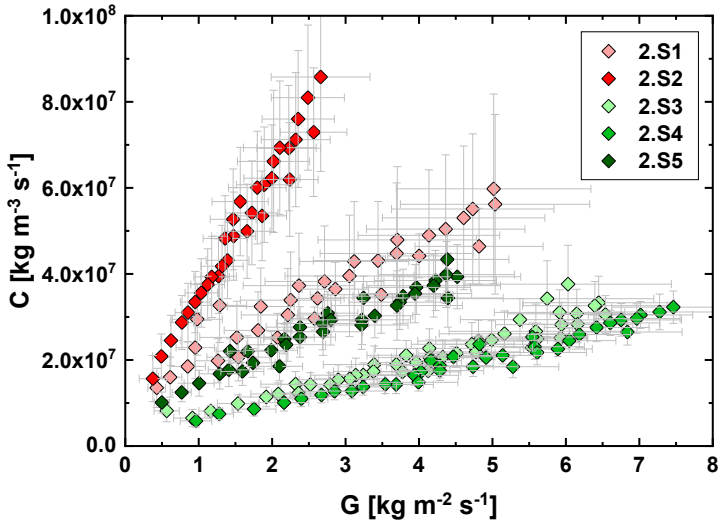

Figure 29: Linear plot of *C* vs. *G* for poly(epoxide)MIPEs 2.S1-2.S5

Calculating the permeability using the equation for non-Darcy flow leads to results that are up to ten times higher than predicted from viscous flow. In all cases, the permeabilities are overestimated. This is potentially due to the onset of form drag at various stages in different pores.

Table 3: Permeabilities k_{DF} and Forchheimer factors *b* determined from *C* vs. *G* plots

	b [m^{-1}]	k_{DF} [mD]
2.S1	$1.48 \times 10^7 \pm 1.31 \times 10^7$	2134 ± 1291
2.S2	$2.97 \times 10^7 \pm 1.17 \times 10^7$	3156 ± 2402
2.S3	$4.34 \times 10^6 \pm 1.42 \times 10^6$	5912 ± 2261
2.S4	$4.12 \times 10^6 \pm 7.01 \times 10^5$	6998 ± 3570
2.S5	$7.30 \times 10^6 \pm 2.56 \times 10^6$	2402 ± 840

4.3.2. Diffusivity *(Paper I)*

In *Paper I*, diffusivity measurements on sandstones are described using the same apparatus as for the determination of the gas permeability, after minor changes to the setup (**Figure 30**).

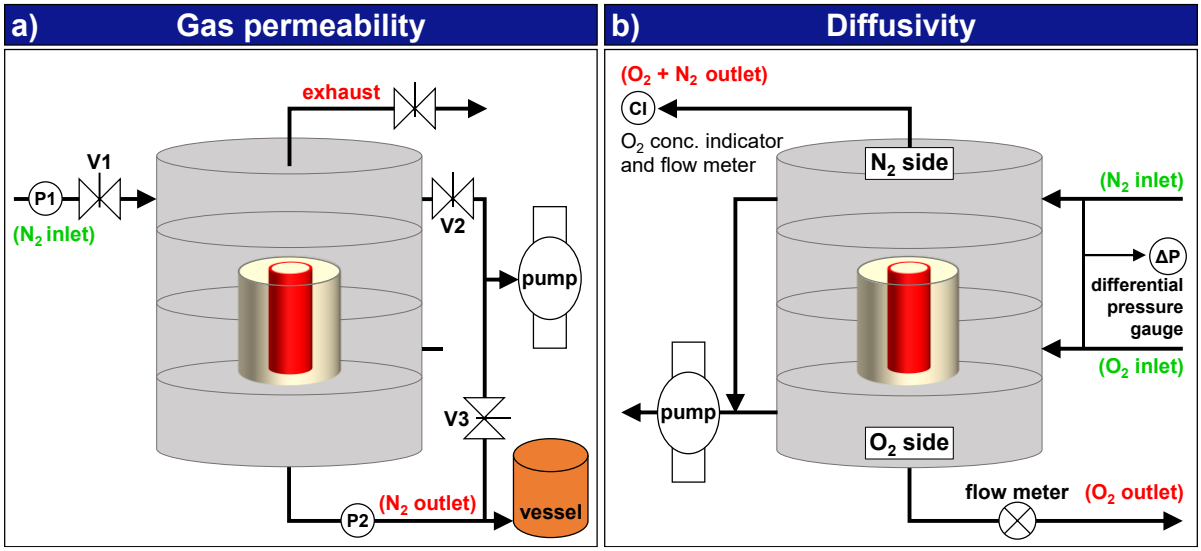

Figure 30: Comparison of the setups for gas permeability (a) and diffusivity (b) testing.

Prior to the diffusion experiments, apparatus and sample were evacuated thoroughly, down to approximately 10 Pa. After removing any pressure difference between the two surfaces by adjusting the inlet pressures of N_2 and O_2, N_2 was fed into the system to fill apparatus including the porous specimen. Subsequently, O_2 was released into the oxygen side of the device and the gas pressures were once again adjusted accordingly to ensure that there was no pressure gradient over the sample. An O_2 analyser (800 Series Zirconia Cell Oxygen Analyser Model

810, Systech Instruments Ltd., Thame, UK), also used for measuring the flow rate of the nitrogen purge stream, continuously monitored the O_2 concentration in the N_2 side, which after some time (approximately 10-15 min) an equilibrium value $(c_{O-N})_{t=\infty}$ was reached (range 0.1 ppm to 100%, accuracy 0.2% absolute, repeatability 0.2% of measured value). The tests were stopped when the rate of change was below 5%.

Uncertainty analysis of the apparatus for both permeability and diffusivity characterisation was performed considering all potential systematic and fixed errors. The uncertainty of our device for permeability and diffusivity measurements was determined to be 13% and 8% (see supplementary information *Paper I*), respectively.

5. Results & Discussion

5.1. Araldite®2020 poly(epoxide)MIPEs *(Paper II)*

Driven by the motivation to explore and advance the field of porous emulsion-templated polyepoxides, the commercial low-viscosity two-component epoxy adhesive Araldite®2020 was chosen as model system. Surfactant screening was performed using molecular emulsifiers covering the entire HLB range, from which Span®20 (sorbitan mono laurate, HLB 8.6) emerged as the most promising candidate for adequately stabilising water-in-Araldite®2020 emulsion templates.

An aqueous internal phase (10 g/l $CaCl_2 \cdot 2H_2O$) was added at a rate of 2 ml/min to an organic external/continuous phase, comprising epoxy system (resin + hardener) and surfactant, using a syringe pump. Constant stirring during injection was responsible for droplet break-up and consequently dispersion of the droplets and emulsion homogenization. Using 20 vol% Span®20, stable emulsions with up to 60 vol% internal phase ratio could be prepared, higher portions of aqueous phase resulted in incomplete emulsification. After curing (at 60°C) and removal of the template phase, epoxy foams with porosities ranging between 40 – 64%, thus classified as polyMIPEs, were obtained, which is in good agreement with the employed IPR (**Table 4**). Skeletal densities ρ_s of 2.S1-2.S5 did not show any dependence of the amount of surfactant or IPR, indicating that the composition of the matrices was not affected by alterations of the emulsion formulation.

Table 4: Summary of emulsion formulations and properties of epoxy polyMIPEs 2.S1-2.S5

	Resin/Hardener/Surfactant	**IPR**	**P**	**E_c**	**σ_c**	**T_g**	**k**
	[vol%][a] / [vol%][a] / [°C][a]	[vol%][a]	[%]	[MPa]	[MPa]	[°C]	[mD]
2.S1	63 / 22 / 16	49	43 ± 3	193 ± 14	6.4 ± 0.2	37.7 ± 0.1	93 ± 29
2.S2	63 / 22 / 16	56	58 ± 3	190 ± 5	6.2 ± 0.1	32.6 ± 1.1	37 ± 12
2.S3	59 / 21 / 20	49	54 ± 3	72 ± 9	2.2 ± 0.3	28.4 ± 0.7	94 ± 19
2.S4	59 / 21 / 20	54	54 ± 4	65 ± 14	2.0 ± 0.3	24.9 ± 0.4	85 ± 21
2.S5	59 / 21 / 20	60	62 ± 2	100 ± 10	3.2 ± 0.1	31.7 ± 0.1	147 ± 42

[a] with respect to the volume of the continuous phase

[b] relative to the total emulsion volume

Analysis of foam fracture surfaces using SEM revealed open-porous structures with heterogeneous pore size distributions. Images of 2.S1 and 2.S2 showed similar pore morphologies and were dominated by few very large pores (several 100 µm) with pore throats up to 200 µm (**Figure 31**). Although occupying the bigger part of the volume, these few huge pores contributed only a few percent to the total number of analysed pores, as illustrated and detailed in *Paper II* and its ESI.

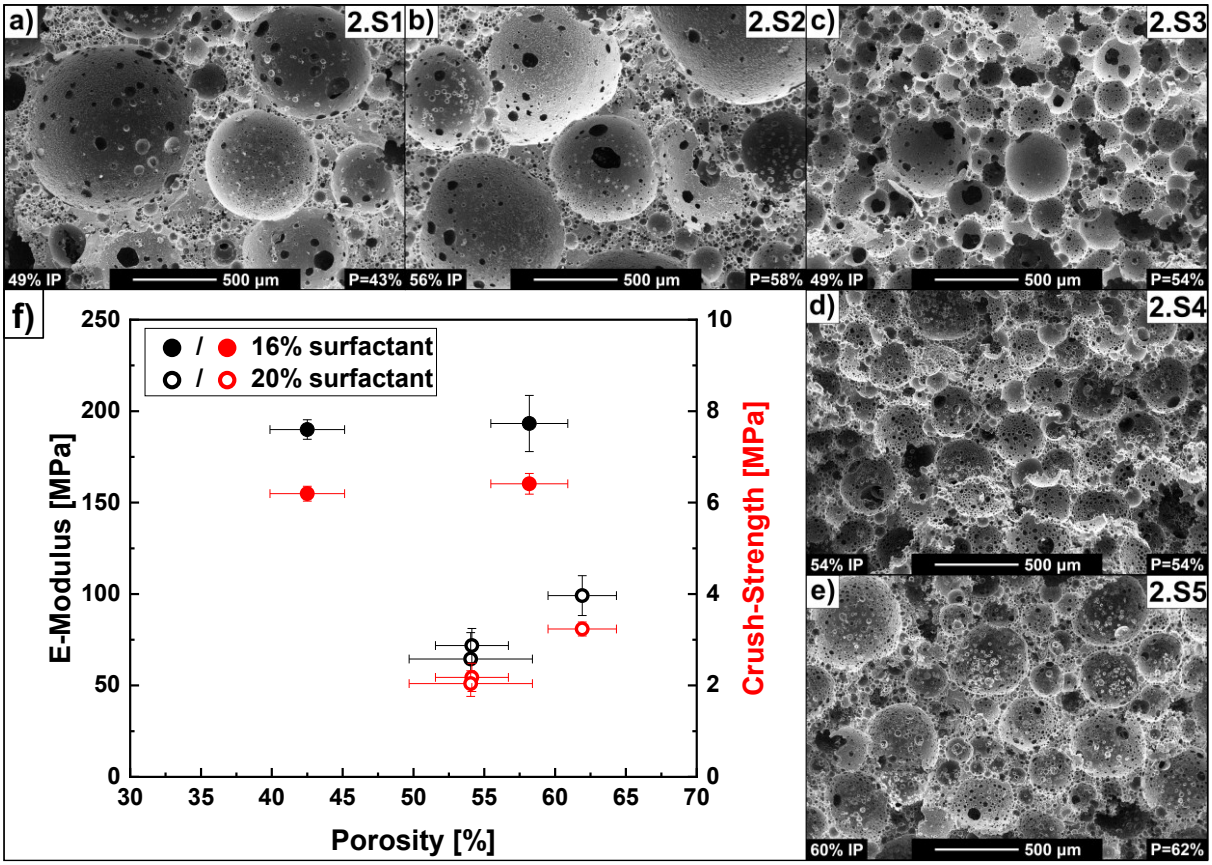

Figure 31: a-e) SEM images of epoxy polyMIPEs 2.S1-2.S5; f) compressive performance of the same foams

Generally, a higher surfactant ratio leads to a higher degree of interconnectivity by formation of pore throats. Similarly, the likelihood for open-porous materials increases with increasing internal phase ratios also resulting in a higher porosity. The formation of pore throats and a high porosity strongly influence permeability but ultimately, in case of interconnected spherical pores, it is the smallest pore throat diameter $d_{pt,min}$ of the largest pore connecting top and bottom of a porous material, which dictates and limits the flow of fluids through porous materials. Measured gas permeabilities for 2.S1-2.S5 (integral properties over a large sample, rather than a snapshot as viewed by SEM (**Figure 31**)) were in the range between 20 and

200 mD. These permeabilities are in the range of those reported for sandstones[261] and poly(styrene-co-DVB)MIPEs and -HIPEs produced by polymerisation of surfactant-stabilised emulsion templates.[309]

Differential scanning calorimetry measurements showed that epoxy polyMIPE 2.S1 had the highest glass transition temperature, 37.7 ± 0.1°C (compared to 39.5°C for pure Araldite®2020), while 2.S4 had the lowest T_g, 24.9 ± 0.4°C (**Table 4**). The T_g of epoxy polyMIPEs prepared by curing of emulsion templates stabilised with 20 vol% Span®20 were slightly lower than those prepared with only 16 vol% of surfactant, indicating a plasticizing effect of the surfactant.

The epoxy polyMIPEs were compressed by 60% of their original height to determine their elastic modulus E_c and compression strength σ_c. PolyMIPEs 2.S1 and 2.S2 had with about 190 MPa both significantly higher E-moduli than 2.S3-2.S5 with about 60-100 MPa (**Table 4, Figure 31f**), which can be explained by their thicker and less porous pore walls (**Figure 31a-e**). The same trend was observed for the crush strengths of the epoxy foams. Increasing amount of surfactant used to stabilise the MIPE templates for 2.S3-2.S5 resulted in thinner pore walls of the cured epoxy foams reducing their mechanical properties. The use of 16 vol% Span®20 (2.S1, 2.S2) resulted in epoxy polyMIPEs with 2-3x higher stiffness and strength compared to those prepared with 20 vol% (2.S3-2.S5), because of their thicker pore walls that can carry more load. Nevertheless, it showed that both parameters, porosity/IPR and surfactant content, are crucial in manufacturing materials with tailored properties.

Chemical resistance and degree of crosslinking of the porous polyepoxides were visualised through swelling tests in various solvents. The average swelling extent was practically the same for all samples, i.e. they reacted in a similar way to the exposure to a particular solvent. Swelling happened fairly quickly and the full extent of swelling was reached already after about one hour. DMSO, DMF and THF clearly caused the highest volume increases, leading to swelling ratios of about 1.7-1.8 (**Figure 32**). Isopropanol, acetone and benzene extended the foam volumes by about 20-40%, while Diesel oil had only a small impact on the sample volume.

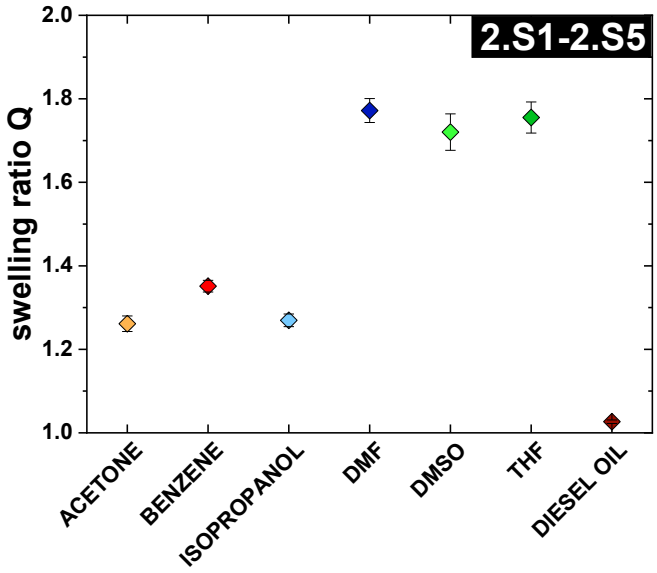

Figure 32: Average swelling ratios of Araldite®2020 polyMIPEs 2.S1-2.S5. No values for 2.S1-DMF and 2.S2-DMSO were included because the respective samples fell apart during swelling measurements.

The weight loss during the swelling tests was for all samples located in a very narrow range of 10 ± 3%. A marginal trend to higher weight loss was found for the foam cubes with higher swelling ratios, i.e. those being immersed in DMSO, DMF and THF. The higher degree of swelling of the polymer matrix probably facilitated the extraction of unbound surfactant molecules or loose polymer chains.

5.2. Flexible poly(epoxide)MIPEs *(Paper III)*

Flexible porous polyepoxides were produced from emulsion templates containing epoxy resin (EF80), hardener (EF80), surfactant (Pluronic L-81) and different amounts of MWCNTs or SiO_2 nanoparticles in the continuous phase (polyMIPEs 3.S2-3.S10). Even though emulsions prepared without emulsifier and additives remained stable during curing at room temperature (23°C) due to the already high viscosity of their epoxy formulation and the amphiphilic nature of the hardener, employing a surfactant was necessary to achieve some interconnectivity which facilitated thorough drying of the polyMIPEs. Higher temperature (50°C), applied with the intention to accelerate curing, led to a decrease in viscosity of the epoxy system and consequently lowered the stability of the emulsion templates, resulting in phase separation. Thus, in order to enhance the viscosity of the continuous phase, MWCNTs (3.S2-3.S8) or Si-NP (3.S9, 3.S10) were added to the organic continuous phase of the emulsions.

Table 5: Formulation and morphological and mechanical properties of the prepared epoxy foams

	Surfactant/IPR/Curing T	MWCNTs	P	d_p	E_c	σ_c
	[vol%][a] / [vol%][c] / [°C]	[wt%][b]	[%]	[µm]	[MPa]	[MPa]
3.S1	9 / 60 / 23	0	60 ± 1	6 ± 1	0.25 ± 0.01	0.034 ± 0.003
3.S2	9 / 60 / 23	0.4	63 ± 2	14 ± 4	0.32 ± 0.02	0.039 ± 0.005
3.S3	9 / 60 / 50	0.4	56 ± 5	112 ± 26	0.30 ± 0.02	0.038 ± 0.003
3.S4	9 / 60 / 50	0.8	64 ± 2	170 ± 50	0.21 ± 0.01	0.028 ± 0.001
3.S5	9 / 60 / 50	1.2	67 ± 2	400 ± 100	0.19 ± 0.01	0.030 ± 0.002
3.S6	9 / 70 / 50	0.4	71 ± 1	118 ± 35	0.20 ± 0.03	0.026 ± 0.010
3.S7	- / 60 / 50	0.4	64 ± 4	108 ± 12	0.32 ± 0.06	0.038 ± 0.009
3.S8	- / 70 / 50	0.4	72 ± 1	100 ± 40	0.18 ± 0.01	0.023 ± 0.002
3.S9	9 / 60 / 50	0.4[d]	61 ± 1	145 ± 37	0.40 ± 0.02	0.061 ± 0.003
3.S10	9 / 60 / 50	1.2[d]	59 ± 1	215 ± 79	0.45 ± 0.06	0.054 ± 0.010

[a] with respect to the volume of the continuous phase
[b] wt% MWCNTs relative to the monomers
[c] relative to the total emulsion volume
[d] use of modified SiO_2 (Wacker HDK H18) instead of MWCNTs

5.2.1. MWCNTs-stabilised poly(epoxide)MIPEs

First, the impact of utilising MWCNTs as rheology modifiers was investigated (3.S1-3.S6). The key results of the characterisations are summarised in **Table 5** and further illustrated in **Figure 33**. Addition of 0.4 wt% MWCNTs to the organic phase (3.S2), otherwise emulsion formulation and curing conditions were identical, resulted in slightly larger pores (6 µm vs 14 µm) and improved mechanical properties compared to polyMIPE 3.S1 (**Table 5**). The energy provided through stirring might have not been enough to achieve the droplet break up of 3.S1 due to the MWCNT-mediated higher viscosity of the emulsion template. Porous polyepoxides produced from curing MIPEs at 50°C exhibited significantly larger pores (d_p > 100 µm) and pore throats than those solidified at RT (**Figure 33**). This can be justified by the temperature-induced viscosity reduction of the liquid epoxy mixture combined with accelerated and distinctive coalescence, causing droplets to merge. However, the relatively higher viscosity of the formulation containing MWCNTs prevented phase separation. Porosities of all foams, ranged between 50 – 70 %, were in good agreement with the employed IPR. Minor losses of internal phase during curing can explain negative deviations of the determined porosities from the ones expected from the nominal IPR. Epoxy polyMIPEs S1-S6 possessed a pore structure with spherical pores interconnected by pore throats. Raising the CNT loading from 0.4 wt% to 0.8 wt% and 1.2 wt% resulted in increasingly higher viscosities and thus enlarged pores,

112 ± 26 µm, 170 ± 50 and 400 ± 100 µm, respectively. Moreover, the high viscosity impeded the homogeneous dispersion of the carbon nanotubes in the resin phase and limited the IPR that could be added to 70% (3.S6).

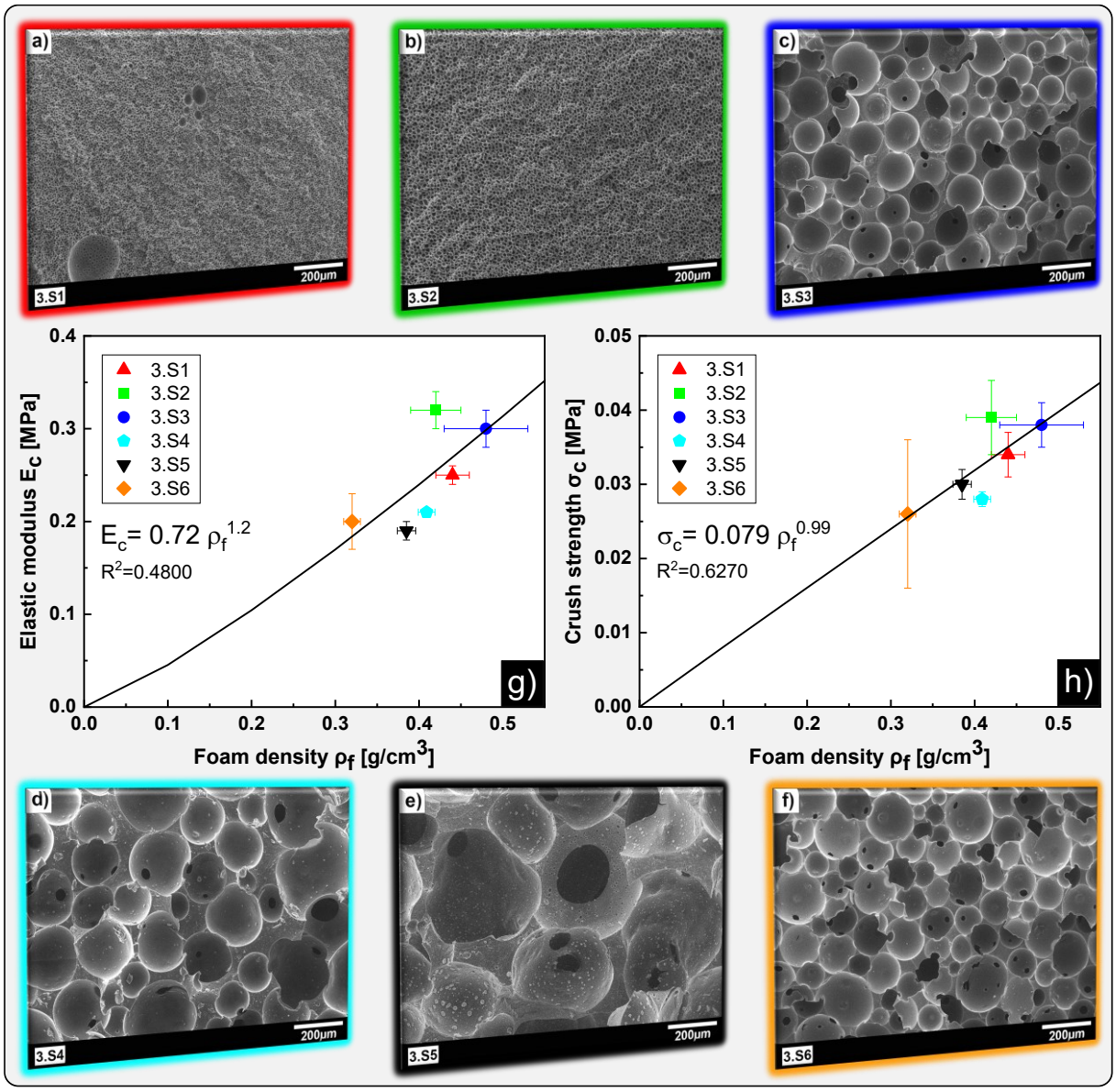

Figure 33: (a)-(f): SEM-images of flexible polyMIPEs 3.S1-3.S6 and their elastic moduli E_c (g) and crush strengths σ_c (h) as function of their foam density ρ_f.

Single uniaxial compression tests were carried out in *Paper III* to determine the mechanical properties of poly(epoxide)MIPEs 3.S1-3.S6. Elastic moduli E_c, plateau moduli E_p and compressive strengths σ_c were determined from stress-strain curves, recorded during application of the compressive load. Until the end of the tests at 70% compression, no visible failure (e.g. breaking, cracking or tearing) was observed and the foams recovered to their original height after removal of the load. The elastic moduli of the porous polyepoxides 3.S1-

3.S6 ranged from 0.2 MPa to 0.3 MPa and crush strengths from 0.02 MPa to 0.04 MPa, with foam densities between 0.3 g/cm^3 and 0.5 g/cm^3 (*Paper II*). Both, E_c and σ_c, increased with increasing foam densities and thus followed the well-established Gibson-Ashby correlations (**Figure 33g,h**):[58,237,310]

The normalised modulus (elastic modulus over foam density) of 3.S1 was 0.57 MPa / (g/cm^3), while that of 3.S2 was 0.76 MPa / (g/cm^3) probably due to the presence of CNTs. The normalised modulus of 3.S3, however, was only 0.63 MPa / (g/cm^3), despite its identical composition as 3.S2. This indicated that the larger pores with randomly distributed yet large pore throats did assist the air release from the foam during compression, while small pores and pore throats hindered the gas release from the foam, resulting in a small increase of the stiffness. A further increase in pore and pore throat sizes of 3.S4 and 3.S5 resulted in normalised moduli of 0.51 MPa / (g/cm^3) and 0.49 MPa / (g/cm^3), respectively. Although the CNTs loadings in 3.S4 and 3.S5 were different from those in 3.S2 and 3.S3, the decreased normalised moduli could also partially be attributed to the increased pore and pore throat sizes.

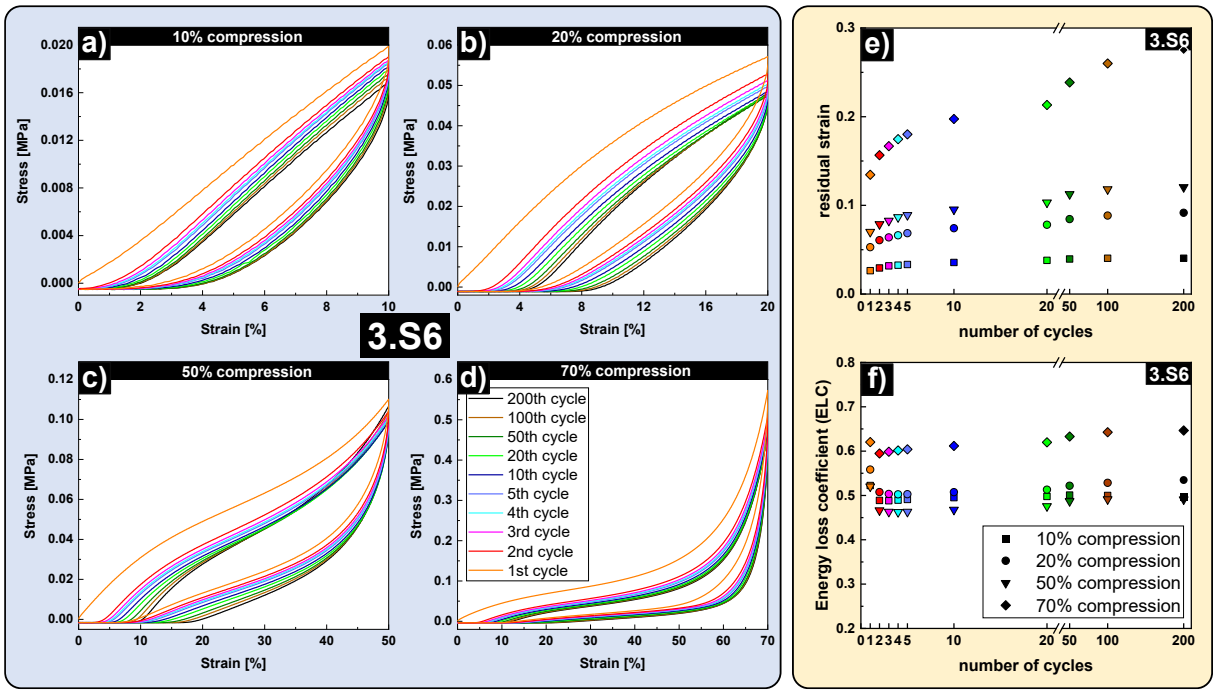

Figure 34: a-d) Cyclic compression tests performed on polyMIPE 3.S6 for different limiting strains; e+f) development of residual strain and energy loss coefficient with increasing cycle numbers.

The poly(epoxide)MIPEs S1-S3 and S6 were subjected to cyclic compression tests at predefined strain amplitudes of 10%, 20%, 50% and 70% for 200 cycles. The lower stress on

an unloading curve as compared to that at corresponding strain on the loading curve was because of the viscoelastic behaviour of the poly(epoxide)MIPEs (**Figure 34**).[198,311] During compression, the polymer chains were deformed elastically, while slippage of polymer chains occurred simultaneously. The elastic deformation of the polymer chains recovered and responded (in stress) instantly during unloading, while the slippage (viscous deformation) of the polymer chains did not recover simultaneously, leading to a lower stress. With increasing cycle numbers, the loading and unloading curves shifted downwards. The softening effect was most significant in the first cycle, represented by a large drop of the loading and unloading curve in the second cycle.

Energy loss coefficients (ELC), as quantitative measure for the energy adsorbed by a material, were evaluated using the areas beneath loading and unloading curves of each cycle (**Figure 16**). All polyMIPEs had ELCs ranging from 0.4 to 0.65, indicating an energy absorption of 40% to 65% by the foams, within the 200 loading cycles (**Figure 34f**). In the first and second loading cycles, the ELC experienced a reduction, corresponding to the pronounced softening effect in these two cycles. Afterwards, the ELC of most of the polyMIPEs reached constant values; this phenomenon was also observed in our previous work on flexible polyHIPEs.[312,313] However, in some cyclic loading tests, e.g. 3.S3 and 3.S6 loaded to a strain of 70%, the ELC increased slightly after 20 cycles. Our hypothesis is that the cyclic loading could cause some pore walls to stick to each other. Moreover, with increasing loading cycles, closure of pore throats became more influential and hindered the recovery of the polyMIPEs by impeding air flowing back into the pore structure during unloading.

The polyMIPEs do not recover their shape fully when unloaded, i.e. no stress applied (Figure 34**a-d**). Residual strains, shown in Figure 34**e-f**, were higher when the polyMIPEs were compressed by higher strains. Again, the residual strain increased within the first couple of loading cycles and then approached a constant value. For some of the foams, the residual strains increased from 20 loading cycles, which was corresponding to the increased energy adsorption after 20 loading cycles. It is noted that 3.S3 and 3.S6, which had identical polymer phase formulation and average pore and pore throat size but different porosities, had residual

strains of 0.16 and 0.29, respectively, when being compressed by 70%. With a higher porosity, 3.S6 did require more air to flow back into the polyMIPE to assist the recovery of the foams during unloading.

5.2.2. Si-NP-stabilised poly(epoxide)MIPEs *(Paper III)*

To investigate an alternative rheology modifier, hydrophobic silica nanoparticles HDK H18 were added to the continuous organic phase (3.S9 & 3.S10) instead of MWCNTs. The epoxy foams with silica nanoparticles had porosities of approximately 60%, which was expected from emulsion templates prepared with 60% IPR. The polyMIPE 3.S9 containing 0.4% silica nanoparticles had a higher elastic modulus as compared to those with corresponding loadings of CNTs. This could be explained by a more homogeneous distribution of the hydrophobized silica particles throughout the continuous phase of the emulsions, after curing the silica particles reinforced the epoxy polymer. In contrast, CNTs tend to form large agglomerates, which have to be broken up by applying high shear forces, which are not easily applied in liquid resin formulations. Nevertheless, the pore sizes of the epoxy foams with 0.4% silica particles were slightly larger than those (112 ± 26 µm) with 0.4% CNTs. This indicated that during the curing of the emulsions at elevated temperature, the silica nanoparticles, even when homogeneously distributed, did not act as a better thickening agent as compared to CNTs, which, due to their 2D shape, are more effective to increase the viscosity of the continuous phase. Increasing the silica nanoparticle loading to 1.2% in the epoxy based emulsion templates resulted after curing in epoxy foams with larger pore sizes. Yet, the increase of the pore sizes was not as pronounced as that of epoxy foams with CNTs.

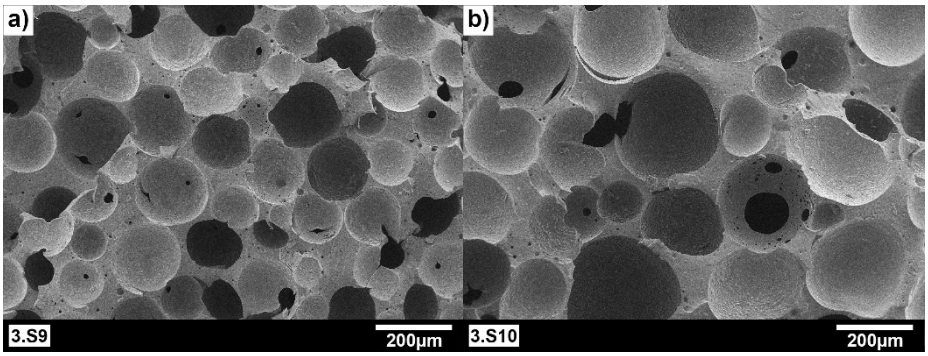

Figure 35: SEM images of epoxy polyMIPEs 3.S9 (a) and 3.S10 (b), prepared from emulsion templates with 0.4 and 1.2 wt% silica nanoparticles, respectively.

This indicated that the increased loading did not affect the dispersion of the silica. As such, the stiffness of the epoxy foams containing 1.2% silica nanoparticles were identical within error to that of the epoxy foams with 0.4% silica particles.

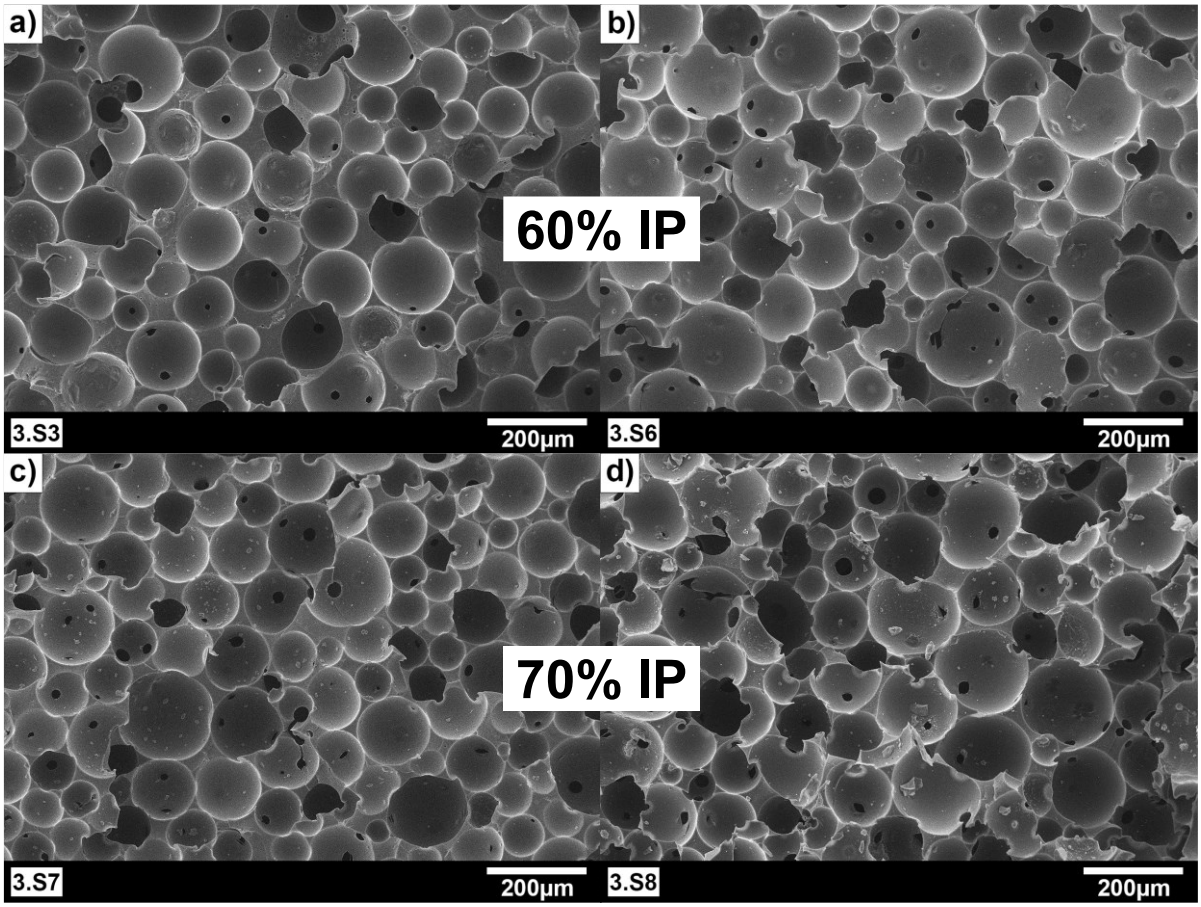

Figure 36: SEM images of epoxy polyMIPEs 3.S3, 3.S6, 3.S7 and 3.S8, prepared from emulsion templates with 60% IPR (a,b) and 70% IPR (c,d). The MWCNT content was 0.4 wt% for all four samples. A small amount of surfactant (9 vol%) was employed in 3.S3 and 3.S6.

5.2.3. Surfactant-free poly(epoxide)MIPEs *(Paper III)*

The preliminary experiment in producing polyMIPEs from MIPEs without surfactant indicated that the viscosity of the formulation had a significant impact on the stability of the emulsions and the morphology of the subsequent polyMIPEs, while the surfactant played a minor role in the properties of the emulsions and epoxy foams. Therefore, 3.S7 and 3.S8 were cured from emulsion templates with MWCNTs but no surfactant. 3.S7 and 3.S8 showed both pore morphology and mechanical properties in analogy to their corresponding polyMIPEs (3.S3 and 3.S6, respectively). This provided a method to produce epoxy foams without the presence of surfactant.

6. Conclusions

This dissertation reports the preparation of porous polyepoxides using the method of emulsion templating. Within its scope, limitations of emulsion templated epoxy-based porous polymers, often related to emulsion stability and internal phase content, thus porosity, were explored. Epoxy resins were chosen because of their versatile properties and their good price-to-performance ratio, compared to expensive high-performance polymers, such as PEEK, PEKK or polyimides for instance. Macroporous polyepoxide foams were prepared from surfactant-stabilised MIPEs, with a continuous phase based on a commercial Bisphenol A epoxy adhesive (Araldite®2020). Pore structure, porosity and permeability were tuneable through internal phase ratio and the surfactant concentration in the continuous phase.

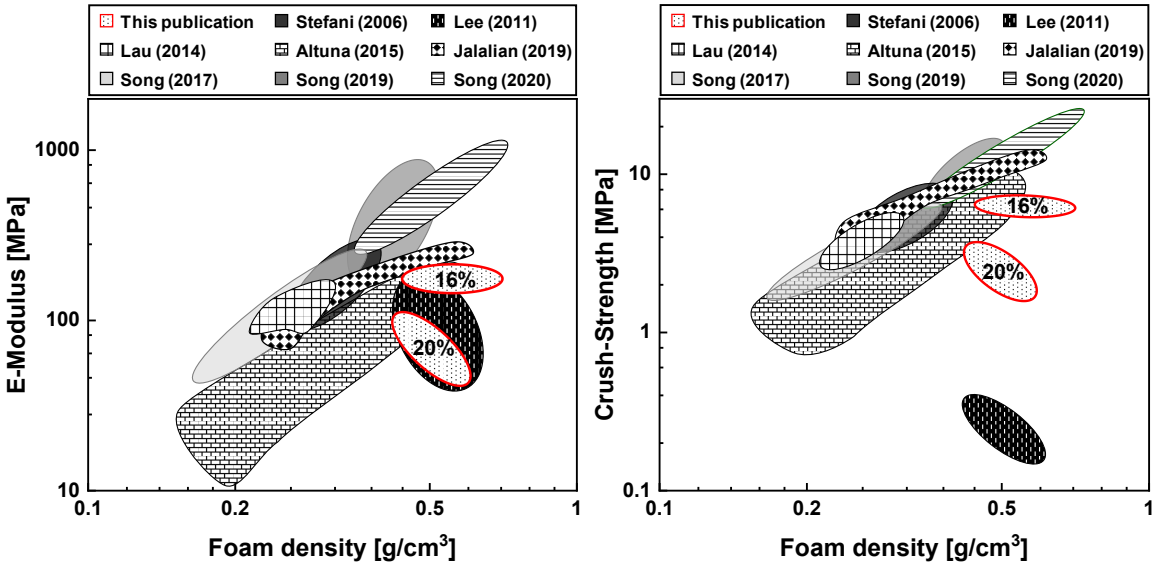

Figure 37: E-modulus and crush-strength of poly(epoxide)MIPEs prepared by us in comparison with results from literature.[58,59,204,216-219,314]

Due to thinner pore walls, mechanical compression properties, i.e. elastic/compression modulus and crush/compressive strength, were significantly lower for samples prepared from MIPEs with higher surfactant concentrations (**Figure 37**). Even though our proof-of-concept poly(epoxide)MIPEs did not outperform previously reported epoxy foams prepared using other methods, it becomes evident from **Figure 37** that emulsion templating is nevertheless a viable method for producing polyepoxide foams, especially considering advantages such as the

higher safety due to the aqueous internal phase compared to foam templating. The presence of H_2O as heat sink allows for the production of thick samples.

Furthermore, flexible macroporous poly(epoxide)MIPEs were manufactured from emulsions containing epoxy resin & hardener (EF80), emulsifier and carbon nanotubes in the minor continuous phase and an aqueous droplet phase. Due to the decrease of viscosity with increasing temperature, curing of the emulsion templates at 50°C required the addition of MWCNTs as thickening agent to counteract the accelerated emulsion destabilisation. Nonetheless, the higher curing temperature resulted in materials with significantly larger pores than those of MIPEs cured at room temperature. Further increase of the CNT-loading led to a further increase in viscosity of the continuous phase and consequently even larger pores, in the range of several hundred micrometres, due to hindered dispersion of the droplets of the template phase in the highly viscous surrounding. Cyclic compression tests, repeated loading-unloading, did not cause any visible failure or fracture in the foams. Energy loss coefficients, representing the energy adsorbed during compressive loading and ranged between 40 and 60%, showed the potential as cushioning or packaging materials.

A fully integrated gas transport apparatus, able to determine permeability and diffusivity of porous materials covering a broad porosity range, was developed. Accuracy and validity of the measurement method was established by measurements on sandstones and poly(epoxide)MIPEs. The device further allows evaluation of tortuosity, effective porosity and effective pore diameter from steady state diffusion of oxygen in nitrogen.

7. Outlook – suggestions for future work

The work presented in this thesis demonstrates that epoxy resins are a suitable monomer system to be used for emulsion templating, or from a different point of view, that emulsion templating is a viable method for the production of porous polyepoxides with tailorable properties. Building on the laid foundation, future work can follow different paths. On one hand, it is essential to find means to stabilise emulsions to an extent which allows for higher internal phase ratios and thus preparation of materials with higher porosities, in the range of polyHIPEs ($P > 74\%$). Another approach to gain additional porosity can be the integration of expandable beads or hollow spheres.

On the other hand, work should be dedicated to the potential use of high performance epoxy systems. However, many of them are not well processable at ambient conditions or moderately elevated temperatures because of their high viscosities. Application of high temperature and/or pressure is not compatible with the use of an aqueous internal phase, as it would be prone to evaporate prior to solidification of the continuous phase. Therefore, the use of a different internal phase could be considered, supercritical carbon dioxide or ionic liquids for instance, going along with incomparably higher procedural and financial effort though, consequently also bearing the challenge of up-scaling.

Epoxy-based emulsion templates are highly dimensionally stable as they maintain their size and shape during solidification. Their liquid nature in combination with the low or even negligible shrinkage on curing makes them predestined for being moulded into any kind of shapes. Higher glass transition temperatures can potentially be achieved by hypercrosslinking of porous poly(epoxide)MIPEs. Mechanical testing in different loading conditions, by means of the Arcan test, can be performed to gain further information and understanding of mechanical properties not accessible from uniaxial compression tests.[315]

8. References

1. Ashby, M. F.; Medalist, R. F. M., The mechanical properties of cellular solids. *Metallurgical Transactions A* **1983,** *14* (9), 1755-1769; https://dx.doi.org/10.1007/BF02645546
2. Berro, S.; El Ahdab, R.; Hajj Hassan, H.; Khachfe, H. M.; Hajj-Hassan, M., From Plastic to Silicone: The Novelties in Porous Polymer Fabrications. *Journal of Nanomaterials* **2015,** *2015*, 142195; https://dx.doi.org/10.1155/2015/142195
3. Silverstein, M. S., The Chemistry of Porous Polymers: The Holey Grail. *Israel Journal of Chemistry* **2020,** *60* (1-2), 140-150; https://dx.doi.org/10.1002/ijch.202000003
4. Wu, D.; Xu, F.; Sun, B.; Fu, R.; He, H.; Matyjaszewski, K., Design and Preparation of Porous Polymers. *Chemical Reviews* **2012,** *112* (7), 3959-4015; https://dx.doi.org/10.1021/cr200440z
5. Barbetta, A.; Dentini, M.; Leandri, L.; Ferraris, G.; Coletta, A.; Bernabei, M., Synthesis and characterization of porous glycidylmethacrylate–divinylbenzene monoliths using the high internal phase emulsion approach. *Reactive and Functional Polymers* **2009,** *69* (9), 724-736; https://dx.doi.org/10.1016/j.reactfunctpolym.2009.05.007
6. Eaves, D., *Handbook of Polymer Foams*. Rapra Technology Ltd.: Shrewsbury, UK, 2004;
7. Kmetty, Á.; Litauszki, K.; Réti, D., Characterization of Different Chemical Blowing Agents and Their Applicability to Produce Poly(Lactic Acid) Foams by Extrusion. *Applied Sciences* **2018,** *8*, 1960; https://dx.doi.org/10.3390/app8101960
8. Stehr, J., Chemical Blowing Agents in the Rubber Industry. Past – Present – and Future? *International Polymer Science and Technology* **2016,** *43* (5), 1-10; https://dx.doi.org/10.1177/0307174x1604300501
9. Jones, S. F.; Evans, G. M.; Galvin, K. P., Bubble nucleation from gas cavities — a review. *Advances in Colloid and Interface Science* **1999,** *80* (1), 27-50; https://dx.doi.org/10.1016/S0001-8686(98)00074-8
10. Salerno, A.; Iannace, S.; Netti, P. A., Open-pore biodegradable foams prepared via gas foaming and microparticulate templating. *Macromol Biosci* **2008,** *8* (7), 655-64; https://dx.doi.org/10.1002/mabi.200700278
11. Bonnaillie, L. M.; Wool, R. P., Thermosetting foam with a high bio-based content from acrylated epoxidized soybean oil and carbon dioxide. *Journal of Applied Polymer Science* **2007,** *105* (3), 1042-1052; https://dx.doi.org/10.1002/app.26182
12. Tai, H.; Mather, M. L.; Howard, D.; Wang, W.; White, L. J.; Crowe, J. A.; Morgan, S. P.; Chandra, A.; Williams, D. J.; Howdle, S. M.; Shakesheff, K. M., Control of pore size and structure of tissue engineering scaffolds produced by supercritical fluid processing. *Eur Cell Mater* **2007,** *14*, 64-77; https://dx.doi.org/10.22203/ecm.v014a07
13. Ghalia, M. A.; Dahman, Y., Chapter 6 - Advanced nanobiomaterials in tissue engineering: Synthesis, properties, and applications. In *Nanobiomaterials in Soft Tissue Engineering*, Grumezescu, A. M., Ed. William Andrew Publishing: 2016; pp 141-172; https://dx.doi.org/10.1016/B978-0-323-42865-1.00006-4
14. Matsuyama, H.; Teramoto, M.; Kuwana, M.; Kitamura, Y., Formation of polypropylene particles via thermally induced phase separation. *Polymer* **2000,** *41* (24), 8673-8679; https://dx.doi.org/10.1016/S0032-3861(00)00268-8

15. Nam, Y. S.; Park, T. G., Biodegradable polymeric microcellular foams by modified thermally induced phase separation method. *Biomaterials* **1999,** *20* (19), 1783-1790; https://dx.doi.org/10.1016/S0142-9612(99)00073-3

16. Rusakov, D.; Menner, A.; Bismarck, A., High-Performance Polymer Foams by Thermally Induced Phase Separation. *Macromol Rapid Comm* **2020,** *41* (11), 2000110; https://dx.doi.org/10.1002/marc.202000110

17. Conoscenti, G.; La Carrubba, V.; Brucato, V., A Versatile Technique to Produce Porous Polymeric Scaffolds: The Thermally Induced Phase Separation (TIPS) Method. *Archives in Chemical Research* **2017,** *1* (2); https://dx.doi.org/10.21767/2572-4657.100012

18. Tan, X.; Rodrigue, D., A Review on Porous Polymeric Membrane Preparation. Part I: Production Techniques with Polysulfone and Poly (Vinylidene Fluoride). *Polymers* **2019,** *11* (7), 1160;

19. Guillen, G. R.; Pan, Y.; Li, M.; Hoek, E. M. V., Preparation and Characterization of Membranes Formed by Nonsolvent Induced Phase Separation: A Review. *Ind Eng Chem Res* **2011,** *50* (7), 3798-3817; https://dx.doi.org/10.1021/ie101928r

20. Dong, X.; Al-Jumaily, A.; Escobar, I. C., Investigation of the Use of a Bio-Derived Solvent for Non-Solvent-Induced Phase Separation (NIPS) Fabrication of Polysulfone Membranes. *Membranes (Basel)* **2018,** *8* (2), 23; https://dx.doi.org/10.3390/membranes8020023

21. Young, T.-H.; Cheng, L.-P.; Lin, D.-J.; Fane, L.; Chuang, W.-Y., Mechanisms of PVDF membrane formation by immersion-precipitation in soft (1-octanol) and harsh (water) nonsolvents. *Polymer* **1999,** *40* (19), 5315-5323; https://dx.doi.org/10.1016/S0032-3861(98)00747-2

22. Qian, L.; Zhang, H., Porogen Incorporation and Phase Inversion. In *Porous Polymers*, 2011; pp 79-117; https://dx.doi.org/10.1002/9780470929445.ch3

23. Wan, C. T.-C.; Jacquemond, R. R.; Chiang, Y.-M.; Nijmeijer, K.; Brushett, F. R.; Forner-Cuenca, A., Non-Solvent Induced Phase Separation Enables Designer Redox Flow Battery Electrodes. *Adv Mater* **2021,** *33* (16), 2006716; https://dx.doi.org/10.1002/adma.202006716

24. Loera, A. G.; Cara, F.; Dumon, M.; Pascault, J. P., Porous Epoxy Thermosets Obtained by a Polymerization-Induced Phase Separation Process of a Degradable Thermoplastic Polymer. *Macromolecules* **2002,** *35* (16), 6291-6297; https://dx.doi.org/10.1021/ma011567i

25. Soulé, E.; de la Mata, M. G.; Borrajo, J.; Oyanguren, P. A.; Galante, M. J., Reaction-induced phase separation in an epoxy/low molecular weight solvent system. *J Mater Sci* **2003,** *38* (13), 2809-2814; https://dx.doi.org/10.1023/A:1024420132081

26. Kiefer, J.; Hedrick, J. L.; Hilborn, J. G., Macroporous Thermosets by Chemically Induced Phase Separation. In *Macromolecular Architectures*, Hilborn, J. G.; Dubois, P.; Hawker, C. J.; Hedrick, J. L.; Hilborn, J. G.; Jérôme, R.; Kiefer, J.; Labadie, J. W.; Mecerreyes, D.; Volksen, W., Eds. Springer Berlin Heidelberg: Berlin, Heidelberg, 1999; pp 161-247; https://dx.doi.org/10.1007/3-540-49196-1_4

27. Li, J.; Du, Z.; Li, H.; Zhang, C., Porous epoxy monolith prepared via chemically induced phase separation. *Polymer* **2009,** *50* (6), 1526-1532; https://dx.doi.org/10.1016/j.polymer.2009.01.049

28. Mi, Y.; Liu, S.; Zhang, Y.; Sun, J.; Zhou, W., The Roles Played by DMF in the Structure Formation of Epoxy-Based Porous Monolith. *Polymer Science, Series B* **2020,** *62*; https://dx.doi.org/10.1134/S1560090420050097
29. Dubinsky, S.; Petukhova, A.; Gourevich, I.; Kumacheva, E., Hybrid porous material produced by polymerization-induced phase separation. *Chem Commun* **2010,** *46* (15), 2578-2580; https://dx.doi.org/10.1039/B924373A
30. Kiefer, J.; Hilborn, J. G.; Hedrick, J. L., Chemically induced phase separation: a new technique for the synthesis of macroporous epoxy networks. *Polymer* **1996,** *37* (25), 5715-5725; https://dx.doi.org/10.1016/S0032-3861(96)00436-3
31. Tran-Cong-Miyata, Q.; Nakanishi, H., Phase separation of polymer mixtures driven by photochemical reactions: current status and perspectives. *Polymer International* **2017,** *66* (2), 213-222; https://dx.doi.org/10.1002/pi.5243
32. Deore, B.; Sampson, K. L.; Lacelle, T.; Kredentser, N.; Lefebvre, J.; Young, L. S.; Hyland, J.; Amaya, R. E.; Tanha, J.; Malenfant, P. R. L.; de Haan, H. W.; Paquet, C., Direct printing of functional 3D objects using polymerization-induced phase separation. *Nature Communications* **2021,** *12* (1), 55; https://dx.doi.org/10.1038/s41467-020-20256-3
33. Williams, R. J. J.; Rozenberg, B. A.; Pascault, J.-P., Reaction-induced phase separation in modified thermosetting polymers. In *Polymer Analysis Polymer Physics*, Springer Berlin Heidelberg: Berlin, Heidelberg, 1997; pp 95-156; https://dx.doi.org/10.1007/3-540-61218-1_7
34. Bailey, B. M.; Hui, V.; Fei, R.; Grunlan, M. A., Tuning PEG-DA hydrogel properties via solvent-induced phase separation (SIPS). *J Mater Chem* **2011,** *21* (46), 18776-18782; https://dx.doi.org/10.1039/C1JM13943F
35. Bailey, B. M.; Fei, R.; Munoz-Pinto, D.; Hahn, M. S.; Grunlan, M. A., PDMS(star)-PEG hydrogels prepared via solvent-induced phase separation (SIPS) and their potential utility as tissue engineering scaffolds. *Acta biomaterialia* **2012,** *8* (12), 4324-4333; https://dx.doi.org/10.1016/j.actbio.2012.07.034
36. Venault, A.; Chang, Y.; Wang, D.-M.; Bouyer, D., A Review on Polymeric Membranes and Hydrogels Prepared by Vapor-Induced Phase Separation Process. *Polymer Reviews* **2013,** *53*; https://dx.doi.org/10.1080/15583724.2013.828750
37. Chae Park, H.; Po Kim, Y.; Yong Kim, H.; Soo Kang, Y., Membrane formation by water vapor induced phase inversion. *Journal of Membrane Science* **1999,** *156* (2), 169-178; https://dx.doi.org/10.1016/S0376-7388(98)00359-7
38. Ulbricht, M., Separation Membranes. In *Porous Polymers*, 2011; pp 275-321; https://dx.doi.org/10.1002/9780470929445.ch8
39. Pervin, R.; Ghosh, P.; Basavaraj, M. G., Tailoring pore distribution in polymer films via evaporation induced phase separation. *Rsc Adv* **2019,** *9* (27), 15593-15605; https://dx.doi.org/10.1039/C9RA01331H
40. Yoshihara, H.; Yamamura, M., Formation mechanism of asymmetric porous polymer films by photoinduced phase separation in the presence of solvent. *Journal of Applied Polymer Science* **2019,** *136* (34), 47867; https://dx.doi.org/10.1002/app.47867
41. Liu, K.; Kiran, E., Pressure-Induced Phase Separation in Polymer Solutions: Kinetics of Phase Separation and Crossover from Nucleation and Growth to Spinodal Decomposition in Solutions of Polyethylene in n-Pentane. *Macromolecules* **2001,** *34* (9), 3060-3068; https://dx.doi.org/10.1021/ma000816k

42. Kiran, E.; Liu, K.; Bayraktar, Z., Polymer Solutions at High Pressures: Pressure-Induced Miscibility and Phase Separation in Near-critical and Supercritical Fluids. In *Computational Studies, Nanotechnology, and Solution Thermodynamics of Polymer Systems*, Dadmun, M. D.; Van Hook, W. A.; Noid, D. W.; Melnichenko, Y. B.; Sumpter, B. G., Eds. Springer US: Boston, MA, 2002; pp 55-68; https://dx.doi.org/10.1007/0-306-47110-8_6

43. Altuna, F. I.; Espósito, L.; Ruseckaite, R. A.; Stefani, P. M., Syntactic foams from copolymers based on epoxidized soybean oil. *Composites Part A: Applied Science and Manufacturing* **2010,** *41* (9), 1238-1244; https://dx.doi.org/10.1016/j.compositesa.2010.05.006

44. Liu, X. M.; He, C. J.; Li, H. J.; Peng, H. Y., Water Absorption and Diffusion in Hollow Glass Microsphere Filled Epoxy Syntactic Foams. *Advanced Materials Research* **2011,** *143-144*, 370-374; https://dx.doi.org/10.4028/www.scientific.net/AMR.143-144.370

45. Wang, W.-T.; Watkins, L. In *Flexible Epoxy Syntactic Foam Thermal Insulation for High Temperature Deepsea Reelable Pipelay Installations*, ASME 2010 29th International Conference on Ocean, Offshore and Arctic Engineering, 2010; pp 269-273; https://dx.doi.org/10.1115/omae2010-21014

46. Song, W.; Tagarielli, V. L.; Lee, K.-Y., Enhancing the Fracture Resistance and Impact Toughness of Mechanically Frothed Epoxy Foams with Hollow Elastomeric Microspheres. *Macromolecular Materials and Engineering* **2018,** *303* (12), 1800363; https://dx.doi.org/10.1002/mame.201800363

47. Cameron, N. R.; Krajnc, P.; Silverstein, M. S., Colloidal Templating. In *Porous Polymers*, 2011; pp 119-172; https://dx.doi.org/10.1002/9780470929445.ch4

48. Stubenrauch, C.; Menner, A.; Bismarck, A.; Drenckhan, W., Emulsion and Foam Templating—Promising Routes to Tailor-Made Porous Polymers. *Angewandte Chemie International Edition* **2018,** *57* (32), 10024-10032; https://dx.doi.org/10.1002/anie.201801466

49. Salonen, A.; Drenckhan-Andreatta, W.; Rio, E.; Saint-Jalmes, A.; Langevin, D., Foaming emulsion. **2010**;

50. Salonen, A.; Lhermerout, R.; Rio, E.; Langevin, D.; Saint-Jalmes, A., Dual gas and oil dispersions in water: production and stability of foamulsion. *Soft Matter* **2012,** *8* (3), 699-706; https://dx.doi.org/10.1039/C1SM06537H

51. Elsing, J.; Stefanov, T.; Gilchrist, M. D.; Stubenrauch, C., Monodisperse polystyrene foams via polymerization of foamed emulsions: structure and mechanical properties. *Phys Chem Chem Phys* **2017,** *19* (7), 5477-5485; https://dx.doi.org/10.1039/c6cp06612g

52. Schüler, F.; Schamel, D.; Salonen, A.; Drenckhan, W.; Gilchrist, M. D.; Stubenrauch, C., Synthesis of macroporous polystyrene by the polymerization of foamed emulsions. *Angewandte Chemie (International ed. in English)* **2012,** *51* (9), 2213-2217; https://dx.doi.org/10.1002/anie.201107806

53. Dabrowski, M. L.; Hamann, M.; Stubenrauch, C., Formulation and polymerization of foamed 1,4-BDDMA-in-water emulsions. *Rsc Adv* **2020,** *10* (15), 8917-8926; https://dx.doi.org/10.1039/D0RA00254B

54. Dabrowski, M. L.; Stubenrauch, C., Methacrylate-Based Polymer Foams with Controllable Pore Sizes and Controllable Polydispersities via Foamed Emulsion

Templating. *Advanced Engineering Materials* **2021,** *23* (3), 2001013; https://dx.doi.org/10.1002/adem.202001013

55. Hong, Y.; Zhou, J. G.; Yao, D., Porogen Templating Processes: An Overview. *Journal of Manufacturing Science and Engineering* **2014,** *136* (3); https://dx.doi.org/10.1115/1.4026899

56. Liang, X.; Qi, Y.; Pan, Z.; He, Y.; Liu, X.; Cui, S.; Ding, J., Design and preparation of quasi-spherical salt particles as water-soluble porogens to fabricate hydrophobic porous scaffolds for tissue engineering and tissue regeneration. *Materials Chemistry Frontiers* **2018,** *2* (8), 1539-1553; https://dx.doi.org/10.1039/C8QM00152A

57. Drenckhan, W.; Saint-Jalmes, A., The science of foaming. *Advances in Colloid and Interface Science* **2015,** *222*, 228-259; https://dx.doi.org/10.1016/j.cis.2015.04.001

58. Jalalian, M.; Jiang, Q.; Bismarck, A., Air Templated Macroporous Epoxy Foams with Silica Particles as Property-Defining Additive. *ACS Applied Polymer Materials* **2019,** *1* (3), 335-343; https://dx.doi.org/10.1021/acsapm.8b00084

59. Lau, T. H. M.; Wong, L. L. C.; Lee, K.-Y.; Bismarck, A., Tailored for simplicity: creating high porosity, high performance bio-based macroporous polymers from foam templates. *Green Chem.* **2014,** *16* (4), 1931-1940; https://dx.doi.org/10.1039/c3gc41807c

60. Lee, K.-Y.; Wong, L. L. C.; Blaker, J. J.; Hodgkinson, J. M.; Bismarck, A., Bio-based macroporous polymer nanocomposites made by mechanical frothing of acrylated epoxidised soybean oil. *Green Chem* **2011,** *13* (11), 3117-3123; https://dx.doi.org/10.1039/C1GC15655A

61. Barbetta, A.; Rizzitelli, G.; Bedini, R.; Pecci, R.; Dentini, M., Porous gelatin hydrogels by gas-in-liquid foam templating. *Soft Matter* **2010,** *6* (8), 1785-1792; https://dx.doi.org/10.1039/B920049E

62. Barbetta, A.; Carrino, A.; Costantini, M.; Dentini, M., Polysaccharide based scaffolds obtained by freezing the external phase of gas-in-liquid foams. *Soft Matter* **2010,** *6* (20), 5213-5224; https://dx.doi.org/10.1039/C0SM00616E

63. Zhu, X.; Lee, L.; Jackson, J.; Tong, Y.; Wang, C.-H., Characterization of porous poly(D,L-lactic-co-glycolic acid) sponges fabricated by supercritical CO2 gas-foaming method as a scaffold for three-dimensional growth of Hep3B cells. *Biotechnology and bioengineering* **2008,** *100*, 998-1009; https://dx.doi.org/10.1002/bit.21824

64. Bartl, V. H.; Von Bonin, W., Über die Polymerisation in umgekehrter Emulsion. *Die Makromolekulare Chemie* **1962,** *57* (1), 74-95; https://dx.doi.org/10.1002/macp.1962.020570105

65. Lissant, K. J., The Geometry of High-Internal-Phase-Ratio Emulsions. *J Colloid Interf Sci* **1966,** *22*, 7; https://dx.doi.org/10.1002/macp.1962.020570105

66. Barby, D.; Haq, Z. Low density porous cross-linked polymeric materials and their preparation. 1982.

67. Ruckenstein, E.; Hong, L., Sedimentation polymerization. *Polymer* **1995,** *36* (14), 2857-2860; https://dx.doi.org/10.1016/0032-3861(95)93669-D

68. Mudassir, M. A.; Hussain, S. Z.; Asma, S. T.; Zhang, H.; Ansari, T. M.; Hussain, I., Fabrication of Emulsion-Templated Poly(vinylsulfonic acid)–Ag Nanocomposite Beads with Hierarchical Multimodal Porosity for Water Cleanup. *Langmuir* **2019,** *35* (40), 13165-13173; https://dx.doi.org/10.1021/acs.langmuir.9b02518

69. Wang, W.-c.; Pan, Y.-x.; Shi, K.; Peng, C.; Ji, X.-l., Hierarchical porous polymer beads prepared by polymerization-induced phase separation and emulsion-template in a microfluidic device. *Chinese Journal of Polymer Science* **2014,** *32* (12), 1646-1654; https://dx.doi.org/10.1007/s10118-014-1547-1

70. Mudassir, M. A.; Hussain, S. Z.; Jilani, A.; Zhang, H.; Ansari, T. M.; Hussain, I., Magnetic Hierarchically Macroporous Emulsion-Templated Poly(acrylic acid)–Iron Oxide Nanocomposite Beads for Water Remediation. *Langmuir* **2019,** *35* (27), 8996-9003; https://dx.doi.org/10.1021/acs.langmuir.9b01121

71. Zhang, H.; Hardy, G. C.; Rosseinsky, M. J.; Cooper, A. I., Uniform Emulsion-Templated Silica Beads with High Pore Volume and Hierarchical Porosity. *Adv Mater* **2003,** *15* (1), 78-81; https://dx.doi.org/10.1002/adma.200390017

72. Zhang, H.; Cooper, A. I., Synthesis of Monodisperse Emulsion-Templated Polymer Beads by Oil-in-Water-in-Oil (O/W/O) Sedimentation Polymerization. *Chemistry of Materials* **2002,** *14* (10), 4017-4020; https://dx.doi.org/10.1021/cm0206643

73. Ruckenstein, E.; Park, J. S., Stable concentrated emulsions as precursors for hydrophilic-hydrophobic polymer composites. *Polymer* **1992,** *33* (2), 405-417; https://dx.doi.org/10.1016/0032-3861(92)91001-I

74. Ruckenstein, E.; Sun, F., Concentrated Emulsion Pathway to Novel Composite Polymeric Membranes and Their Use in Pervaporation. *Ind Eng Chem Res* **1995,** *34* (10), 3581-3589; https://dx.doi.org/10.1021/ie00037a048

75. Cameron, N. R., High internal phase emulsion templating as a route to well-defined porous polymers. *Polymer* **2005,** *46* (5), 1439-1449; https://dx.doi.org/10.1016/j.polymer.2004.11.097

76. Zhang, H.; Cooper, A. I., Synthesis and applications of emulsion-templated porous materials. *Soft Matter* **2005,** *1* (2), 107; https://dx.doi.org/10.1039/b502551f

77. Kimmins, S. D.; Cameron, N. R., Functional Porous Polymers by Emulsion Templating: Recent Advances. *Advanced Functional Materials* **2011,** *21* (2), 211-225; https://dx.doi.org/10.1002/adfm.201001330

78. Pulko, I.; Krajnc, P., High internal phase emulsion templating--a path to hierarchically porous functional polymers. *Macromol Rapid Commun* **2012,** *33* (20), 1731-46; https://dx.doi.org/10.1002/marc.201200393

79. Silverstein, M. S., Emulsion-templated porous polymers: A retrospective perspective. *Polymer* **2014,** *55* (1), 304-320; https://dx.doi.org/10.1016/j.polymer.2013.08.068

80. Silverstein, M. S., PolyHIPEs: Recent advances in emulsion-templated porous polymers. *Progress in Polymer Science* **2014,** *39* (1), 199-234; https://dx.doi.org/10.1016/j.progpolymsci.2013.07.003

81. Tebboth, M.; Menner, A.; Kogelbauer, A.; Bismarck, A., Polymerised high internal phase emulsions for fluid separation applications. *Curr Opin Chem Eng* **2014,** *4*, 114-120; https://dx.doi.org/10.1016/j.coche.2014.03.001

82. Silverstein, M. S., Emulsion-templated polymers: Contemporary contemplations. *Polymer* **2017,** *126*, 261-282; https://dx.doi.org/10.1016/j.polymer.2017.07.046

83. Zhang, T.; Sanguramath, R. A.; Israel, S.; Silverstein, M. S., Emulsion Templating: Porous Polymers and Beyond. *Macromolecules* **2019,** *52* (15), 5445-5479; https://dx.doi.org/10.1021/acs.macromol.8b02576

84. Aldemir Dikici, B.; Claeyssens, F., Basic Principles of Emulsion Templating and Its Use as an Emerging Manufacturing Method of Tissue Engineering Scaffolds. *Frontiers in*

Bioengineering and Biotechnology **2020,** *8*, 875; https://dx.doi.org/10.3389/fbioe.2020.00875

85. Kramer, S.; Cameron, N. R.; Krajnc, P., Porous Polymers from High Internal Phase Emulsions as Scaffolds for Biological Applications. *Polymers* **2021,** *13* (11), 1786; https://dx.doi.org/10.3390/polym13111786
86. Foudazi, R., HIPEs to PolyHIPEs. *Reactive and Functional Polymers* **2021,** *164*, 104917; https://dx.doi.org/10.1016/j.reactfunctpolym.2021.104917
87. Okazawa, T.; Bron, J., On thermodynamically stable emulsions: I. Thermodynamic Background. *J Colloid Interf Sci* **1979,** *69* (1), 86-96; https://dx.doi.org/10.1016/0021-9797(79)90083-3
88. Tadros, T. F., Emulsion Formation, Stability, and Rheology. In *Emulsion Formation and Stability*, Tadros, T. F., Ed. Wiley-VCH: 2013; pp 1-75; https://dx.doi.org/10.1002/9783527647941.ch1
89. Richardson, J. F.; Zaki, W. N., Sedimentation and fluidisation: Part I. *Chemical Engineering Research and Design* **1997,** *75*, S82-S100; https://dx.doi.org/10.1016/S0263-8762(97)80006-8
90. Walstra, P., Emulsions. In *Fundamentals of Interface and Colloid Science*, Lyklema, J., Ed. Academic Press: 2005; Vol. 5, pp 8.1-8.94; https://dx.doi.org/10.1016/S1874-5679(05)80012-1
91. Tadros, T. F., *Emulsions - Formation, Stability, Industrial Applications*. De Gruyter: 2016; https://dx.doi.org/10.1515/9783110452242
92. Fauchais, P.; Vardelle, A.; Vardelle, M., Chapter 10 - Thermally Sprayed Nanoceramic and Nanocomposite Coatings. In *Handbook of Nanoceramic and Nanocomposite Coatings and Materials*, Makhlouf, A. S. H.; Scharnweber, D., Eds. Butterworth-Heinemann: 2015; pp 225-256; https://dx.doi.org/10.1016/B978-0-12-799947-0.00010-9
93. McClements, D. J., *Food Emulsions: Principles, Practices, and Techniques*. 3rd ed. ed.; CRC Press: 2015; https://dx.doi.org/10.1201/b18868
94. Tadros, T. F., Interparticle Interactions and Their Combination. In *Rheology of Dispersions*, Tadros, T. F., Ed. Wiley VCH: 2010; pp 7-36; https://dx.doi.org/10.1002/9783527631568.ch2
95. *Modern Aspects of Emulsion Science*. 1st ed. ed.; The Royal Society of Chemistry: London, U.K., 1998; https://dx.doi.org/10.1039/9781847551474
96. Graeber, N. A Study of Fundamentals in Emulsion Templating for the Preparation of Macroporous Polymer Foams. Imperial College London, London, 2013;
97. Esquena, J.; Sankar; Solans, C., Highly Concentrated W/O Emulsions Prepared by the PIT Method as Templates for Solid Foams. *Langmuir* **2003,** *19* (7), 2983-2988; https://dx.doi.org/10.1021/la026129z
98. Xu, X.-X., Study on oil–water two-phase flow in horizontal pipelines. *J Petrol Sci Eng* **2007,** *59* (1), 43-58; https://dx.doi.org/10.1016/j.petrol.2007.03.002
99. Salager, J.-L., Phase Transformation and Emulsion Inversion on the Basis of Catastrophe Theory. In *Encyclopedia of Emulsion Technology - Basic Theory, Measurement, Applications. Vol.4*, Becher, P., Ed. Marcel Dekker: New York, USA, 1987;

100. Salager, J.-L.; Márquez, L.; Peña, A. A.; Rondón, M.; Silva, F.; Tyrode, E., Current Phenomenological Know-How and Modeling of Emulsion Inversion. *Ind Eng Chem Res* **2000,** *39* (8), 2665-2676; https://dx.doi.org/10.1021/ie990778x
101. Brooks, B. W.; Richmond, H. N., Dynamics of liquid—liquid phase inversion using non-ionic surfactants. *Colloids and Surfaces* **1991,** *58* (1), 131-148; https://dx.doi.org/10.1016/0166-6622(91)80203-Z
102. Taylor, P., Ostwald ripening in emulsions. *Advances in Colloid and Interface Science* **1998,** *75* (2), 107-163; https://dx.doi.org/10.1016/S0001-8686(98)00035-9
103. Kabalnov, A., Ostwald Ripening and Related Phenomena. *Journal of Dispersion Science and Technology* **2001,** *22* (1), 1-12; https://dx.doi.org/10.1081/DIS-100102675
104. Meier, G. H., Curved surfaces. In *Thermodynamics of Surfaces and Interfaces: Concepts in Inorganic Materials*, Meier, G. H., Ed. Cambridge University Press: Cambridge, 2014; pp 148-183; https://dx.doi.org/10.1017/CBO9781139047029.007
105. Butt, H.-J.; Graf, K.; Kappl, M., Liquid Surfaces. In *Physics and Chemistry of Interfaces*, Wiley-VCH: 2003; pp 4-25; https://dx.doi.org/10.1002/3527602313.ch2
106. Kontogeorgis, G. M.; Kiil, S., Fundamental Equations in Colloid and Surface Science. In *Introduction to Applied Colloid and Surface Chemistry*, John Wiley & Sons, Ltd.: 2016; pp 74-95; https://dx.doi.org/10.1002/9781118881194.ch4
107. Kuz, V. A., A vapor pressure equation for droplets. *Langmuir* **1993,** *9* (12), 3722-3723; https://dx.doi.org/10.1021/la00036a059
108. Kaptay, G., The Gibbs Equation versus the Kelvin and the Gibbs-Thomson Equations to Describe Nucleation and Equilibrium of Nano-Materials. *Journal of nanoscience and nanotechnology* **2012,** *12*, 2625-33; https://dx.doi.org/10.1166/jnn.2012.5774
109. Skinner, L. M.; Sambles, J. R., The Kelvin equation - a review. *J Aerosol Sci* **1972,** *3* (3), 199-210; https://dx.doi.org/10.1016/0021-8502(72)90158-9
110. Galvin, K. P., A conceptually simple derivation of the Kelvin equation. *Chem Eng Sci* **2005,** *60* (16), 4659-4660; https://dx.doi.org/10.1016/j.ces.2005.03.030
111. Wu, W.; Nancollas, G. H., A New Understanding of the Relationship Between Solubility and Particle Size. *Journal of Solution Chemistry* **1998,** *27* (6), 521-531; https://dx.doi.org/10.1023/A:1022678505433
112. Náraigh, L.; Gloster, A., *A large-scale statistical study of the coarsening rate in models of Ostwald-Ripening*. 2019;
113. Rahn-Chique, K.; Urbina-Villalba, G., Use of the Lifshitz-Slyosov-Wagner Theory for the Prediction of the Drop Size of an Emulsion Subject to Flocculation and Coalescence. *Interciencia* **2015,** *40*, 847-853;
114. Baldan, A., Review Progress in Ostwald ripening theories and their applications to nickel-base superalloys Part I: Ostwald ripening theories. *J Mater Sci* **2002,** *37* (11), 2171-2202; https://dx.doi.org/10.1023/A:1015388912729
115. Kahlweit, M., Ostwald ripening of precipitates. *Advances in Colloid and Interface Science* **1975,** *5* (1), 1-35; https://dx.doi.org/10.1016/0001-8686(75)85001-9
116. Marqusee, J. A.; Ross, J., Kinetics of phase transitions: Theory of Ostwald ripening. *The Journal of Chemical Physics* **1983,** *79* (1), 373-378; https://dx.doi.org/10.1063/1.445532

117. Taylor, P.; Ottewill, R. H., The formation and ageing rates of oil-in-water miniemulsions. *Colloids and Surfaces A: Physicochemical and Engineering Aspects* **1994,** *88* (2), 303-316; https://dx.doi.org/10.1016/0927-7757(94)02853-2

118. Jiang, J.; Mei, Z.; Xu, J.; Sun, D., Effect of inorganic electrolytes on the formation and the stability of water-in-oil (W/O) emulsions. *Colloids and Surfaces A: Physicochemical and Engineering Aspects* **2013,** *429*, 82-90; https://dx.doi.org/10.1016/j.colsurfa.2013.03.039

119. Kundu, P.; Agrawal, A.; Mateen, H.; Mishra, I. M., Stability of oil-in-water macro-emulsion with anionic surfactant: Effect of electrolytes and temperature. *Chem Eng Sci* **2013,** *102*, 176-185; https://dx.doi.org/10.1016/j.ces.2013.07.050

120. Mei, Z.; Xu, J.; Sun, D., O/W nano-emulsions with tunable PIT induced by inorganic salts. *Colloids and Surfaces A: Physicochemical and Engineering Aspects* **2011,** *375* (1), 102-108; https://dx.doi.org/10.1016/j.colsurfa.2010.11.069

121. Shinoda, K.; Takeda, H., The effect of added salts in water on the hydrophile-lipophile balance of nonionic surfactants: The effect of added salts on the phase inversion temperature of emulsions. *J Colloid Interf Sci* **1970,** *32* (4), 642-646; https://dx.doi.org/10.1016/0021-9797(70)90157-8

122. Soma, J.; Papadopoulos, K. D., Ostwald Ripening in Sodium Dodecyl Sulfate-Stabilized Decane-in-Water Emulsions. *J Colloid Interf Sci* **1996,** *181* (1), 225-231; https://dx.doi.org/10.1006/jcis.1996.0374

123. Binks, B. P., Chapter 1 Emulsions — Recent Advances in Understanding. In *Modern Aspects of Emulsion Science*, The Royal Society of Chemistry: 1998; pp 1-55; https://dx.doi.org/10.1039/9781847551474-00001

124. McClements, D. J., Nanoemulsions versus microemulsions: terminology, differences, and similarities. *Soft Matter* **2012,** *8* (6), 1719-1729; https://dx.doi.org/10.1039/C2SM06903B

125. Solans, C.; Izquierdo, P.; Nolla, J.; Azemar, N.; Garcia-Celma, M. J., Nano-emulsions. *Current Opinion in Colloid & Interface Science* **2005,** *10* (3), 102-110; https://dx.doi.org/10.1016/j.cocis.2005.06.004

126. Rosen, M. J.; Kunjappu, J. T., Emulsification by Surfactants. In *Surfactants and Interfacial Phenomena*, Rosen, M. J.; Kunjappu, J. T., Eds. John Wiley & Sons: 2012; pp 336-367; https://dx.doi.org/10.1002/9781118228920.ch8

127. Sudol, E. D.; El-Aasser, M., Miniemulsion Polymerization. In *Emulsion Polymerization and Emulsion Polymers*, Lovell, P. A.; El-Aasser, M., Eds. John Wiley & Sons: Chichester, U.K., 1997;

128. Delmas, T.; Piraux, H.; Couffin, A.-C.; Texier, I.; Vinet, F.; Poulin, P.; Cates, M. E.; Bibette, J., How To Prepare and Stabilize Very Small Nanoemulsions. *Langmuir* **2011,** *27* (5), 1683-1692; https://dx.doi.org/10.1021/la104221q

129. Gupta, A.; Eral, H. B.; Hatton, T. A.; Doyle, P. S., Nanoemulsions: formation, properties and applications. *Soft Matter* **2016,** *12* (11), 2826-2841; https://dx.doi.org/10.1039/C5SM02958A

130. Landfester, K.; Tiarks, F.; Hentze, H.-P.; Antonietti, M., Polyaddition in miniemulsions: A new route to polymer dispersions. *Macromolecular Chemistry and Physics* **2000,** *201* (1), 1-5; https://dx.doi.org/10.1002/(SICI)1521-3935(20000101)201:1<1::AID-MACP1>3.0.CO;2-N

131. Tang, P. L.; Sudol, E. D.; Silebi, C. A.; El-Aasser, M. S., Miniemulsion polymerization—a comparative study of preparative variables. *Journal of Applied Polymer Science* **1991,** *43* (6), 1059-1066; https://dx.doi.org/10.1002/app.1991.070430604

132. Forgiarini, A.; Esquena, J.; González, C.; Solans, C., Formation of Nano-emulsions by Low-Energy Emulsification Methods at Constant Temperature. *Langmuir* **2001,** *17* (7), 2076-2083; https://dx.doi.org/10.1021/la001362n

133. Mason, T. G.; Wilking, J. N.; Meleson, K.; Chang, C. B.; Graves, S. M., Nanoemulsions: formation, structure, and physical properties. *Journal of Physics: Condensed Matter* **2006,** *18* (41), R635-R666; https://dx.doi.org/10.1088/0953-8984/18/41/r01

134. Slomkowski, S.; Alemán, J. V.; Gilbert, R. G.; Hess, M.; Horie, K.; Jones, R. G.; Kubisa, P.; Meisel, I.; Mormann, W.; Penczek, S.; Stepto, R. F. T., Terminology of polymers and polymerization processes in dispersed systems (IUPAC Recommendations 2011). *Pure Appl Chem* **2011,** *83* (12), 2229-2259; https://dx.doi.org/10.1351/PAC-REC-10-06-03

135. Izquierdo, P.; Esquena, J.; Tadros, T. F.; Dederen, C.; Garcia, M. J.; Azemar, N.; Solans, C., Formation and Stability of Nano-Emulsions Prepared Using the Phase Inversion Temperature Method. *Langmuir* **2002,** *18* (1), 26-30; https://dx.doi.org/10.1021/la010808c

136. Wilde, P. J., Improving Emulsion Stability Through Selection of Emulsifiers and Stabilizers. In *Reference Module in Food Science*, Elsevier: 2019; https://dx.doi.org/10.1016/B978-0-08-100596-5.22337-8

137. Erbil, H. Y., Liquid Solution Surfaces. In *Surface Chemistry of Solid and Liquid Interfaces*, Erbil, H. Y., Ed. Blackwell Publishing: 2006; pp 156-222; https://dx.doi.org/10.1002/9781444305401.ch5

138. Emulsions. In *Surfactant Science and Technology*, 2005; pp 280-322; https://dx.doi.org/10.1002/047174607X.ch9

139. Pasquali, R.; Sacco, N.; Bregni, C., The Studies on Hydrophilic-Lipophilic Balance (HLB): Sixty Years after William C. Griffin's Pioneer Work (1949-2009). *Latin American Journal of Pharmacy* **2009,** *28*;

140. Yamashita, Y.; Sakamoto, K., Hydrophilic–Lipophilic Balance (HLB): Classical Indexation and Novel Indexation of Surfactant. In *Encyclopedia of Biocolloid and Biointerface Science 2V Set*, 2016; pp 570-574; https://dx.doi.org/10.1002/9781119075691.ch45

141. Davis, H. T., Factors determining emulsion type: Hydrophile—lipophile balance and beyond. *Colloids and Surfaces A: Physicochemical and Engineering Aspects* **1994,** *91*, 9-24; https://dx.doi.org/10.1016/0927-7757(94)02929-6

142. Tadros, T. F., Emulsion Science and Technology: A General Introduction. In *Emulsion Science and Technology*, 2009; pp 1-56; https://dx.doi.org/10.1002/9783527626564.ch1

143. Griffin, W. C., Calculation of HLB Values of Non-ionic Surfactants. *J. Soc. Cosmet. Chem.* **1954,** *5*, 249-256;

144. Griffin, W. C., Classification of surface-active agents by "HLB". *J. Soc. Cosmet. Chem.* **1949,** *1*, 311-326;

145. Guo, X.; Rong, Z.; Ying, X., Calculation of hydrophile–lipophile balance for polyethoxylated surfactants by group contribution method. *J Colloid Interf Sci* **2006,** *298* (1), 441-450; https://dx.doi.org/10.1016/j.jcis.2005.12.009

146. Davies, J. T. In *A quantitative kinetic theory of emulsion type. - I. Physical chemistry of the emulsifying agent*, 2nd International Congress Surface Activity, London, Davies, J. T., Ed. Proc. Int. Congress Surface Activity, 2nd ed.: London, 1957; p 426;

147. Arai, H.; Shinoda, K., The effect of mixing of oils and of nonionic surfactants on the phase inversion temperatures of emulsions. *J Colloid Interf Sci* **1967,** *25* (3), 396-400; https://dx.doi.org/10.1016/0021-9797(67)90047-1

148. Shinoda, K.; Arai, H., The effect of phase volume on the phase inversion temperature of emulsions stabilized with nonionic surfactants. *J Colloid Interf Sci* **1967,** *25* (3), 429-431; https://dx.doi.org/10.1016/0021-9797(67)90051-3

149. Kronberg, B.; Holmberg, K.; Lindman, B., Emulsions and Emulsifiers. In *Surface Chemistry of Surfactants and Polymers*, Kronberg, B.; Holmberg, K.; Lindman, B., Eds. John Wiley & Sons, Ltd.: 2014; pp 431-445; https://dx.doi.org/10.1002/9781118695968.ch24

150. Shinoda, K., The Comparison between the PIT System and HLB-value System to Emulsifier Selection. *Nippon kagaku zassi* **1968,** *89* (5), 435-442; https://dx.doi.org/10.1246/nikkashi1948.89.5_435

151. Witthayapanyanon, A.; Harwell, J. H.; Sabatini, D. A., Hydrophilic–lipophilic deviation (HLD) method for characterizing conventional and extended surfactants. *J Colloid Interf Sci* **2008,** *325* (1), 259-266; https://dx.doi.org/10.1016/j.jcis.2008.05.061

152. Nguyen, T. T.; Morgan, C.; Poindexter, L.; Fernandez, J., Application of the Hydrophilic–Lipophilic Deviation Concept to Surfactant Characterization and Surfactant Selection for Enhanced Oil Recovery. *Journal of Surfactants and Detergents* **2019,** *22* (5), 983-999; https://dx.doi.org/10.1002/jsde.12305

153. Abbott, S., *Surfactand Science: Principles and Practice*. DEStech Publications, Inc.: Lancaster, Pennsylvania, 2019;

154. Aubry, J.-M.; Ontiveros, J. F.; Salager, J.-L.; Nardello-Rataj, V., Use of the normalized hydrophilic-lipophilic-deviation (HLDN) equation for determining the equivalent alkane carbon number (EACN) of oils and the preferred alkane carbon number (PACN) of nonionic surfactants by the fish-tail method (FTM). *Advances in Colloid and Interface Science* **2020,** *276*, 102099; https://dx.doi.org/10.1016/j.cis.2019.102099

155. Holtzscherer, C.; Candau, F., Application of the cohesive energy ratio concept (CER) to the formation of polymerizable microemulsions. *Colloids and Surfaces* **1988,** *29* (4), 411-423; https://dx.doi.org/10.1016/0166-6622(88)80151-3

156. Vaughan, C. D.; Rice, D. A., Predicting O/W emulsion stability by the 'required HLB equation'. *Journal of Dispersion Science and Technology* **1990,** *11* (1), 83-91; https://dx.doi.org/10.1080/01932699008943238

157. Israelachvili, J. N.; Mitchell, D. J.; Ninham, B. W., Theory of self-assembly of hydrocarbon amphiphiles into micelles and bilayers. *Journal of the Chemical Society, Faraday Transactions 2: Molecular and Chemical Physics* **1976,** *72* (0), 1525-1568; https://dx.doi.org/10.1039/F29767201525

158. Yan, N.; Gray, M. R.; Masliyah, J. H., On water-in-oil emulsions stabilized by fine solids. *Colloids and Surfaces A: Physicochemical and Engineering Aspects* **2001,** *193* (1), 97-107; https://dx.doi.org/10.1016/S0927-7757(01)00748-8

159. Chevalier, Y.; Bolzinger, M.-A., Emulsions stabilized with solid nanoparticles: Pickering emulsions. *Colloids and Surfaces A: Physicochemical and Engineering Aspects* **2013,** *439*, 23-34; https://dx.doi.org/10.1016/j.colsurfa.2013.02.054

160. Aveyard, R.; Binks, B. P.; Clint, J. H., Emulsions stabilised solely by colloidal particles. *Advances in Colloid and Interface Science* **2003,** *100-102*, 503-546; https://dx.doi.org/10.1016/S0001-8686(02)00069-6

161. Binks, B. P.; Horozov, T. S., *Colloidal Particles at Liquid Interfaces*. Cambridge University Press: Cambridge, 2006; https://dx.doi.org/10.1017/CBO9780511536670

162. Pugh, R. J., Particle-stabilized foams. In *Bubble and Foam Chemistry*, Pugh, R. J., Ed. Cambridge University Press: Cambridge, 2016; pp 269-306; https://dx.doi.org/10.1017/CBO9781316106938.009

163. Lam, S.; Velikov, K. P.; Velev, O. D., Pickering stabilization of foams and emulsions with particles of biological origin. *Current Opinion in Colloid & Interface Science* **2014,** *19* (5), 490-500; https://dx.doi.org/10.1016/j.cocis.2014.07.003

164. Salager, J.-L.; Marquez, N.; Graciaa, A.; Lachaise, J., Partitioning of Ethoxylated Octylphenol Surfactants in Microemulsion−Oil−Water Systems: Influence of Temperature and Relation between Partitioning Coefficient and Physicochemical Formulation. *Langmuir* **2000,** *16* (13), 5534-5539; https://dx.doi.org/10.1021/la9905517

165. Horozov, T. S., Foams and foam films stabilised by solid particles. *Current Opinion in Colloid & Interface Science* **2008,** *13* (3), 134-140; https://dx.doi.org/10.1016/j.cocis.2007.11.009

166. Horozov, T. S.; Binks, B. P., Particle-Stabilized Emulsions: A Bilayer or a Bridging Monolayer? *Angewandte Chemie International Edition* **2006,** *45* (5), 773-776; https://dx.doi.org/10.1002/anie.200503131

167. Hunter, T. N.; Pugh, R. J.; Franks, G. V.; Jameson, G. J., The role of particles in stabilising foams and emulsions. *Advances in Colloid and Interface Science* **2008,** *137* (2), 57-81; https://dx.doi.org/10.1016/j.cis.2007.07.007

168. Kralchevsky, P. A.; Ivanov, I. B.; Ananthapadmanabhan, K. P.; Lips, A., On the Thermodynamics of Particle-Stabilized Emulsions: Curvature Effects and Catastrophic Phase Inversion. *Langmuir* **2005,** *21* (1), 50-63; https://dx.doi.org/10.1021/la047793d

169. Lopetinsky, R. J. G.; Masliyah, J. H.; Xu, Z., Solids-Stabilized Emulsions: A Review. In *Colloidal Particles at Liquid Interfaces*, Binks, B. P.; Horozov, T. S., Eds. Cambridge University Press: Cambridge, 2006; pp 186-224; https://dx.doi.org/10.1017/CBO9780511536670.007

170. Liang, F.; Liu, B.; Cao, Z.; Yang, Z., Janus Colloids toward Interfacial Engineering. *Langmuir* **2018,** *34* (14), 4123-4131; https://dx.doi.org/10.1021/acs.langmuir.7b02308

171. Aveyard, R., Can Janus particles give thermodynamically stable Pickering emulsions? *Soft Matter* **2012,** *8* (19), 5233-5240; https://dx.doi.org/10.1039/C2SM07230K

172. Hirose, Y.; Komura, S.; Nonomura, Y., Adsorption of Janus particles to curved interfaces. *The Journal of Chemical Physics* **2007,** *127* (5), 054707; https://dx.doi.org/10.1063/1.2756828

173. Jiang, S.; Granick, S., Janus balance of amphiphilic colloidal particles. *The Journal of Chemical Physics* **2007,** *127* (16), 161102; https://dx.doi.org/10.1063/1.2803420

174. Tu, F.; Park, B. J.; Lee, D., Thermodynamically Stable Emulsions Using Janus Dumbbells as Colloid Surfactants. *Langmuir* **2013,** *29* (41), 12679-12687; https://dx.doi.org/10.1021/la402897d

175. Perro, A.; Reculusa, S.; Ravaine, S.; Bourgeat-Lami, E.; Duguet, E., Design and synthesis of Janus micro- and nanoparticles. *J Mater Chem* **2005,** *15* (35-36), 3745-3760; https://dx.doi.org/10.1039/B505099E

176. Williams, J. M.; Wrobleski, D. A., Spatial-Distribution of the Phases in Water-in-Oil Emulsions - Open and Closed Microcellular Foams from Cross-Linked Polystyrene. *Langmuir* **1988,** *4* (3), 656-662; https://dx.doi.org/10.1021/la00081a027

177. Mason, T. G.; Bibette, J., Shear Rupturing of Droplets in Complex Fluids. *Langmuir* **1997,** *13* (17), 4600-4613; https://dx.doi.org/10.1021/la9700580

178. Ikem, V. O.; Menner, A.; Bismarck, A., Tailoring the mechanical performance of highly permeable macroporous polymers synthesized via Pickering emulsion templating. *Soft Matter* **2011,** *7* (14), 6571-6577; https://dx.doi.org/10.1039/c1sm05272a

179. Wong, L. L. C.; Ikem, V. O.; Menner, A.; Bismarck, A., Macroporous Polymers with Hierarchical Pore Structure from Emulsion Templates Stabilised by Both Particles and Surfactants. *Macromol Rapid Comm* **2011,** *32* (19), 1563-1568; https://dx.doi.org/10.1002/marc.201100382

180. Cameron, N. R.; Sherrington, D. C.; Albiston, L.; Gregory, D. P., Study of the formation of the open-cellular morphology of poly(styrene/divinylbenzene) polyHIPE materials by cryo-SEM. *Colloid & Polymer Sci* **1996,** *274* (6), 592-595; https://dx.doi.org/10.1007/BF00655236

181. Menner, A.; Bismarck, A., New evidence for the mechanism of the pore formation in polymerising High Internal Phase Emulsions or why polyHIPEs have an interconnected pore network structure. *Macromol Symp* **2006,** *242*, 19-24; https://dx.doi.org/10.1002/masy.200651004

182. Williams, J. M.; Gray, A. J.; Wilkerson, M. H., Emulsion Stability and Rigid Foams from Styrene or Divinylbenzene Water-in-Oil Emulsions. *Langmuir* **1990,** *6* (2), 437-444; https://dx.doi.org/10.1021/la00092a026

183. Aronson, M. P.; Petko, M. F., Highly Concentrated Water-in-Oil Emulsions: Influence of Electrolyte on Their Properties and Stability. *J Colloid Interf Sci* **1993,** *159* (1), 134-149; https://dx.doi.org/10.1006/jcis.1993.1305

184. Horozov, T. S.; Binks, B. P.; Gottschalk-Gaudig, T., Effect of electrolyte in silicone oil-in-water emulsions stabilised by fumed silica particles. *Physical Chemistry Chemical Physics* **2007,** *9* (48), 6398-6404; https://dx.doi.org/10.1039/B709807N

185. Okay, O., Macroporous copolymer networks. *Progress in Polymer Science* **2000,** *25* (6), 711-779; https://dx.doi.org/10.1016/S0079-6700(00)00015-0

186. C. Sherrington, D., Preparation, structure and morphology of polymer supports. *Chem Commun* **1998,** (21), 2275-2286; https://dx.doi.org/10.1039/A803757D

187. Carnachan, R. J.; Bokhari, M.; Przyborski, S. A.; Cameron, N. R., Tailoring the morphology of emulsion-templated porous polymers. *Soft Matter* **2006,** *2* (7), 608-616; https://dx.doi.org/10.1039/B603211G

188. Huš, S.; Kolar, M.; Krajnc, P., Tailoring morphological features of cross-linked emulsion-templated poly(glycidyl methacrylate). *Designed Monomers and Polymers* **2015,** *18*, 698-703; https://dx.doi.org/10.1080/15685551.2015.1070503

189. Wu, R. T.; Menner, A.; Bismarck, A., Macroporous polymers made from medium internal phase emulsion templates: Effect of emulsion formulation on the pore structure of polyMIPEs. *Polymer* **2013,** *54* (21), 5511-5517; https://dx.doi.org/10.1016/j.polymer.2013.08.029

190. Cameron, N. R.; Barbetta, A., The influence of porogen type on the porosity, surface area and morphology of poly(divinylbenzene) PolyHIPE foams. *J Mater Chem* **2000,** *10*, 7; https://dx.doi.org/10.1039/B003596N

191. Akay, G.; Downes, S.; Price, V. J. Microcellular polymers as growth media and novel polymers. 2002.

192. Zhou, J.; Wang, L.; Qiao, X.; Binks, B. P.; Sun, K., Pickering emulsions stabilized by surface-modified Fe3O4 nanoparticles. *J Colloid Interface Sci* **2012,** *367* (1), 213-24; https://dx.doi.org/10.1016/j.jcis.2011.11.001

193. Tebboth, M.; Kogelbauer, A.; Bismarck, A., Highly permeable macroporous polymers via controlled agitation of emulsion templates. *Chem Eng Sci* **2015,** *137*, 786-795; https://dx.doi.org/10.1016/j.ces.2015.06.047

194. Reports, B. I. Huge Investment in Epoxy Foam Market Expected to Witness the Highest Growth 2024. https://www.openpr.com/news/1893715/huge-investment-in-epoxy-foam-market-expected-to-witness (accessed 27/01/2022).

195. Pascault, J.-P.; Williams, R. J. J., General Concepts about Epoxy Polymers. In *Epoxy Polymers - New Materials and Innovations*, 2010; pp 1-12; https://dx.doi.org/10.1002/9783527628704.ch1

196. Jin, F.-L.; Li, X.; Park, S.-J., Synthesis and application of epoxy resins: A review. *Journal of Industrial and Engineering Chemistry* **2015,** *29*, 1-11; https://dx.doi.org/10.1016/j.jiec.2015.03.026

197. Boyle, M. A.; Martin, C. J.; Neuner, J. D., Epoxy Resins. In *Composites*, Miracle, D. B.; Donaldson, S. L., Eds. ASM International: 2001; Vol. 21, p 0; https://dx.doi.org/10.31399/asm.hb.v21.a0003362

198. Brostow, W.; Goodman, S. H.; Wahrmund, J., Epoxies. In *Handbook of Thermoset Plastics (Third Edition)*, Dodiuk, H.; Goodman, S. H., Eds. William Andrew Publishing: Boston, 2014; pp 191-252; https://dx.doi.org/10.1016/B978-1-4557-3107-7.00008-7

199. Kochetkov, V. A.; Maksimov, R. D., Water absorption and swelling of glass/epoxy syntactic foams. *Mechanics of Composite Materials* **1996,** *32* (1), 61-70; https://dx.doi.org/10.1007/BF02254649

200. Anderson, T.; Madenci, E., Graphite/epoxy foam sandwich panels under quasi-static indentation. *Engineering Fracture Mechanics* **2000,** *67* (4), 329-344; https://dx.doi.org/10.1016/S0013-7944(00)00066-7

201. Akay, M.; Hanna, R., A comparison of honeycomb-core and foam-core carbon-fibre/epoxy sandwich panels. *Composites* **1990,** *21* (4), 325-331; https://dx.doi.org/10.1016/0010-4361(90)90347-Y

202. Jin, F.-L.; Zhao, M.; Park, M.; Park, S.-J., Recent Trends of Foaming in Polymer Processing: A Review. *Polymers* **2019,** *11* (6), 953; https://dx.doi.org/10.3390/polym11060953

203. Alonso, M. V.; Auad, M. L.; Nutt, S., Short-fiber-reinforced epoxy foams. *Composites Part A: Applied Science and Manufacturing* **2006,** *37* (11), 1952-1960; https://dx.doi.org/10.1016/j.compositesa.2005.12.011

204. Altuna, F. I.; Ruseckaite, R. A.; Stefani, P. M., Biobased Thermosetting Epoxy Foams: Mechanical and Thermal Characterization. *ACS Sustainable Chemistry & Engineering* **2015,** *3* (7), 1406-1411; https://dx.doi.org/10.1021/acssuschemeng.5b00114

205. Burt, S. L. Epoxy resin foaming process. US003320187, 1967.

206. Cavasin, M.; Giannis, S.; Salvo, M.; Casalegno, V.; Sangermano, M., Mechanical and thermal characterization of an epoxy foam as thermal layer insulation for a glass fiber reinforced polymer. *Journal of Applied Polymer Science* **2018,** *135* (47), 46864; https://dx.doi.org/10.1002/app.46864

207. Chang, Y.; Luo, Y.; Xu, C.; Zhao, J., Polysilazane as a new foaming agent to prepare high-strength, low-density epoxy foam. *Royal Society Open Science* **2019,** *6* (5), 182119; https://dx.doi.org/10.1098/rsos.182119

208. Chen, K.; Tian, C.; Lu, A.; Zhou, Q.; Jia, X.; Wang, J., Effect of SiO2 on rheology, morphology, thermal, and mechanical properties of high thermal stable epoxy foam. *Journal of Applied Polymer Science* **2014,** *131* (7); https://dx.doi.org/10.1002/app.40068

209. Mazzon, E.; Habas-Ulloa, A.; Habas, J.-P., Lightweight rigid foams from highly reactive epoxy resins derived from vegetable oil for automotive applications. *European Polymer Journal* **2015,** *68*, 546-557; https://dx.doi.org/10.1016/j.eurpolymj.2015.03.064

210. Mondy, L. A.; Celina, M.; Kropka, J. M.; Russick, E.; Rao, R. R. In *Design of Chemically Blown Epoxy Foams*, 27th World Congress of the Polymer Processing Society, Marrakech, Morocco, Marrakech, Morocco, 2011;

211. Ren, Q.; Zhu, S., One-Pack Epoxy Foaming with CO2 as Latent Blowing Agent. *ACS Macro Letters* **2015,** *4* (7), 693-697; https://dx.doi.org/10.1021/acsmacrolett.5b00320

212. Burgert, B. E.; Moore, W. G. Polyepoxide foam. US3373121A, 1968.

213. Ito, A.; Semba, T.; Taki, K.; Ohshima, M., Effect of the molecular weight between crosslinks of thermally cured epoxy resins on the CO2-bubble nucleation in a batch physical foaming process. *Journal of Applied Polymer Science* **2014,** *131* (12); https://dx.doi.org/10.1002/app.40407

214. Russick, E. M.; Rand, P. B. Epoxy foams using multiple resins and curing agents. US6110982A, 2000.

215. Yadav, R.; Shabeer, A.; Sundararaman, S.; Chandrashekhara, K.; Flanigan, V.; Kapila, S., Development and characterization of soy-based epoxy foams. *International SAMPE Symposium and Exhibition (Proceedings)* **2006,** *51*;

216. Lee, K.-Y.; Wong, L. L. C.; Blaker, J. J.; Hodgkinson, J. M.; Bismarck, A., Bio-based macroporous polymer nanocomposites made by mechanical frothing of acrylated epoxidised soybean oil. *Green Chem* **2011,** *13* (11), 3117; https://dx.doi.org/10.1039/c1gc15655a

217. Song, W.; Barber, K.; Lee, K.-Y., Heat-induced bubble expansion as a route to increase the porosity of foam-templated bio-based macroporous polymers. *Polymer* **2017,** *118*, 97-106; https://dx.doi.org/10.1016/j.polymer.2017.04.058

218. Song, W.; Konstantellos, G.; Li, D.; Lee, K.-Y., Short carbon fibre-reinforced epoxy foams with isotropic cellular structure and anisotropic mechanical response produced from liquid foam templates. *Compos Sci Technol* **2019,** *184*, 107871; https://dx.doi.org/10.1016/j.compscitech.2019.107871

219. Song, W.; Magid, A.; Li, D.; Lee, K.-Y., Application of recycled carbon-fibre-reinforced polymers as reinforcement for epoxy foams. *Journal of Environmental Management* **2020,** *269*, 110766; https://dx.doi.org/10.1016/j.jenvman.2020.110766

220. Zowada, R.; Foudazi, R., Polyfoam: Foam-Templated Microcellular Polymers. *Langmuir* **2020**; https://dx.doi.org/10.1021/acs.langmuir.0c00932

221. Khundamri, N.; Aouf, C.; Fulcrand, H.; Dubreucq, E.; Tanrattanakul, V., Bio-based flexible epoxy foam synthesized from epoxidized soybean oil and epoxidized mangosteen tannin. *Industrial Crops and Products* **2019,** *128*, 556-565; https://dx.doi.org/10.1016/j.indcrop.2018.11.062

222. Gu, R.; Sain, M.; Konar, S., Development and characterization of flexible epoxy foam with reactive liquid rubber and starch. *J Mater Sci* **2014,** *49* (8), 3125-3134; https://dx.doi.org/10.1007/s10853-014-8013-x

223. Hashimoto, M.; Harada, T.; Kiso, Y.; Kaneko, I.; Suzuki, G. Epoxy resin, process for the preparation thereof and process for the production of epoxy foam. US005166184A, 1992.

224. Buddhacosa, N.; Galos, J.; Khatibi, A.; Kandare, E., *Mechanical and vibration damping properties of multifunctional composites incorporating elastomeric particulates*. 2019;

225. Wang, J.; Zhang, C.; Du, Z.; Xiang, A.; Li, H., Formation of porous epoxy monolith via concentrated emulsion polymerization. *J Colloid Interface Sci* **2008,** *325* (2), 453-8; https://dx.doi.org/10.1016/j.jcis.2008.06.012

226. Wang, J.; Du, Z.; Li, H.; Xiang, A.; Zhang, C., Interconnected porous epoxy monoliths prepared by concentrated emulsion templating. *J Colloid Interface Sci* **2009,** *338* (1), 145-50; https://dx.doi.org/10.1016/j.jcis.2009.06.013

227. Tu, J.; Du, Z.; Li, H.; Zhang, C., Development and characterization of porous epoxy monoliths via pore-initiated polymerization. *Colloids and Surfaces A: Physicochemical and Engineering Aspects* **2011,** *375* (1-3), 68-75; https://dx.doi.org/10.1016/j.colsurfa.2010.11.059

228. Anusha, L.; Zakaria, Z.; Kahar, A. W. M.; Lan, D. N. U., Effect of Emulsion Temperature on Properties of Conductive Epoxy Porous Prepared by Single Emulsion Technique. *IOP Conference Series: Materials Science and Engineering* **2018,** *429*, 012061; https://dx.doi.org/10.1088/1757-899x/429/1/012061

229. Andrieux, S.; Quell, A.; Stubenrauch, C.; Drenckhan, W., Liquid foam templating - A route to tailor-made polymer foams. *Adv Colloid Interface Sci* **2018,** *256*, 276-290; https://dx.doi.org/10.1016/j.cis.2018.03.010

230. Shirshova, N.; Bismarck, A.; Steinke, J. H., Ionic liquids as internal phase for non-aqueous polyHIPEs. *Macromol Rapid Commun* **2011,** *32* (23), 1899-904; https://dx.doi.org/10.1002/marc.201100472

231. Giustiniani, A.; Guégan, P.; Marchand, M.; Poulard, C.; Drenckhan, W., Generation of Silicone Poly-HIPEs with Controlled Pore Sizes via Reactive Emulsion Stabilization. *Macromol Rapid Comm* **2016,** *37* (18), 1527-1532; https://dx.doi.org/10.1002/marc.201600281

232. Shirshova, N.; Bismarck, A.; Carreyette, S.; Fontana, Q. P. V.; Greenhalgh, E. S.; Jacobsson, P.; Johansson, P.; Marczewski, M. J.; Kalinka, G.; Kucernak, A. R. J.; Scheers, J.; Shaffer, M. S. P.; Steinke, J. H. G.; Wienrich, M., Structural supercapacitor electrolytes based on bicontinuous ionic liquid–epoxy resin systems. *J Mater Chem A* **2013,** *1* (48), 15300; https://dx.doi.org/10.1039/c3ta13163g

233. Silverstein, M. S.; Cameron, N. R., PolyHIPEs - Porous Polymers from High Internal Phase Emulsions. In *Encyclopedia of Polymer Science and Technology*, 2010; https://dx.doi.org/10.1002/0471440264.pst571

234. Gibson, I. J.; Ashby, M. F., The mechanics of three-dimensional cellular materials. *Proceedings of the Royal Society of London. A. Mathematical and Physical Sciences* **1982,** *382* (1782), 43-59; https://dx.doi.org/doi:10.1098/rspa.1982.0088

235. Gibson, L. J.; Ashby, M. F.; Schajer, G. S.; Robertson, C. I., The mechanics of two-dimensional cellular materials. *Proceedings of the Royal Society of London. A. Mathematical and Physical Sciences* **1982,** *382* (1782), 25-42; https://dx.doi.org/doi:10.1098/rspa.1982.0087

236. Gibson, L. J.; Ashby, M. F., *Cellular Solids: Structure and Properties*. 2 ed.; Cambridge University Press: Cambridge, 1997; https://dx.doi.org/10.1017/CBO9781139878326

237. Ashby, M. F., The properties of foams and lattices. *Philos Trans A Math Phys Eng Sci* **2006,** *364* (1838), 15-30; https://dx.doi.org/10.1098/rsta.2005.1678

238. Li, K.; Gao, X. L.; Subhash, G., Effects of cell shape and strut cross-sectional area variations on the elastic properties of three-dimensional open-cell foams. *Journal of the Mechanics and Physics of Solids* **2006,** *54* (4), 783-806; https://dx.doi.org/10.1016/j.jmps.2005.10.007

239. Gholami, M. S.; Doutres, O.; Atalla, N., Effect of microstructure closed-pore content on the mechanical properties of flexible polyurethane foam. *International Journal of Solids and Structures* **2017,** *112*, 97-105; https://dx.doi.org/10.1016/j.ijsolstr.2017.02.016

240. Lin-Gibson, S.; Cooper, J. A.; Landis, F. A.; Cicerone, M. T., Systematic Investigation of Porogen Size and Content on Scaffold Morphometric Parameters and Properties. *Biomacromolecules* **2007,** *8* (5), 1511-1518; https://dx.doi.org/10.1021/bm061139q

241. Huš, S.; Krajnc, P., PolyHIPEs from Methyl methacrylate: Hierarchically structured microcellular polymers with exceptional mechanical properties. *Polymer* **2014,** *55* (17), 4420-4424; https://dx.doi.org/10.1016/j.polymer.2014.07.007

242. Jiang, B.; Wang, Z.; Zhao, N., Effect of pore size and relative density on the mechanical properties of open cell aluminum foams. *Scripta Mater* **2007,** *56* (2), 169-172; https://dx.doi.org/10.1016/j.scriptamat.2006.08.070

243. Williams, J. M.; Bartos, J. J.; Wilkerson, M. H., Elastic-Modulus Dependence on Density for Polymeric Foams with Systematically Changing Microstructures. *J Mater Sci* **1990,** *25* (12), 5134-5141; https://dx.doi.org/10.1007/Bf00580141

244. Kovačič, S.; Žagar, E.; Slugovc, C., Strength versus toughness of emulsion templated Poly(Dicyclopentadiene) foams. *Polymer* **2019,** *169*, 58-65; https://dx.doi.org/10.1016/j.polymer.2019.02.045

245. Owen, R.; Sherborne, C.; Paterson, T.; Green, N. H.; Reilly, G. C.; Claeyssens, F., Emulsion templated scaffolds with tunable mechanical properties for bone tissue engineering. *J Mech Behav Biomed* **2016,** *54*, 159-172; https://dx.doi.org/10.1016/j.jmbbm.2015.09.019

246. Owen, R.; Sherborne, C.; Reilly, G. C.; Claeyssens, F., Data for the analysis of PolyHIPE scaffolds with tunable mechanical properties for bone tissue engineering. *Data in Brief* **2015,** *5*, 616-620; https://dx.doi.org/10.1016/j.dib.2015.09.051

247. Karageorgiou, V.; Kaplan, D., Porosity of 3D biomaterial scaffolds and osteogenesis. *Biomaterials* **2005,** *26* (27), 5474-91; https://dx.doi.org/10.1016/j.biomaterials.2005.02.002

248. Collins, R. E., *Flow Of Fluids through Porous Materials*. Reinhold Publishing Corporation: USA, 1961; p 22;

249. Ishizaki, K.; Komareneni, S.; Nanko, M., *Porous Materials - Process Technology and Applications*. Springer US: 1998; Vol. 4, p 240; https://dx.doi.org/10.1007/978-1-4615-5811-8

250. Katz, A. J.; Thompson, A. H., Quantitative prediction of permeability in porous rock. *Phys Rev B* **1986,** *34* (11), 8179-8181; https://dx.doi.org/10.1103/PhysRevB.34.8179

251. van Brakel, J.; Modrý, S.; Svatá, M., Mercury porosimetry: state of the art. *Powder Technol* **1981,** *29* (1), 1-12; https://dx.doi.org/10.1016/0032-5910(81)85001-2

252. Lock, P. A.; Jing, X.; Zimmerman, R. W.; Schlueter, E. M., Predicting the permeability of sandstone from image analysis of pore structure. *J Appl Phys* **2002,** *92* (10), 6311-6319; https://dx.doi.org/10.1063/1.1516271

253. Wang, R.; Mair, R. W.; Rosen, M. S.; Cory, D. G.; Walsworth, R. L., Simultaneous measurement of rock permeability and effective porosity using laser-polarized noble gas NMR. *Phys Rev E* **2004,** *70* (2); https://dx.doi.org/10.1103/PhysRevE.70.026312

254. Mitchell, J.; Chandrasekera, T. C., Understanding generalized inversions of nuclear magnetic resonance transverse relaxation time in porous media. *The Journal of Chemical Physics* **2014,** *141* (22), 224201; https://dx.doi.org/10.1063/1.4903311

255. Wei, D. F.; Liu, X. P.; Hu, X. X., Applicability of Classical Permeability Estimation Models Based on NMR Logging in Tight Sandstones. *Advanced Materials Research* **2013,** *772*, 814-818; https://dx.doi.org/10.4028/www.scientific.net/AMR.772.814

256. Coates, G. R.; Xiao, L.; Prammer, M. G., NMR Permeability. In *NMR logging : principles and applications*, Sigal, R. F.; Bollich, S. J., Eds. Halliburton Energy Services: Houston (USA), 1999; pp 9-11;

257. Darcy, H., Appendix D. In *Les fontaines publiques de la Ville de Dijon*, Dalmont, V., Ed. Librairie des Corps Imperiaux des Ponts et Chaussées et des Mines: Paris, 1856; pp 559-603;

258. Miguel, A. F.; Serrenho, A., On the experimental evaluation of permeability in porous media using a gas flow method. *J Phys D Appl Phys* **2007,** *40* (21), 6824-6828; https://dx.doi.org/10.1088/0022-3727/40/21/050

259. Wyckoff, R. D.; Botset, H. G.; Muskat, M.; Reed, D. W., The measurement of the permeability of porous media for homogeneous fluids. *Rev Sci Instrum* **1933,** *4* (7), 394-405; https://dx.doi.org/10.1063/1.1749155

260. Loosveldt, H.; Lafhaj, Z.; Skoczylas, F., Experimental study of gas and liquid permeability of a mortar. *Cement & Concrete Research* **2002,** *32*, 1357-1363; https://dx.doi.org/10.1016/S0008-8846(02)00793-7

261. Manley, S. S.; Steindl, P.; Hewitt, G. F.; Bismarck, A., An integrated method for measuring gas permeability and diffusivity of porous solids. *Chem Eng Sci* **2020,** *223*; https://dx.doi.org/10.1016/j.ces.2020.115725

262. Seguin, D.; Montillet, A.; Comiti, J., Experimental characterisation of flow regimes in various porous media—I: Limit of laminar flow regime. *Chem Eng Sci* **1998,** *53* (21), 3751-3761; https://dx.doi.org/10.1016/S0009-2509(98)00175-4

263. Huang, H.; Ayoub, J., Applicability of the Forchheimer Equation for Non-Darcy Flow in Porous Media. *Spe J* **2008,** *March 2008*; https://dx.doi.org/10.2118/102715-PA

264. Comiti, J.; Sabiri, N. E.; Montillet, A., Experimental characterization of flow regimes in various porous media - III: limit of Darcy's or creeping flow regime for Newtonian and purely viscous non-Newtonian fluids. *Chem Eng Sci* **2000,** *55* (15), 3057-3061; https://dx.doi.org/10.1016/S0009-2509(99)00556-4

265. Schumacher, E. E.; Ferguson, L., A convenient apparatus for measuring the diffusion of gases and vapors through membranes. *Journal of the American Chemical Society* **1927,** *49*, 427-428; https://dx.doi.org/10.1021/ja01401a013

266. Bokhoven, C.; Hoogschagen, J., Diffusion in Porous Catalysts. *J Chem Phys* **1953,** *21* (1), 159-160; https://dx.doi.org/10.1063/1.1698571

267. Wakao, N.; Smith, J. M., Diffusion in Catalyst Pellets. *Chem Eng Sci* **1962,** *17* (11), 825-834; https://dx.doi.org/10.1016/0009-2509(62)87015-8

268. Satterfield, C. N.; Cadle, P. J., Diffusion in Commercially Manufactured Pelleted Catalysts. *Ind Eng Chem Proc Dd* **1968,** *7* (2), 256; https://dx.doi.org/10.1021/i260026a017

269. Garrouch, A. A.; Ali, L.; Qasem, F., Using diffusion and electrical measurements to assess tortuosity of porous media. *Ind Eng Chem Res* **2001,** *40* (20), 4363-4369; https://dx.doi.org/10.1021/ie010070u

270. Ovalle-Villamil, W.; Sasanakul, I., Investigation of Non-Darcy Flow for Fine Grained Materials. *Geotech Geol Eng* **2019,** *37* (1), 413-429; https://dx.doi.org/10.1007/s10706-018-0620-x

271. Carman, P. C., *Flow of Gases Through Porous Media*. Butterworths Scientific Publications: Belfast, 1956; p 69;

272. Tanikawa, W.; Shimamoto, T., Klinkenberg effect for gas permeability and its comparison to water permeability for porous sedimentary rocks. *Hydrol. Earth Syst. Sci. Discuss.* **2006,** *2006*, 1315-1338; https://dx.doi.org/10.5194/hessd-3-1315-2006

273. Cengel, Y. A.; Cimbala, J. M., Flow in Pipes. In *Fluid Mechanics - Fundamentals and Applications*, McGraw-Hill: New York, 2006; pp 321-398;

274. Wilkes, J. O., Fluid Friction in Pipes. In *Fluid Mechanics for Chemical Engineers*, 2nd ed.; Pearson Education: 2006; pp 126-134;

275. Chierici, G. L., Reservoir Rocks. In *Principles of Petroleum Reservoir Engineering: Volume 1*, Springer Berlin Heidelberg: Berlin, Heidelberg, 1994; pp 47-116; https://dx.doi.org/10.1007/978-3-662-02964-0_3

276. Millikan, R. A., Coefficients of Slip in Gases and the Law of Reflection of Molecules from the Surfaces of Solids and Liquids. *Phys Rev* **1923,** *21* (3), 217-238; https://dx.doi.org/10.1103/PhysRev.21.217

277. Hewitt, G. F., Approximate Equations for the Diffusion and Flow of Gases in Porous Media. *UKAEA Report No. AERE R5492* **1967,** (August);

278. Hewitt, G. F.; Hawtin, P., Flow of Gases in Porous Solids. *Nature* **1967,** *215* (5108), 1415-1416;

279. Biloé, S.; Mauran, S., Gas flow through highly porous graphite matrices. *Carbon* **2003,** *41*, 525-537; https://dx.doi.org/10.1016/S0008-6223(02)00363-9

280. Lin, H.; Freeman, B. D., Gas solubility, diffusivity and permeability in poly(ethylene oxide). *Journal of Membrane Science* **2004,** *239* (1), 105-117; https://dx.doi.org/10.1016/j.memsci.2003.08.031

281. Jannot, Y.; Lasseux, D., A new quasi-steady method to measure gas permeability of weakly permeable porous media. *Rev Sci Instrum* **2012,** *83* (1), 015113; https://dx.doi.org/10.1063/1.3677846

282. Ziarani, A. S.; Aguilera, R., Knudsen's Permeability Correction for Tight Porous Media. *Transport Porous Med* **2011,** *91* (1), 239-260; https://dx.doi.org/10.1007/s11242-011-9842-6

283. Berg, C. F., Permeability Description by Characteristic Length, Tortuosity, Constriction and Porosity. *Transport Porous Med* **2014,** *103* (3), 381-400; https://dx.doi.org/10.1007/s11242-014-0307-6

284. Kawagoe, Y.; Oshima, T.; Tomarikawa, K.; Tokumasu, T.; Koido, T.; Yonemura, S., A study on pressure-driven gas transport in porous media: from nanoscale to microscale. *Microfluidics and Nanofluidics* **2016,** *20* (12), 162; https://dx.doi.org/10.1007/s10404-016-1829-8

285. Liu, R.; Jiang, Y.; Li, B.; Yu, L., Estimating permeability of porous media based on modified Hagen–Poiseuille flow in tortuous capillaries with variable lengths. *Microfluidics and Nanofluidics* **2016,** *20* (8); https://dx.doi.org/10.1007/s10404-016-1783-5

286. Klinkenberg, L. J., Analogy between Diffusion and Electrical Conductivity in Porous Rocks. *Geol Soc Am Bull* **1951,** *62* (6), 559-563; https://dx.doi.org/10.1130/0016-7606(1951)62[559:Abdaec]2.0.Co;2

287. Knudsen, M., Die Gesetze der Molekularströmung und der inneren Reibungsströmung der Gase durch Röhren. *Ann Phys-Berlin* **1909,** *333* (1), 75-130; https://dx.doi.org/10.1002/andp.19093330106

288. Hewitt, G. F., Gaseous Mass Transport Within Graphite. In *Chemistry and Physics of Carbon. A Series of Advances. Vol.1*, Walker, P. L., Ed. Marcel Dekker Inc.: New York, 1965;

289. Mason, E. A.; Malinauskas, A. P.; Evans, R. B., Flow and Diffusion of Gases in Porous Media. *The Journal of Chemical Physics* **1967,** *46* (8), 3199-3216; https://dx.doi.org/10.1063/1.1841191

290. Moody, L. F., Friction factors for pipe flow. *Transactions of the ASME* **1944,** *66*, 671-684;

291. Burcharth, H. F.; Christensen, C. *On Stationary and Non-stationary Porous Flow in Coarse Granular Materials : European Community, MAST G6-S: Project 1, Wave Action on and in coastal structures*; Aalborg, 1991.

292. Dybbs, A.; Edwards, R. V., A New Look at Porous Media Fluid Mechanics — Darcy to Turbulent. In *Fundamentals of Transport Phenomena in Porous Media*, Bear, J.; Corapcioglu, M. Y., Eds. Springer Netherlands: Dordrecht, 1984; pp 199-256; https://dx.doi.org/10.1007/978-94-009-6175-3_4

293. Skjetne, E.; Auriault, J. L., New insights on steady, non-linear flow in porous media. *European Journal of Mechanics - B/Fluids* **1999,** *18* (1), 131-145; https://dx.doi.org/10.1016/S0997-7546(99)80010-7

294. Jolls, K. R.; Hanratty, T. J., Transition to turbulence for flow through a dumped bed of spheres. *Chem Eng Sci* **1966,** *21* (12), 1185-1190; https://dx.doi.org/10.1016/0009-2509(66)85038-8

295. Hall, M. J.; Hiatt, J. P., Measurements of pore scale flows within and exiting ceramic foams. *Exp Fluids* **1996,** *20* (6), 433-440; https://dx.doi.org/10.1007/BF00189382

296. Seguin, D.; Montillet, A.; Comiti, J.; Huet, F., Experimental characterization of flow regimes in various porous media—II: Transition to turbulent regime. *Chem Eng Sci* **1998,** *53* (22), 3897-3909; https://dx.doi.org/10.1016/S0009-2509(98)80003-1

297. van Lopik, J. H.; Snoeijers, R.; van Dooren, T. C. G. W.; Raoof, A.; Schotting, R. J., The Effect of Grain Size Distribution on Nonlinear Flow Behavior in Sandy Porous Media. *Transport Porous Med* **2017,** *120* (1), 37-66; https://dx.doi.org/10.1007/s11242-017-0903-3

298. Carrier, W. D., Goodbye, Hazen; Hello, Kozeny-Carman. *Journal of Geotechnical and Geoenvironmental Engineering* **2003,** *129* (11), 1054-1056; https://dx.doi.org/doi:10.1061/(ASCE)1090-0241(2003)129:11(1054)

299. Odong, J., Evaluation of Empirical Formulae for Determination of Hydraulic Conductivity based on Grain-Size Analysis. *Journal of American Science* **2007,** *3*;

300. Shih, R. W. K., Permeability Characteristics of Rubble Material – New Formulae. In *Coastal Engineering 1990*, 1991; pp 1499-1512; https://dx.doi.org/doi:10.1061/9780872627765.114

301. Macdonald, I. F.; El-Sayed, M. S.; Mow, K.; Dullien, F. A. L., Flow through Porous Media-the Ergun Equation Revisited. *Ind Eng Chem Fund* **1979,** *18* (3), 199-208; https://dx.doi.org/10.1021/i160071a001

302. Burdine, N. T., Relative Permeability Calculations From Pore Size Distribution Data. *J Petrol Technol* **1953,** *5* (03), 71-78; https://dx.doi.org/10.2118/225-g

303. Dullien, F. A. L.; El-Sayed, M. S.; Batra, V. K., Rate of capillary rise in porous media with nonuniform pores. *J Colloid Interf Sci* **1977,** *60* (3), 497-506; https://dx.doi.org/10.1016/0021-9797(77)90314-9

304. Dias, R.; Fernandes, C.; Teixeira, J.; Mota, M.; Yelshin, A., Permeability analysis in bisized porous media: Wall effect between particles of different size. *Journal of Hydrology* **2008,** *349*, 470-474; https://dx.doi.org/10.1016/j.jhydrol.2007.11.020

305. Lage, J. L.; Antohe, B. V., Darcy's experiments and the deviation to nonlinear flow regime. *J Fluid Eng-T Asme* **2000,** *122* (3), 619-625; https://dx.doi.org/10.1115/1.1287722

306. Zimmerman, R. W., *Fluid Flow in Porous Media*. World Scientific: 2018;

307. Ovalle-Villamil, W.; Sasanakul, I., A new insight into the behaviour of seepage flow in centrifuge modelling. *Physical Modelling in Geotechnics, Vol 1* **2018**, 259-264;

308. Hewitt, G. F., Some Measurements of the Gas Permeability of Graphite. *AERE* **1961,** *M851*;

309. Manley, S. S.; Graeber, N.; Grof, Z.; Menner, A.; Hewitt, G. F.; Stepanek, F.; Bismarck, A., New insights into the relationship between internal phase level of emulsion templates and gas-liquid permeability of interconnected macroporous polymers. *Soft Matter* **2009,** *5* (23), 4780-4787; https://dx.doi.org/10.1039/b900426b

310. Wang, L.; Yang, X.; Zhang, J.; Zhang, C.; He, L., The compressive properties of expandable microspheres/epoxy foams. *Composites Part B: Engineering* **2014,** *56*, 724-732; https://dx.doi.org/10.1016/j.compositesb.2013.09.030

311. Manas, C., Plastics Properties and Testing. In *Plastics Technology Handbook*, CRC Press: 2017; https://dx.doi.org/10.1201/9781315155876-3

312. Jiang, Q.; Morand, A.; Menner, A.; Bismarck, A., Emulsion templated resilient macroporous elastomers. *Polymer* **2020,** *186*, 122023; https://dx.doi.org/10.1016/j.polymer.2019.122023

313. Jiang, Q.; Barkan, H.; Menner, A.; Bismarck, A., Micropatterned, macroporous polymer springs for capacitive energy harvesters. *Polymer* **2017,** *126*, 419-424; https://dx.doi.org/10.1016/j.polymer.2017.04.018

314. Stefani, P. M.; Cyras, V.; Tejeira Barchi, A.; Vazquez, A., Mechanical properties and thermal stability of rice husk ash filled epoxy foams. *Journal of Applied Polymer Science* **2006,** *99* (6), 2957-2965; https://dx.doi.org/10.1002/app.23001

315. Wu, R.; Jones, M. P.; Jiang, Q.; Hodgkinson, J. M.; Menner, A.; Bismarck, A., Assessing shear, tensile and fracture properties of macroporous nanocomposites using the Arcan test. *Polymer Testing* **2022,** *107*, 107490; https://dx.doi.org/10.1016/j.polymertesting.2022.107490

Paper I (*published*)

An integrated method for measuring gas permeability and diffusivity of porous solids. Manley, S. S.; *Steindl, P.*; Hewitt, G. F.; Bismarck, A. Chemical Engineering Science, 2020, 223, article 115725

Chemical Engineering Science 223 (2020) 115725

Contents lists available at ScienceDirect

Chemical Engineering Science

journal homepage: www.elsevier.com/locate/ces

An integrated method for measuring gas permeability and diffusivity of porous solids

Shu San Manley [a], Patrick Steindl [b], Geoffrey F. Hewitt [a,1], Alexander Bismarck [a,b,*]

[a] Department of Chemical Engineering, Imperial College London, South Kensington Campus, London SW7 2AZ, UK
[b] Polymer and Composite Engineering (PaCE) Group, Institute of Materials Chemistry and Research, University of Vienna, Währinger Strasse 42, 1090 Vienna, Austria

HIGHLIGHTS

- New apparatus enables concurrent determination of permeability and diffusivity.
- Large range of permeabilities, from nano Darcy to Darcy, can be measured.
- Tortuosities reliably accessible through transient diffusion experiments.

GRAPHICAL ABSTRACT

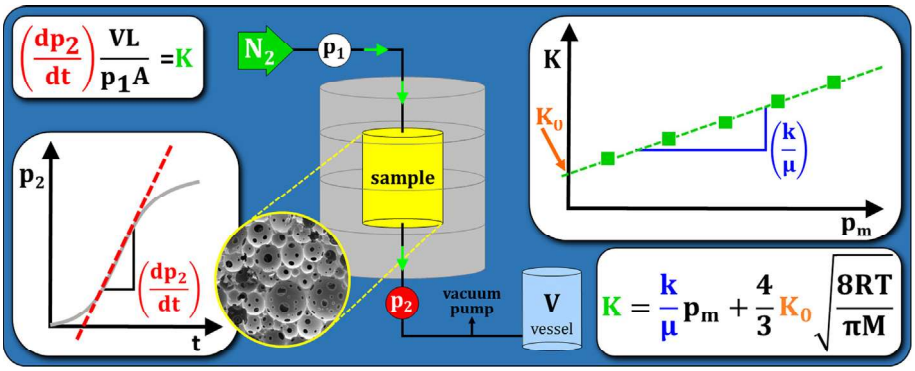

ARTICLE INFO

Article history:
Available online 15 April 2020

Keywords:
Gas permeability
N_2/O_2 diffusion
Porosity
Porous material
Slip

ABSTRACT

An integrated gaseous transport apparatus was designed not only to measure permeability (by the pressure rise technique) but also to study both steady state and (importantly) transient diffusion of oxygen in nitrogen in the pores of a porous material. The apparatus allows for the characterisation of porous media with a wide range of permeabilities and yielded accurate values of the viscous permeability and the slip flow coefficient. Experiments were also carried out in the non-Darcy flow regime. The diffusion measurements provide information on the ratio of the diffusion coefficient in the media to that in free space; this ratio is also a specific property of porous media. Combining the steady state and transient diffusion measurements, it was possible to deduce the effective porosity and the pore length. Berea sandstones with a range of porosities were analysed using both techniques and the results of the measurements are presented.

1. Introduction

In recent years, interest in porous media characterisation has increased considerably, in particular due to issues associated with oil and gas production (Berkowitz, 2002; Ghanizadeh et al., 2015; Song et al., 2016) as well as porous scaffolds, used for a multitude of tissue engineering applications, which focus on restoring, repairing or replacing damaged tissues. The most significant properties of porous solids that affect fluid flow, i.e. permeability, are porosity,

* Corresponding author at: Polymerand Composite Engineering (PaCE) Group, Institute of Materials Chemistry and Research, University of Vienna, Währinger Strasse 42, 1090 Vienna, Austria.
E-mail address: alexander.bismarck@univie.ac.at (A. Bismarck).

[1] Unfortunately our colleague, mentor and teacher Prof. Geoff F. Hewitt FRS FREng passed away on 18.01.2019. He heavily contributed to this study. We dedicate this paper to him.

https://doi.org/10.1016/j.ces.2020.115725
0009-2509/

Nomenclature

k	viscous permeability [m^2]
K	permeability coefficient [$m^2 \cdot s^{-1}$]
K_0	slip coefficient [m]
Kn	Knudsen number [–]
A	sample cross-section area [m^2]
t	time [s]
L	sample length [m]
L_{eff}	effective pore length [m]
Δp	total pressure drop across sample [Pa]
V	volume [m^3]
Q	volumetric flow rate [$m^3 \cdot s^{-1}$]
D_{eff}	effective diffusion coefficient [$m^2 \cdot s^{-1}$]
D_{AB}	free diffusion coefficient of O_2 in N_2 [$m^2 \cdot s^{-1}$]
τ	tortuosity [–]
ε	porosity [%]
ε_{eff}	effective porosity [%]
d	capillary/pore diameter [m]
u	fluid superficial velocity [$m \cdot s^{-1}$]
$\bar{u}$	mean gas velocity [$m \cdot s^{-1}$]
$\bar{u}_v$	viscous flow contribution [$m \cdot s^{-1}$]
u_0	slip effect [$m \cdot s^{-1}$]
u_{lO}	superficial velocity of O_2 entering the sample [$m \cdot s^{-1}$]
$\bar{v}$	mean molecular gas velocity [$m \cdot s^{-1}$]
R	universal gas constant = 8.3145 [$J \cdot mol^{-1} \cdot K^{-1}$]
T	absolute temperature [K]
M	molecular weight (of transporting species) [$g \cdot mol^{-1}$]
μ	gas viscosity [Pa·s]
λ	mean free path length [m]
ρ	density [$g \cdot cm^{-3}$]
ρ_{abs}	absolute density [$g \cdot cm^{-3}$]
ρ_{bulk}	bulk density [$g \cdot cm^{-3}$]
p	pressure [Pa]
p_0	pressure at which Q is measured [Pa]
p_1	N_2-pressure applied in permeability tests [Pa]
p_2	N_2-pressure after passing the sample (chamber) [Pa]
p_{lO}	partial pressure of O_2 at the O_2 end [Pa]
p_m	mean pressure [Pa]
n_O	molar transport rate of oxygen [$mol \cdot s^{-1}$]
Q_N	N_2 flow rate [$m^3 \cdot s^{-1}$]
c_O	concentration of O_2 [$mol \cdot m^{-3}$]
$c_{O\text{-}N}$	oxygen concentration in N_2 - efflux stream [ppm by V]
Δc_O	oxygen concentration difference across the sample [$mol \cdot m^{-3}$]
r_D	D_{eff}/D_{AB} [–]
Γ	correction factor for D_{eff}/D_{AB} [–]
$\left(\frac{dp_2}{dt}\right)$	rate of pressure rise [$Pa \cdot s^{-1}$]
C	$= \frac{(p_1^2 - p_2^2)M}{2RTLG}$ [$Pa \cdot m^2 \cdot s^{-1}$]
a	represents viscous flow (=μ/k)
b	measure of inertial effects
G	total mass flux
G_1, G_2	mass fluxes through two groups of pores

pore interconnectivity and pore tortuosity (Le Coq, 2008; Matyka et al., 2008). The flow of fluids in porous solids is determined by the nature of the pores and pore throats. Understanding the pore size distribution and structure of this network is important in understanding the characteristics of fluid flow through the porous medium. Measurement and understanding of these transport processes is not only important in itself, but also throws light on many structural aspects of the porous material (Manley et al., 2009). The challenges associated with the characterisation of porous solids have been of interest to engineers and scientists for many decades (see reviews of Collins, 1961, Dullien, 1975; Wyckoff et al., 1933).

Many reports deal with the characterisation of porous media and how the structures of these materials affect fluid flow (see for instance Baraka-Lokmane, 2002; Biloé and Mauran, 2003; Loosveldt et al., 2002). Attention has been focused on properties that have direct and significant effects on the flow of fluids through the material, most prominently porosity and permeability. Methods for the characterisation of porous media have been reviewed by (Dietrich et al., 2005 and Sing, 2004).

Permeability is one of the most commonly measured properties of porous solids. It is the property that characterises the ease of a fluid flowing through a porous solid (Collins, 1961). In short, permeability is the fluid conductivity of a porous material. As such it provides information about pore structure and pore interconnectivity (Ishizaki et al., 1998). Measurement techniques include indirect prediction from mercury porosimetry (Katz and Thompson, 1986; van Brakel et al., 1981) and image analysis (Lock et al., 2002), as well as methods involving nuclear magnetic resonance spectroscopy (Coates et al., 1999; Mitchell and Chandrasekera, 2014; Rigler, 2018; Wang et al., 2004; Wei et al., 2013). However, the most common experimental technique used to determine fluid permeability is the application of a pressure gradient across a porous solid.

Darcy (1856) investigated the flow of water through sandstone and other porous media and derived a basic equation, now known as Darcy's law[2] (Eq. (1)), which relates the volumetric flow rate Q [$m^3\ s^{-1}$] to the pressure gradient *(dp/dx)* driving the flow:

$$Q = \frac{dV}{dt} = -\frac{k}{\mu} A \left(\frac{dp}{dx}\right) \tag{1}$$

where *A* [m^2] is sample cross-sectional area, μ [Pa s] fluid viscosity and *k* [m^2] the permeability. The ratio of flow rate and cross-section area, *Q/A*, is called fluid superficial velocity $\bar{u}$ [m s^{-1}].

By measuring the volumetric fluid flow rate *Q* through the material, the permeability *k* [m^2] can be calculated (Loosveldt et al., 2002; Miguel and Serrenho, 2007; Wyckoff et al., 1933).

Gas diffusivity is of interest in technologies, such as catalysis (Bokhoven and Hoogschagen, 1953; Satterfield and Cadle, 1968; Wakao and Smith, 1962; Weisz and Schwartz, 1962), tissue engineering (Radisic et al., 2005) and petroleum engineering (Al-Quraishi and Khairy, 2005; Gerritsen and Durlofsky, 2005). The gas molecules have to take a tortuous path through the pores of a porous material. Experimental determination of the effective diffusion coefficient D_{eff} (Weisz and Schwartz, 1962; Youngquist, 1970) provides the foundation for the quantification of tortuosity τ *(=L_{eff}/L)* and subsequently effective porosity ε_{eff} and effective pore length L_{eff}:

$$\frac{D_{eff}}{D_{AB}} = \frac{\varepsilon_{eff}}{\tau^2} \tag{2}$$

where D_{eff} [$m^2\ s^{-1}$] is the effective diffusion coefficient of oxygen in nitrogen through the porous material, D_{AB} the free diffusion coefficient of oxygen in nitrogen ($D_{AB} = 1.81 \cdot 10^{-5}$ $m^2 s^{-1}$) (Bird et al., 2002; Higgins and Binous, 2013). Tortuosity is commonly determined by gas diffusion measurements (Bokhoven and Hoogschagen, 1953; Satterfield and Cadle, 1968; Schumacher and

[2] Darcy established empirically that the energy loss Δh in water flowing through a permeable formation is proportional to the length of the sediment column ΔL: Q = -KA*(dh/dx); He did not consider the fluid viscosity.

Ferguson, 1927; Wakao and Smith, 1962) or electrical conductivity of a non-conducting porous material when saturated with brine (Garrouch et al., 2001). In the past, permeability and diffusion measurements have conventionally been performed using different and separate apparatus.

It was our aim to develop an integrated apparatus, which can be used for the determination of both permeability and diffusivity, including transient diffusion and diffusion under the influence of a pressure gradient. This apparatus can be used for the characterisation of a multitude of porous media ranging from sandstone to porous polymers. Integrated methods consist of a single piece of apparatus, which encompasses several characterisation techniques and can be used to determine multiple independent properties simultaneously. Integrated methods can significantly improve the efficiency of characterisation of flow properties. Our paper discusses design, construction and commissioning of such an apparatus, together with results obtained from permeability measurements of porous rocks.

2. Theoretical background

2.1. Permeability

Darcy's law (Eq. (1)) states that the rate of fluid flow through a porous medium is directly proportional to the applied pressure gradient. Therefore, it can be used to determine the permeability of porous materials by means of a pressure-rise method. In order to assure its validity, it is necessary that a number of conditions are fulfilled: the fluid flow must be laminar (Loosveldt et al., 2002). Furthermore, it is assumed that the resistance to flow is entirely due to viscous drag and that the porous material is inert to the fluid.

Reynold's number *Re* and friction factor *f* are dimensionless numbers used to describe fluid flow through porous media. The interstitial *Re* (Huang and Ayoub, 2008) is calculated:

$$Re = \frac{\rho\,\bar{u}\,D_g}{\mu\varepsilon} \tag{3}$$

where ρ [kg m^{-3}] is the density of the fluid, $\bar{u}$ [m s^{-1}]the superficial fluid velocity, D_g [m] the average grain size, which can be determined by image analysis of resin potted polished cross-sections of porous media, ε the measured sample porosity and μ [Pa s] the fluid viscosity. The friction factor can be calculated as follows (Comiti et al., 2000; Ovalle-Villamil and Sasanakul, 2019):

$$f = \frac{16}{Re} + 0.1936 \tag{4}$$

There are two major differences between gas and liquid flow in porous media; the compressibility of the gas needs to be taken into account. As such, Darcy's law can be applied locally to relate fluid velocity and pressure gradient, but the velocity will actually change along the flow path according to a parabolic profile (Cengel and Cimbala, 2006; Wilkes, 2006). The other factor, which has to be considered (particularly at low pressures), is that of 'slip' between the flowing gas and the wall. The slip effect was described by Millikan (1923); its application to porous media was reported, for example by Hewitt (1967) and Hewitt & Hawtin (1967). More recent work on this topic has been performed by Berg, 2014; Biloé and Mauran, 2003; Jannot and Lasseux, 2012; Kawagoe et al., 2016; Lin and Freeman, 2004; Liu et al., 2016; Tanikawa and Shimamoto, 2006; Ziarani and Aguilera, 2011. Klinkenberg (1951). was the first who recognised that the difference in permeabilities to gases and liquids is caused by the slip effect. Therefore, this phenomenon is often called the 'Klinkenberg effect'.

Without slip, the rate of transport of momentum to the wall (i.e. the wall shear stress), dictated by the pressure gradient, could not be achieved. The slip term becomes significant for gases and thus has to be included in equations describing the fluid transport. An approach for describing gas flow through porous media, is to consider first the case of single component flow through a single capillary of diameter *d*. Here, the mean gas velocity $\bar{u}$ at a position along the capillary can be calculated as the sum of viscous flow $\bar{u}_v$ and slip flow $\bar{u}_0$ (Hewitt, 1967; Hewitt and Hawtin, 1967):

$$\bar{u} = \bar{u}_v + \bar{u}_0 \tag{5}$$

$$\bar{u} = -\frac{d^2}{32\mu}\left(\frac{dp}{dx}\right) - \frac{\pi d}{16}\frac{\bar{v}}{p}\left(\frac{dp}{dx}\right) \tag{6}$$

$$\bar{v} = \sqrt{\frac{8RT}{\pi M}} \tag{7}$$

where $\bar{v}$ [m s^{-1}] is the mean molecular velocity of the gas as derived by the *kinetic theory of gases*, *R* [J mol^{-1} K^{-1}] the universal gas constant, *T* [K] the absolute temperature and *M* [g mol^{-1}] the molecular weight of the transported species.

Friction between fluid and capillary wall, the wall shear stress, opposes the flow and hence leads to a decrease of fluid pressure in the direction of flow, which is represented by the negative pressure gradient (-*dp/dx*) in Eq. (1) and (6). Consequently, gas molecules can move more freely because of the reduced resistance at low pressures. The mean free path length λ becomes greater than the pore diameter ($\lambda \gg d$) and molecules collide more frequently with the walls than with each other (Fig. 1). This flow is called Knudsen diffusion. In this case, viscosity no longer contributes to the flow. Gas movement is enhanced by molecular diffusion (= 'slip') and the fluid velocity across the tube increases by u_0 (Eq. (5)), leading to an apparent increase in permeability (Fig. 2). At low mean pressures, where flow occurs purely by Knudsen diffusion, the permeability coefficient may be higher than the extrapolated slip coefficient. The influence of the slip component decreases steadily with increasing pressure so that the right term of Eq. (6) does not have to be considered at high pressures.

The ratio of mean free path length to pore diameter provides a measure to characterise the type of flow. This dimensionless ratio is referred to as Knudsen number $Kn = \lambda/d$. At Knudsen numbers $Kn < 0.01$, collisions between gas molecules are prevailing and the term accounting for the slip flow in Eq.(6) can be omitted. When slip is negligible (as is usually the case for liquid flows), Eq. (6) reduces to the Hagen-Poiseuille equation:

$$\bar{u} = \frac{Q}{A} = -\frac{d^2}{32\mu}\left(\frac{dp}{dx}\right) \overset{d=2R,A=R^2\pi}{\longrightarrow} Q = \frac{dV}{dt} = -\frac{\pi R^4}{8\mu}\left(\frac{dp}{dx}\right) \tag{8a, b}$$

When gas flows through a porous medium, changes in driving pressure affect the gas density as well as the mean flow velocity $\bar{u}$. However, the mass flux of the gas, which is the product of velocity *u* and density ρ, remains constant. Since temperature is

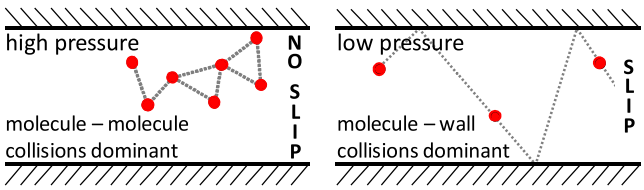

Fig. 1. Gas flow in tubes/pores without (left) and with (right) slip.

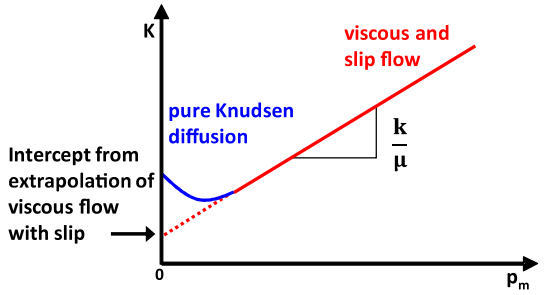

Fig. 2. At low pressures an artificial increase in permeability can be observed.

assumed to be constant, and density is proportional to pressure ($\rho = \frac{nM}{V} = \frac{pM}{RT}$), the product $u \cdot p$ is also constant and it follows from Eq. (6) that:

$$up = -\left(\frac{d^2}{32\mu}p + \frac{\pi d}{16}\mathrm{V}\right)\frac{dp}{dx} = constant \tag{9}$$

Integrating Eq. (9) over the length L of a porous medium and the pressure difference ($p = p_1$ *at* $x = 0$ and $p = p_2$ at $x = L$) results in:

$$\bar{u}_1 p_1 L = \frac{d^2}{32\mu}\left(\frac{p_1^2 - p_2^2}{2}\right) + \frac{\pi d}{16}\bar{v}(p_1 - p_2) \tag{10}$$

Substituting $\frac{p_1+p_2}{2} = p_m$ and $(p_1 - p_2) = \Delta p$ reduces Eq. (10) to:

$$\frac{\bar{u}_1 p_1 L}{\Delta p} = \frac{d^2}{32\mu}p_m + \frac{\pi d}{16}\bar{v} \tag{11}$$

Considering porous media as systems of capillaries, Carman (1956) derived the following equation:

$$K = \frac{Q_0 p_0 L}{\Delta p A} = \frac{k}{\mu}p_m + \frac{4}{3}K_0\sqrt{\frac{8RT}{\pi M}} \tag{12a}$$

where K [m^2 s^{-1}] is the permeability coefficient, p_0 [Pa] the pressure at which Q is measured, Δp [Pa] the pressure difference across the sample, k [m^2] the viscous permeability (analogous to $d^2/32$ for a single capillary – see Eq. (11)), $(4/3)K_0$ [m] the slip coefficient (analogous to $\pi d/16$ for the single capillary case).

Considering that $Q_0 p_0 = Qp = V\left(\frac{dp_2}{dt}\right)$ and using the assumption that if $p_1 >> p_2$, then $\Delta p \approx p_1$ and $p_m \approx \frac{p_1}{2}$, allows to rewrite Eq. (12a) in order to obtain the final expression for determining the gas permeability:

$$K = \frac{V\left(\frac{dp_2}{dt}\right)L}{p_1 A} = \frac{k}{\mu}\frac{p_1}{2} + \frac{4}{3}K_0\sqrt{\frac{8RT}{\pi M}} \tag{12b}$$

The origin of the factor 4/3 remains unclear, but this factor is retained here for consistency with other publications (Carman, 1956; Hewitt, 1965; Mason et al., 1967). A linear plot of K vs. p_m has the gradient $\frac{k}{\mu}$ from which the viscous permeability is determined. The Knudsen flow coefficient K_0 is determined by extrapolation to the intercept ($\frac{4}{3}K_0\sqrt{\frac{8RT}{\pi M}}$) of the linear plot $K = f(p_m)$ (Fig. 2) and can be related to the average pore diameter.

2.2. Steady-state diffusion through porous media

Hewitt & Sharratt (1963, 1964) and Hewitt & Morgan (1964) described measurements where oxygen is passed over one end of a porous sample and nitrogen over the other one, at equal pressures. By determining the concentration of oxygen in the efflux nitrogen, it is possible to evaluate the oxygen diffusion rate through the porous medium.

The molar transport rate of oxygen n_O [mol s^{-1}] through the medium is the product of the nitrogen flowrate over the nitrogen side of the porous medium Q_N [m^3 s^{-1}] and the concentration of oxygen in that stream c_O [mol m^{-3}] (Eq. (13)):

$$n_0 = Q_N c_0 \tag{13}$$

Consequently, the effective diffusion coefficient D_{eff} [m^2 s^{-1}] through the porous medium can be defined:

$$n_0 = D_{eff} A\frac{\Delta c_0}{L} \tag{14}$$

where Δc_O is the oxygen concentration difference across the sample. Considering the oxygen concentration is zero on the nitrogen side of the sample at the start of the measurement (t = 0), and furthermore assuming a linear relationship between c_O and the partial pressure of oxygen at constant applied pressure but at $\Delta p = 0$ across the sample *at* $t = 0$, Eq. (14) transforms to:

$$u_{1O} p_{1O} = -D_{eff}\frac{\Delta p_O}{L} \tag{15}$$

where u_{1O} is the superficial velocity of oxygen entering the sample, p_{1O} the partial pressure of oxygen at the oxygen end and Δp_O the difference in partial pressure of oxygen across the sample. Since $p_{1O} \approx -\Delta p_O$ it follows:

$$D_{eff} = \frac{10^{-6} L Q_N c_{O-N}}{A} \tag{16}$$

where $c_{O\text{-}N}$ [ppm by volume] is the oxygen concentration in the nitrogen efflux stream. The ratio $r_D = D_{eff}/D_{AB}$, where D_{AB} is the equimolar binary diffusion coefficient for the gas pair being considered (oxygen and nitrogen in our case), would be expected to be characteristic for the porous medium and hence to be independent of the diffusing species. However, the equations above do not consider net drift. Even at constant pressure, there is no equimolar counter diffusion in porous media for gases of different molecular weight. If we assume that the fluxes of the two gases were equal, then the momentum transfer to the channel surfaces would imply that a pressure gradient must exist if the molecular weights are different. This issue was considered by Hewitt (1967) and Hewitt & Morgan (1964). They introduced a correction factor Γ for D_{eff}/D_{AB}, giving the true value of the ratio, independent of the diffusing species:

$$\Gamma = \frac{1}{1 - \sqrt{M_A/M_B}}log\left(\frac{1}{1 - \sqrt{M_A/M_B}}\right) \tag{17}$$

where M_A, M_B [kg mol^{-1}]are the molecular weights of the diffusing species.

The result of $r_D = D_{eff}/D_{AB}$ provides information about the pore morphology of the porous material (You et al., 2013). The diffusing fluid has only access to parts of the cross-section of the porous medium (equivalent to the effective porosity ε_{eff}). Moreover, the tortuosity τ has to be considered, which is done by multiplying the sample length L by τ, resulting in a higher effective pore length L_{eff}. Consequently, the ratio r_D is less than unity. Weisz & Schwartz (1962), Hewitt and Morgan (1964) and Youngquist (1970) proposed an equation (Eq. (18)) allowing to calculate ε_{eff} or τ, given the other of the two parameters are known:

$$r_D = \frac{D_{eff}}{D_{AB}} = \frac{\varepsilon_{eff}}{\tau^2} \tag{18}$$

Transient diffusion measurements offer the possibility to determine the tortuosity independently (and hence ε_{eff}).

This publication focuses on normal or bulk diffusion. As described earlier, there is, however, a connection between the mean free path length of gas molecules, which depends on the pore

diameter and the type of diffusion taking place in a porous medium. Garrouch et al. (Garrouch et al., 2001) demonstrated the predominance of Knudsen diffusion in pores smaller than 10 nm, whereas normal diffusion occurs when pore diameters exceed 1 μm. In-between these pore diameters, both diffusion mechanisms do contribute.

2.3. Transient diffusion through porous media

Hewitt & Morgan (1964) reported transient diffusion experiments on porous materials, which they performed in a system with constant oxygen/nitrogen pressure. At the starting point (at time $t = 0$), the specimen was completely filled with nitrogen, while the concentration of oxygen on the nitrogen side was kept zero. Oxygen was then passed over one end of the sample and its rate of efflux into the nitrogen side determined by measuring the concentration of oxygen in the nitrogen efflux stream (Fig. 3 left axis). The efflux rate is proportional to the negative concentration gradient at this point according to Fick's second law. However, it is more convenient to express the measured data as fraction F, where F is the ratio of the efflux rate over its final value (Eq.(19)). The concentration of O_2 is consequently plotted as fraction F against time (Fig. 3 right axis).

Based on the solutions of Fick's second law of diffusion (Barrer, 1941), Hewitt & Morgan (1961) derived an expression for the ratio F of the oxygen efflux rate, at the nitrogen purged end of a sample, to its final steady rate at infinite time (Eq. (19)):

$$F = \frac{(c_{O-N})_t}{(c_{O-N})_{t=\infty}} = 1 + 2\sum_{n=1}^{\infty} cosn\pi exp\left(-\frac{D_{AB}n^2\pi^2 t}{L_{eff}^2}\right) \tag{19}$$

Solving Eq. (19) gives theoretical values of F as a function of the dimensionless group $\left(\frac{D_{AB}t}{L_{eff}^2}\right)$ (see Supplementary Information S.1 – Fitting Procedure), which allows to determine the effective pore length L_{eff}, which cannot be measured directly. Experimental data is fitted to the calculated data by solving $\left(\frac{D_{AB}t}{L_{eff}^2}\right)$ for various values of t. Consequently, the value of X giving the best fit is inserted into Eq. (20) to determine the effective pore length L_{eff}, which is then used in Eq. (21) to calculate the tortuosity τ. ε_{eff} can be estimated by inserting L_{eff} and the measured value of r_D into Eq. (18).

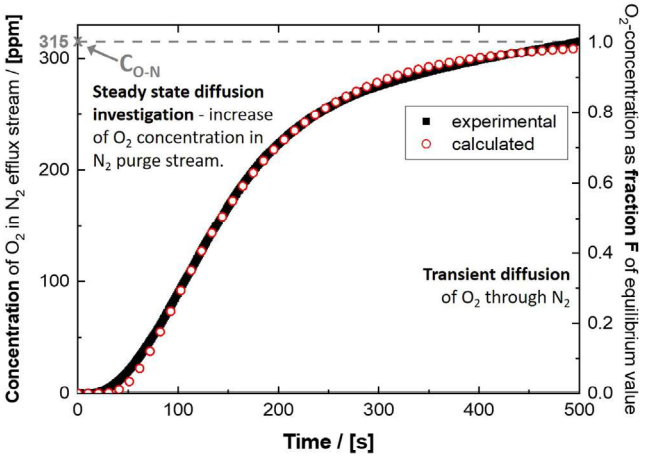

Fig. 3. Rate of oxygen diffusion through sandstone sample S3 measured experimentally for steady state diffusion interaction: increase of O_2 concentration in N_2 purge stream, as well as experimental transient diffusion of O_2 as fraction of the final equilibrium value.

$$\frac{D_{AB}}{L_{eff}^2} = X \rightarrow L_{eff} = \sqrt{\frac{D_{AB}}{X}} \tag{20}$$

$$\tau = \frac{L_{eff}}{L} \tag{21}$$

3. Experimental procedures

3.1. Materials

Sandstone cores with different porosities were provided by Berea® Sandstone (Petroleum Cores, Ohio, USA). These samples were selected to demonstrate the versatility of the combined permeability/diffusivity apparatus. All sandstone fragments were thoroughly dried in a vacuum oven at 120 °C for at least 10 h. The porosity of all samples was determined by density measurements. The bulk density ρ_{bulk} was evaluated indirectly by simply measuring mass and volume of the samples; absolute density ρ_{abs} was measured using helium displacement pycnometry (AccuPyc 1330, Micrometrics Ltd. Dunstable, UK), after crushing sandstone pieces by means of a hammer. The porosity ε of the samples was calculated as follows (Eq. (20)):

$$\varepsilon = 1 - \frac{\rho_{bulk}}{\rho_{abs}} \tag{22}$$

The sandstone samples were divided into two groups: Set 1 included the higher porosity sandstones S1 – S4 with porosities ranging from 32 to 22%; Set 2 included sandstones S5-S8 with lower porosities between 7 and 4%. The gases used in the experiments were nitrogen (>99.999% purity) and oxygen (99.5% purity) obtained from BOC Edwards Ltd., Crawley, UK.

3.2. Sample preparation

Fluid leakage from the sample via crossflow was prevented by sealing the sandstone samples, 13 mm in diameter, with a thin layer of a non-permeable, highly viscous epoxy adhesive (Araldite® Precision Adhesive RS Components Ltd. Corby, UK). The coating was cured at ambient conditions, before the cylindrical sample was fixed to the bottom of a cylindrical PTFE-mould. Prior to use, the inner side of the mould was covered with a thin layer of silicon release agent (Silicone mould release spray, Electrolube, RS Components Ltd., Corby UK), for easy removal of the sample from the mould. Resin and hardener of the two-component epoxy system Araldite® 2020 (RS Components Ltd., Corby UK) were mixed and poured into the mould surrounding the sample before left to cure at room temperature for 24 h.

Once coated and sealed, the cores were machined at both ends to reveal the faces of the sample, a representation of the coated sample is shown in Fig. 4.

3.3. Permeability measurements

The gas permeability was measured using a purpose-built apparatus, Fig. 5a and which can also be seen in Fig. 5b. The device is

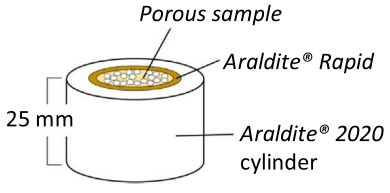

Fig. 4. Coated sample dimensions.

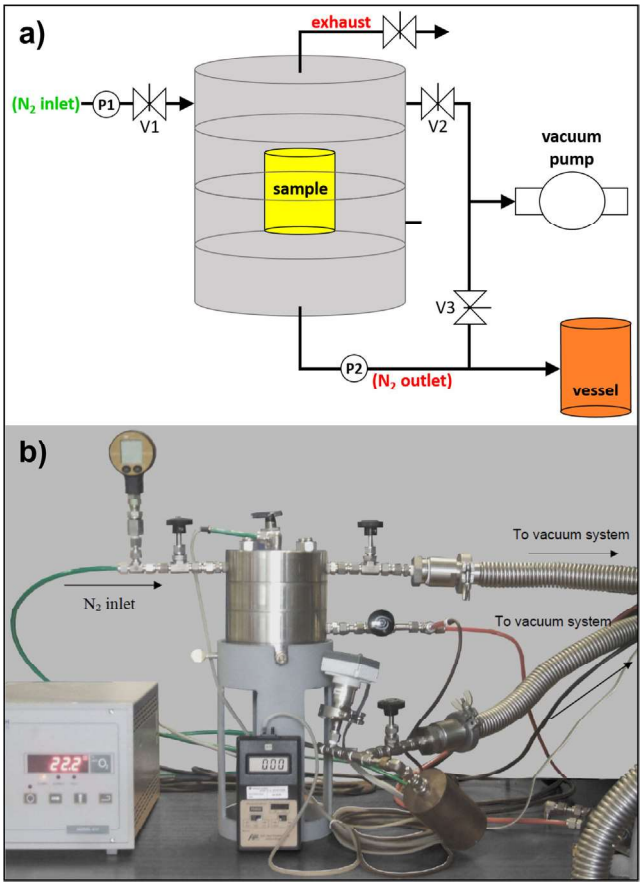

Fig. 5. a) schematic (a) and photograph (b) of the permeability cell set-up (not to scale).

presented in more detail and with measures in Fig. 6. A detailed CAD drawing of the entire apparatus can be found in the supplementary information (Figure S.3) and the CAT file is also available, which should allow anyone interested to build the same device.

After inserting the coated and embedded sandstone core into the sample chamber, the whole vessel was evacuated to a pressure of 10 Pa using a vacuum pump (Model E-Lab-2 Vacuum Pump, BOC Edwards Ltd., Crawley, UK). The vacuum system consisted of 25 mm diameter vacuum hoses and a vacuum trap, (both supplied by Leybold Vaccum UK Ltd., Chessington, UK).

The pressure was monitored using a Pirani vacuum gauge (Pirani APG-M-NW16 with Active Pirani Gauge ADL Active Digital Controller, BOC Edwards Ltd., Crawley, UK).

Valve V2 was used to close the connection between inlet side and vacuum pump, while vessel and outlet side of the sample were maintained at a low pressure p_2, which was monitored using pressure gauge P2 (Digital Manometer LEO 2 Keller (UK) Ltd., Dorchester, UK, accuracy RT < 0.1% FS, total error band (0–50 °C) < 0.2% FS).

Pressure gauge P1 (same model as P2) was used to set the desired inlet pressure p_1 of oxygen free nitrogen. Opening V1 released gas into the system. When V3 was closed, the gas was directed through the sample and collected in a vessel of known volume V. Depending on the permeability of the porous a material of interest, vessels of different size can be utilised. The pressure rise in the known volume was recorded using P2 and plotted against time. The slope of the resulting curve is equal to the rate of pressure rise $\left(\frac{dp_2}{dt}\right)$ at an applied p_1.

The procedure was repeated for various inlet pressures p_1. For low mean pressure experiments, N_2 fed into the inlet side, was simultaneously evacuated through V2 and the balance between feed and bleed was adjusted to result in a constant (sub-atmospheric) pressure. A schematic overview of the evaluation of the viscous permeability k and the slip coefficient K_0 is shown in Fig. 7.

If the expected permeabilities are very low, a smaller vessel with $V_{small} = 2.40 \cdot 10^{-4}$ m^3 should be used, otherwise a the larger one with $V_{large} = 1.97 \cdot 10^{-3}$ m^3. In case of expected permeabilities in the nano Darcy (nD) range, for instance for shale samples (Sakhaee-Pour and Bryant, 2012), no vessel should be used, instead only the tubing volume $V_{tube} = 9.03 \cdot 10^{-6}$ m^3 is sufficient as low-pressure reservoir.

Measurements were performed at ambient temperature. The viscosity of N_2 at a temperature T can be estimated using Sutherland's formula (Crane.Co., 2010; Lemmon and Jacobsen, 2004). The following viscosity for N_2 was used for nitrogen $\mu = 1.75 \cdot 10^{-5}$ Pa s. The variation of viscosity with pressure in the used pressure range is small for most gases and can be neglected.

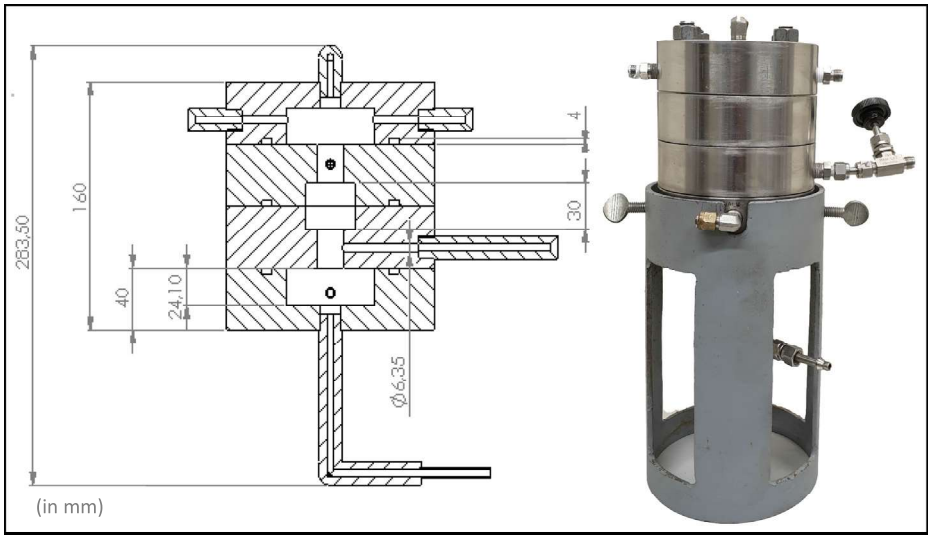

Fig. 6. CAD drawing (with measures in mm) and picture of the main corps of the apparatus.

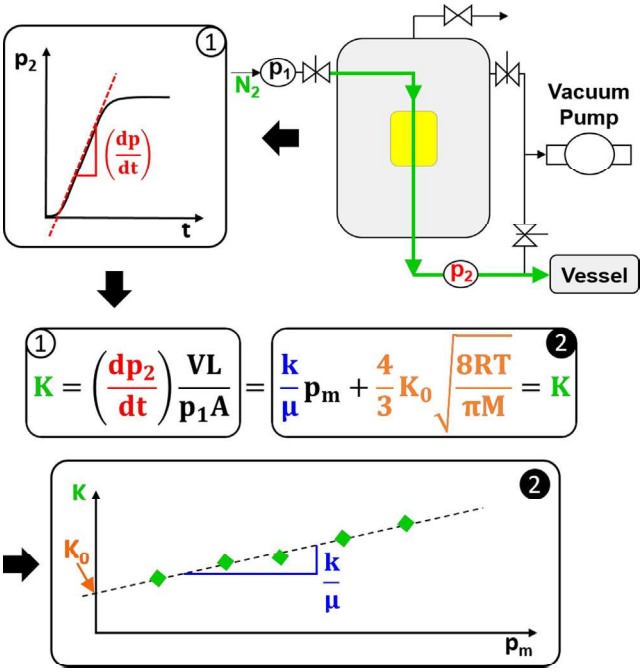

Fig. 7. Schematic representation of a gas permeability measurement. The pressure gradient (dp_2/dt) is determined by plotting the recorded pressure over time. The results of the left part (1) of the equation are inserted into the right part. Consequently, the viscous permeability k and the slip coefficient K_0 are evaluated from slope and intercept.

First, the permeability coefficient K is calculated by inserting pressure gradient (dp_2/dt), vessel volume V, sample length L, sample cross-section area A and the applied pressure p_1 into the left part of the equation shown in Fig. 7 (=Eq. (12a)). After calculating K for all p_1, the viscous permeability coefficient k and the slip coefficient K_0 are obtained from a K vs. p_m plot: dividing the slope by the fluid viscosity gives k; K_0 can easily be calculated from the expression for the intercept, as all other constants are known.

3.4. Diffusivity measurements

The same apparatus was used for diffusivity measurements on the same samples, only a few minor changes to the set-up were necessary (Fig. 8).

Prior to the diffusion experiments, apparatus and sample were evacuated thoroughly, down to approximately 10 Pa. After adjusting the inlet pressures of N_2 and O_2 to a pressure difference of zero, N_2 was fed into the system to fill the apparatus including the porous specimen.

In the next step, O_2 was released into the oxygen side of the apparatus and the gas pressures were adjusted accordingly to ensure that there was no pressure gradient over the sample.

An O_2 analyser (800 Series Zirconia Cell Oxygen Analyser Model 810, Systech Instruments Ltd., Thame, UK), also used for measuring the flow rate of the nitrogen purge stream, continuously monitored the O_2 concentration in the N_2 side, which after some time (approximately 10–15 min) reached an equilibrium value $(c_{O-N})_{t=\infty}$ (range 0.1 ppm to 100%, accuracy 0.2% absolute, repeatability 0.2% of measured value). The measurements were stopped when the rate of change was less than 5%.

Uncertainty analysis of the apparatus for both permeability and diffusivity characterisation was performed taking into account all potential systematic and fixed errors. The uncertainty of our apparatus for permeability and diffusivity measurements was determined to be 13% and 8% (see supplementary information), respectively.

4. Results and discussion

4.1. Gas permeability of sandstone samples

The linear relationship between the mean pressure p_m and the permeability coefficients K is shown in Fig. 9 & Fig. 10. The viscous permeability k can then be determined from the slope of the linear fit of the experimental data of the gas permeability measurements for S1 - S4.

Of these sandstone cores S1 exhibited with 1050 ± 166 mD ($1.05 \pm 0.166 \times 10^{-12}$ m^2) the highest permeability. The results of sample set two (S5 – S8), consisting of cores with lower porosity, are shown in Fig. 10. Comparing the results of all analysed samples S1 – S8, it can be seen that the permeability of sandstones depended strongly on their porosity. Accordingly, the sample with the lowest porosity, S8, has the lowest permeability.

The slip flow coefficients K_0 were extracted from the intercepts of the linear fits with the y-axis of the plot $K = f(p_m)$. Similar to the viscous permeabilities, K_0 also decreases with decreasing porosity.

The highest Knudsen flow coefficient, $1.08 \times 10^{-5} \pm 1.68 \times 10^{-6}$ m, was found for S1. It is expected that slip flow influences the gaseous transport more significantly the smaller the pores of the analysed material and, hence, the lower its viscous permeability. This presumption is supported and reflected in our results. Table 1

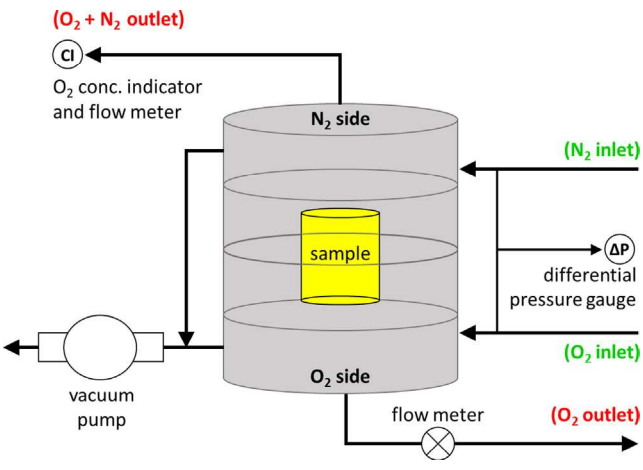

Fig. 8. Schematic of the diffusion cell set-up (not to scale).

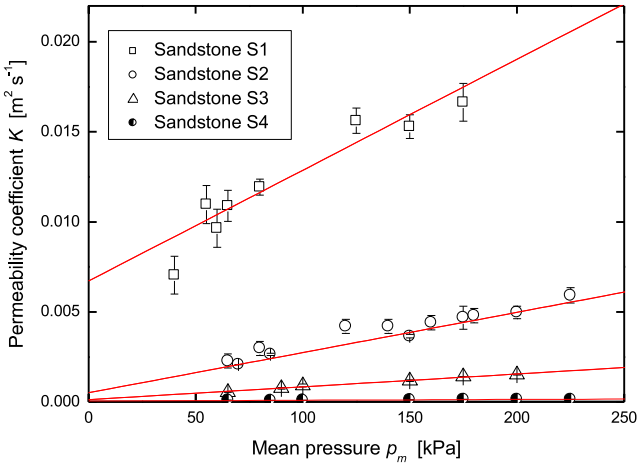

Fig. 9. Permeability coefficient at various mean pressures for sandstone samples S1 – S4.

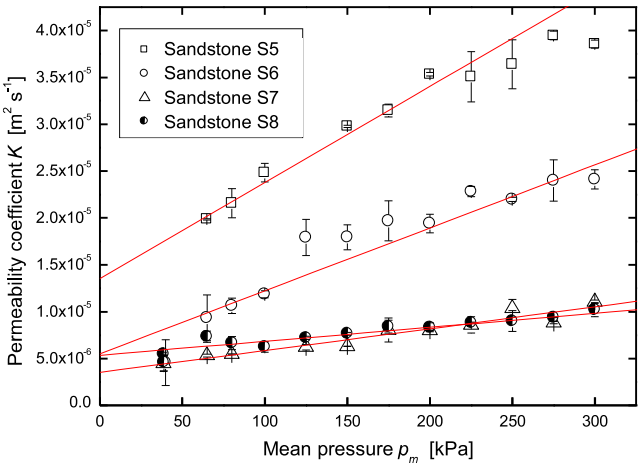

Fig. 10. Permeability coefficient at various mean pressures for samples S5 – S8.

summarises the results of the density measurements (ρ_{abs}, ρ_{bulk}) including porosity (ε) and lists the determined viscous permeabilities k and Knudsen diffusion coefficients K_0.

4.2. Non-Darcy flow through sandstone

At higher flowrates, i.e. interstitial $Re > 1$ (but in our case $Re < 80$, see supplementary information Fig.S.1), the fluid flow behaviour through porous media is not purely dictated by Darcy (viscous) flow anymore, because contributions of the bulk form drag effect start to become significant. To take these contributions into account, Darcy's equation was extended by a quadratic term by Dupuit and Forchheimer (see Lage & Antohe (2000)) so that the pressure drop per unit length is described as follows (Eq. (23)):

$$\frac{dp}{dx} = au + b\rho u^2 \tag{23}$$

where coefficient $a\left(=\frac{\mu}{k}\right)$ represents the viscous flow, while coefficient b is the form factor (Forchheimer coefficient). The form drag force, described by the quadratic term, stems from the porous medium obstructing fluid flow. Based on Eq. (23), a methodology for describing such flows was developed (Hewitt, 1961).

The mass flux G can be estimated directly from measurements since:

$$G = \rho_2 \frac{Q_2}{A} = Q_2 p_2 \frac{M}{RTA} \overset{Q_2 p_2 = V\frac{dp_2}{dt}}{\Rightarrow} = V\left(\frac{dp_2}{dt}\right)\frac{M}{RTA} \tag{24}$$

In case of isothermal flow of gases, the superficial velocity $u = \frac{G}{\rho}$ can be inserted into Eq. (23), where $\rho = \frac{pM}{RT}$. After integration and rearrangements, the following equation is obtained:

$$C = \frac{(p_1^2 - p_2^2)M}{2RTLG} = \frac{\mu}{k} + bG \tag{25}$$

Using $K = \frac{V\left(\frac{dp_2}{dt}\right)L}{p_1 A}$ from Eq. (12b), C can first be simplified to Eq. (26a) and in a next step to Eq. (26b), by assuming that $(p_1^2 - p_2^2) \cong p_1^2$.

$$C = \frac{(p_1^2 - p_2^2)}{2Kp_1} \tag{26a}$$

$$C = \frac{p_1}{2K} = \frac{p_m}{K} \tag{26b}$$

Plotting C against the total mass flux G, which is proportional to $V\left(\frac{dp_2}{dt}\right)$, is expected to give a straight line that intersects the ordinate at $a\left(=\frac{\mu}{k}\right)$ and the slope provides the Forchheimer coefficient b.

The data obtained from permeability measurements was used to investigate non-Darcy flow. As exemplified in Fig. 11, a plot of C vs. G for sandstone S1 is indeed linear, which is an indicator for the contribution of form drag exerted on the gas by sandstone grains. The results of S2 – S7 (see supplementary information Figure S.4) fortify this finding.

From the intercept $a\left(=\frac{\mu}{k}\right)$ it is straightforward to calculate the permeability k. The derived permeabilities k_{DF} and Forchheimer factors b are summarised in Table 2.

Calculating the permeability using the equation for non-Darcy flow leads to results that are up to three times higher than predicted from viscous flow. In all cases, the permeabilities are overestimated. This is potentially due to the onset of form drag at various stages in different pores. Presuming that there are two groups of pores it is possible to describe their relationship as follows:

$$\frac{dp}{dx} = a_1 u_1 + b_1 \rho u_1^2 \tag{22}$$

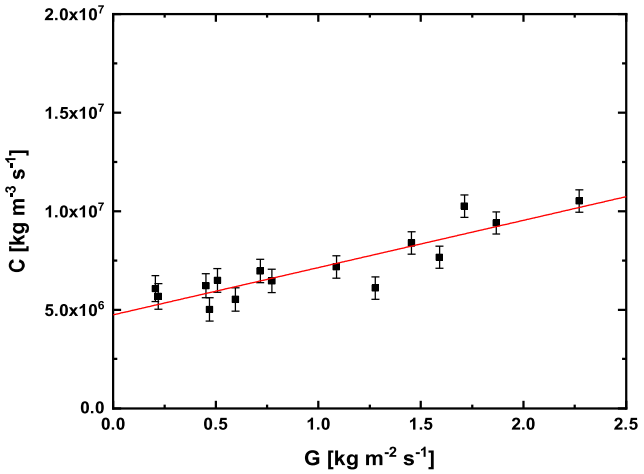

Fig. 11. Linear plot of C vs. G for sandstone sample S1.

Table 1
Absolute ρ_{abs} and bulk density ρ_{bulk}, porosity ε and determined viscous permeability k and Knudsen diffusion coefficient K_0.

Sample	ρ_{abs}/[kg m^{-3}]	ρ_{bulk}/[kg m^{-3}]	ε/[%]	k/[m^2]	K_0/[m]
S1	2707 ± 19	1825 ± 97	32.6 ± 7.5	$1.05 \times 10^{-12} \pm 1.66 \times 10^{-13}$	$1.08 \times 10^{-5} \pm 1.68 \times 10^{-6}$
S2	2789 ± 15	1902 ± 14	30.3 ± 0.7	$3.50 \times 10^{-13} \pm 2.07 \times 10^{-14}$	$1.45 \times 10^{-6} \pm 3.41 \times 10^{-7}$
S3	2841 ± 7.6	2213 ± 25	21.9 ± 1.1	$1.26 \times 10^{-13} \pm 2.98 \times 10^{-15}$	$1.10 \times 10^{-7} \pm 4.61 \times 10^{-8}$
S4	2789 ± 2.9	2172 ± 17	22.1 ± 1.1	$9.81 \times 10^{-15} \pm 2.60 \times 10^{-16}$	$5.14 \times 10^{-8} \pm 3.11 \times 10^{-9}$
S5	2675 ± 16	2488 ± 13	7.0 ± 0.4	$1.38 \times 10^{-15} \pm 1.10 \times 10^{-16}$	$2.54 \times 10^{-8} \pm 1.99 \times 10^{-9}$
S6	2647 ± 8	2507 ± 19	5.3 ± 1.1	$1.11 \times 10^{-15} \pm 4.00 \times 10^{-16}$	$8.71 \times 10^{-9} \pm 8.58 \times 10^{-10}$
S7	2651 ± 12	2552 ± 50	3.8 ± 3.3	$3.70 \times 10^{-16} \pm 1.00 \times 10^{-17}$	$5.16 \times 10^{-9} \pm 1.07 \times 10^{-10}$
S8	2658 ± 6.1	2560 ± 13	3.7 ± 0.7	$2.40 \times 10^{-16} \pm 1.00 \times 10^{-17}$	$8.46 \times 10^{-9} \pm 2.36 \times 10^{-10}$

Table 2
Permeabilities k_{DF} and Forchheimer factors b determined from C vs. G plots.

Sample	k_{DF}/[m^2]	b/[m^{-1}]
S1	$3.65 \times 10^{-12} \pm 7.07 \times 10^{-13}$	$2.23 \times 10^{06} \pm 1.01 \times 10^{06}$
S2	$5.55 \times 10^{-13} \pm 6.22 \times 10^{-14}$	$8.15 \times 10^{06} \pm 3.85 \times 10^{06}$
S3	$1.67 \times 10^{-13} \pm 6.25 \times 10^{-15}$	$9.64 \times 10^{07} \pm 6.91 \times 10^{07}$
S4	$1.99 \times 10^{-14} \pm 1.97 \times 10^{-15}$	$1.75 \times 10^{10} \pm 1.30 \times 10^{10}$
S5	$5.65 \times 10^{-15} \pm 5.55 \times 10^{-16}$	$5.05 \times 10^{11} \pm 5.24 \times 10^{10}$
S6	$3.53 \times 10^{-15} \pm 1.62 \times 10^{-15}$	$1.22 \times 10^{12} \pm 5.73 \times 10^{11}$
S7	$1.27 \times 10^{-15} \pm 1.73 \times 10^{-16}$	$6.66 \times 10^{12} \pm 1.95 \times 10^{12}$
S8	$1.79 \times 10^{-15} \pm 1.98 \times 10^{-16}$	$9.41 \times 10^{12} \pm 2.79 \times 10^{11}$

$$\frac{dp}{dx} = a_2 u_2 + b_2 \rho u_2^2 \tag{23}$$

Integration of the combination of the two equations leads to:

$$C = (a_1 + a_2)\frac{G_1 G_2}{G^2} + (b_1 G_1 + b_2 G_2)\frac{G_1 G_2}{G^2} \tag{24}$$

where G_1, G_2 are the mass fluxes through the two groups of pores. Thus, a plot of C versus G will only extrapolate to $(a_1 + a_2)$ in the special case when $G = G_1 = G_2$.

4.2.1. Non-Darcy flow effects on gas permeability

Analysis shows the occurrence of non-Darcy flow in the pores of sandstone cores S1 – S8. This is indicated by deviations from linearity in a plot $C = f(G)$. The permeabilities, extracted from the ordinate intercepts, are plotted in Fig. 12. The results from the permeability measurements k_{gas} are expected to conform with those obtained from evaluating non-Darcy (Dupuit-Forchheimer) flow k_{DF} (as observed, for instance, by (Hewitt, 1961)). This is indeed the case; values for k_{gas} and k_{DF} agree fairly well, except for overestimated permeabilities of S1 and S2. A possible explanation is the presence of multiple groups of pores causing different onsets of non-Darcy flow by form drag. For instance, Eq. (24) considers only a bimodal pore size distribution, not more.

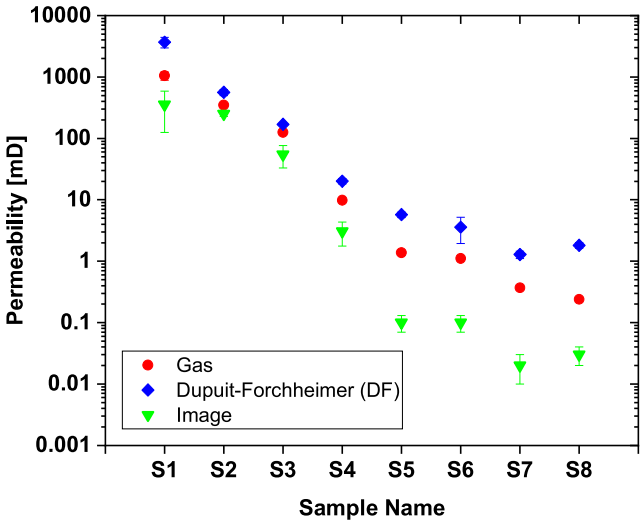

Fig. 12. Permeability from pressure-rise measurements using Darcy and non-Darcy flow and predictions from image analysis according to Koplik et al. (1984). Characteristic polished cross-sections of resin filled sandstone samples are shown in Figure S.5.

4.3. Diffusion of oxygen through nitrogen saturated sandstone

4.3.1. Steady state diffusion

The diffusivity of sandstone samples S1 – S8 for gases was determined using our apparatus. The results of our measurements, i.e. final equilibrium concentration c, effective diffusion coefficient D_{eff}, tortuosity τ, effective pore length L_{eff} and porosity ε_{eff} are summarized in Table 3. It is straightforward that the oxygen diffusion rate increases with permeability. Opposing trends can be observed between permeability and effective length; L_{eff} increases the less permeable the sample.

The effective porosity shows the same behaviour towards the effective length, which means the lower the effective porosity, the higher the effective pore length.

According to Eq. (18), the effective diffusion coefficients for the first sample set (S1 – S4) are higher than for the second one (S5 – S8), due to their higher permeabilities and porosities. The substantial difference between the two sample sets is furthermore illustrated in a plot porosity vs. effective porosity (Fig. 13).

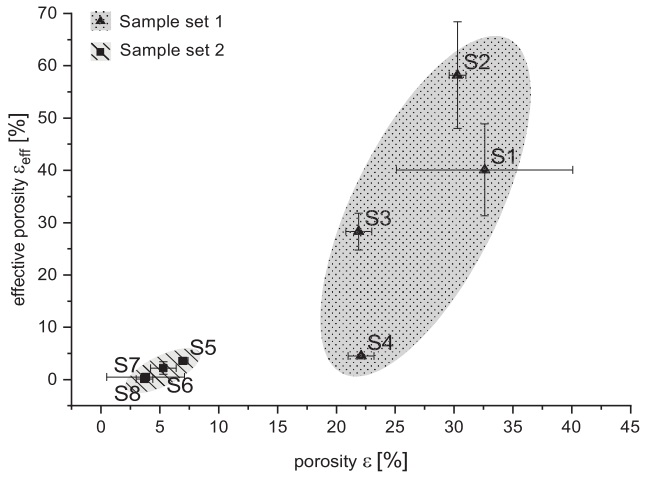

Fig. 13. The distinct difference between the sandstones of the two sample sets becomes even more apparent in a porosity vs. effective porosity plot.

Table 3
Summary of diffusivity results.

	Steady state analysis		Transient analysis		
Sample	c/[ppm]	$D_{eff} \times 10^9$/[m^2 s^{-1}]	τ^2	L_{eff}/[mm]	ε_{eff}/[%]
S1	25300 ± 300	1446 ± 6.95	5.1 ± 1.2	49.5 ± 3.5	40.1 ± 8.8
S2	11150 ± 150	638 ± 8.48	16.7 ± 2.7	110 ± 7.7	58.2 ± 10.2
S3	322.3 ± 15.3	18.2 ± 8.65	28.0 ± 2.1	132 ± 4.7	28.3 ± 3.5
S4	464.5 ± 11.5	26.3 ± 0.65	31.1 ± 1.2	139 ± 3.9	4.5 ± 0.3
S5	325.0 ± 23.0	19.0 ± 1.30	35.6 ± 0.7	149 ± 3.3	3.6 ± 0.2
S6	213.3 ± 11.3	11.4 ± 0.64	32.4 ± 5.4	142 ± 10	2.2 ± 1.2
S7	67.3 ± 3.0	0.04 ± 0.01	26.1 ± 1.5	128 ± 3.1	0.5 ± 0.1
S8	1.3 ± 0.1	0.07 ± 0.01	14.6 ± 0.1	95.4 ± 2.1	0.1 ± 0.0

Comparison with literature shows that tortuosity values of sandstone published earlier among others by Donaldson et al. (1976), Spearing & Matthews (1991) and Zhan et al. (2011) are at the same order of magnitude than the results presented in Table 3.

It was noted that the total measured porosities are prevailingly higher than the calculated ε_{eff} (see Table 1). However, for sandstone cores with high porosity, the values given in Table 1 are sometimes even higher than the measured ones. This observation has not been elucidated yet and needs further investigation.

5. Conclusions

Our purpose-built apparatus allows the concurrent determination of permeability and diffusivity of a range of porous materials with vastly different permeabilities. In order to perform permeability or diffusivity measurements, only minor adaptations to the same apparatus are necessary. The measurements are based on a pressure-rise technique, i.e. a stepwise increased pressure is applied driving the gas flow through the porous medium. This allows for the evaluation of the viscous permeability and the Knudsen flow coefficient, two important parameters describing the gas flow through porous media, as well as non-Darcy flow permeability and Forchheimer factor, if the interstitial Re exceeds 1.

After analysing one shale and eight sandstone cores with varying porosities, we can conclude the following:

- Measurements of the viscous permeability and slip flow showed that the apparatus was capable of measuring permeabilities as low as 0.24 mD (2.4×10^{-16} m^2) and as high as 1050 mD (1.05×10^{-12} m^2).
- Effective diffusion coefficients of porous materials with porosities between 3.7 and
- 32.6% can be deduced from gas diffusion measurements
- Transient diffusion analysis allows the calculation of effective pore length and effective porosity. Comparison of the calculated effective porosity with the absolute porosity indicates the extent of pore interconnectivity of the sample.
- The lower the mean pressure, the more significant becomes the contribution of the slip effect on gas flow, which is accommodated for by the introduction of the slip flow coefficient K_0. At very low pressures, the transport mechanism changes gradually to a diffusive one with free molecule (Knudsen) diffusion becoming the operative mechanism at the lowest pressure.
- Steady state diffusion of oxygen in nitrogen in the pores of the sandstone cores was measured at constant pressure. Combining the results of steady state and transient diffusion allows for the calculation of effective pore length (and hence the ratio of the effective pore length – the tortuosity) and effective porosity.
- The tortuosities determined for Berea sandstones are in a similar range to those reported in the literature.

CRediT authorship contribution statement

Shu San Manley: Conceptualization, Formal analysis, Investigation, Methodology, Validation, Visualization, Writing - original draft. **Patrick Steindl:** Conceptualization, Formal analysis, Validation, Visualization, Writing - review & editing. **Geoffrey F. Hewitt:** Conceptualization, Formal analysis, Funding acquisition, Methodology, Supervision. **Alexander Bismarck:** Conceptualization, Formal analysis, Funding acquisition, Methodology, Project administration, Resources, Supervision, Writing - review & editing.

Declaration of Competing Interest

The authors declared that there is no conflict of interest.

Acknowledgements

SSM acknowledges funding for her PhD through the UK Engineering and Physical Sciences Research Council (EPSRC UK) via a CASE DTA and PS the support of the Austrian Science Foundation (FWF) (grant I1800). We are grateful for funding support from Halliburton Energy Services and the help of Johnny Johnson from the Halliburton Technology Center (Duncan, OK, USA), who built the test apparatus. For helpful discussions on the physics of flow we thank Dr. Hans-Werner Müller (PaCE).

Appendix A. Supplementary material

Supplementary data to this article can be found online at https://doi.org/10.1016/j.ces.2020.115725.

References

Al-Quraishi, A., Khairy, M., 2005. Pore pressure versus confining pressure and their effect on oil-water relative permeability curves. J. Petrol. Sci. Eng. 48, 120–126. https://doi.org/10.1016/j.petrol.2005.04.006.

Baraka-Lokmane, S., 2002. Hydraulic versus pneumatic measurements of fractured sandstone permeability. Journal of Petroleum Science and Engineering 36, 183–192. https://doi.org/10.1016/S0920- 4105(02)00317-0.

Barrer, R.M., 1941. Diffusion in and through solids. Cambridge University Press, Cambridge.

Berg, C.F., 2014. Permeability description by characteristic length, tortuosity, constriction and porosity. Transp. Porous Media 103, 381–400. https://doi.org/10.1007/s11242-014-0307-6.

Berkowitz, B., 2002. Characterizing flow and transport in fractured geological media: A review. Advances in Water Resources 25, 861–884. https://doi.org/10.1016/S0309-1708(02)00042-8.

Biloé, S., Mauran, S., 2003. Gas flow through highly porous graphite matrices. Carbon 41, 525–537. https://doi.org/10.1016/S0008-6223(02)00363-9.

Bird, R.B., Stewart, W.E., Lightfoot, E.N., 2002. Diffusivity and the Mechanisms of Mass Transport, Transport Phenomena. John Wiley & Sons Inc, pp. 513–528.

Bokhoven, C., Hoogschagen, J., 1953. Diffusion in Porous Catalysts. J. Chem. Phys. 21, 159–160. https://doi.org/10.1063/1.1698571.

Carman, P.C., 1956. Flow of Gases Through Porous Media. Butterworths Scientific Publications, Belfast.

Cengel, Y.A., Cimbala, J.M., 2006. Flow in Pipes. Fluid Mechanics - Fundamentals and Applications. McGraw-Hill, New York, pp. 321–398.

Coates, G.R., Xiao, L., Prammer, M.G., 1999. NMR Permeability. In: Sigal, R.F., Bollich, S.J. (Eds.), NMR Logging - Principles & Applications. Halliburton Energy Services, Houston (USA), pp. 9–11.

Collins, R.E., 1961. Flow Of Fluids through Porous Materials. Reinhold Publishing Corporation, USA.

Comiti, J., Sabiri, N.E., Montillet, A., 2000. Experimental characterization of flow regimes in various porous media - III: limit of Darcy's or creeping flow regime for Newtonian and purely viscous non-Newtonian fluids. Chem. Eng. Sci. 55, 3057–3061. https://doi.org/10.1016/S0009-2509(99)00556-4.

Crane.Co., 2010. Flow of Fluids through Valves, Fittings and Pipe - Technical Paper No.410. Crane Co, New York..

Darcy, H., 1856. Appendix D. In: Dalmont, V. (Ed.), Les fontaines publiques de la Ville de Dijon. Librairie des Corps Imperiaux des Ponts et Chaussées et des Mines, Paris, pp. 559–603.

Dietrich, P., Helmig, R., Sauter, M., Hötzl, H., Köngeter, J., Teutsch, G., 2005. Flow and Transport in Fractured Porous Media. Springer, Berlin, Heidelberg.

Donaldson, E.C., Kendall, R.F., Manning, F.S., 1976. Dispersion and Tortuosity in Sandstones, SPE Annual Fall Technical Conference and Exhibition. Society of Petroleum. Engineers, New Orleans, Louisiana, p. 16.

Dullien, F.A.L., 1975. Single phase flow through porous media and pore structure. The Chemical Engineering Journal 10, 1–34. https://doi.org/10.1016/0300-9467(75)88013-0.

Garrouch, A.A., Ali, L., Qasem, F., 2001. Using diffusion and electrical measurements to assess tortuosity of porous media. Ind. Eng. Chem. Res. 40, 4363–4369. https://doi.org/10.1021/ie010070u.

Gerritsen, M.G., Durlofsky, L.J., 2005. Modeling fluid flow in oil reservoirs. Annu. Rev. Fluid Mech. 37, 211–238. https://doi.org/10.1146/annurev.fluid.37.061903.175748.

Ghanizadeh, A., Clarkson, C.R., Aquino, S., Ardakani, O.H., Sanei, H., 2015. Petrophysical and geomechanical characteristics of Canadian tight oil and liquid-rich gas reservoirs: I. Pore network and permeability characterization. Fuel 153, 664–681. https://doi.org/10.1016/j.fuel.2015.03.020.

Hewitt, G.F., 1961. Some Measurements of the Gas Permeability of Graphite. AERE M851.

Hewitt, G.F., 1965. Gaseous Mass Transport Within Graphite. In: Walker, P.L. (Ed.), Chemistry and Physics of Carbon. A Series of Advances, Vol. 1. Marcel Dekker Inc., New York.

Hewitt, G.F., 1967. Approximate Equations for the Diffusion and Flow of Gases in Porous Media. UKAEA Report No, AERE, p. R5492.
Hewitt, G.F., Hawtin, P., 1967. Flow of Gases in Porous Solids. Nature 215, 1415–1416.
Hewitt, G.F., Morgan, J.R., 1961. The Diffusion of Oxygen in Nitrogen in the Pores of Graphite - Systematic Investigation of a Cross-Section of a Block Pile of Graphite. AERE R 3814, 58.
Hewitt, G.F., Morgan, J.R., 1964. The diffusion of oxygen in nitrogen in the pores of graphite. Progress in Applied Materials Research 5, 167–204.
Hewitt, G.F., Sharratt, E.W., 1963. Gaseous Diffusion in Porous Media with particular reference to graphite. Nature 198, 952–957.
Hewitt, G.F., Sharratt, E.W., 1964. The Effect of back-pressure on the counter diffusion of gases in graphite. J. Nucl. Mater. 13, 197–206.
Higgins, B.G., Binous, H., 2013. Binary Diffusion Coefficients for Gases, http://demonstrations.wolfram.com/BinaryDiffusionCoefficientsForGases/..
Huang, H., Ayoub, J., 2008. Applicability of the Forchheimer Equation for Non-Darcy Flow in Porous Media. Spe Journal March 2008. doi:10.2118/102715-PA..
Ishizaki, K., Komareneni, S., Nanko, M., 1998. Porous Materials - Process Technology and Applications. Springer, US.
Jannot, Y., Lasseux, D., 2012. A new quasi-steady method to measure gas permeability of weakly permeable porous media. Rev. Sci. Instrum. 83,. https://doi.org/10.1063/1.3677846 015113.
Katz, A.J., Thompson, A.H., 1986. Quantitative prediction of permeability in porous rock. Physical Review B 34, 8179–8181. https://doi.org/10.1103/PhysRevB.34.8179.
Kawagoe, Y., Oshima, T., Tomarikawa, K., Tokumasu, T., Koido, T., Yonemura, S., 2016. A study on pressure-driven gas transport in porous media: from nanoscale to microscale. Microfluid. Nanofluid. 20, 162. https://doi.org/10.1007/s10404-016-1829-8.
Klinkenberg, L.J., 1951. Analogy between Diffusion and Electrical Conductivity in Porous Rocks. Geol. Soc. Am. Bull. 62, 559–563. https://doi.org/10.1130/0016-7606(1951)62[559:Abdaec]2.0.Co;2.
Koplik, J., Lin, C., Vermette, M., 1984. Conductivity and Permeability from Microgeometry. J. Appl. Phys. 56, 3127–3131. https://doi.org/10.1063/1.333872.
Lage, J.L., Antohe, B.V., 2000. Darcy's experiments and the deviation to nonlinear flow regime. J. Fluids Eng.-Trans. ASME 122, 619–625. https://doi.org/10.1115/1.1287722.
Le Coq, L., 2008. Influence on permeability of the structural parameters of heterogeneous porous media. Environmental Technology 29, 141–149. https://doi.org/10.1080/09593330802028477.
Lemmon, E.W., Jacobsen, R.T., 2004. Viscosity and Thermal Conductivity Equations for Nitrogen, Oxygen, Argon, and Air. Int. J. Thermophys. 25, 21–69. https://doi.org/10.1023/B:IJOT.0000022327.04529.f3.
Lin, H., Freeman, B.D., 2004. Gas solubility, diffusivity and permeability in poly (ethylene oxide). J. Membr. Sci. 239, 105–117. https://doi.org/10.1016/j.memsci.2003.08.031.
Liu, R., Jiang, Y., Li, B., Yu, L., 2016. Estimating permeability of porous media based on modified Hagen-Poiseuille flow in tortuous capillaries with variable lengths. Microfluid. Nanofluid. 20. https://doi.org/10.1007/s10404-016-1783-5.
Lock, P.A., Jing, X., Zimmerman, R.W., Schlueter, E.M., 2002. Predicting the permeability of sandstone from image analysis of pore structure. J. Appl. Phys. 92, 6311–6319. https://doi.org/10.1063/1.1516271.
Loosveldt, H., Lafhaj, Z., Skoczylas, F., 2002. Experimental study of gas and liquid permeability of a mortar. Cem. Concr. Res. 32, 1357–1363. https://doi.org/10.1016/S0008-8846(02)00793-7.
Manley, S.S., Graeber, N., Zdenek, G., Menner, A., Hewitt, G.F., Stepanek, F., Bismarck, A., 2009. New insights into the relationship between internal phase level of emulsion templates and gas–liquid permeability of interconnected macroporous polymers. Soft Matter 5 (23), 4780–4787. https://doi.org/10.1039/B900426B.
Mason, E.A., Malinauskas, A.P., Evans, R.B., 1967. Flow and Diffusion of Gases in Porous Media. J. Chem. Phys. 46, 3199–3216. https://doi.org/10.1063/1.1841191.
Matyka, M., Khalili, A., Koza, Z., 2008. Tortuosity-porosity relation in porous media flow. Physical Review E 78. https://doi.org/10.1103/PhysRevE.78.026306.
Miguel, A.F., Serrenho, A., 2007. On the experimental evaluation of permeability in porous media using a gas flow method. J. Phys. D-Appl. Phys. 40, 6824–6828. https://doi.org/10.1088/0022-3727/40/21/050.
Millikan, R.A., 1923. Coefficients of Slip in Gases and the Law of Reflection of Molecules from the Surfaces of Solids and Liquids. Phys. Rev. 21, 217–238. https://doi.org/10.1103/PhysRev.21.217.
Mitchell, J., Chandrasekera, T.C., 2014. Understanding generalized inversions of nuclear magnetic resonance transverse relaxation time in porous media. J. Chem. Phys. 141,. https://doi.org/10.1063/1.4903311 224201.
Ovalle-Villamil, W., Sasanakul, I., 2019. Investigation of Non-Darcy Flow for Fine Grained Materials. Geotech. Geol. Eng. 37, 413–429. https://doi.org/10.1007/s10706-018-0620-x.
Radisic, M., Deen, W., Langer, R., Vunjak-Novakovic, G., 2005. Mathematical model of oxygen distribution in engineered cardiac tissue with parallel channel array perfused with culture medium containing oxygen carriers. Am. J. Physiol.-Heart Circulatory Physiol. 288, H1278–H1289. https://doi.org/10.1152/ajpheart.00787.2004.
Rigler, B., 2018. Porosity and Permeability Values - Filling the Gaps with NMR. AGS Magazine, 20–25.
Sakhaee-Pour, A., Bryant, S., 2012. Gas Permeability of Shale. SPE Reservoir Eval. Eng. 15 (04), 401–409. https://doi.org/10.2118/146944-PA.
Satterfield, C.N., Cadle, P.J., 1968. Diffusion in Commercially Manufactured Pelleted Catalysts. Ind. Eng. Chem. Process Des. Dev. 7, 256. https://doi.org/10.1021/i260026a017.
Schumacher, E.E., Ferguson, L., 1927. A convenient apparatus for measuring the diffusion of gases and vapors through membranes. J. Am. Chem. Soc. 49, 427–428. https://doi.org/10.1021/ja01401a013.
Sing, K.S.W., 2004. Characterization of porous materials: past, present and future. Colloids and Surfaces A Physicochemical and Engineering Aspects 241, 3–7. https://doi.org/10.1016/j.colsurfa.2004.04.003.
Song, W., Yao, J., Li, Y., Sun, H., Zhang, L., Yang, Y., Zhao, J., Sui, H., 2016. Apparent gas permeability in an organic-rich shale reservoir. Fuel 181, 973–984. https://doi.org/10.1016/j.fuel.2016.05.011.
Spearing, M., Matthews, G.P., 1991. Modelling Characteristic Properties of Sandstones. Transp. Porous Media 6, 71–90. https://doi.org/10.1007/BF00136822.
Tanikawa, W., Shimamoto, T., 2006. Klinkenberg effect for gas permeability and its comparison to water permeability for porous sedimentary rocks. Hydrol. Earth Syst. Sci. Discuss. 2006, 1315–1338. https://doi.org/10.5194/hessd-3-1315-2006.
van Brakel, J., Modrý, S., Svatá, M., 1981. Mercury porosimetry: state of the art. Powder Technol. 29, 1–12. https://doi.org/10.1016/0032-5910(81)85001-2.
Wakao, N., Smith, J.M., 1962. Diffusion in Catalyst Pellets. Chem. Eng. Sci. 17, 825–834. https://doi.org/10.1016/0009-2509(62)87015-8.
Wang, R., Mair, R.W., Rosen, M.S., Cory, D.G., Walsworth, R.L., 2004. Simultaneous measurement of rock permeability and effective porosity using laser-polarized noble gas NMR. Phys Rev E Stat Nonlin Soft Matter Phys 70,. https://doi.org/10.1103/PhysRevE.70.026312 026312.
Wei, D.F., Liu, X.P., Hu, X.X., 2013. Applicability of Classical Permeability Estimation Models Based on NMR Logging in Tight Sandstones. Adv. Mater. Res. 772, 814–818. https://doi.org/10.4028/www.scientific.net/AMR.772.814.
Weisz, P.B., Schwartz, A.B., 1962. Diffusivity of Porous-Oxide-Gel Derived Catalyst Particles. J. Catal. 1, 399–406. https://doi.org/10.1016/0021-9517(62)90090-8.
Wilkes, J.O., 2006. Fluid Friction in Pipes, Fluid Mechanics for Chemical Engineers. Pearson Education, pp. 126–134.
Wyckoff, R.D., Botset, H.G., Muskat, M., Reed, D.W., 1933. The measurement of the permeability of porous media for homogeneous fluids. Rev. Sci. Instrum. 4, 394–405. https://doi.org/10.1063/1.1749155.
You, L., Xue, K., Kang, Y., Liao, Y., Kong, L., 2013. Pore Structure and Limit Pressure of Gas Slippage Effect in Tight Sandstone. Sci. World J. 2013, 7. https://doi.org/10.1155/2013/572140.
Youngquist, G.R., 1970. Diffusion and Flow of Gases in Porous Solids. Ind. Eng. Chem. 62, 52. https://doi.org/10.1021/ie50728a006.
Zhan, X., Zhu, Z., Nafi Toksöz, M., 2011. Quantitative DC and high frequency AC seismoelectric measurement on Berea sandstone. SEG Technical Program Expanded Abstracts. https://doi.org/10.1190/1.3627655.
Ziarani, A.S., Aguilera, R., 2011. Knudsen's Permeability Correction for Tight Porous Media. Transp. Porous Media 91, 239–260. https://doi.org/10.1007/s11242-011-9842-6.

Supplementary information for

An integrated method for measuring gas permeability and diffusivity of porous solids

Shu San Manley[a], Patrick Steindl[b], Geoffrey F. Hewitt[a†] and Alexander Bismarck[a, b*]

[a]Department of Chemical Engineering, Imperial College London, South Kensington Campus, London, SW7 2AZ, UK.

[b]Polymer and Composite Engineering (PaCE) Group, Institute of Materials Chemistry and Research, University of Vienna, Währinger Strasse 42, 1090 Vienna, Austria

[*]Corresponding author email: alexander.bismarck@univie.ac.at

Content supplementary information:

S.1	Fitting procedure for transient diffusion measurements	p.2
Figure S.1	Gas permeability of shale	p.8
Figure S.2	Forchheimer plot	p.8
Figure S.3	CAD drawing of the gas permeability & diffusivity apparatus	p.9
Figure S.4 a-g	C vs. G plots of samples S2-S8	p.10
Figure S.5 a-g	Microscope images of the sandstone samples	p.14
Table S.1	Uncertainty analysis of the apparatus for both operating modes	p.16

S.1: Fitting procedure for transient diffusion measurements

Raw data files (**Figure A.1**) contain the data collected using the software *MaddClient*: **CONCENTRATION OF O_2** in the N_2 efflux stream and the **TIME.**

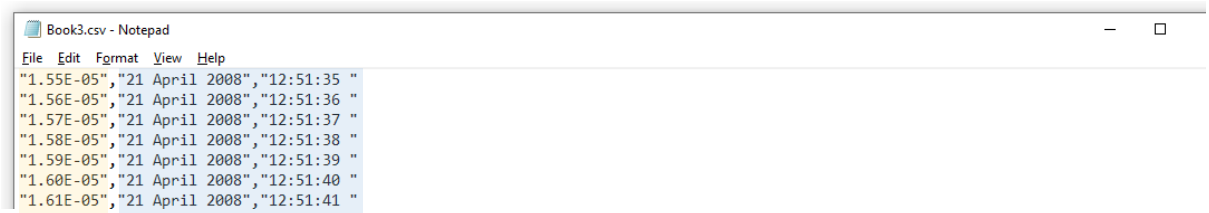

Figure A.1: structure of an input file: on the left hand side the O_2 concentration, on the right one the time.

After import into a spreadsheet software (e.g. Microsoft Excel), the data needs to be prepared for analysis (**Figure A.2**):

- conversion of the time data into the actual measurement time (in seconds) by subtracting t_0 from all other values (t_1-t_0, t_2-t_0,…)
- multiplication of the concentration data
  - by 10^2 to obtain the O_2 content in the N_2 purge stream in *%*
  - by 10^6 to get the O_2 concentration in *ppm by volume*

t / [s]	c_{input}
1	1.55E-05
2	1.56E-05
3	1.58E-05
4	1.58E-05
5	1.59E-05
6	1.59E-05
7	1.60E-05
8	1.62E-05
⋮	⋮

x 10^2

x 10^6

c / [%]	c / [ppm]
1.55E-03	1.55E+01
1.56E-03	1.56E+01
1.58E-03	1.58E+01
1.58E-03	1.58E+01
1.59E-03	1.59E+01
1.59E-03	1.59E+01
1.60E-03	1.60E+01
1.62E-03	1.62E+01
⋮	⋮

Figure A.2: The input data needs to be processed before it can be used for further evaluation.

Concentration (either in *%* or *ppm*) is plotted against time (**Figure A.3**). From this plot, the final equilibrium concentration of O_2 after diffusing through the porous medium, $c_{O\text{-}N}$, can be determined. The corresponding value in c_{input} is subsequently used to calculate the O_2 concentration as a fraction F of the equilibrium value: $c_{input} / c_{O\text{-}N,\ input}$ (**Figure A.4**).

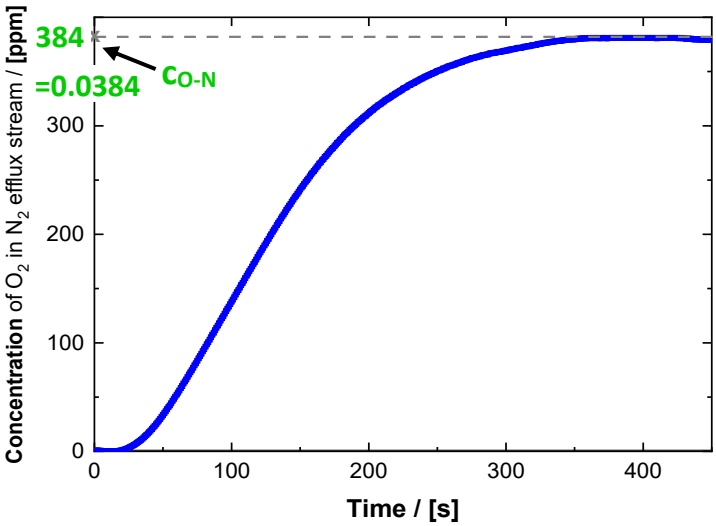

Figure A.3: The equilibrium concentration of O_2 in the N_2 outlet flow, $c_{O\text{-}N}$, can be extracted from a concentration vs. time plot.

⋮	⋮
400	**3.84E-04**

$c_{O\text{-}N,input}$

⋮	⋮
3.84E-02	**3.84E+02**

$c_{O\text{-}N}$

t / [s]	c_{input}		Fraction F
1	1.55E-05	: 3.84E-04	0.0405
2	1.56E-05	: $c_{O\text{-}N,input}$	0.0407
3	1.58E-05		0.0412
4	1.58E-05		0.0412
6	1.59E-05		0.0414
7	1.60E-05		0.0416
8	1.62E-05		0.0423
⋮	⋮		⋮
400	**3.84E-04**		**1.0000**

Figure A.4: O_2 concentration as fraction of the equilibrium value is obtained after dividing c_{input} by $c_{O\text{-}N}$.

L_{eff} can be estimated by fitting calculated, theoretical values to experimental data. In **Eq. A.1**, D_{AB} is a constant for the gas pair O_2 – N_2, L_{eff} is the parameter of interest and a set of values for F is given, which leaves only t. Theoretical values of F as a function of the dimensionless group $\left(D_{AB}t/L_{eff}^2\right)$ can be obtained by iteratively solving **Eq. A.1** and arranging the results in form of a matrix (**Table A.1**) or simply in two columns (**Figure A.5**), which is more convenient in this case. **Table A.1** must be read as mathematical table, which means the column headings add one decimal to the value of the expression of interest from one of the row headings (e.g. 0.33 corresponds to F = 0.9230).

$$F = \frac{(c_{O-N})_t}{(c_{O-N})_{t=\infty}} = 1 - 2\sum_{n=1}^{\infty} cos\, n\pi\, exp\left(-n^2\pi^2 \frac{\boldsymbol{D_{AB}t}}{\boldsymbol{L_{eff}^2}}\right) \quad \text{(A.1)}$$

Table A.1: Theoretically calculated values of F (in the matrix of the table) as a function of $\left(\boldsymbol{D_{AB}t/L_{eff}^2}\right)$.

$\left(\frac{D_{AB}t}{L_{eff}^2}\right)$	**0.00**	**0.01**	**0.02**	**0.03**	**0.04**	**0.05**	**0.06**	**0.07**	**0.08**	**0.09**	**0.10**
0.0	0.00000	0.00000	0.00003	0.00157	0.01089	0.03400	0.07142	0.11991	0.17528	0.23386	0.29290
0.1	0.29290	0.35053	0.40559	0.45741	0.50567	0.55028	0.59131	0.62888	0.66319	0.69446	0.72292
0.2	0.72292	0.74879	0.77228	0.79361	0.81295	0.83049	0.84640	0.86082	0.87389	0.88573	0.89647
0.3	0.89647	0.90619	0.91501	0.92299	0.93023	0.93023	0.93679	**0.94811**	**0.95299**	0.95740	0.96141
0.4	0.96141	0.96503	0.96832	0.97130	0.97400	0.97644	0.98066	0.98066	0.98248	0.98412	0.98562
0.5	0.98562	0.98697	0.98819	0.98930	0.99031	0.99122	0.99204	0.99279	0.99347	0.99408	0.99464
0.6	0.99464	0.99514	0.99560	0.99601	0.99639	0.99673	0.99703	0.99731	0.99757	0.99779	0.99800
0.7	0.99800	0.99819	0.99836	0.99851	0.99865	0.99878	0.99889	0.99900	0.99909	0.99918	0.99926
0.8	0.99926	0.99933	0.99939	0.99934	0.99950	0.99955	0.99959	0.99963	0.99966	0.99969	0.99972
0.9	0.99972	0.99965	0.99972	0.99965	0.99977	0.99979	0.99981	0.99983	0.99985	0.99986	0.99990
1.0	0.99990	0.99991	0.99992	0.99992	0.99993	0.99994	0.99995	0.99995	0.99995	0.99996	0.99996
1.1	0.99996	0.99997	0.99997	0.99997	0.99997	0.99998	0.99998	0.99998	0.99998	0.99998	0.99999
1.2	0.99999	0.99999	0.99999	0.99999	0.99999	0.99999	0.99999	0.99999	0.99999	0.99999	0.99999
1.3	1.00000	1.00000	1.00000	1.00000	1.00000	1.00000	1.00000	1.00000	1.00000	1.00000	1.00000

The fractions in F_{fit} can be chosen freely but are ideally evenly distributed over the whole range from

0 to 1. The numbers from F_{fit} and F_{table} are compared the two values which enclose it are determined (**Figure A.5**). Interpolation between the two corresponding time designations gives $\left(D_{AB}t/L_{eff}^2\right)$. A general formula for interpolation is given in **Eq. A.2**; its use is demonstrated in **Eq. A.2a** for F=0.95.

$$\frac{D_{AB}t}{L_{eff}^2} = \frac{(x - x_1)}{(x_2 - x_1)}(y_2 - y_1) + y_1 \quad \text{(A.2)}$$

$$\left(\frac{D_{AB}t}{L_{eff}^2}\right)_{F=0.95} = \frac{(0.95 - 0.94811)}{(0.95299 - 0.94811)}(0.38 - 0.37) + 0.37 = \mathbf{0.373873} \quad \text{(A.2a)}$$

Each value of F_{fit} is compared with the ones calculated from experiments in column *Fraction F* (**Figure A.6**), the time of the best match is inserted as t_{exp}. The fitting parameter *X* can now be calculated as the quotient of $\left(D_{AB}t/L_{eff}^2\right)$ and t_{exp}:

$$\frac{\left(\frac{D_{AB}t}{L_{eff}^2}\right)}{t_{exp}} = X \quad \rightarrow \quad t_{calc,table} = \frac{\left(\frac{D_{AB}t}{L_{eff}^2}\right)}{X} \tag{A.3}$$

	F_{table}	$(D_{AB}t/L_{eff}^2)_{table}$			F_{fit}	$D_{AB}t/L_{eff}^2$	t_{exp}	X
	0.00000	0.00		x	0.95	0.373873		
	⋮	⋮			0.90			
	0.94273	0.36			0.85			
x_1	**0.94811**	**0.37**	y_1		0.80			
x_2	**0.95299**	**0.38**	y_2		0.75			
	0.95740	0.39						
	⋮	⋮						
	1.00000	> 1.3						

Figure A.5: The dimensionless group $\left(D_{AB}t/L_{eff}^2\right)$ is calculated by interpolation of two tabulated values.

t / [s]	Fraction F
0	0.000000
⋮	⋮
176	0.741739
177	0.745915
178	0.748890
179	0.752875
180	0.756262
181	0.759741
⋮	⋮
	1.000000

F_{fit}	$D_{AB}t/L_{eff}^2$	t_{exp}	X
0.95	0.373873		
0.90	0.303632		
0.85	0.262497		
0.80	0.233304		
0.75	0.210515	178	**0.00118**
0.74	0.206602		
0.73	0.202737		
0.72	0.198974		
0.71	0.195460		
0.70	0.191947		

Figure A.6: t_{exp} is evaluated from comparison with experimental data; afterwards it is possible to calculate the fitting parameter *X*.

The calculation of *X* finally allows to determine the time values $t_{calc,table}$ corresponding to F_{calc} (**Eq.A.3**, **Figure A.7**). The quality of the fit becomes clearer when *F vs. t* and F_{table} *vs.* $t_{calc,table}$ are plotted. If the result is not satisfying, i.e. when the curve of the theoretical values deviates drastically from the curve created from experimental data, then other *X*'s have to be tried, until a good fit is obtained (**Figure A.8**). The *X* resulting in the best fit is used to calculate first effective pore length L_{eff} and then tortuosity (**Eq.A.4 & A.5**).

F_{fit}	$D_{AB}t/L_{eff}^2$	t_{exp}	X
0.95	0.373873	275	0.00136
0.90	0.303632	238	0.00128
0.85	0.262497	213	0.00123
0.80	0.233304	194	0.00120
0.75	0.210515	178	**0.00118**
⋮	⋮	⋮	⋮
0.45	0.128570	115	0.00112
0.40	0.118985	107	0.00111
0.35	0.109908	98	0.00112
0.30	0.101232	89	0.00114
0.25	0.092734	80	0.00116
0.20	0.084220	72	0.00117
0.15	0.075434	63	0.00120
0.10	0.135612	53	0.00256

$t_{calc,table}$	F_{table}	$(D_{AB}t/L_{eff}^2)_{table}$
0.0	0.00000	0.00
8.5	0.00000	0.01
16.9	0.00003	0.02
25.4	0.00157	0.03
33.8	0.01089	0.04
42.3	0.03400	0.05
50.7	0.07142	0.06
59.2	0.11991	0.07
67.6	0.17528	0.08
76.1	0.23386	0.09
84.6	0.29290	0.10
93.0	0.35053	0.11
101.5	0.40559	0.12
⋮	⋮	⋮

Figure A.7: Only one value of *X* is necessary for the calculation of one set of $t_{calc,table}$.

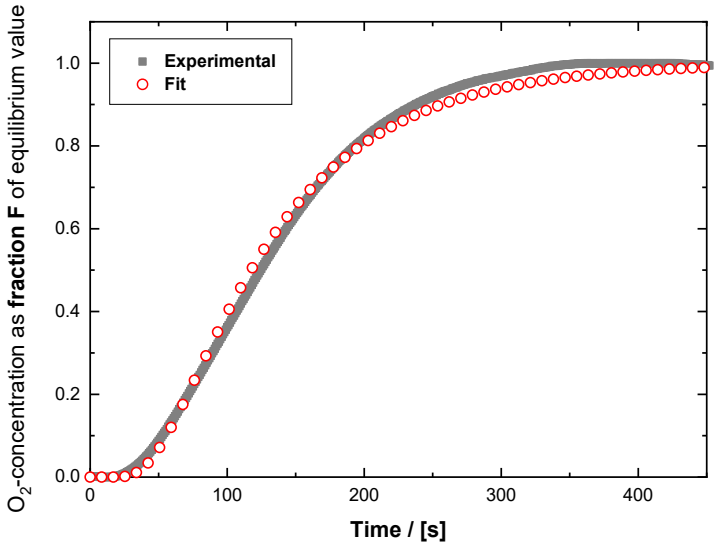

Figure A.8: A good fit of the theoretically calculated values to the experimental data.

$$\frac{D_{AB}}{L_{eff}^2} = X \rightarrow \boldsymbol{L_{eff}} = \sqrt{\frac{\boldsymbol{D_{AB}}}{\boldsymbol{X}}} \tag{A.4}$$

$$\boldsymbol{\tau} = \frac{\boldsymbol{L_{eff}}}{\boldsymbol{L}} \tag{A.5}$$

input		1.			2.		8.	3.		4.	5.	6.	7.
t / [s]	c	c / [%]	c / [ppm]	t / [s]	Fraction F		t_{calc}	F_{table}	$D_{AB}t/L_{eff}^2$	F_{fit}	$D_{AB}t/L_{eff}^2$	t_{exp}	X
1	1.55E-05	1.55E-03	1.55E+01	0	0.00002		0.0	0.00000	0.00	0.95	0.373873	275	0.00136
2	1.56E-05	1.56E-03	1.56E+01	1	0.00020		8.5	0.00000	0.01	0.90	0.303632	238	0.00128
3	1.58E-05	1.58E-03	1.58E+01	2	0.00042		16.9	0.00003	0.02	0.85	0.262497	213	0.00123
4	1.58E-05	1.58E-03	1.58E+01	3	0.00075		25.4	0.00157	0.03	0.80	0.233304	194	0.00120
5	1.59E-05	1.59E-03	1.59E+01	4	0.00121		33.8	0.01089	0.04	0.75	0.210515	178	0.00118
6	1.59E-05	1.59E-03	1.59E+01	5	0.00182		42.3	0.03400	0.05	0.74	0.206602	176	0.00117
7	1.60E-05	1.60E-03	1.60E+01	6	0.00255		50.7	0.07142	0.06	0.73	0.202737	173	0.00117
8	1.62E-05	1.62E-03	1.62E+01	7	0.00343		59.2	0.11991	0.07	0.72	0.198974	170	0.00117
⋮	⋮	⋮	⋮	8	0.00447		67.6	0.17528	0.08	0.71	0.195460	168	0.00116
				⋮	⋮		76.1	0.23386	0.09	0.70	0.191947	165	0.00116
							84.6	0.29290	0.10	0.65	0.175622	154	0.00114
							93.0	0.35053	0.11	0.60	0.162313	143	0.00114
							101.5	0.40559	0.12	0.55	0.149937	134	0.00112
							⋮	⋮	⋮	0.50	0.138825	124	0.00112
										0.45	0.128570	115	0.00112
										0.40	0.118985	107	0.00111
										0.35	0.109908	98	0.00112
										0.30	0.101232	89	0.00114
										0.25	0.092734	80	0.00116
										0.20	0.084220	72	0.00117
										0.15	0.075434	63	0.00120
										0.10	0.135612	53	0.00256

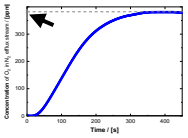

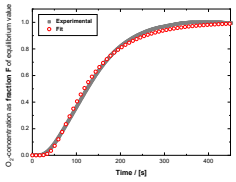

input, fixed values
calculated values
from table
from comparison with experimental data

Figure A.9: Overview over the entire fitting process

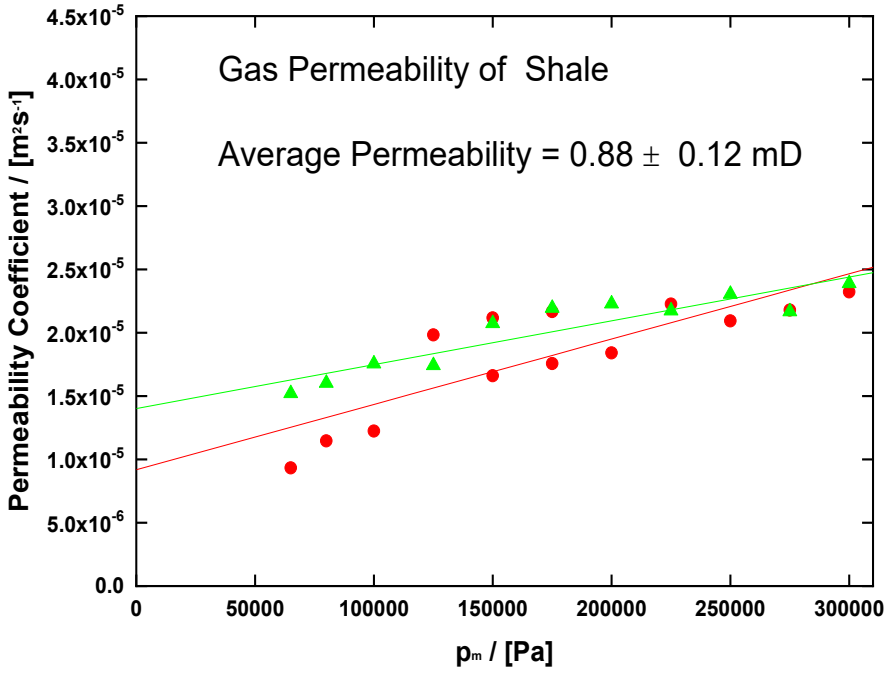

Figure S.1: Permeability coefficient as a function of mean pressure for shale

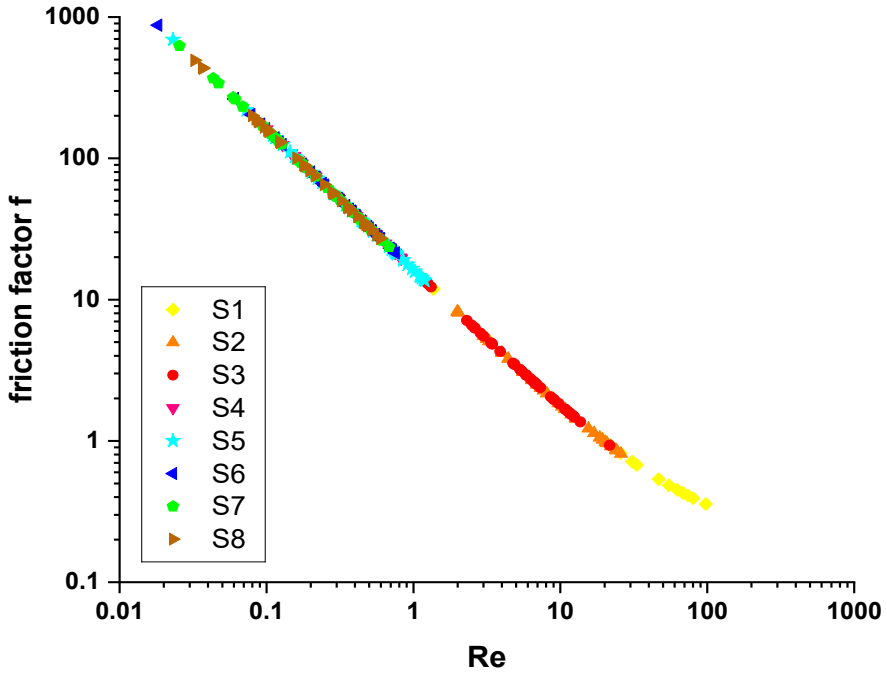

Figure S.2: Forchheimer plot - the fluid flow in most measurements was clearly in the Darcy regime; slight deviations from the linear behaviour, indicating the Dupuit-Forchheimer regime, could only be observed for samples S1 and S2.

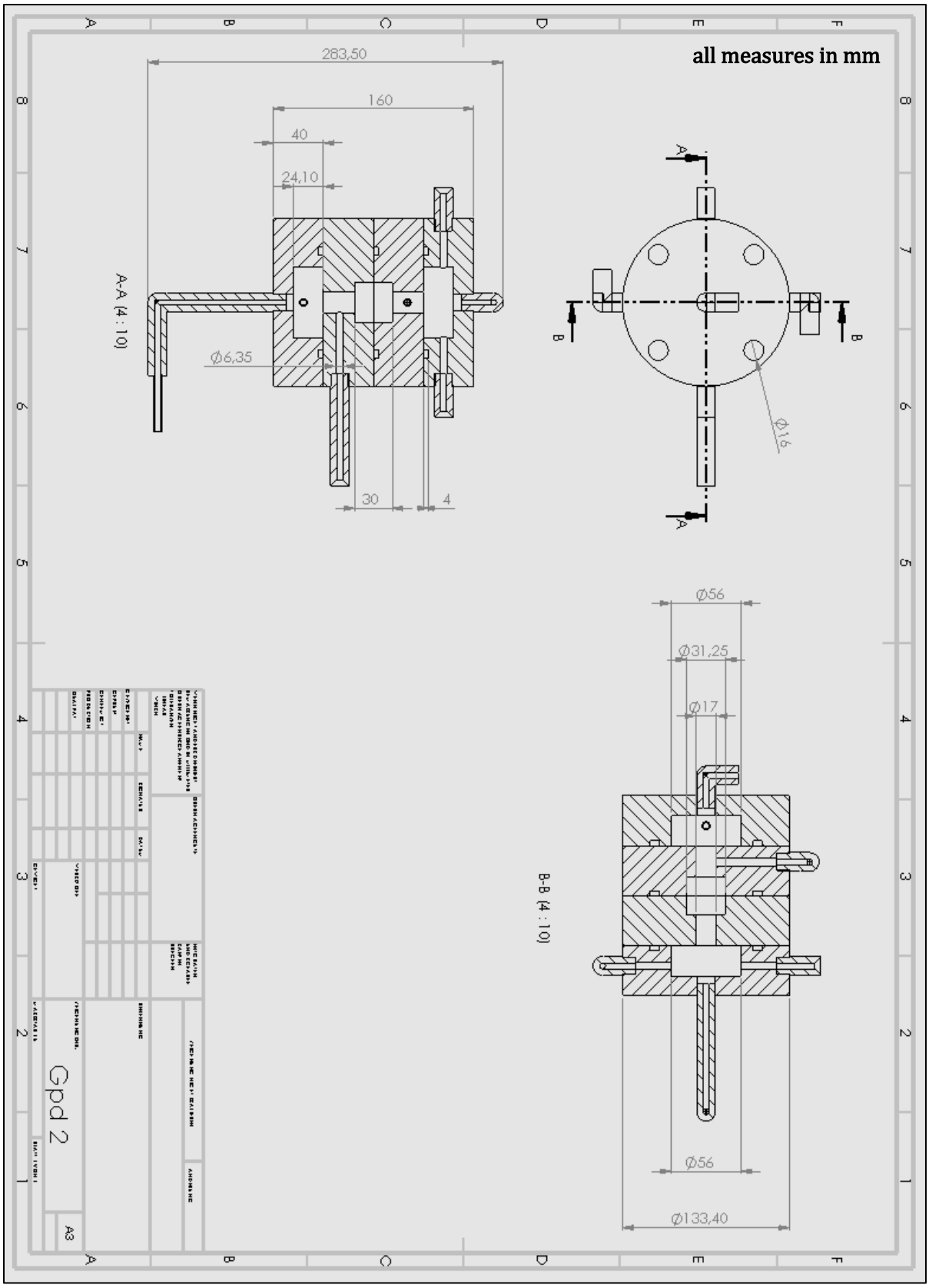

Figure S.3: CAD drawing of the integrated gas permeability and diffusivity apparatus.

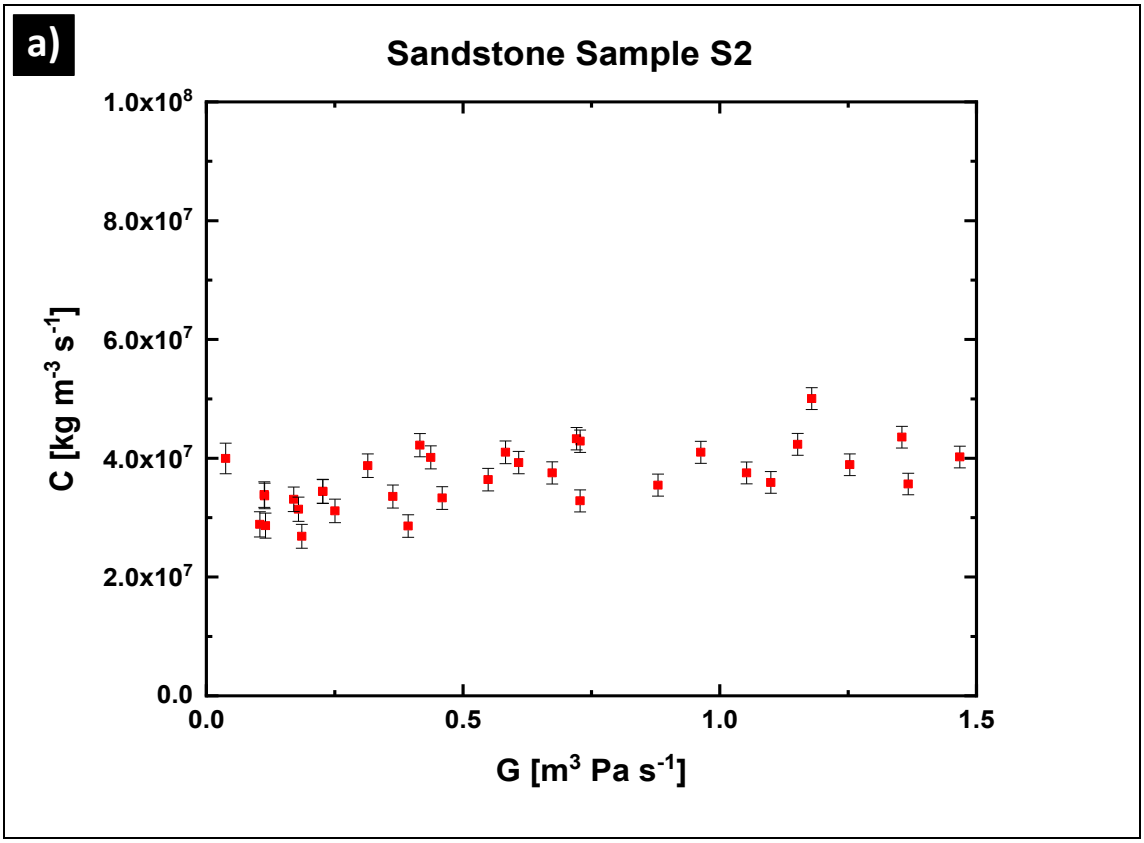
a)
Sandstone Sample S2
1.0x10^8
8.0x10^7
6.0x10^7
4.0x10^7
2.0x10^7
0.0
C [kg m^-3 s^-1]
0.0
0.5
1.0
1.5
G [m^3 Pa s^-1]

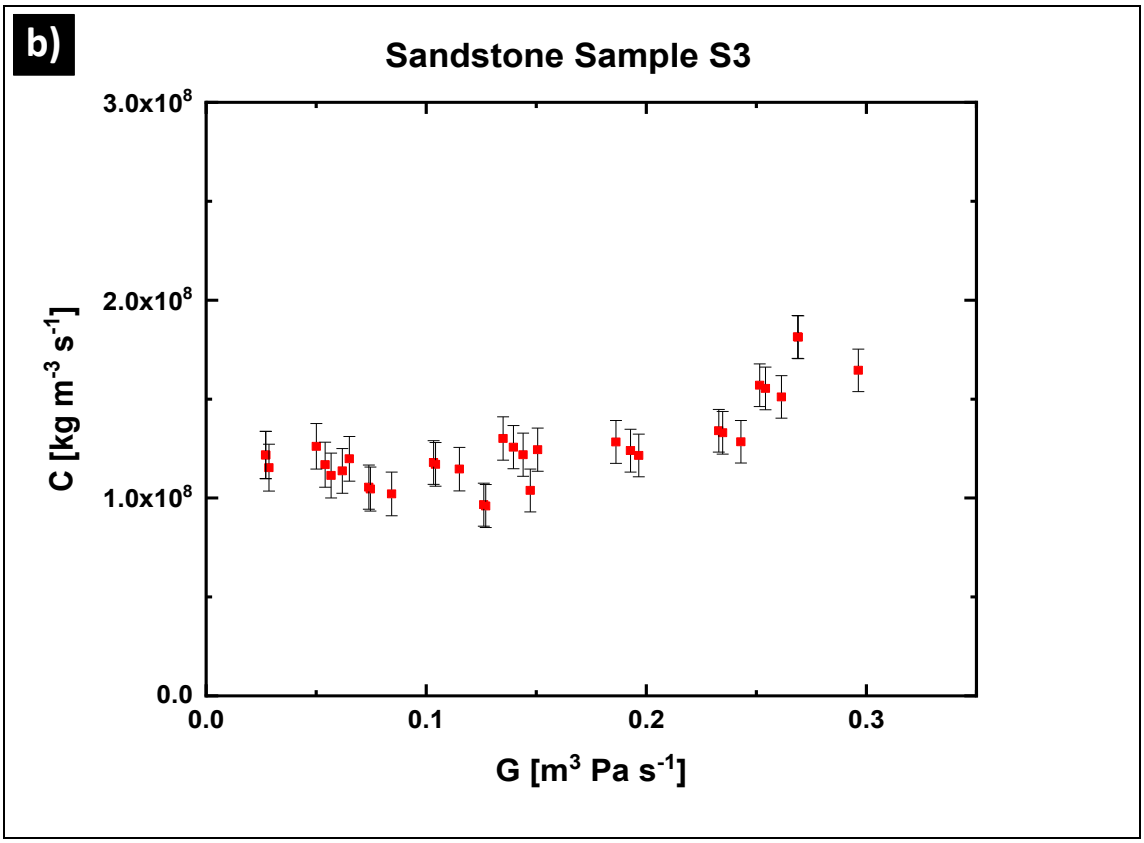
b)
Sandstone Sample S3
3.0x10^8
2.0x10^8
1.0x10^8
0.0
C [kg m^-3 s^-1]
0.0
0.1
0.2
0.3
G [m^3 Pa s^-1]

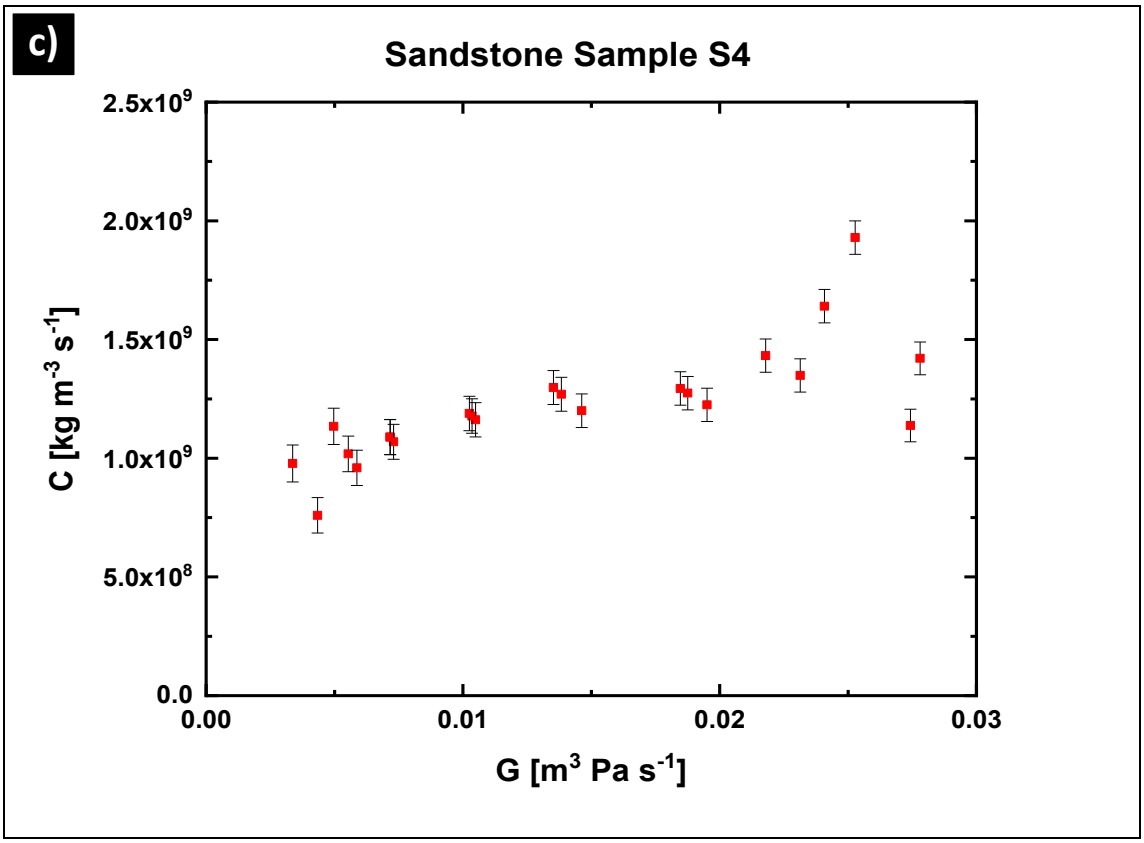
c)
Sandstone Sample S4
2.5x10^9
2.0x10^9
1.5x10^9
1.0x10^9
5.0x10^8
0.0
C [kg m^-3 s^-1]
0.00
0.01
0.02
0.03
G [m^3 Pa s^-1]

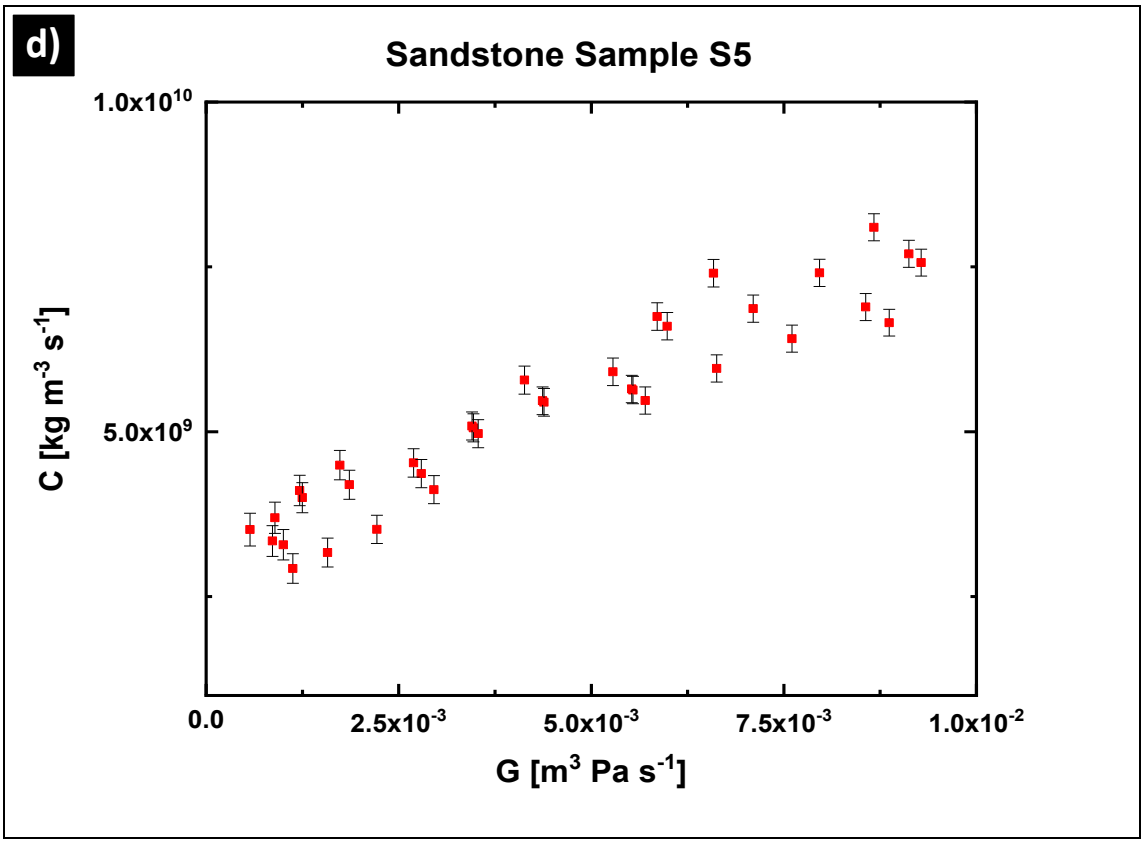
d)
Sandstone Sample S5
1.0x10^10
5.0x10^9
C [kg m^-3 s^-1]
0.0
2.5x10^-3
5.0x10^-3
7.5x10^-3
1.0x10^-2
G [m^3 Pa s^-1]

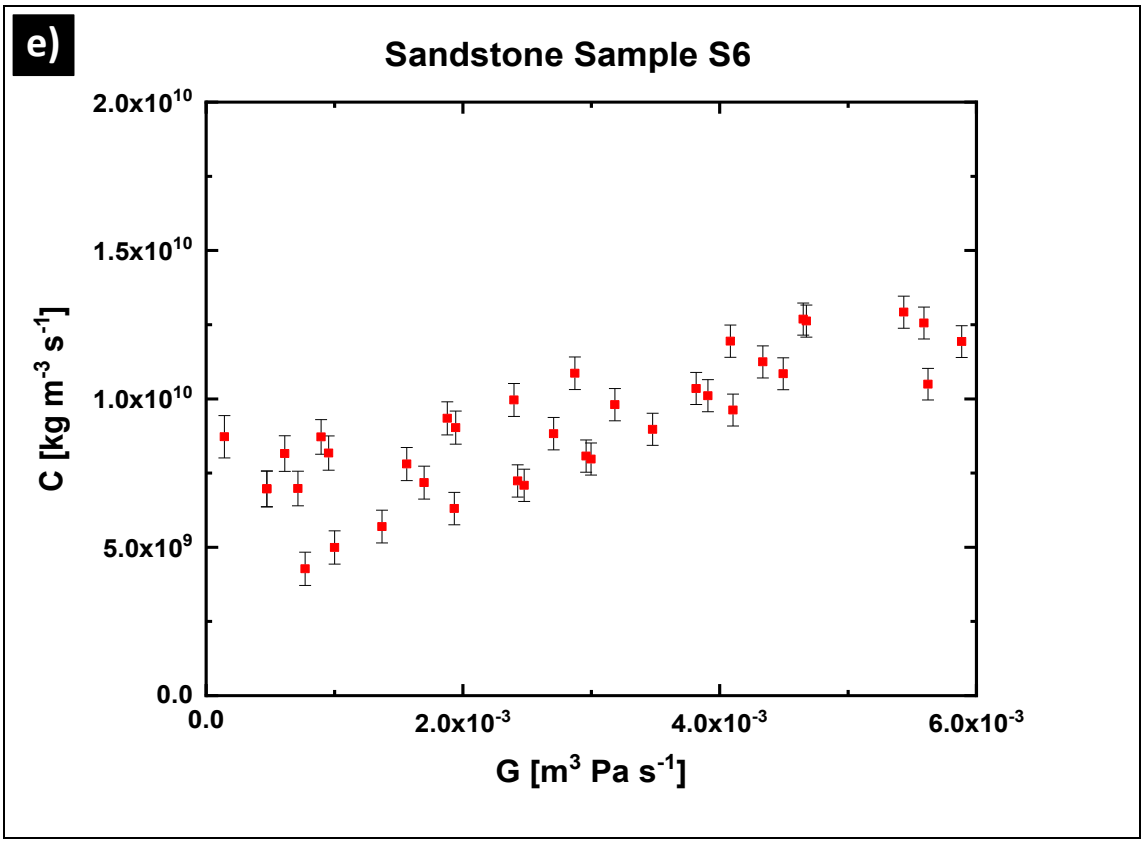
e)
Sandstone Sample S6
2.0x10^10
1.5x10^10
1.0x10^10
5.0x10^9
0.0
C [kg m^-3 s^-1]
0.0
2.0x10^-3
4.0x10^-3
6.0x10^-3
G [m^3 Pa s^-1]

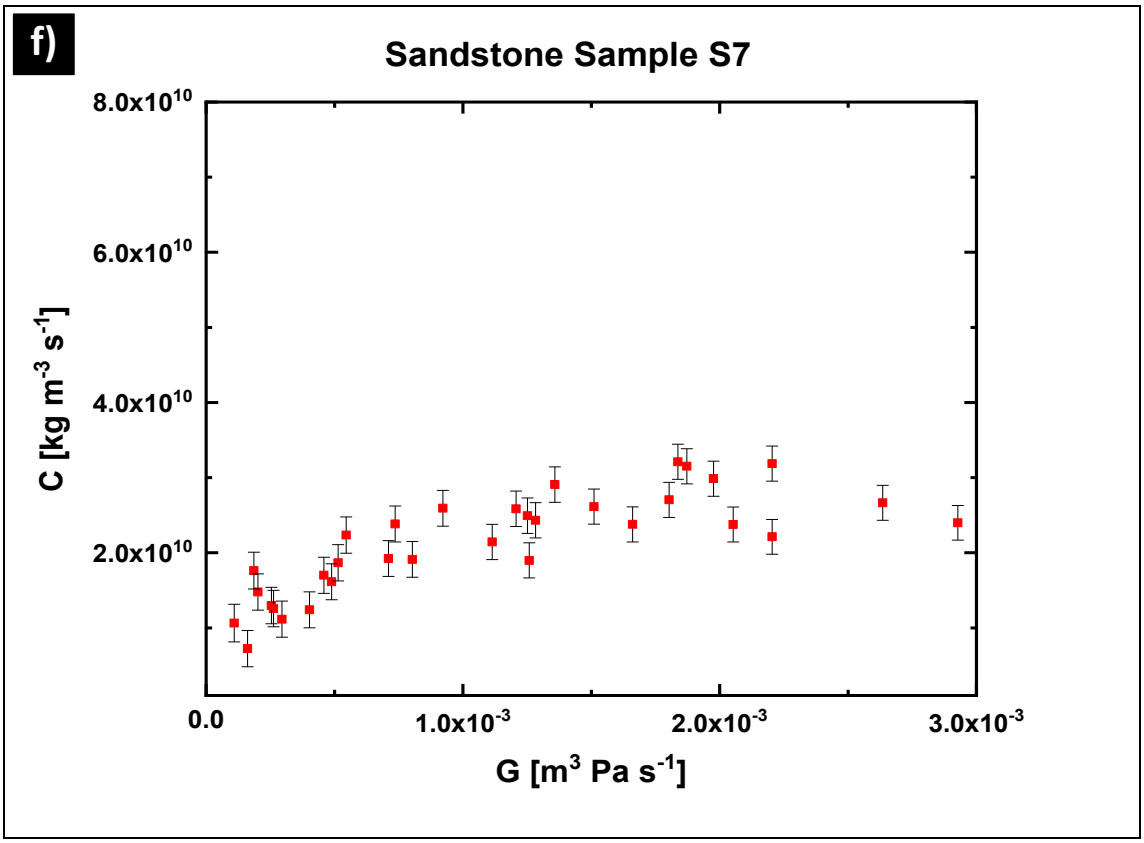
f)
Sandstone Sample S7
8.0x10^10
6.0x10^10
4.0x10^10
2.0x10^10
C [kg m^-3 s^-1]
0.0
1.0x10^-3
2.0x10^-3
3.0x10^-3
G [m^3 Pa s^-1]

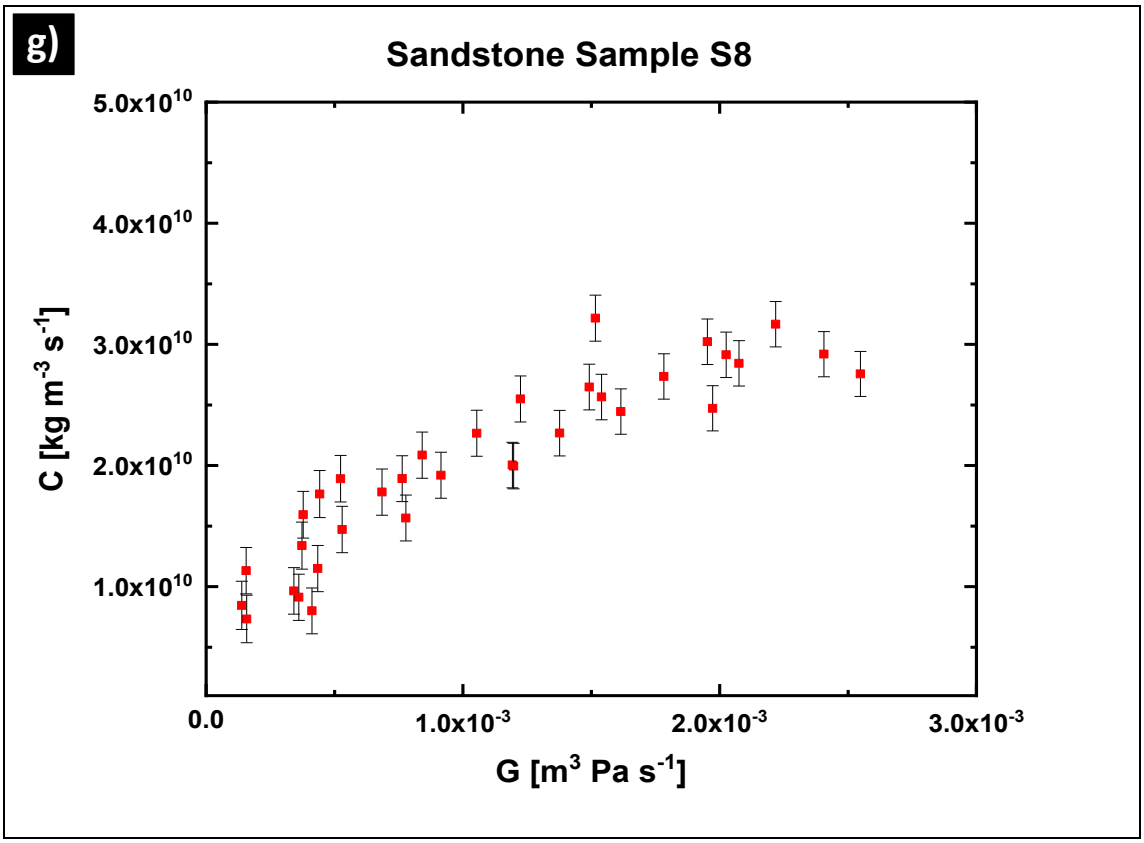

Figure S.4 a-g: Linear plots of C vs. G for sandstone samples S2-S8

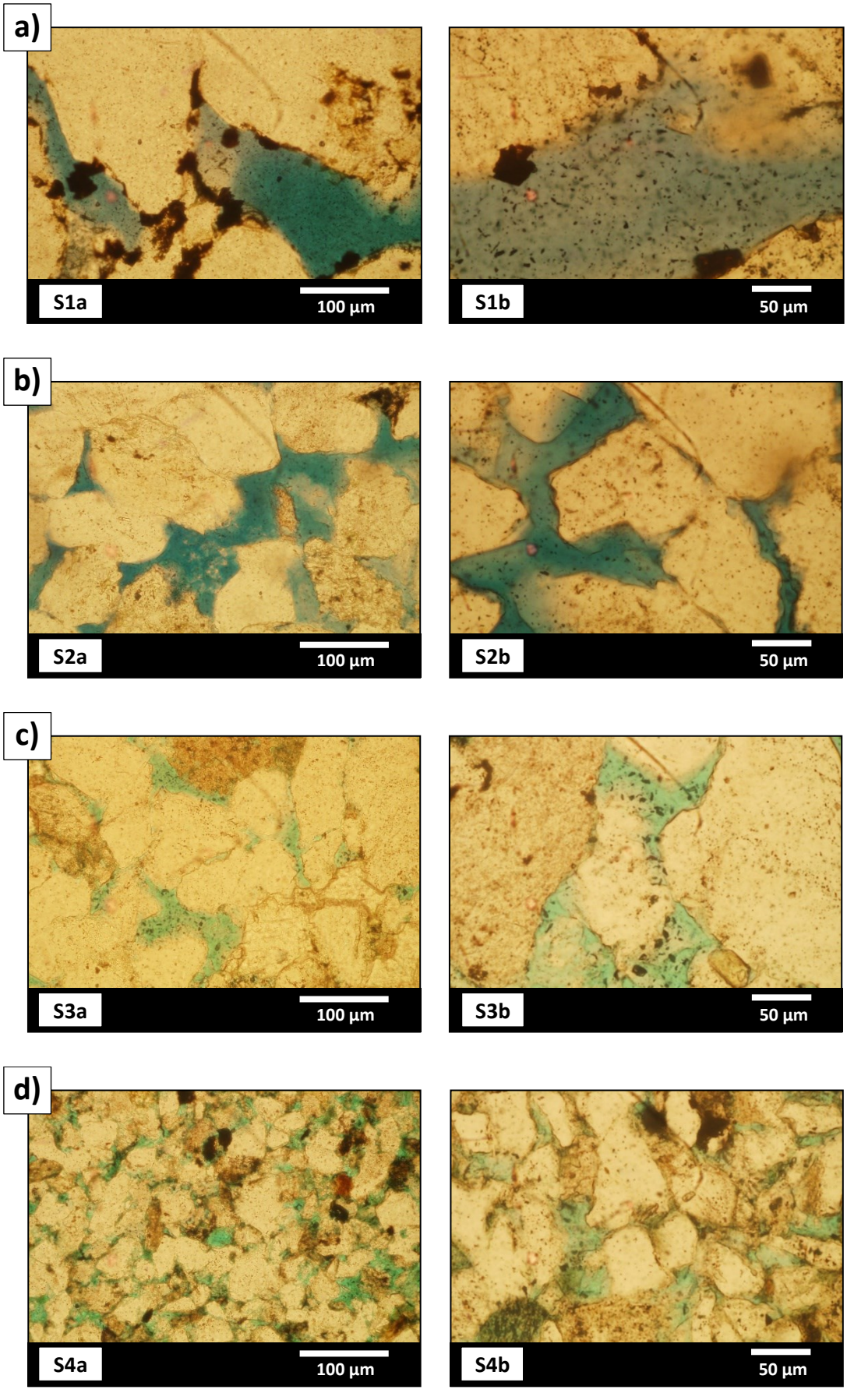
a)
S1a
100 µm
S1b
50 µm
b)
S2a
100 µm
S2b
50 µm
c)
S3a
100 µm
S3b
50 µm
d)
S4a
100 µm
S4b
50 µm

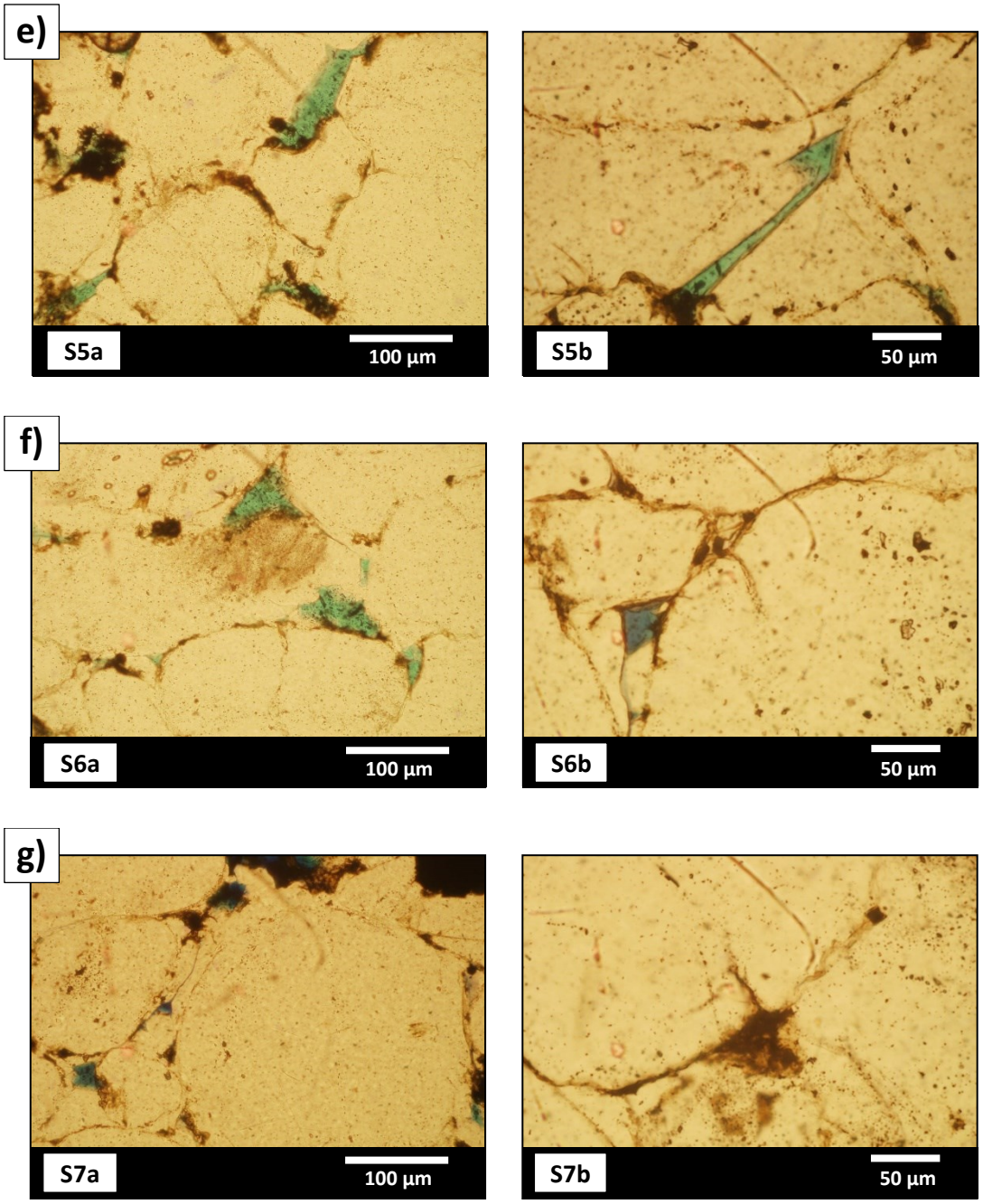

Figure S.5 a-g: Characteristic microscope images of sandstone samples S1-S7

Table S.2: Uncertainty analysis of both a) gas permeability and b) diffusivity measurements.

a) Gaspermeability	symbol	parameter	SI units	value	uncertainty	rel. uncertainty (%)
	p_1	inlet pressure	Pa = kg m s^{-2}			0.2%
	p_2	outlet pressure	Pa = kg m s^{-2}			0.2%
	t	time	s			0.5%
	D	sample diameter	m	1.30E-02	5.00E-04	4%
	r	sample radius	m	6.50E-03	2.50E-04	4%
	A	cross-section area sample	m^2	1.33E-04	1.02E-05	8%
	V_{small}	volume small vessel	m^3	2.40E-04	1.00E-06	0.4%
	V_{large}	volume large vessel	m^3	1.97E-03	1.00E-06	0.1%
	V_s	sample volume	m^3	3.32E-06	2.64E-07	8%
	L	sample length	m	2.50E-02	5.00E-04	2%
	T	temperature	K	290	1	0.3%
	R	ideal gas constant	kg m^2 s^{-2} mol^{-1} K^{-1}	8.3145	-	-
	μ (N_2)	viscosity nitrogen (fluid)	Pa s = kg m s^{-1}	1.75E-05	1.75E-06	10%
	M (N_2)	molecular mass nitrogen	kg mol^{-1}	2.80E-02	-	-
						13%

b) Diffusivity	symbol	parameter	SI units	value	uncertainty	rel. uncertainty (%)
	A	cross-section area sample	m^2	1.33E-04	1.02E-05	8%
	L	sample length	m	2.50E-02	5.00E-04	2%
	t	time	s			0.5%
	D_{AB}	binary diffusion coefficient O_2-N_2	m^2 s^{-1}	1.81E-05	-	0.6%
	M (O_2)	molecular mass oxygen	kg mol^{-1}	3.20E+01	-	-
	M (N_2)	molecular mass nitrogen	kg mol^{-1}	2.80E-02	-	-
	T	temperature	K	2.90E+02	1	0.3%
	R	gas constant	kg m^2 s^{-2} mol^{-1} K^{-1}	8.31E+00	-	-
	Q_N	N^2 flow rate over N_2-rich end	[m^3 s^{-1}]			0.2%
	c_O	oxygen concentration in N_2 purge stream	ppm by volume			0.2%
						8%

Paper II (*published*)

Permeable emulsion-templated porous polyepoxides. *Steindl, P.*; Menner, A.; Bismarck, A. Polymer, 2022, 240, article 124476

Polymer 240 (2022) 124476

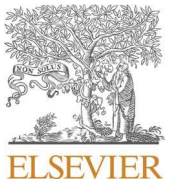

Contents lists available at ScienceDirect

Polymer

journal homepage: www.elsevier.com/locate/polymer

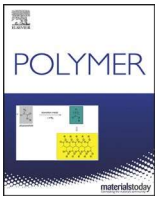

Permeable emulsion-templated porous polyepoxides

Patrick Steindl [a], Angelika Menner [a], Alexander Bismarck [a,b,*]

[a] Polymer and Composite Engineering (PaCE) Group, Institute of Materials Chemistry and Research, University of Vienna, Währinger Strasse 42, 1090, Vienna, Austria
[b] Department of Chemical Engineering, Imperial College London, South Kensington Campus, London, SW7 2AZ, UK

ARTICLE INFO

Keywords:
Emulsion templating
Epoxy foams
Polyepoxide
Gas permeability
Compression properties

ABSTRACT

Porous polyepoxides are attractive materials for a range of applications. Liquid foam precursors can be net-shaped by moulding. We report preparation of permeable polyepoxide, Araldite®2020, foams with porosities in the range of 45–60% from surfactant-stabilised W/O medium internal phase emulsion templates. Alteration of internal phase volume ratio and surfactant concentration were used to tailor the properties of the resulting polyMIPEs. These polyepoxide foams had elastic moduli in the range of 60–200 MPa and compression strengths between 2 and 6.5 MPa with permeabilities up to 200 mD. The theoretical average molecular weight between crosslinks was 534 g mol^{-1}, while the foams had 500 ± 50 g mol^{-1}. Swelling tests confirmed the excellent chemical stability of the porous epoxy. However, the swelling ratio depended on the polarity of the solvents used. It decreased with decreasing solvent polarity.

1. Introduction

Epoxy foams enjoy high popularity, mainly driven by their excellent weight-to-performance ratio and their versatility, combining the wide range of properties of epoxides with the advantages of porous materials. Epoxy resins are known for high stiffness, high dimensional, thermal and chemical stability, dielectric properties and good adhesion [1–4], while porous materials are attractive because of their low density as well as thermal and acoustic insulation, and shock absorption [5,6]. These features make epoxy foams attractive for applications in packaging, sealing and as adhesives or cores in composite sandwich structures [7,8] or when filled with a liquid electrolyte as matrix for structural composite energy storage devices [9].

Epoxy foams are conventionally prepared by chemical and physical blowing [10]. Chemical or physical blowing agents are mixed with an epoxy formulation, including resin and hardener, as well as other additives. Chemical blowing agents generate gas upon a chemical reaction [11–19], while physical blowing agents [20–23] (usually low boiling point chemicals, such as hexane) gasify upon heating; the gas froths the epoxy formulations into stable liquid foams, which result after curing in solid epoxide foams. In this case to control the foaming behaviour it is sometimes necessary to pre-cure the epoxy resin to adjust its viscosity [24]. Low porosity (2–9%) polyepoxide foams have also been prepared by chemically induced phase separation (CIPS) [25–28]. Epoxy formulations were dissolved in low molecular weight solvents and upon curing the solution phase separated into a polymer-rich and a solvent-rich phase. Pores form after solvent extraction. The addition of hollow or expandable spheres to an epoxy resin formulation has been popular to prepare syntactic foams [29]. Foam templating (or mechanical frothing) has also been used to produce macroporous epoxy resins [30–37]. Air was mechanically beaten in preferably highly viscous mixtures of epoxy monomers and hardeners to produce stable liquid foam templates, which were subsequently cured. The dispersed air bubbles serve as templates for controlling the pore size and shape as well as the porosity of the cured epoxy foam. Unfortunately, mechanical frothing resulted always in foams with a bimodal hierarchical pore size distribution, in which large (several hundred micrometres) pores were surrounded by smaller (15–50 μm) pores. The major issue with this approach is the control of the curing exotherm by heat dissipation from an insulating foam, which can result in fire (ESI Fig. S1) or at least partial carbonisation of the resin in case of fast curing systems. In order to produce polyepoxide foams with adjustable porosity and controlled pore size distribution, other approaches are required.

Emulsion templating, first reported in 1962 by Bartl and von Bonin [38], could be such an approach to access polyepoxide foams. This technique is well-established and reliable for producing macroporous polymers [39–41]. Besides foam templating, it is the second method under the umbrella of colloidal templating. Typically, emulsions with a

* Corresponding author. Polymer and Composite Engineering (PaCE) Group, Institute of Materials Chemistry and Research, University of Vienna, Währinger Strasse 42, 1090 Vienna, Austria.
E-mail address: alexander.bismarck@univie.ac.at (A. Bismarck).

https://doi.org/10.1016/j.polymer.2021.124476
Received 3 October 2021; Received in revised form 24 November 2021; Accepted 22 December 2021
Available online 25 December 2021

continuous organic phase containing monomers and an internal (aqueous) templating phase are prepared. They are categorised as high, medium or low internal phase emulsions (HIPEs, MIPEs, LIPEs), once the internal phase volume ratio (IPR) exceeds 74 vol%, is between 30 vol% and 74 vol% or below 30 vol%, respectively [42,43]. Polymerisation of the continuous phase followed by removal of the internal phase of the emulsions, results in macroporous polymers called poly-HIPEs/MIPEs/LIPEs, correspondingly [44]. These materials feature well-defined porosities and pore sizes which can be controlled by tuning emulsion formulation and emulsification conditions. It is the higher degree of control (including heat dissipation during polymerisation) that renders emulsion templating in many respects superior to foam templating, which offers only limited possibilities to influence a material's pore structure and related properties [45]. Furthermore, the presence of significant amounts of water in emulsion templates allows the control of reaction exotherms by acting as a heat sink within the template.

We believe that to approach the full potential of emulsion templating and porous polymers prepared therewith, further research on this subject is indispensable. Considering the multitude and diversity of adhesive systems on the market, the range of monomer systems, and thus polymerisation mechanisms, employed for emulsion templating, is still limited. Many links between emulsion formulation, emulsification and the properties of the final material have yet to be understood. Thus far, only a few papers on emulsion-templated epoxides have previously been published. Wang et al. synthesised emulsion templated epoxy foams; the continuous phase contained one of two epoxy systems, a bisphenol-A diglycidyl ether (DGEBA) [46] or glycidyl amino epoxy [47], together with a low molecular weight polyamide as curing agent, nonyl phenol polyoxyethylene as surfactant and 4-methyl-2-pentanon as solvent. An aqueous suspension of colloidal silica was in both cases employed as internal phase. The influence of the volume fraction of the dispersed phase, the amount of silica in the internal phase and the optimal hydrophilic-lipophilic balance (HLB) of the surfactant on the pore morphology were investigated. However, it was only possible to produce polyepoxide foams with porosities ranging between 30 and 40% when using epoxy resin bisphenol-A diglycidyl ether (DGEBA) [46] and between 35 and 55% at internal phase volume fractions between 70 and 80% for a low viscosity glycidyl amino epoxy resin (AFG 90) [47], both cured with a low molecular weight polyamide resin (LPA) as hardener. In both cases it was necessary to use a colloidal silica suspension as internal aqueous phase as it was impossible to produce stable emulsion templates with just water.

Tu et al. [48] prepared epoxy foams in a similar way as Wang et al. [47] and subsequently hydrophilized the surface by swelling the porous monolith in an acetone solution with 10 wt% azobisisobutyronitrile (AIBN), immersing the dried foam into an acrylic acid solution and finally grafting acrylic acid molecules onto the surface by initiating the radical polymerisation through heat. The surface modification caused a significant improvement of wettability and water absorption of the porous epoxy monolith. Anusha et al. [49] succeeded to prepare emulsion-templated conductive epoxy foams by adding carbon black to the resin formulation. The produced polyepoxide foams, however, resembled more a fused-bead structure rather than a structure typical for emulsion-templated macroporous polymers.

As of yet, none of the above-mentioned publications do report any mechanical properties.

The primary objective behind the production of porous polymers is the reduction of weight while preserving a material's mechanical properties as much as possible – achieving a good weight-to-performance ratio; pore morphology is investigated only superficially. Permeability measurements can contribute an essential part in understanding porous materials when in-depth information of pore structure and pore network is needed.

This paper presents the preparation of polyepoxide foams in an intermediate density range using a commercial low viscosity two-component resin formulation (Araldite®2020) by W/O emulsion templating, without the addition of any fillers to either aqueous or organic phase. We show that adjustment of the emulsion formulation - the amount of surfactant and internal phase ratio (IPR) - allows producing poly(epoxide)MIPEs with a tailored pore structure. Furthermore, it is our intention to push the porosity limits reported for macroporous epoxide systems produced by emulsion templating. Wang et al. [47] showed that polyepoxide foams with a porosity of 55.4% could be produced but required emulsion templates with 80% internal phase volume, indicating a limited stability of their templates. We will address this point. Open-porous foams were characterised for mechanical, thermal and chemical stability. Furthermore, we quantified the gas permeability of the produced polymer foams and elaborated on the connection between pore morphology and permeability. We will show that open-porous polyepoxide foams with attractive mechanical properties can be produced using a formulated commercial epoxy resin system, for a potential use as foamed adhesive.

2. Experimental section

2.1. Materials

The two-component (resin (A) and hardener (B)) epoxy system Araldite®2020 was purchased from Huntsman (Huntsman Corporation, Switzerland). Component A consists of a mixture of diglycidyl ether of bisphenol A (DGEBA) ($M_n < 700$, CAS No. 25068-38-6) and diglycidyl ether of 1,4-butanediol (DGEBOH) (CAS No. 2425-79-8) as reactive diluent. Component B is formed by the cycloaliphatic isophorone diamine (IPDA) ($M = 170.30$ g mol^{-1}, CAS No. 2855-13-2). The non-ionic surfactant sorbitan monolaurate (Span®20, HLB 8.6) purchased from Sigma-Aldrich (Vienna, Austria) was used to stabilise W/O emulsions. Calcium chloride dihydrate ($CaCl_2{\cdot}2H_2O$) was purchased from Sigma-Aldrich (Vienna, Austria) and Araldite® Rapid from Araldite® Precision Adhesive RS Components Ltd. (Corby, UK). The solvents isopropanol, acetone, dimethyl formamide (DMF), dimethyl sulfoxide (DMSO), tetrahydrofuran (THF) and benzene were purchased from Sigma-Aldrich, diesel oil from Shell. All chemicals were used as received.

2.2. Emulsion preparation

Emulsions were prepared in a reaction vessel with three-neck flat flange lid which was fitted with a glass paddle rod connected to an overhead stirrer (Phoenix Instruments RSO-20D) (Fig. 1). A plastic tube, on one end equipped with a quick-fit, connected a syringe pump (Harvard Apparatus PHD 4400) with the glass apparatus. The vessel was preloaded with the components of the external organic phase – the two-component epoxy system Araldite®2020 and the non-ionic surfactant Span®20. A preliminary surfactant screening identified Span®20 to be the most suitable surfactant (see ESI2 screening). Chemical structures of resin, hardener and Span®20 are depicted in Fig. 1. To achieve a homogeneous suspension, the mixture was first stirred for 3 min at 200 rpm, followed by 2 min at 600 rpm. The total volume of epoxy monomers and hardener was kept constant throughout all experiments, at the fixed ratio of 100 : 35 vol%, while the amounts of surfactant and internal phase volume were varied to study their influence on the final porous material.

The aqueous internal phase, a 0.068 M solution of $CaCl_2{\cdot}2H_2O$, was added under constant stirring (1000 rpm) at an injection speed of 2 ml/min using a syringe pump. The higher stirring speed should cause the break-up of large droplets into smaller ones. The salt, acting as electrolyte, had the purpose to suppress Ostwald ripening and thus increase emulsion stability. Once the addition of the aqueous phase finished, the stirring speed was increased to 1200 rpm for 3 min for further homogenization, yielding creamy-white viscous emulsions (see ESI Fig. S2). Table 1 summarizes the compositions of the medium internal phase emulsions (MIPEs).

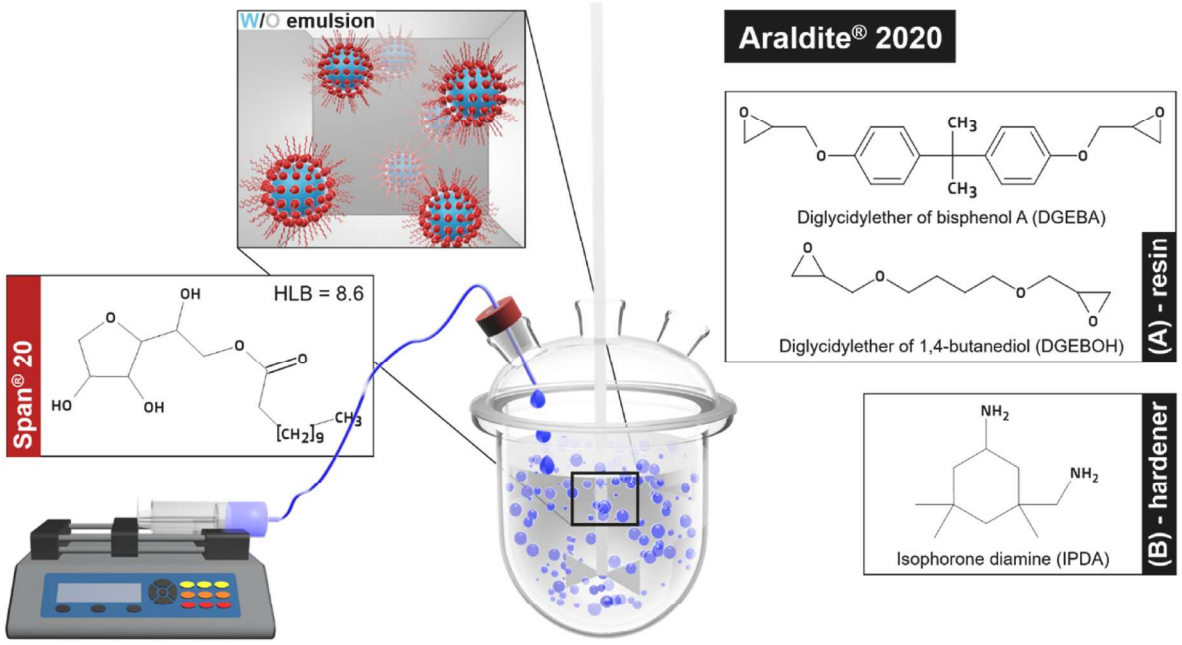

Fig. 1. Simplified emulsion templating setup and chemical structures of the components of the external organic phase: epoxy system Araldite®2020 and surfactant Span®20.

Table 1
Composition and curing temperature of emulsion templates based on epoxy formulations.

	CONTINUOUS PHASE			INTERNAL PHASE		
	Araldite®2020		Span®20		stirring	curing
	resin [vol %][a]	hardener [vol%][a]	surfactant [vol%][a]	aq. $CaCl_2 \cdot 2H_2O$ [vol%][b]	speed [rpm]	temp. [°C]
A	65	23	13	49	400	60
B	65	23	13	49	600	60
C	65	23	13	49	800	60
S1	63	22	16	49	1000	60
S2	63	22	16	56	1000	60
S3	59	21	20	49	1000	60
S4	59	21	20	54	1000	60
S5	59	21	20	60	1000	60

[a] With respect to the volume of the continuous phase.
[b] Relative to the total emulsion volume.

MIPEs were filled into free-standing polypropylene Falcon® tubes, sealed, and cured for 24h in an oven at 60 °C. The cured epoxy foams were washed with distilled water to remove the salt of the internal phase. The polyMIPEs were dried for 48h at 60 °C under atmospheric pressure, followed by vacuum drying overnight at the same temperature to remove any remaining moisture.

2.3. Characterisation of the polyepoxide foams

Foam structure and pore morphology of the epoxy polyMIPEs were investigated using scanning electron microscopy (SEM, JCM-6000 Neoscope, JEOL Ltd., Eching, Germany). Thin fracture surfaces of each sample, about 1 cm^2 in size, were mounted on an SEM stub using a conductive carbon sticker. Prior to observation, the fracture surfaces were sputter-coated with gold (45s) using JFC-1200 Fine Coater (JEOL Ltd., Eching, Germany) to achieve sufficient electrical conductivity. The SEM was operated in secondary electron mode at an acceleration voltage of 15 kV. The software package ImageJ was used for further analysis of the micrographs (ESI S3).

2.4. Porosity

Skeletal densities ρ_s were determined using gas (helium) displacement pycnometry (AccuPyc II 1340, Micromeritics Ltd., Aachen, Germany). Small foam fragments were pulverised prior to analysis. Skeletal densities were obtained as the quotient of sample mass and the measured skeletal volume [50,51].

Measurements of foam densities ρ_f were based on graphite powder displacement pycnometry (GeoPyc 1360 V1.03 Envelope Density Analyzer, Micromeritics Ltd., Aachen, Germany) [52]. A minimum of three measurements per sample was performed. Foam densities were calculated in analogy to the skeletal densities. The percentage porosity P was calculated using Eq. (1):

$$P = \left(1 - \frac{\rho_f}{\rho_s}\right) \cdot 100\% \quad (1)$$

2.5. Equilibrium swelling experiments

Swelling tests were performed to evaluate the chemical resistance of the produced polyepoxide foams. The influence of the following solvents (ESI Table S7), in descending order of polarity, was investigated at room temperature (21 °C): isopropanol, dimethyl sulfoxide (DMSO), (N,N)-dimethylformamide (DMF), tetrahydrofuran (THF), acetone, benzene and diesel oil. Cuboid aliquots (about 5 mm × 5 mm x 10 mm) were prepared from samples S1–S5 using a bandsaw. Initial weight and exact dimensions of the dry unswollen monoliths were measured prior to placing them in vials (ESI Fig. S8) and addition of 10 ml solvent. Weight and dimensions of the swollen polyMIPEs were recorded after 1h, 2h, 4h, 8h, 1d, 2d, 4d, 6d, 8d and 11d, before drying them in a vacuum oven for 24h at 60 °C and weighing them again, to determine the mass of the dry network after extraction of soluble materials.

Volumina of the swollen V_{sw} and initial dry polyMIPEs V_0 were used to calculate the swelling ratio Q and the inversely proportional polymer volume fraction at swelling equilibrium φ_p:

$$Q = \frac{V_{sw}}{V_0} = \frac{1}{\varphi_p} \quad (2)$$

Molecules that were not integrated into the polymer network, e.g.

excess surfactant, were extracted during the swelling process. The ratio of extracted material ω_{sol} was quantified by comparing the weight of the dry polyMIPEs before immersion into a solvent and after removal of the solvent at the end of the swelling test after eleven days, m_0 and m_{dry} respectively (Eq. (3)):

$$\omega_{sol} = \frac{m_{dry} - m_0}{m_0} \quad (3)$$

2.6. Thermal analysis: differential scanning calorimetry (DSC)

Glass transition temperature T_g of the epoxy polyMIPEs was investigated using differential scanning calorimetry (Discovery DSC, TA Instruments, Eschborn, Germany). Small amounts of foam powder were subjected to a temperature program comprising two heating and cooling cycles in a temperature range from -30 °C to 200 °C, at a heating rate of 5 °C/min. T_g was obtained from the midpoints of the step-shaped endothermic change of the specific heat capacity c_p.

2.7. Compression tests

Mechanical properties of the epoxy foams were tested under compression using a universal mechanical testing machine (Instron Series 5969, Instron Ltd., UK) equipped with a 50 kN load cell. The polyMIPEs were cut into disks, 10 mm in height and 25 mm in diameter, before being compressed at room temperature by 60% of their original height at a speed of 1 mm/min. The elastic moduli E_c were determined from the slope of the initial linear regions of the stress-strain curves, the plateau moduli E_p from the slope of the rubber plateau. The compression strengths σ_c, the maximum stress at the end of the initial linear elastic section, were obtained from the interceptions of the extensions of linear regressions to the initial linear region and the second linear plateau region. For every polyMIPE at least five specimens were tested.

2.8. Gas permeability

Sample preparation, apparatus, measurement and data evaluation were described in detail by Manley et al. [53]. In brief, poly(epoxide) MIPEs, about 15 mm in diameter, were sealed with Araldite® Rapid to avoid unwanted gas leakage. The coated samples were embedded in Araldite®2020 using a PTFE mould impregnated with a thin film of release agent WD-40 (ESI Fig. S14). The epoxy was allowed to cure overnight at ambient conditions. The sample chamber was loaded with one of the cylindrical specimens, cut to a height of 25 mm, and evacuated to a pressure of about 10 Pa. A nitrogen stream of constant pressure was applied to the upper side of the sample, inducing a gas flow from the high- to the low-pressure side, where the gas was collected in a vessel of known volume (Fig. 2).

The rate of pressure rise Q_2 was evaluated as slope of a plot of the pressure at the low-pressure side p_2 vs. time t (Fig. 2 (1)) and the permeability coefficient K [$m^2 \cdot s^{-1}$] calculated. K was plotted against the mean pressure $p_m = \frac{p_1}{2}$ (Fig. 2 (2)), assuming p_2 to be negligibly small. Slip coefficient (or Knudsen permeability) K_0 [m] and viscous permeability k [m^2] were determined from this plot. The whole working equation was reported by Carman (Eq. (4)) [54]:

$$K = \frac{Q_2 p_2 L}{\Delta p A} = \frac{V\left(dp_2/dt\right)L}{p_1 A} = \frac{k}{\mu} p_m + \frac{4}{3} K_0 \sqrt{\frac{8RT}{\pi M}} \quad (4)$$

where Q_2 is the volumetric flow rate downstream (low pressure side) [$m^3 \cdot s^{-1}$], p_1 the gas inlet pressure [Pa], p_2 the downstream pressure [Pa], Δp the pressure difference across the sample [Pa], L the sample length [m], A the sample cross section area [m^2], V the vessel volume [m^3], t the time [s], μ the gas viscosity [Pa·s], M the molar mass of gas [$g \cdot mol^{-1}$], R the gas constant [$J \cdot mol^{-1} \cdot K^{-1}$] and T the temperature [K].

3. Results & discussion

The formation of an emulsion is facilitated if continuous and internal phase have similar viscosities. Therefore, dispersing the significantly less viscous aqueous phase ($\eta_{H2O} \approx 0.89$ mPa s at 25 °C) [55] in the much more viscous external phase ($\eta_{Ar2020} \approx 150$ mPa s at 25 °C) [56], consisting of the two-component epoxy system Araldite®2020, presented the first challenge. It was crucial to identify the most suitable surfactant for this system; a variety of non-ionic surfactants, covering a broad range of HLB-values (hydrophilic-lipophilic balance), was tested: Pluronic® L-81 (HLB 2), Span®80 (4.3), Hypermer® 2296 (4.9), Hypermer® 1083 (4–6), Hypermer® B246 (6), Span®20 (8.6), Brij® O10 (12.4), Triton® X-100 (13.4), Tween®80 (15), Tween®20 (16.7) and Triton® X-405 (17.6) (see ESI2 screening). Literature commonly states that the ideal HLB-range of surfactants for the preparation of W/O emulsions is 4–6. However, the surfactant screening revealed that Span®20 with an HLB of 8.6 was most suitable for our system.

Poly(epoxide)MIPEs with 49 vol% internal phase ratio could be stabilised using 13 vol% Span®20 as emulsifier. After curing of the external phase at 60 °C, the aqueous internal phase was removed by drying the material at the same temperature, leaving a solid foam behind. Preparation of MIPEs with a lower surfactant content, at the same internal phase volume ratio, was either not successful or the

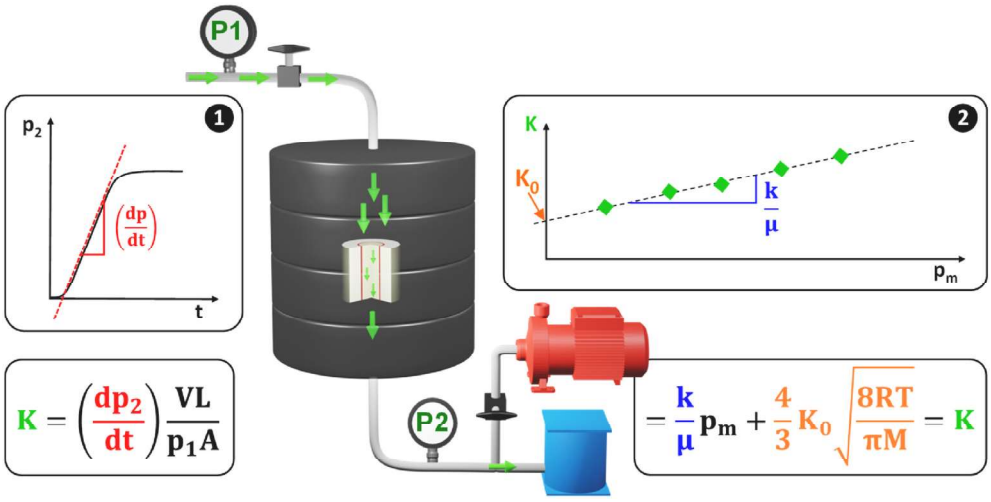

Fig. 2. Schematic representation of the gas permeability apparatus and the data evaluation.

emulsions underwent phase separation during curing. This was most likely due to insufficient stabilisation. The energy input was varied in order to identify the best emulsification procedure; this was done by using different stirring speeds during addition of the internal phase, namely 400, 600, 800 rpm. Pore morphologies of the resulting polyMIPEs are shown in Fig. 3. All three samples exhibited a predominantly closed-cell pore structure with only few pore throats present. The pore size distribution was fairly homogenous and had roughly the same pore diameters.

To explore the limits of this particular monomer/surfactant system and to produce open porous polyepoxides, the surfactant amount and internal phase ratio were gradually increased (Table 1). When using 16 vol% surfactant, the IPR could be pushed only up to a maximum of 56 vol%. Emulsions containing higher portions of aqueous phase did not remain stable or not the entire volume of internal phase could be emulsified in the first place. In the latter case, there was some excess internal phase on top of the highly viscous emulsion (ESI Fig. S2c). Using 20 vol% Span®20, stable emulsions with up to 60 vol% internal phase volume ratio could be prepared. Neither a higher IPR nor the use of more surfactant, at constant IPR, allowed for the formation of stable MIPEs.

Representative fracture surfaces of polyMIPEs S1–S5 were analysed using scanning electron microscopy (Fig. 4). Evaluation of the micrographs revealed heterogeneous pore size distributions for all polyMIPEs. Because of the polydispersity, it was not meaningful to specify a mean pore diameter as single parameter to characterise the pore size distribution in the prepared porous polyepoxides. Instead, the parameters d_{10}, d_{50}, d_{90}, d[3,2] and d_{v10} provided more information regarding structure and morphology of our materials (Table 2, ESI Table S5) [57].

The right-hand side of Fig. 4 shows histograms of the pore size distributions of S1–S5. Additionally, the cumulative number frequency (*cnf*, blue), as well as the cumulative volume frequency (*cvf*, red) curves, were added to the plots.

S1 and S2 had very similar pore morphologies (Fig. 4a and b) but also sections of thick non-porous pore walls. SEM images were dominated by few very large pores in the size range of several 100 μm with pore throats up to 200 μm. This was not reflected in their *cnf* curves: only about 2% of all measured pores of any formulation S1–S5 were larger than 200 μm, almost 50% between 10 and 20 μm and 15–20% between 0-10 μm and 20–30 μm. The *cvf* curves support the observation; they illustrate that pores sized below 200 μm occupied only about 2.5% and 5% of the total pore volumes of S1 and S2, respectively, which confirms the visual predominance of these large pores.

SEM images Fig. 4a–e reveal the open-porous character of the pore structure of S1–S5. However, the number of pore throats visible in the SEM images (Fig. 4c–e) increases and the pore walls became thinner, suggesting a higher degree of interconnectivity for these poly(epoxide) MIPEs than for S1 and S2. The *cnf* for S3–S5 were similar compared to S1 and S2, 93–97% of pores below 200 μm, *cvf* showed that pores below 200 μm attributed for a much higher percentage of the total pore volume than in S1 and S2. Almost 1/3 of the pore volume of S3 and S4 was occupied by pores smaller than 200 μm, followed by S5 with about 12%. The huge gap between the values for d_{10} and d_{v10} (ESI Table S5), marking the upper limits of the first 10% of *cnf* and *cvf*, respectively, underlined these observations. Average pore throat diameters d_{pt} (Table 2) are briefly treated in the section about gas permeability and are further illustrated by means of histograms in ESI Fig. S4.

Differential scanning calorimetry measurements showed that epoxy polyMIPE S1 had the highest glass transition temperature, 37.7 ± 0.1 °C (compared to 39.5 °C for pure Araldite®2020), while S4 had the lowest T_g, 24.9 ± 0.4 °C (Table 3). The T_g of epoxy polyMIPEs prepared by curing of emulsion templates stabilised with 20 vol% Span®20 were slightly lower than those prepared with only 16 vol% of surfactant, indicating a plasticizing effect of the surfactant.

Skeletal densities $\rho_{skeletal}$ of S1–S5 were identical within error, no dependence of the amount of surfactant or IPR was observed (Table 3). These results indicated that the composition of the matrices was not affected by alterations of the emulsion formulation. Foam densities ρ_{foam} and thus porosities *P* varied with the IPR. The emulsion of S5, prepared with the largest amount of internal phase (60 vol%), resulted in the foam with the highest porosity, i.e. 62 %, the highest reported porosity thus far for emulsion templated polyepoxide foams. The entire sample set covered a porosity range from 43 to 62%. Therefore, all our epoxy foams were classified as polyMIPEs.

SEM usually provides information whether a material has a closed-cell or open-porous structure. However, it is difficult to distinguish between 'just' an open-porous system and a fully interconnected one, in which pores and pore throats form channels spanning from one side of a sample to the other. Gas permeability tests do provide more insight [53]. Generally, a higher surfactant ratio leads to a higher degree of interconnectivity by formation of pore throats. The competition between

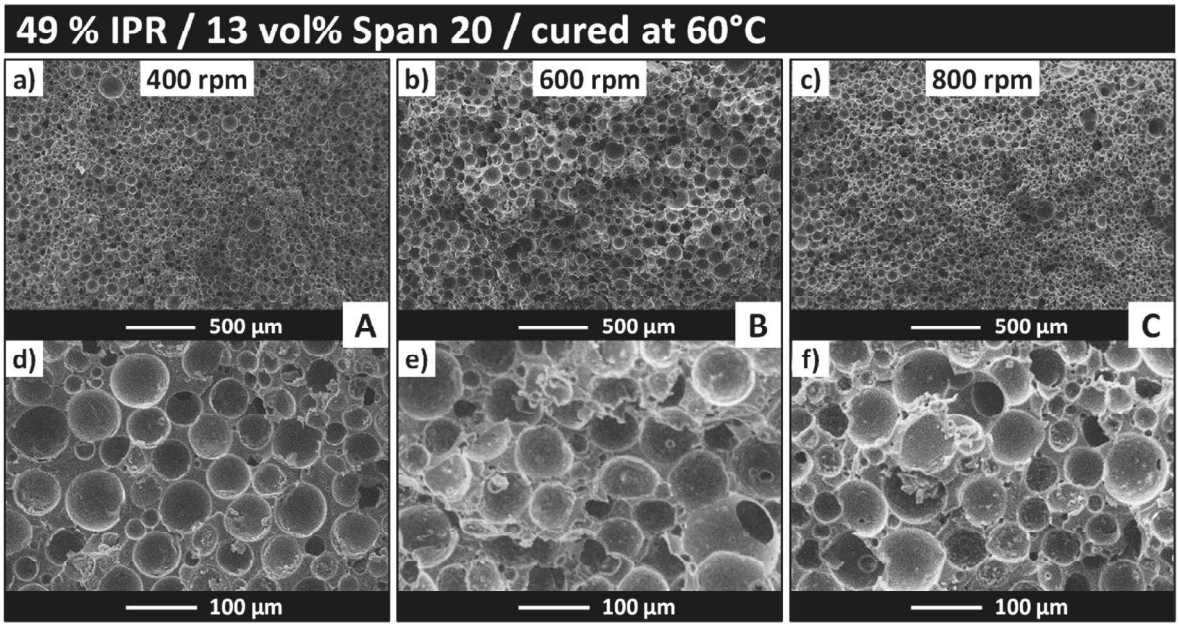

Fig. 3. SEM images showing the predominantly closed-cell pore structure of poly(epoxide)MIPEs emulsified at different stirring rates, 400, 600 and 800 rpm.

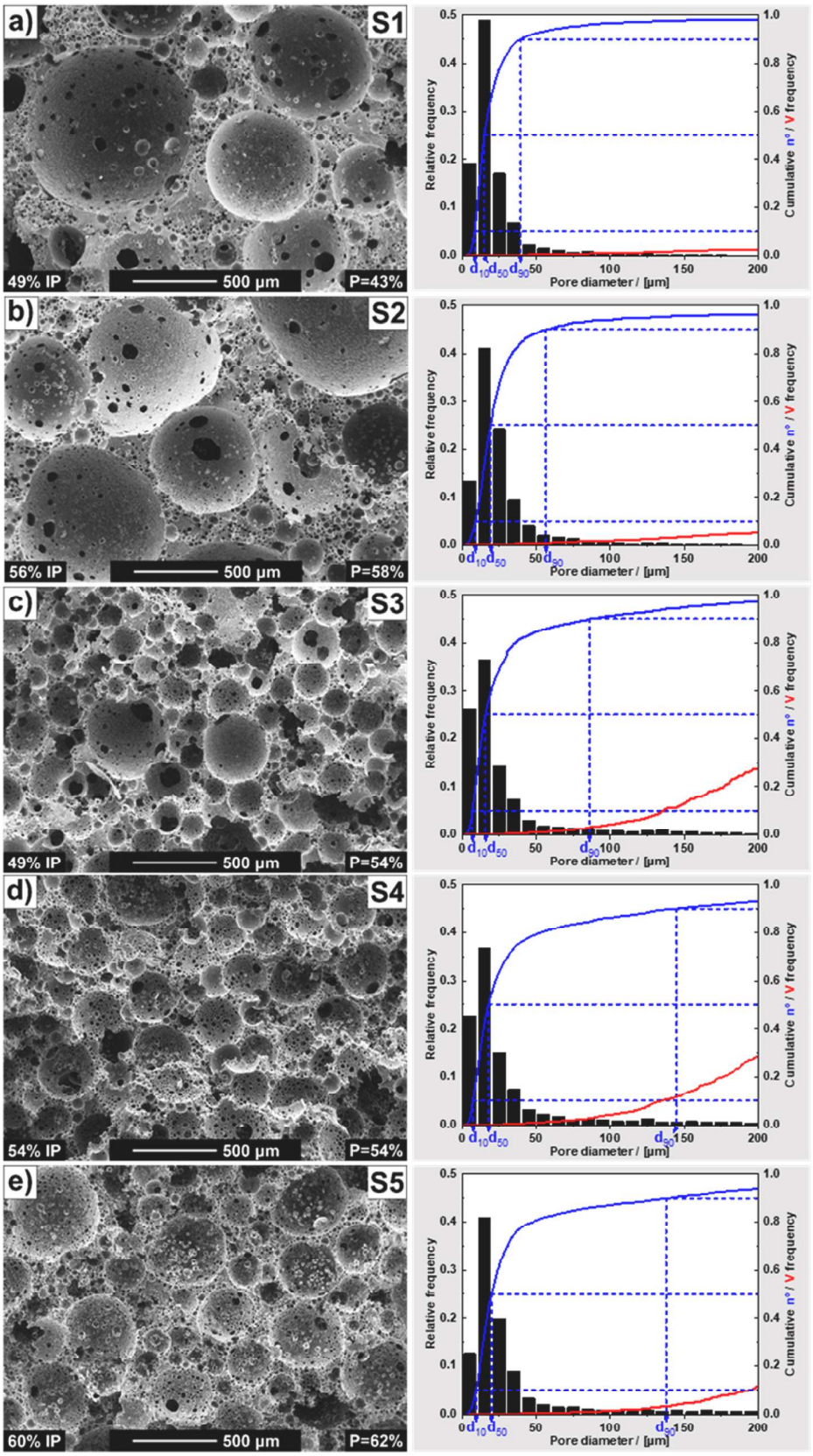

Fig. 4. Scanning electron micrographs show distinct differences in pore morphology of poly-MIPEs prepared by curing MIPEs stabilised with 16 vol% (a, b) and 20 vol% (c–e) surfactant. Analyses of the pore size distributions are on the right hand side. The cumulative volume frequency (red) curves confirm the visual differences seen in the micrographs. Please note, some of the debris formed during fracturing of the samples, remained present in the pores. (For interpretation of the references to colour in this figure legend, the reader is referred to the Web version of this article.)

Table 2
Summary of the analysis of pore and pore throat diameters and results of the gas permeability measurements.

	Pores (in [μm])					Pore throats	K_0	k
	d [1,0]	**d_{50}**	**d_{90}**	**d [3,2]**	**d_{v10}**	**d_{pt}/ [μm]**	[m]	[mD]
S1	28.3	15.0	39.5	518.8	400.5	9.7 ± 12.2	1.1E-05 ± 3.8E-06	93 ± 29
S2	31.3	19.2	56.5	426.8	290.5	6.5 ± 8.6	8.3E-06 ± 1.8E-06	37 ± 12
S3	34.6	15.7	86.1	211.4	135.8	7.0 ± 7.1	2.1E-05 ± 3.5E-06	94 ± 19
S4	37.6	17.8	144.7	210.8	134.4	8.0 ± 8.1	2.1E-05 ± 2.8E-06	85 ± 21
S5	48.3	19.8	137.8	303.9	193.5	10.1 ± 8.5	7.3E-06 ± 2.6E-06	147 ± 42

Table 3
Summarised properties of epoxy polyMIPEs S1–S5.

—	$\rho_{skeletal}$ [g·cm^{-3}]	ρ_{foam} [g·cm^{-3}]	Porosity [%]	E_c [MPa]	σ_c [MPa]	T_g (DSC) [°C]
S1	1.155 ± 0.005	0.667 ± 0.029	43 ± 3	193.3 ± 14	6.4 ± 0.2	37.7 ± 0.1
S2	1.161 ± 0.005	0.486 ± 0.034	58 ± 3	189.9 ± 4.9	6.2 ± 0.1	32.6 ± 1.1
S3	1.158 ± 0.005	0.531 ± 0.031	54 ± 3	71.8 ± 8.7	2.2 ± 0.3	28.4 ± 0.7
S4	1.161 ± 0.01	0.533 ± 0.05	54 ± 4	64.5 ± 14	2.0 ± 0.3	24.9 ± 0.4
S5	1.148 ± 0.004	0.437 ± 0.007	62 ± 2	99.1 ± 10	3.2 ± 0.1	31.7 ± 0.1

polymerisation-induced surfactant depletion attraction and the strength of interfacial films governs pore throat formation. Weak interfacial areas result in pore throats in polyMIPEs of the same size as the flattened interfacial areas between adjacent droplets in MIPEs [58]. Similarly, the likelihood for open-porous materials increases with increasing internal phase ratios also resulting in a higher porosity. The formation of pore throats and a high porosity strongly influence permeability but ultimately, in case of interconnected spherical pores, it is the smallest pore throat diameter $d_{pt,min}$ of the largest pore connecting top and bottom of a porous material, which dictates and limits the flow of fluids through porous materials.

Measured gas permeabilities for S1–S5 (integral properties over a large sample, rather than a snapshot as viewed by SEM (Fig. 4)) were in the range between 20 and 200 mD. These permeabilities are in the range of those reported for sandstones [53] and poly(styrene-*co*-DVB)MIPEs and -HIPEs produced from surfactant-stabilised emulsion templates [59], but are not due to the presence of cracks or other imperfections in our samples (ESI Fig. S6). Given that a porous medium with a permeability of 1 D has pores with a limiting pore throat area of 0.9869 μm^2 ($d_{pt} > 1.12$ μm) we can estimate the limiting pore throat diameter of our porous polyepoxides to be 0.22 μm–0.43 μm. The estimated limiting pore throat diameters determined from the gas permeability seem to be an order of magnitude smaller than the average pore throat diameters identified from SEM images. Also for standard polyM/HIPEs, the limiting pore throat diameters, determined by mercury permeability measurements, are also always much smaller than those determined by SEM [59]. However, given the hierarchical nature of the pore structure of our poly(epoxide)MIPEs, i.e. large pores were embedded in porous pore walls containing numerous small diameter pores, it was difficult to accurately determine the average pore throat diameters (ESI Fig. S6), resulting in very large errors (>100%). On the contrary, permeability is a macroscopic property, from which it is possible to determine the actual limiting pore throat diameters, which were at the lower end of the error bands of the average pore throat diameters (Table 2).

The epoxy polyMIPEs were compressed by 60% of their original height to determine their elastic modulus E_c and compression strength σ_c. Representative stress-strain curves of samples S1–S5, illustrating the variation of the compressive load as function of strain, as well as an extensive explanation of the recorded curves are provided in the supplementary information (ESI S12 & ESI Fig. S13). Commonly, the stiffness of foams increases with foam density [60]. The properties of the bulk polymer and structural features, including pore wall thickness, pore size distribution and degree of interconnectivity also considerably affect a material's response to compressive load and thus the exact shape of stress-strain curves [61]. Moreover, curing conditions and the exact emulsion formulation can influence not only the polymerisation process itself but also the degree of crosslinking and accordingly mechanical properties.

PolyMIPEs S1 and S2 had with about 190 MPa both significantly higher E-moduli than S3–S5 with about 60–100 MPa (Table 3), which can be explained by their thicker and less porous pore walls (Fig. 4). The same trend, even slightly more pronounced, was observed for the crush strengths of the epoxy foams (Fig. 5). Increasing amount of surfactant used to stabilise the MIPE templates for S3–S5 resulted in thinner pore walls of the cured epoxy foams reducing their mechanical properties. Moreover, as reported earlier, DSC measurements raised the suspicion that the surfactant might have acted as plasticizer. The use of 16 vol% Span®20 (S1, S2) resulted in epoxy polyMIPEs with 2–3x higher stiffness and strength compared to those prepared with 20 vol% (S3–S5), because of their thicker pore walls that can carry more load. Nevertheless, it showed that both parameters, porosity/IPR and surfactant content, are crucial in manufacturing materials with tailored properties. The higher value for the plateau modulus E_p (Table 4) obtained for polyMIPE S1 indicated the presence of more closed cells than in S2 to S5.

The theoretical average molecular weight between crosslinks at full conversion $M_{c,th}$ was calculated for Araldite®2020 using the composition of the epoxy system and the functionalities of its components (see ESI S15) [62].

The presence of water within the emulsion template during curing can affect the reaction and stoichiometry of epoxy systems. For this reason, we investigated the crosslinking density, which would be influenced, if water is taking part in the reaction. Karayannidou et al. [63] determined the epoxide equivalent weight of component A of Araldite®2020 using titration and reported a value of 224.29 g/eq. The amine hydrogen equivalent weight, defined as the molecular weight per active amine hydrogen, for isophorone diamine is 170.3/4 = 42.57 g/eq, which results in $M_{c,th}$ of 534 g mol^{-1}.

Qualitative assessment of the crosslinking in the prepared epoxy polyMIPEs was based on rubber elasticity theory. It states that the rubber modulus E_r of an elastomeric material is inversely related to the average molecular weight between crosslinks M_c. A higher number of crosslinks restricts the mobility of polymer chains to move freely and thus increases the modulus. Instead of E_r, we used E_p determined from the plateau region of the stress-strain curves obtained from uniaxial compression tests carried out at room temperature (Table 4). In literature, E_r was often determined from dynamical mechanical thermal analysis (DMTA) measurements, but confusingly also the use of elastic moduli was reported [64]. Furthermore, different information about the used temperatures can be found, T_g+40,[65] T_g+50,[66] T_g+60[67] or absolute temperature [68,69] for instance. We do not claim that the modulus E_p evaluated from the plateau of a stress-strain curve recorded during

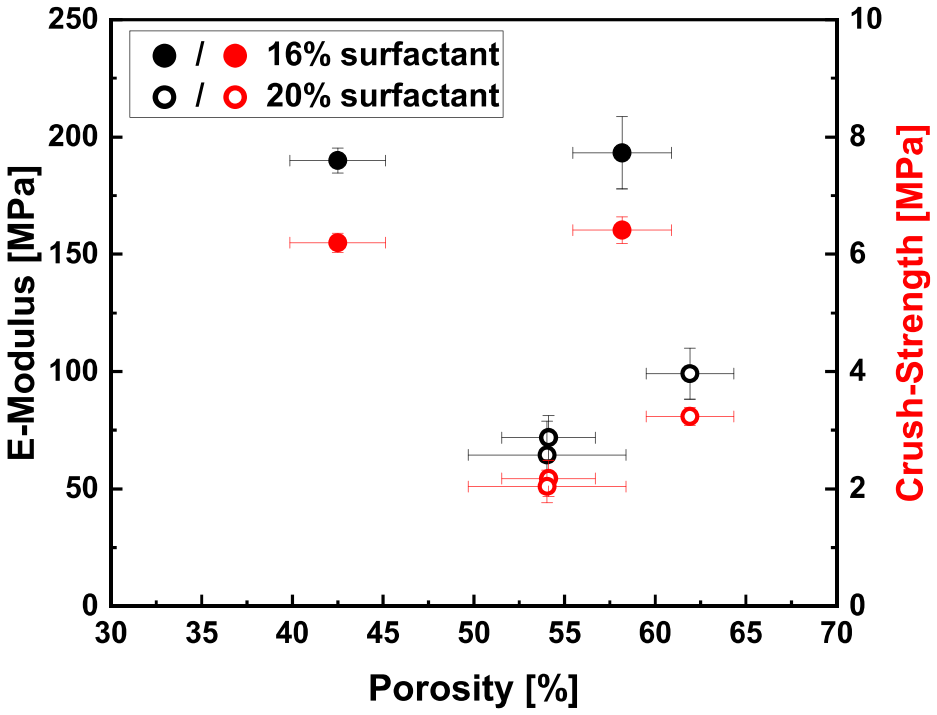

Fig. 5. Influence of porosity and surfactant concentration on the mechanical properties.

Table 4
Crosslink densities and average molecular weights between crosslinks, calculated from the plateau moduli.

—	E_p [MPa]	v_c [mol·cm^{-3}]	M_c [g·mol^{-1}]
S1	10.8 ± 0.3	$1.5 \times 10^{-3} \pm 3.9 \times 10^{-5}$	458 ± 32
S2	7.0 ± 1.3	$9.4 \times 10^{-4} \pm 1.7 \times 10^{-4}$	516 ± 131
S3	7.6 ± 2.4	$1.0 \times 10^{-3} \pm 3.2 \times 10^{-4}$	522 ± 195
S4	7.1 ± 0.4	$9.6 \times 10^{-4} \pm 5.3 \times 10^{-5}$	558 ± 83
S5	7.2 ± 0.2	$9.7 \times 10^{-4} \pm 3.3 \times 10^{-5}$	451 ± 22

compression experiments is directly comparable to E_r obtained by DMTA measurement, although empirically, both moduli should be of the same order of magnitude. Even though not adequate for quantitative analysis, we believe in the validity of using E_p values evaluated from σ-ε curves and that the results served the purpose of determining the crosslink density in our epoxy polyMIPEs. The plateau could be clearly identified in all σ-ε curves (ESI Fig. S13) and the temperature at which the compression tests were carried out was 298 K.

First, the crosslink density ν_c, defined as the moles of elastically effective network chains in unit volume [66,67], was calculated using Eq. (5), then the result was inserted into Eq. (6) to determine M_c from the polymer foam density [69,70]:

$$\nu_c = \frac{E_r}{3qRT} \tag{5}$$

$$v_c = \frac{1}{\bar{v}M_c} \rightarrow M_c = \frac{\rho_f}{\nu_c} \tag{6}$$

where R is the gas constant, T the absolute temperature, $\bar{v}$ the specific volume of the material, i.e. the inverse of the foam density ρ_f, and q a front factor accounting for differences between thermosets and ideal rubbers. Commonly, $q = 1$ has been used for epoxy networks [65,68,69]. The foam density was used, as it determines the mechanical properties of porous materials.

The estimated crosslink densities and average molecular weights between crosslink sites, tabulated in Table 4, are in the range of 0.9–1.5 × 10^{-3} mol cm^{-3} and 450–560 g mol^{-1}, respectively. These results are in good agreement with $M_{c,th}$, 534 g mol^{-1}, and also with other calculations and measurements from literature that were carried out on epoxy networks [62,65,66,69,71]. These results showed that the mechanical compression properties of our poly(epoxide)MIPEs were mainly governed by the porosity of the polymer foams, rather than being influenced by a change in the polymer network density.

A polymer network's degree of crosslinking is inversely related to the degree of swelling; hence, the more crosslinked a network is, the less pronounced the swelling behaviour. Characterisation of crosslinking based on swelling experiments is often prone to errors and can only yield qualitative information because of the approximations made in deriving the Flory-Rehner model. Valentin et al. [72] described in detail the difficulties that frequently occur in the determination of M_c and ν_c from equilibrium swelling tests, among others the determination of the Flory-Huggins parameters.

Chemical resistance and degree of crosslinking of the porous polyepoxides were visualised through swelling tests in various solvents. A plot of Q vs. the immersion time t allowed for a qualitative assessment of the swelling behaviour of the prepared polyMIPEs. On one hand, we compared the extent of swelling of each sample exposed to the various solvents (ESI Fig. S9), on the other hand, we were interested in how the various samples reacted to each solvent (ESI Fig. S10). In addition to the plots, the summarised results are specified in ESI Table S11. Fig. 6 reveals that the average swelling extent was practically the same for all samples, i.e. they reacted in a similar way to the exposure to a particular solvent. Furthermore, the swelling ratios did not show distinct differences between 1h and about 11d immersion. This means that swelling must have happened fairly quickly, and that the full extent of swelling was reached already after about 1 h. DMSO, DMF and THF clearly caused the highest volume increases, leading to swelling ratios of about 1.7–1.8. Isopropanol, acetone and benzene extended the foam volumes by about 20–40%, while Diesel oil had only a small impact on the sample volume.

Some foam blocks did not withstand the exposure to certain solvents (DMSO, DMF) for a long time or were so fragile that they fell apart

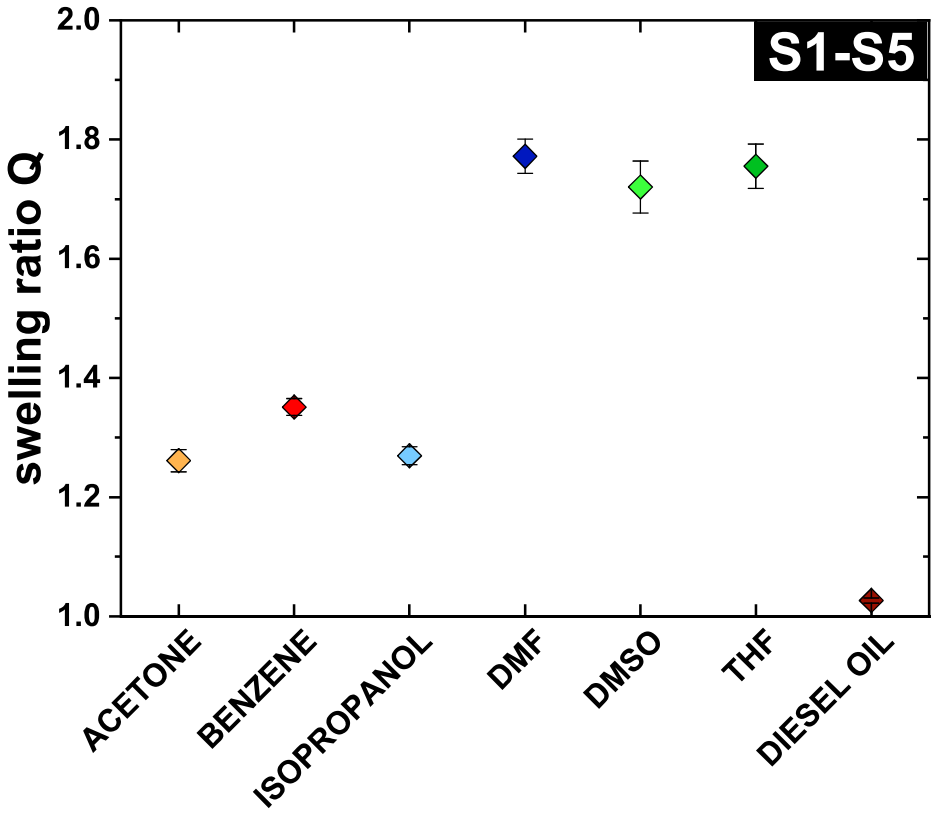

Fig. 6. Average swelling ratios of epoxy polyMIPEs S1–S5. No values for S1-DMF and S2-DMSO were included because the respective samples fell apart.

during measuring their weight or dimensions. This was for instance the case for S1 & S2 in DMF and S1 DMSO.

The sol content ω_{sol} describes the amount of surfactant or loose polymer chains that were extracted during the swelling tests. Generally, the weight loss for all samples was located in a very narrow range of 10 ± 3%. A marginal trend to higher weight loss was found for the foam cubes with higher swelling ratios, i.e. those being immersed in DMSO, DMF and THF (ESI Table S11). The higher degree of swelling of the polymer matrix probably facilitated the extraction of unbound surfactant molecules or loose polymer chains. Moreover, it is possible that small chunks broke off because of repeatedly removing the strongly macerated foam cubes from their solvents, weighing and measuring them.

4. Conclusion

Polyepoxide foams are attractive insulation materials or for application in sandwich cores. We showed that it is possible to prepare porous polyepoxides with foam densities ranging from 400 kg m^{-3} to 700 kg m^{-3} by medium internal phase emulsion templating. We identified the surfactant Span®20 to be most suitable to stabilise such emulsion templates. By adjusting the surfactant concentration during emulsification, it was possible to tailor the pore structure from closed-cell to open-porous. With increasing the porosity from 43% to 64%, the gas permeability increased from 40 mD to 150 mD. Increasing the surfactant concentration used to stabilise the MIPE template by 4 vol% resulted in significantly lower elastic moduli and crush strengths as this resulted in significantly thinner pore walls. These porous polyepoxides had glass transition temperatures in the range of 30 °C. Despite the presence of water in the resin system during the curing process, the crosslinking density of these materials was still in agreement with the theoretical value for this epoxy system. Swelling tests in a variety of solvents confirmed the excellent chemical stability of the epoxide foams. The use of more polar solvents such as DMSO, DMF and THF resulted in swelling ratios up to 1.8, while less polar solvents such as acetone, isopropanol and benzene caused swelling up to 1.3.

CRediT authorship contribution statement

Patrick Steindl: experimental design, visualisation, data collection and analysis, Writing - original draft. **Angelika Menner:** conceptualisation, Supervision, revision of draft, Funding acquisition. **Alexander Bismarck:** conceptualisation, Methodology, Supervision, manuscript draft revision, Writing - review & editing, and proofing, Funding acquisition.

Declaration of competing interest

The authors declare that they have no known competing financial interests or personal relationships that could have appeared to influence the work reported in this paper.

Acknowledgements

The authors acknowledge the support of the Austrian Science Fund (FWF) through the project I1800 for funding PS.

Appendix A. Supplementary data

Supplementary data to this article can be found online at https://doi.org/10.1016/j.polymer.2021.124476.

References

[1] J.-P. Pascault, R.J.J. Williams, General concepts about epoxy polymers, in: Epoxy Polymers - New Materials and Innovations, 2010, pp. 1–12, https://doi.org/10.1002/9783527628704.ch1.
[2] F.-L. Jin, X. Li, S.-J. Park, Synthesis and application of epoxy resins: a review, J. Ind. Eng. Chem. 29 (2015) 1–11, https://doi.org/10.1016/j.jiec.2015.03.026.

[3] M.A. Boyle, C.J. Martin, J.D. Neuner, Epoxy resins, in: D.B. Miracle, S.L. Donaldson (Eds.), Composites, vol. 21, ASM International, 2001, https://doi.org/10.31399/asm.hb.v21.a0003362, 0.

[4] W. Brostow, S.H. Goodman, J. Wahrmund, Epoxies, in: H. Dodiuk, S.H. Goodman (Eds.), Handbook of Thermoset Plastics, third ed., William Andrew Publishing, Boston, 2014, pp. 191–252, https://doi.org/10.1016/B978-1-4557-3107-7.00008-7.

[5] V.A. Kochetkov, R.D. Maksimov, Water absorption and swelling of glass/epoxy syntactic foams, Mech. Compos. Mater. 32 (1) (1996) 61–70, https://doi.org/10.1007/BF02254649.

[6] X.M. Liu, C.J. He, H.J. Li, H.Y. Peng, Water absorption and diffusion in hollow glass microsphere filled epoxy syntactic foams, Adv. Mater. Res. 143–144 (2011) 370–374. https://doi.org/10.13039/10.4028/www.scientific.net/AMR.143-144.370.

[7] T. Anderson, E. Madenci, Graphite/epoxy foam sandwich panels under quasi-static indentation, Eng. Fract. Mech. 67 (4) (2000) 329–344, https://doi.org/10.1016/S0013-7944(00)00066-7.

[8] M. Akay, R. Hanna, A comparison of honeycomb-core and foam-core carbon-fibre/epoxy sandwich panels, Composites 21 (4) (1990) 325–331, https://doi.org/10.1016/0010-4361(90)90347-Y.

[9] Shirshova, N.; Rogaume, T.; Najmi, H.; Poisson, M., The combustion behavior of epoxy-based multifunctional electrolytes. Fire Mater. n/a (n/a); https://dx.doi.org/https://doi.org/10.1002/fam.2967.

[10] F.-L. Jin, M. Zhao, M. Park, S.-J. Park, Recent trends of foaming in polymer processing: a review, Polymers 11 (6) (2019) 953, https://doi.org/10.3390/polym11060953.

[11] F.I. Altuna, R.A. Ruseckaite, P.M. Stefani, Biobased thermosetting epoxy foams: mechanical and thermal characterization, ACS Sustain. Chem. Eng. 3 (7) (2015) 1406–1411, https://doi.org/10.1021/acssuschemeng.5b00114.

[12] S.L. Burt, Epoxy Resin Foaming Process. US003320187, 1967.

[13] M. Cavasin, S. Giannis, M. Salvo, V. Casalegno, M. Sangermano, Mechanical and thermal characterization of an epoxy foam as thermal layer insulation for a glass fiber reinforced polymer, J. Appl. Polym. Sci. 135 (47) (2018), 46864, https://doi.org/10.1002/app.46864.

[14] K. Chen, C. Tian, A. Lu, Q. Zhou, X. Jia, J. Wang, Effect of SiO2 on rheology, morphology, thermal, and mechanical properties of high thermal stable epoxy foam, J. Appl. Polym. Sci. 131 (7) (2014), https://doi.org/10.1002/app.40068.

[15] E. Mazzon, A. Habas-Ulloa, J.-P. Habas, Lightweight rigid foams from highly reactive epoxy resins derived from vegetable oil for automotive applications, Eur. Polym. J. 68 (2015) 546–557, https://doi.org/10.1016/j.eurpolymj.2015.03.064.

[16] L.A. Mondy, M. Celina, J.M. Kropka, E. Russick, R.R. Rao, In *Design Of Chemically Blown Epoxy Foams*, 27th World Congress of the Polymer Processing Society, Marrakech, Morocco, 2011. Marrakech, Morocco.

[17] Q. Ren, S. Zhu, One-pack epoxy foaming with CO2 as latent blowing agent, ACS Macro Lett. 4 (7) (2015) 693–697, https://doi.org/10.1021/acsmacrolett.5b00320.

[18] M.V. Alonso, M.L. Auad, S. Nutt, Short-fiber-reinforced epoxy foams, Compos. Appl. Sci. Manuf. 37 (11) (2006) 1952–1960, https://doi.org/10.1016/j.compositesa.2005.12.011.

[19] Y. Chang, Y. Luo, C. Xu, J. Zhao, Polysilazane as a new foaming agent to prepare high-strength, low-density epoxy foam, R. Soc. Open Sci. 6 (5) (2019), 182119, https://doi.org/10.1098/rsos.182119.

[20] B.E. Burgert, W.G. Moore, Polyepoxide Foam. US3373121A, 1968.

[21] A. Ito, T. Semba, K. Taki, M. Ohshima, Effect of the molecular weight between crosslinks of thermally cured epoxy resins on the CO2-bubble nucleation in a batch physical foaming process, J. Appl. Polym. Sci. 131 (12) (2014), https://doi.org/10.1002/app.40407.

[22] E.M. Russick, P.B. Rand, Epoxy Foams Using Multiple Resins and Curing Agents. US6110982A, 2000.

[23] R. Yadav, A. Shabeer, S. Sundararaman, K. Chandrashekhara, V. Flanigan, S. Kapila, Development and characterization of soy-based epoxy foams, Int. SAMPE Symp. Exhib. (Proc.) (2006) 51.

[24] J. Lyu, T. Liu, Z. Xi, L. Zhao, Effect of pre-curing process on epoxy resin foaming using carbon dioxide as blowing agent, J. Cell. Plast. 53 (2) (2017) 181–197, https://doi.org/10.1177/0021955x16639235.

[25] A.G. Loera, F. Cara, M. Dumon, J.P. Pascault, Porous epoxy thermosets obtained by a polymerization-induced phase separation process of a degradable thermoplastic polymer, Macromolecules 35 (16) (2002) 6291–6297, https://doi.org/10.1021/ma011567i.

[26] E. Soulé, M.G. de la Mata, J. Borrajo, P.A. Oyanguren, M.J. Galante, Reaction-induced phase separation in an epoxy/low molecular weight solvent system, J. Mater. Sci. 38 (13) (2003) 2809–2814, https://doi.org/10.1023/A:1024420132081.

[27] J. Kiefer, J.L. Hedrick, J.G. Hilborn, Macroporous thermosets by chemically induced phase separation, in: J.G. Hilborn, P. Dubois, C.J. Hawker, J.L. Hedrick, J. G. Hilborn, R. Jérôme, J. Kiefer, J.W. Labadie, D. Mecerreyes, W. Volksen (Eds.), Macromolecular Architectures, Springer Berlin Heidelberg, Berlin, Heidelberg, 1999, pp. 161–247, https://doi.org/10.1007/3-540-49196-1_4.

[28] J. Li, Z. Du, H. Li, C. Zhang, Porous epoxy monolith prepared via chemically induced phase separation, Polymer 50 (6) (2009) 1526–1532, https://doi.org/10.1016/j.polymer.2009.01.049.

[29] W.-T. Wang, L. Watkins, In *Flexible Epoxy Syntactic Foam Thermal Insulation For High Temperature Deepsea Reelable Pipelay Installations*, ASME 2010 29th International Conference on Ocean, Offshore and Arctic Engineering, 2010, pp. 269–273, https://doi.org/10.1115/omae2010-21014.

[30] M. Jalalian, Q. Jiang, A. Bismarck, Air templated macroporous epoxy foams with silica particles as property-defining additive, ACS Appl. Polym. Mater. 1 (3) (2019) 335–343, https://doi.org/10.1021/acsapm.8b00084.

[31] T.H.M. Lau, L.L.C. Wong, K.-Y. Lee, A. Bismarck, Tailored for simplicity: creating high porosity, high performance bio-based macroporous polymers from foam templates, Green Chem. 16 (4) (2014) 1931–1940, https://doi.org/10.1039/c3gc41807c.

[32] K.-Y. Lee, L.L.C. Wong, J.J. Blaker, J.M. Hodgkinson, A. Bismarck, Bio-based macroporous polymer nanocomposites made by mechanical frothing of acrylated epoxidised soybean oil, Green Chem. 13 (11) (2011) 3117–3123, https://doi.org/10.1039/C1GC15655A.

[33] W. Song, K. Barber, K.-Y. Lee, Heat-induced bubble expansion as a route to increase the porosity of foam-templated bio-based macroporous polymers, Polymer 118 (2017) 97–106, https://doi.org/10.1016/j.polymer.2017.04.058.

[34] W. Song, G. Konstantellos, D. Li, K.-Y. Lee, Short carbon fibre-reinforced epoxy foams with isotropic cellular structure and anisotropic mechanical response produced from liquid foam templates, Compos. Sci. Technol. 184 (2019), 107871, https://doi.org/10.1016/j.compscitech.2019.107871.

[35] W. Song, A. Magid, D. Li, K.-Y. Lee, Application of recycled carbon-fibre-reinforced polymers as reinforcement for epoxy foams, J. Environ. Manag. 269 (2020), 110766, https://doi.org/10.1016/j.jenvman.2020.110766.

[36] R. Zowada, R. Foudazi, Polyfoam: foam-templated microcellular polymers, Langmuir (2020), https://doi.org/10.1021/acs.langmuir.0c00932.

[37] C. Stubenrauch, A. Menner, A. Bismarck, W. Drenckhan, Emulsion and foam templating—promising routes to tailor-made porous polymers, Angew. Chem. Int. Ed. 57 (32) (2018) 10024–10032, https://doi.org/10.1002/anie.201801466.

[38] V.H. Bartl, W. Von Bonin, Über die Polymerisation in umgekehrter Emulsion, Makromol. Chem. 57 (1) (1962) 74–95, https://doi.org/10.1002/macp.1962.020570105.

[39] B.A. Dikici, F. Claeyssens, Basic principles of emulsion templating and its use as an emerging manufacturing method of tissue engineering Scaffolds, Front. Bioeng. Biotechnol. 8 (875) (2020), https://doi.org/10.3389/fbioe.2020.00875.

[40] T. Zhang, R.A. Sanguramath, S. Israel, M.S. Silverstein, Emulsion templating: porous polymers and beyond, Macromolecules 52 (15) (2019) 5445–5479, https://doi.org/10.1021/acs.macromol.8b02576.

[41] N.R. Cameron, High internal phase emulsion templating as a route to well-defined porous polymers, Polymer 46 (5) (2005) 1439–1449, https://doi.org/10.1016/j.polymer.2004.11.097.

[42] N.R. Cameron, D.C. Sherrington, High internal phase emulsions (HIPEs) - structure, properties and use in polymer preparation, Biopolym. Liquid Cryst. Polym. Phase Emulsion Adv. Polym. Sci. 126 (1996) 163–214, https://doi.org/10.1007/3-540-60484-7_4.

[43] K.J. Lissant, The Geometry of high-internal-phase-ratio emulsions, J. Colloid Interface Sci. 22 (1966) 7, https://doi.org/10.1002/macp.1962.020570105.

[44] F. Feuerabendt, M. Nithitanakul, P. Pakeyyangkoon, Poly(HIPEs), applications and modifications, Int. J. Eng. Res. Rev. 2 (1) (2014) 9.

[45] Q. Jiang, A. Bismarck, A perspective: is viscosity the key to open the next door for foam templating? React. Funct. Polym. 162 (2021), 104877 https://doi.org/10.1016/j.reactfunctpolym.2021.104877.

[46] J. Wang, C. Zhang, Z. Du, A. Xiang, H. Li, Formation of porous epoxy monolith via concentrated emulsion polymerization, J. Colloid Interface Sci. 325 (2) (2008) 453–458, https://doi.org/10.1016/j.jcis.2008.06.012.

[47] J. Wang, Z. Du, H. Li, A. Xiang, C. Zhang, Interconnected porous epoxy monoliths prepared by concentrated emulsion templating, J. Colloid Interface Sci. 338 (1) (2009) 145–150, https://doi.org/10.1016/j.jcis.2009.06.013.

[48] J. Tu, Z. Du, H. Li, C. Zhang, Development and characterization of porous epoxy monoliths via pore-initiated polymerization, Colloids Surf. A Physicochem. Eng. Asp. 375 (1–3) (2011) 68–75, https://doi.org/10.1016/j.colsurfa.2010.11.059.

[49] L. Anusha, Z. Zakaria, A.W.M. Kahar, D.N.U. Lan, Effect of emulsion temperature on properties of conductive epoxy porous prepared by single emulsion technique, IOP Conf. Ser. Mater. Sci. Eng. 429 (2018), 012061, https://doi.org/10.1088/1757-899x/429/1/012061.

[50] AccuPyc II 1345. https://www.micromeritics.com/product-showcase/AccuPyc-II-1340.aspx (accessed 12/02/2021)..

[51] E. Keng, Air and helium pycnometer, Powder Technol. 3 (1970) 179–180, https://doi.org/10.1016/0032-5910(69)80070-7.

[52] GeoPyc 1365 - Envelope Density Analyzer, Micromeritics Instrument Corporation, 2016. https://www.micromeritics.com/Repository/Files/geopyc-1365_brochure_2017.pdf.

[53] S.S. Manley, P. Steindl, G.F. Hewitt, A. Bismarck, An integrated method for measuring gas permeability and diffusivity of porous solids, Chem. Eng. Sci. (2020) 223, https://doi.org/10.1016/j.ces.2020.115725.

[54] P.C. Carman, Flow of Gases through Porous Media, Butterworths Scientific Publications, Belfast, 1956, p. 69.

[55] L. Korson, W. Drost-Hansen, F.J. Millero, Viscosity of water at various temperatures, J. Phys. Chem. 73 (1) (1969) 34–39, https://doi.org/10.1021/j100721a006.

[56] H. Corporation, Araldite, 2012, https://samaro.fr/pdf/FT/Araldite_FT_2020_EN.pdf, 2020.

[57] ASTM E799-03(2020)e1, Standard Practice for Determining Data Criteria and Processing of Liquid Drop Size Analysis, ASTM International, West Conshohocken, PA, 2020, https://doi.org/10.1520/E0799-03R20E01. www.astm.org.

[58] R. Foudazi, HIPEs to PolyHIPEs, React. Funct. Polym. 164 (2021), 104917, https://doi.org/10.1016/j.reactfunctpolym.2021.104917.

[59] S.S. Manley, N. Graeber, Z. Grof, A. Menner, G.F. Hewitt, F. Stepanek, A. Bismarck, New insights into the relationship between internal phase level of emulsion

templates and gas-liquid permeability of interconnected macroporous polymers, Soft Matter 5 (23) (2009) 4780–4787, https://doi.org/10.1039/b900426b.
[60] M.F. Ashby, R.F.M. Medalist, The mechanical properties of cellular solids, Metall. Trans. A 14 (9) (1983) 1755–1769, https://doi.org/10.1007/BF02645546.
[61] L.J. Gibson, M.F. Ashby, Cellular Solids: Structure and Properties, 2 ed., Cambridge University Press, Cambridge, 1997 https://doi.org/10.1017/CBO9781139878326.
[62] E. Crawford, A.J. Lesser, The effect of network architecture on the thermal and mechanical behavior of epoxy resins, J. Polym. Sci. B Polym. Phys. 36 (8) (1998) 1371–1382, https://doi.org/10.1002/(SICI)1099-0488(199806)36:8<1371::AID-POLB11>3.0.CO;2-4.
[63] E.G. Karayannidou, D.S. Achilias, I.D. Sideridou, Cure kinetics of epoxy–amine resins used in the restoration of works of art from glass or ceramic, Eur. Polym. J. 42 (12) (2006) 3311–3323, https://doi.org/10.1016/j.eurpolymj.2006.08.025.
[64] Á. Conejero-García, H.R. Gimeno, Y.M. Sáez, G. Vilariño-Feltrer, I. Ortuño-Lizarán, A. Vallés-Lluch, Correlating synthesis parameters with physicochemical properties of poly(glycerol sebacate), Eur. Polym. J. 87 (2017) 406–419, https://doi.org/10.1016/j.eurpolymj.2017.01.001.
[65] J.A. Schroeder, P.A. Madsen, R.T. Foister, Structure/property relationships for a series of crosslinked aromatic/aliphatic epoxy mixtures, Polymer 28 (6) (1987) 929–940, https://doi.org/10.1016/0032-3861(87)90165-0.
[66] M. Pramanik, E.W. Fowler, J.W. Rawlins, Another look at epoxy thermosets correlating structure with mechanical properties, Polym. Eng. Sci. 54 (9) (2014) 1990–2004, https://doi.org/10.1002/pen.23749.
[67] T. Yang, C. Zhang, X. Hou, J. Cheng, J. Zhang, The network structure and properties of multifunctional epoxy/anhydride systems, High Perform. Polym. 28 (7) (2016) 854–860, https://doi.org/10.1177/0954008315604203.
[68] S.A. Pellice, D.P. Fasce, R.J.J. Williams, Properties of epoxy networks derived from the reaction of diglycidyl ether of bisphenol A with polyhedral oligomeric silsesquioxanes bearing OH-functionalized organic substituents, J. Polym. Sci. B Polym. Phys. 41 (13) (2003) 1451–1461, https://doi.org/10.1002/polb.10494.
[69] V. Pistor, F.G. Ornaghi, H.L. Ornaghi, A.J. Zattera, Dynamic mechanical characterization of epoxy/epoxycyclohexyl–POSS nanocomposites, Mater. Sci. Eng., A 532 (2012) 339–345, https://doi.org/10.1016/j.msea.2011.10.100.
[70] L.W. Hill, Calculation of crosslink density in short chain networks, Prog. Org. Coating 31 (3) (1997) 235–243, https://doi.org/10.1016/S0300-9440(97)00081-7.
[71] J.S. Nakka, K.M.B. Jansen, L.J. Ernst, Effect of chain flexibility in the network structure on the viscoelasticity of epoxy thermosets, J. Polym. Res. 18 (6) (2011) 1879–1888, https://doi.org/10.1007/s10965-011-9595-5.
[72] J.L. Valentín, J. Carretero-González, I. Mora-Barrantes, W. Chassé, K. Saalwächter, Uncertainties in the determination of cross-link density by equilibrium swelling experiments in natural rubber, Macromolecules 41 (13) (2008) 4717–4729, https://doi.org/10.1021/ma8005087.

Supplementary information for

Permeable emulsion-templated porous polyepoxides

Patrick Steindl[a], Angelika Menner[a] and Alexander Bismarck[a,b,*]

[a]Polymer and Composite Engineering (PaCE) Group, Institute of Materials Chemistry and Research, University of Vienna, Währinger Strasse 42, 1090 Vienna, Austria

[b]Department of Chemical Engineering, Imperial College London, South Kensington Campus, London, SW7 2AZ, UK.

[*]Corresponding author email: alexander.bismarck@univie.ac.at

Figure S1: A photograph of buckets containing a mechanically frothed epoxy formulation Epoxy L (EPL) and hardener GL1, purchased from R&G Faserverbundwerkstoffe GmbH (Waldenbuch, Germany) formulation, which started curing during frothing in an industrial mixer (Henschel). We had to discharge the curing formulation quickly from the mixer and distinguish the fire. The material remaining in the mixer we had to remove mechanically – a time consuming undertaking. The highly exothermic curing reaction of epoxy resins can easily result in charring of the resin and even fire of the material, if the heat cannot be dissipated properly, which is difficult if the material contains in excess of 70 vol.% dispersed air.

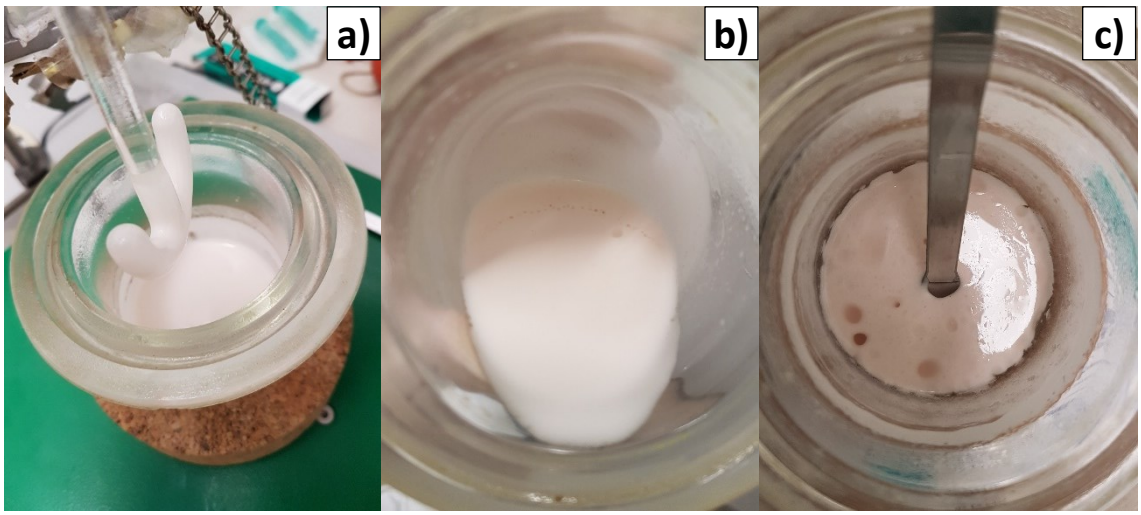

Figure S2: Creamy stable w/epoxy resin emulsion templates

S3 details the procedure used for the determination of pore throat diameters using the software package ImageJ

1. Open an SEM image
2. Calibrate the measuring tool of the software by drawing a line of the length of the scale bar of the micrograph and entering Analyze – Set Scale. ‚Known distance' and ‚unit of length' are adjusted.
3. Select the whole image or the area that you want to analyse
4. Edit the image so that the pore throats/pores/particles stand out against the background. This can be achieved for instance by the following steps (from the menus) : Process - Enhance contrast/Filter – Minima/Smooth, Image - Adjust – Auto local threshold (method: Sauvola). Alternative or additional processing steps can include: Process – FFT – Bandpass filter, Image – Adjust – Threshold (choose B&W in the right drop-down menu).
5. Analyse the objects of interest: Analyze – Analyze particles; adjust 'Size' and 'Circularity' for more accurate results.
6. Save the final result or copy it to a software of your choice (e.g. MS Excel, Origin) and calculate parameters of interest.

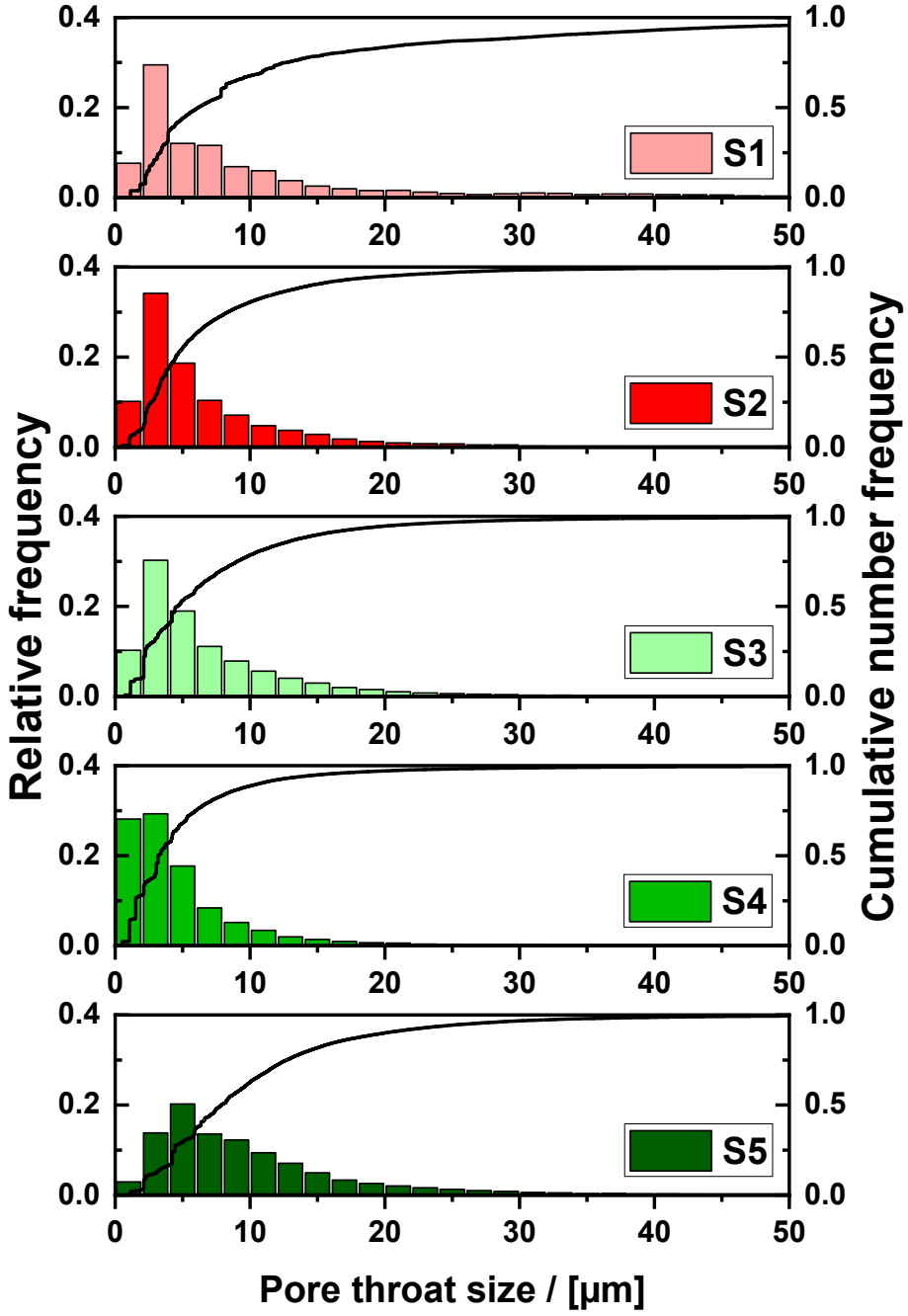

Figure S4: Pore throat size distributions for polyepoxide foams S1-S5.

Table S5: Summarises the various pore dimensions D[1,0], D[2,0], D[3,0], D[3,2], D[4,3], D10, D50, D90, D_{v10}, D_{v50}, D_{v90}, Span and Mode, and the numbers of pores N_p used to determine these parameters. For further details please refer to ASTM E799-03.[1]

in [µm]	S1 16%/49%IP	S2 16%/56%IP	S3 20%/49%IP	S4 20%/54%IP	S5 20%/60%IP
D[1,0]	28.3	31.3	34.6	37.6	48.3
D[2,0]	70.4	65.8	63.2	67.1	91.3
D[3,0]	137.0	122.8	94.5	98.3	136.4
D[3,2]	518.8	426.8	211.4	210.8	303.9
D[4,3]	655.5	590.8	276.2	267.9	381.7
D10	8.4	9.0	6.9	7.3	9.4
D50/Median	15.0	19.2	15.7	17.8	19.8
D90	39.5	56.5	86.1	144.7	137.8
D_{v10}	400.5	290.5	135.8	134.4	193.5
D_{v50}	631.2	603.9	250.7	262.5	373.1
D_{v90}	828.4	802.2	455.2	379.5	583.8
Span	2.1	2.5	5.0	7.7	6.5
Mode	10.1	20.3	30.4	15.0	3.2
N_p	3860	3783	4150	3705	2253

1. ASTM E799-03(2020)e1, Standard Practice for Determining Data Criteria and Processing of Liquid Drop Size Analysis, ASTM International, West Conshohocken, PA, 2020, www.astm.org, https://dx.doi.org/10.1520/E0799-03R20E01

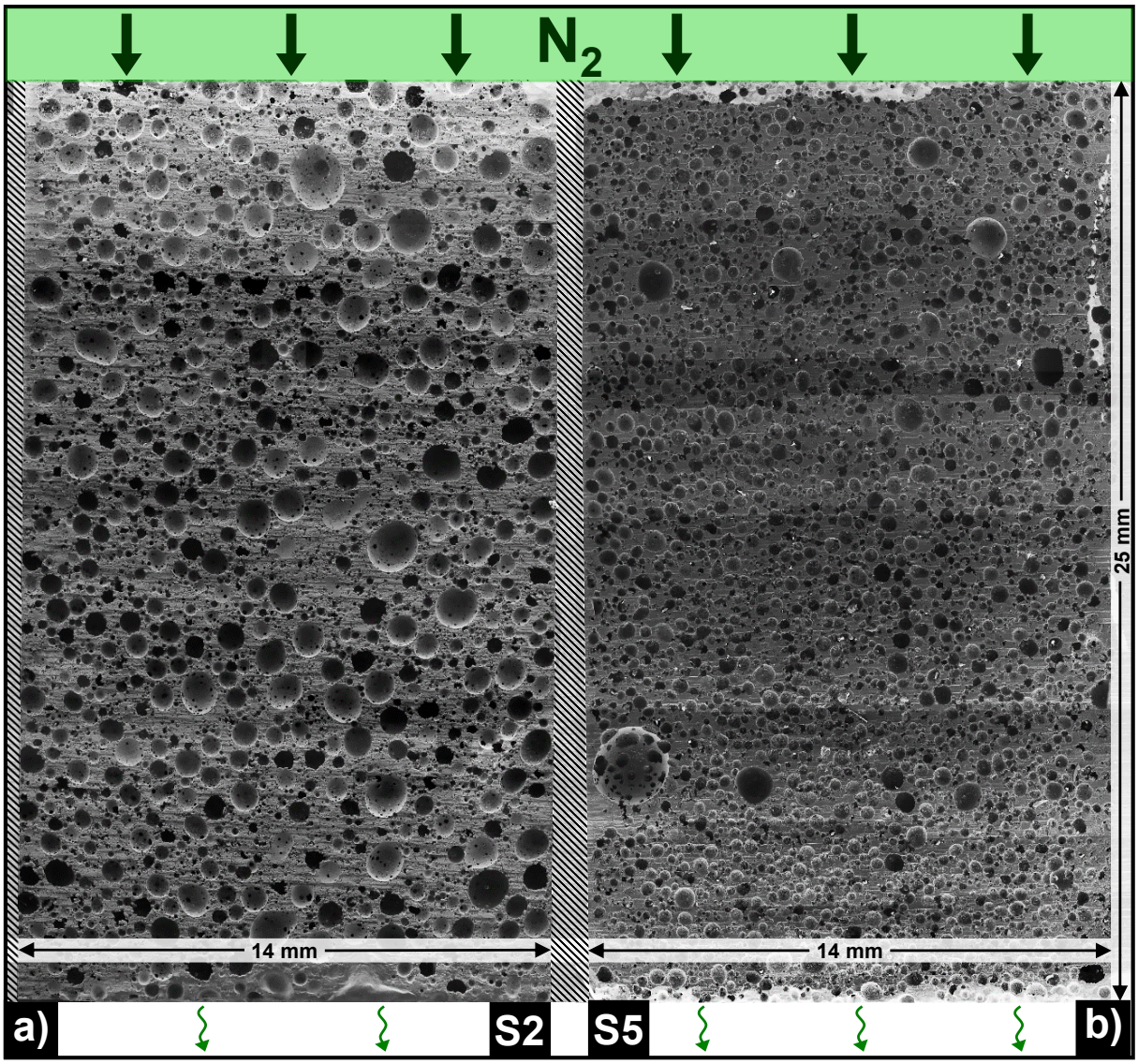

Figure S6: SEM micrographs of S2 (a) and S5 (b): entire cross sections of samples prepared for gas permeability tests were analysed.

Table S7: Solvents used in the swelling tests: molar volumes V_m and Hildebrand solubility parameters δ_s were used to estimate Flory-Huggins parameters χ as a measure of polymer-solvent interaction.

Solvent	Relative polarity[a]	Molar volume[b] V_s [$cm^3 \cdot mol^{-1}$]	Molar weight M_s [$g \cdot mol^{-1}$]	Hildebrand solubility parameter[b] δ [$(MPa)^{1/2}$]	Flory-Huggins parameter χ
Isopropanol	0.546	76.8	66.10	22.5	0.34
DMSO	0.444	71.3	78.13	29.7	0.46
DMF (N,N)	0.386	77.0	73.09	21.7	0.35
Acetone	0.355	74.0	58.08	20.3	0.46
THF	0.207	81.7	72.11	18.6	0.79
Benzene	0.111	89.4	78.11	18.8	0.78
Diesel oil					

[a] values are taken from 'Solvents and Solvent Effects in Organic Chemistry', Wiley-VCH, 2011, 2nd edition, doi:10.1002/9783527632220

[b] taken from 'Polymer Handbook', Brandrup/Immergut/Grulke, Wiley-VCH, 2003, 4th edition, ISBN 0-471-16628-6

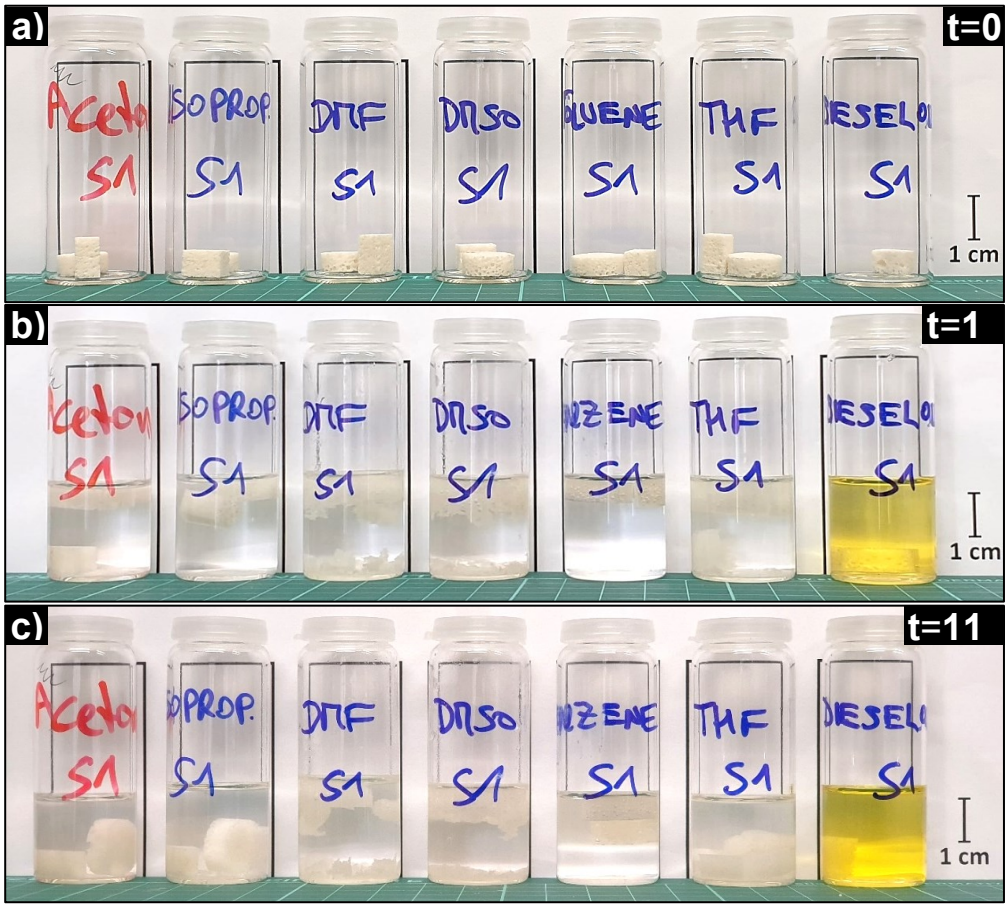

Figure S8: Epoxy polyMIPEs at different stages of the swelling test: a) before solvent addition, b) after one day and c) after eleven days of immersion.

Due to the short interval of 1h at the beginning of the testing series and considering the time necessary to measure weight and dimensions of all foam cubes, the focus was first set only on S1, S3, S5. Later on, data for S2 and S4 was also recorded (**Figure S9** & **Figure S10).**

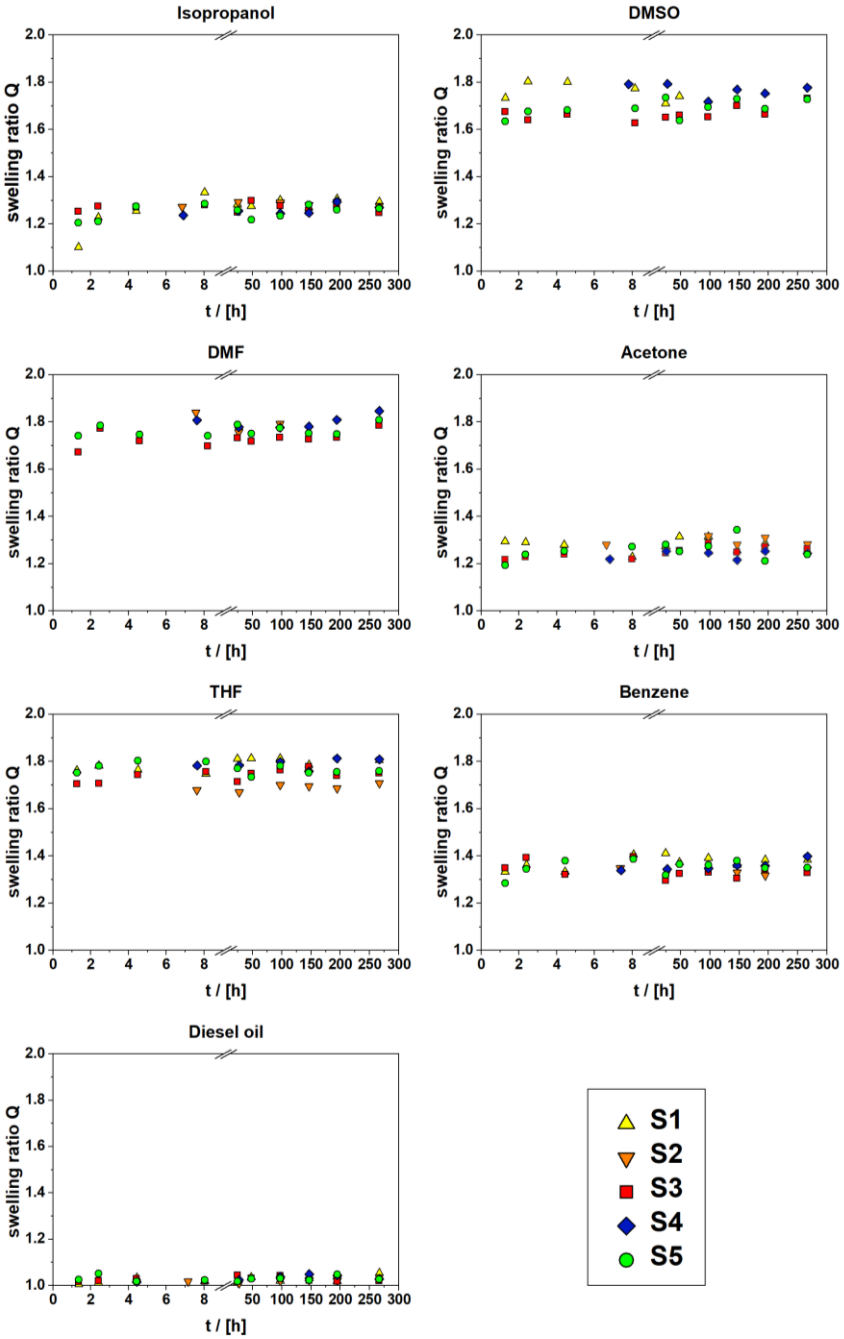

Figure S9: Swelling ratios of polyepoxide foams S1-S5 isopropanol, DMSO, DMF, acetone, THF, benzene and Diesel oil as function of immersion time.

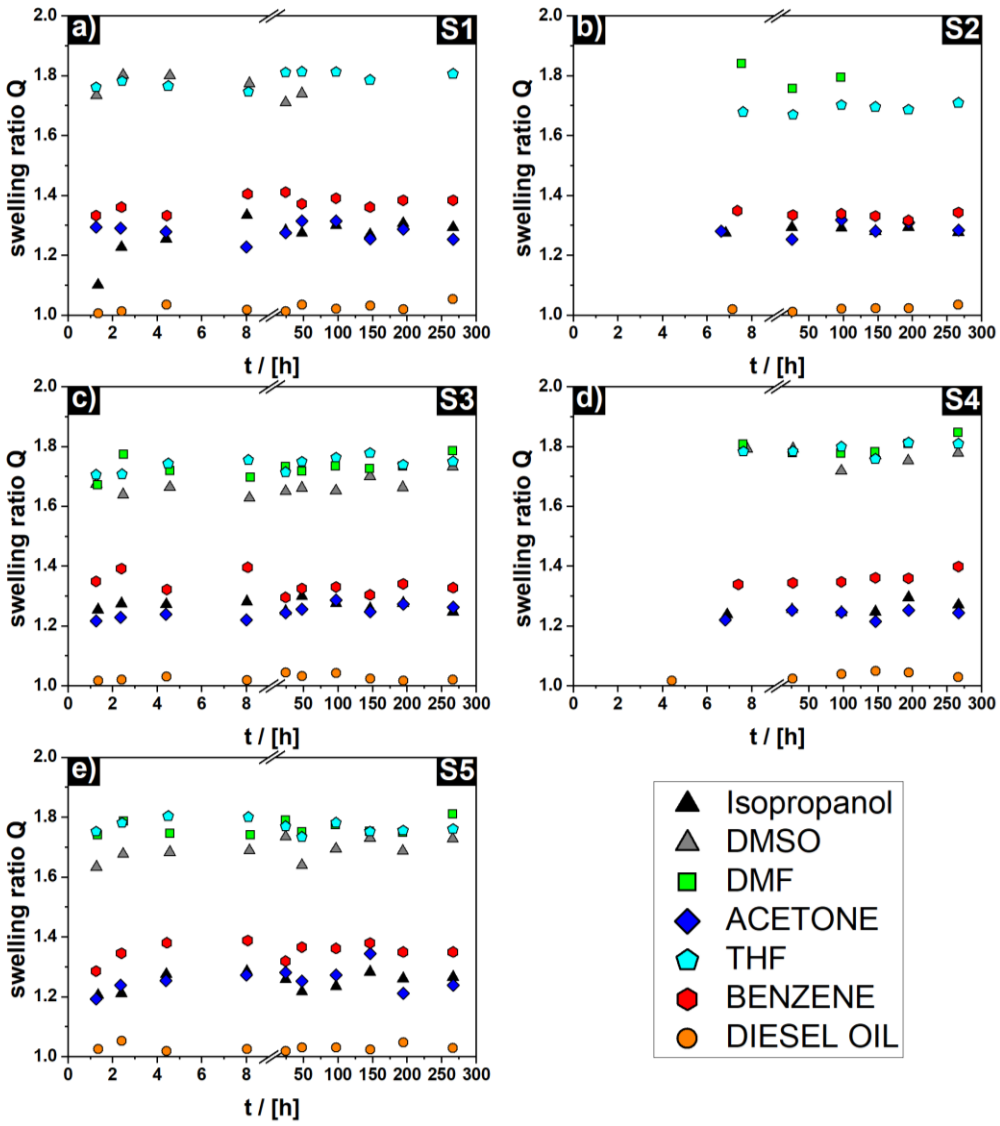

Figure S10: Swelling ratios of foams S1-S5 in solvents with varying polarity. List of solvents seen in the figure legend.

Table S11: Summary of swelling ratios *Q*, their standard deviations and polymer-volume fraction φ_p as well as percentage weight loss after extraction $\omega_{def,sw}$ in various solvents.

		Q	STDEV	φ_p	$\omega_{def,sw}$
Isopropanol	**S1**	1.29	0.016	0.78	-8%
	S2	1.29	0.008	0.78	-8%
	S3	1.27	0.020	0.79	-11%
	S4	1.26	0.021	0.79	-11%
	S5	1.25	0.026	0.80	-10%
DMSO	**S1**	1.76	0.040 f	0.57	-
	S2	-	-	-	-
	S3	1.68	0.034	0.59	-13%
	S4	1.76	0.029	0.57	-12%
	S5	1.70	0.037	0.59	-16%
DMF	**S1**	-	-	-	-
	S2	1.80	0.041	0.56	-
	S3	1.74	0.026	0.58	-14%
	S4	1.80	0.030	0.56	-13%
	S5	1.77	0.026	0.57	-13%
Acetone	**S1**	1.28	0.030	0.78	-8%
	S2	1.29	0.026	0.78	-9%
	S3	1.26	0.015	0.79	-11%
	S4	1.24	0.015	0.81	-11%
	S5	1.25	0.024	0.80	-12%
THF	**S1**	1.80	0.013	0.55	-15%
	S2	1.69	0.015	0.59	-10%
	S3	1.76	0.015	0.57	-12%
	S4	1.79	0.022	0.56	-12%
	S5	1.76	0.017	0.57	-15%
Benzene	**S1**	1.38	0.012	0.73	-5%
	S2	1.33	0.010	0.75	-4%
	S3	1.33	0.013	0.75	-6%
	S4	1.36	0.022	0.73	-6%
	S5	1.36	0.013	0.73	-7%
Diesel oil	**S1**	1.03	0.014	0.97	57%
	S2	1.02	0.008	0.98	30%
	S3	1.03	0.010	0.97	53%
	S4	1.04	0.010	0.96	51%
	S5	1.03	0.009	0.97	45%

S12: All compression responses showed three distinct regions, as expected for this kind of material. A sharp initial increase, recognisable by the direct proportionality of loading force and displacement, depicted the linear elastic region. It commonly extends to a strain of 5% and represents the reversible deformation/bending of the cell walls. While in the elastic region the energy absorbed due to internal friction is used to restore the original shape of the test specimen, mechanical energy is irretrievably lost when the polyMIPEs are compressed beyond their elastic limits.

Subsequently, the curves levelled off and transitioned into the rubber plateau, which is characterised by compression of cells and buckling of cell walls. The slightly positive profile of this region indicated the elastomeric nature of the foams and moreover suggested a certain contribution of closed cells to the compressive responses. On deformation, the gas in closed cells is compressed, the cell gas pressure increasingly contributes to the stiffness of a material and causes a positive slope in the plastic region. In fully open porous materials, on the contrary, compression induces an airflow out of the material, creating viscous forces, which contribute substantially less than the gas pressure and hence leads to almost horizontal plateaus. The rapid rise in stress around 40-50% strain was due to the onset of densification, going along with cell walls crushing into each other and total compaction.

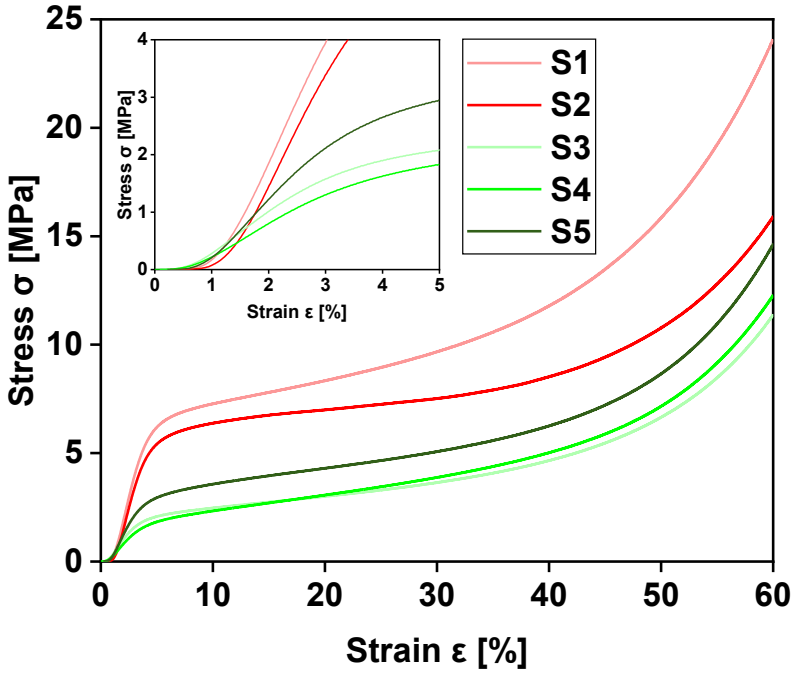

Figure S13: Stress-strain curves of poly(epoxide)MIPEs S1-S5

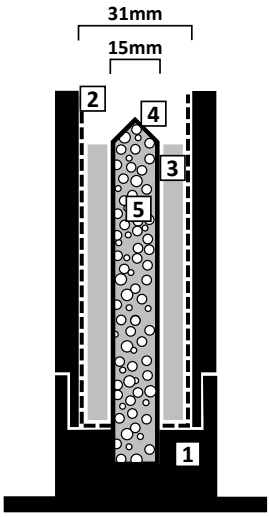

Figure S14: 1) PTFE-mold; 2) thin film of release agent; 3) two-component epoxy system Araldite®2020 (embedding medium); 4) coating to seal the porous monolith; 5) epoxy foam (base: Araldite®2020)

S15:

The theoretical average molecular weight between crosslinks at full conversion $M_{c,th}$ was calculated for Araldite®2020 using the composition of the epoxy system and the functionalities of its components using the following equation:

$$M_{c,th} = \frac{2\left(M_e + \sum_{f=2}^{\infty} \frac{M_f}{f} \Phi_f\right)}{\sum_{f=3}^{\infty} \Phi_f}$$

where M_e is the epoxide equivalent weight (EEW) of the resin, M_f the molecular weight of a hardener with amine functionality f and Φ_f the mol fraction of active amine hydrogens (AHEW), only relevant if more than one curing agent is used. In this case, **Eq. S15**) can be simplified and rewritten as $M_{c,th} = 2(EEW+AHEW)$.

Paper III (*published*)

Emulsion-templated flexible epoxy foams. **Steindl, P.**; Decker, H.; Retzl, B.; Jiang, Q.; Menner, A.; Bismarck, A. Polymer, 2021, 215, article 123380

Polymer 215 (2021) 123380

Contents lists available at ScienceDirect

Polymer

journal homepage: http://www.elsevier.com/locate/polymer

Emulsion-templated flexible epoxy foams

Patrick Steindl [a], Helena Decker [a], Bernhard Retzl [a], Qixiang Jiang [a,**], Angelika Menner [a], Alexander Bismarck [a,b,*]

[a] Polymer and Composite Engineering (PaCE) Group, Institute of Materials Chemistry and Research, University of Vienna, Währinger Strasse 42, 1090, Vienna, Austria
[b] Department of Chemical Engineering, Imperial College London, South Kensington Campus, London, SW7 2AZ, UK

ARTICLE INFO

Keywords:
Flexible epoxy foam
Emulsion templating
Hysteresis
Energy loss coefficient

ABSTRACT

Flexible epoxy foams were successfully prepared by curing medium internal phase emulsions (MIPEs) with a continuous organic phase containing epoxy resin and hardener, surfactant and carbon nanotubes and an aqueous internal phase. Curing the MIPEs at ambient temperature resulted in interconnected polyepoxide foams with average pore size of about 10 μm, while curing the MIPEs (with carbon nanotubes as a thickening agent) at 50 °C resulted in epoxy foams with pore sizes of one magnitude higher. The polyepoxide foams were compressible up to a strain of 70% of their original height and did not fracture. The polyepoxide foams were resilient with energy loss coefficients ranging from 40% to 60%, representing their energy adsorption during cyclic loading.

1. Introduction

Macroporous flexible polymers are important materials in various applications. Commercially, flexible polyurethane (PU) and natural rubber foams occupy a large segment in the market of cushioning and soundproof materials for furniture and automotive applications. Other applications of flexible macroporous polymers are being explored by researchers, such as spring elements for energy harvesters [1], scaffolds for tissue engineering [2], flexible sensors [3,4], adsorbents [5,6] and separation media [7,8]. Physical and chemical blowing is a mature process to produce a wide range of flexible polymer foams, including PU foams on industrial scale. Other methods, such as particle leaching [9], templating [10], phase separation [11,12] and incorporating hollow spheres (e.g. syntactic foams) [13], have also been developed. Emulsion templating, first reported in 1962 by Bartl and von Bonin [14], is a method to produce macroporous polymers with well-defined morphologies [15–18]. Emulsions with monomers in the continuous but minor phase and an internal templating phase are produced. Emulsions with an internal phase volume ratio over 74.05% are called high and below 74.05% medium internal phase emulsions or HIPEs and MIPEs, respectively. The polymerisation of the continuous phase and the subsequent removal of the internal phase result in macroporous polymers called polyHIPEs and polyMIPEs. The droplets in the emulsion templates are the template for the pores in the resulting polymer foams and thus determine their shape, size and volume fraction, i.e. porosity. As compared to blowing methods, emulsion templating is advantageous because the liquid nature of the emulsion precursors, allows for casting or moulding the emulsions into complex shapes thus allowing to produce foams with complex net-shapes [19].

Emulsion templates with a variety of monomers have been used to produce flexible macroporous polymers. By choosing suitable (meth) acrylate based monomers and crosslinkers (e.g. using long chain crosslinkers) and tuning the monomer-to-crosslinker ratio in the emulsion templates flexible poly (meth)acrylate foams have been produced [20]. McGann et al. [21] copolymerised poly (ethylene glycol) diacrylate, sodium/calcium polyacrylate and poly (N-isopropylacrylamide) in the continuous phase of emulsion templates to produce flexible macroporous films for wound dressings.

Polycaprolactone containing methacrylate groups were synthesised and used as monomers in emulsion templates, which were photocured to produce flexible scaffolds for cell supports [22]. Our group has developed polyurethane diacrylate and ethylhexyl acrylate based emulsion templates [23]. The emulsion templates have been deposited and UV-polymerised on dielectrics to form cage walls. The reversibly compressible polyacrylate foams served as microspring and spacer elements in energy harvesters. David and Silverstein reported PU foams synthesised in emulsion templates [24]. The PU foams can be compressed up to a strain of 60% at a stress of only 0.01 MPa. The PU foams

* Corresponding author. Polymer and Composite Engineering (PaCE) Group, Institute of Materials Chemistry and Research, University of Vienna, Währinger Strasse 42, 1090, Vienna, Austria.
** Corresponding author.,
E-mail addresses: qixiang.jiang@univie.ac.at (Q. Jiang), alexander.bismarck@univie.ac.at (A. Bismarck).

https://doi.org/10.1016/j.polymer.2021.123380
Received 31 October 2020; Received in revised form 24 December 2020; Accepted 3 January 2021
Available online 6 January 2021

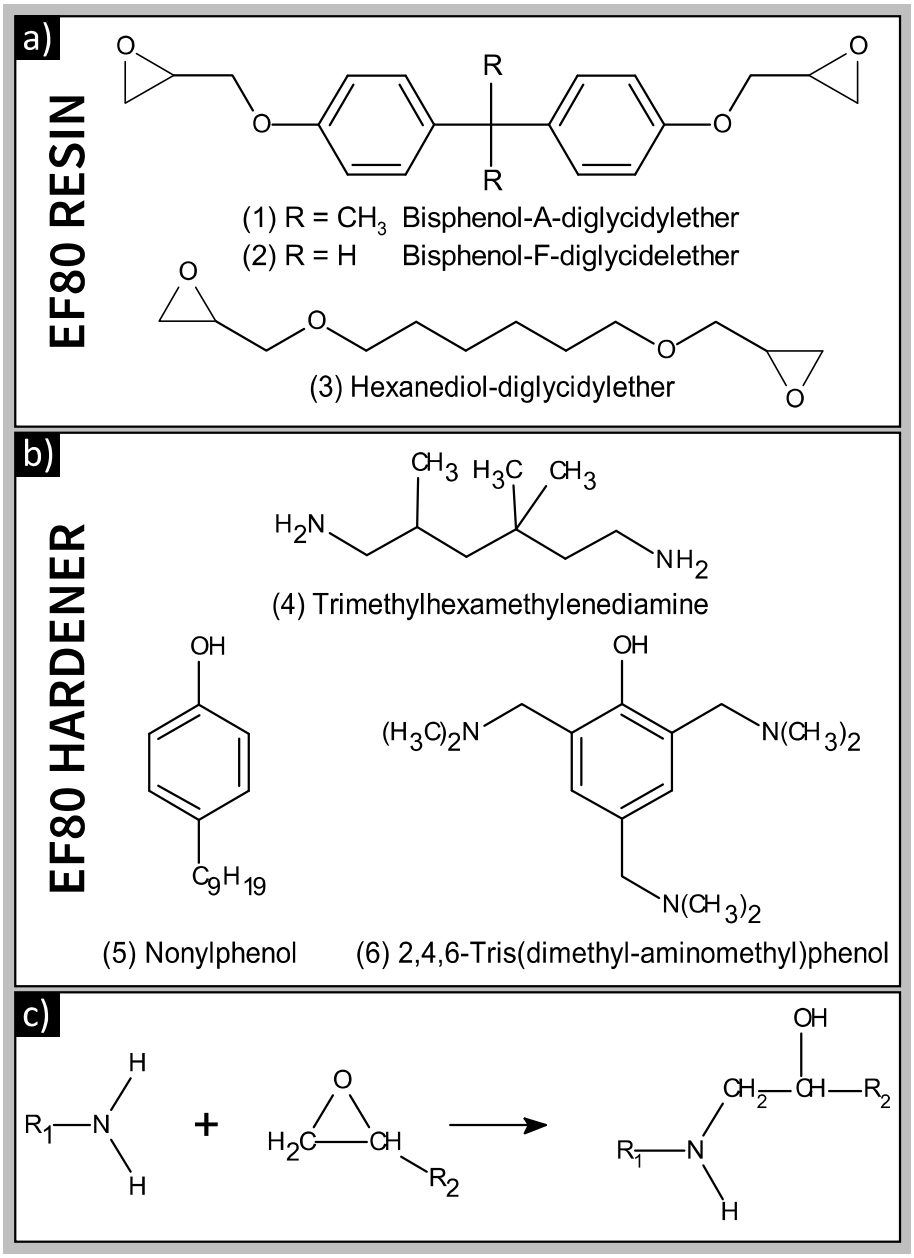

Fig. 1. The main components of EF80 resin (a) and hardener (b). The reaction of amine groups (hardener) with glycidyl groups (resin) is the main curing reaction of epoxies (c).

were synthesised in monomer-in-water emulsions, thus the reaction between water and isocynate moieties created CO_2 bubbles, leading to a bi-model pore distribution in the resultant PU foams. Thereafter, flexible PU foams have also been produced from monomer-in-paraffin oil emulsions [25]. Tebboth et al. [26] produced emulsion templated silicon rubber foams, which possessed closed cell structures. As a result, the flexible rubber foams can be inflated under certain conditions, such as vacuum, rendering them potentially useful in self-sealing containers. Silicone rubber sponges have also been synthesised by emulsion templating. The open-porous rubber foams were modified and used as adsorbents for oil spills. The flexibility of the rubber foams allows them to be squeezed to recover the adsorbed oil [27]. Highly resilient macroporous polymers have been developed by our group [28]. Divinylbenzene and trimethylolpropane tris(3-*mer*-captopropionate) were used as monomers and UV polymerised in emulsion templates. The produced foams were cyclically compressible by strains of 70% and with an energy loss of only 7%.

Flexible epoxy foams are versatile functional materials and found applications as adhesives [29], encapsulants [30], resilient and insulating coatings for subsea equipment [31] and cover stocks for automotive interiors [32]. Flexible epoxy foams have been produced by blowing methods [32,33]. However, so far, only rigid epoxy foams have been produced by emulsion templating [34,35], while emulsion templated flexible epoxy foams have not been reported.

We aimed to produce flexible epoxy foams by emulsion templating to enrich the monomer choices of emulsion templated elastomers. The morphological, physical and mechanical properties of the epoxy foams were investigated. Furthermore, cyclic compression tests were performed to examine reversible compressibility and durability of these polymer foams.

Table 1
Composition and curing temperature of emulsion templates based on epoxy formulations.

	Continuous phase				Internal phase	
	EF80 resin [vol %][a]	EF80 hardener [vol%][a]	Pluronic L-81 [vol %][a]	MWCNTs [wt%][b]	aq. $CaCl_2$·$2H_2O$ [vol %][c]	Curing temperature [°C]
S1	36.4	54.6	9	0	60	23
S2	36.4	54.6	9	0.4	60	23
S3	36.4	54.6	9	0.4	60	50
S4	36.4	54.6	9	0.8	60	50
S5	36.4	54.6	9	1.2	60	50
S6	36.4	54.6	9	0.4	70	50

[a] With respect to the volume of the continuous phase.
[b] Wt% CNT relative to the monomers.
[c] Relative to the total emulsion volume.

2. Experimental section

2.1. Materials

Two-component (resin and hardener) epoxy system EF80 (Fig. 1), whose main components are bisphenol-A (epichlorohydrin) and 1,6-hexanediol diglycidyl ether, was purchased from Easy Composites (Staffordshire, United Kingdom), poly (ethylene glycol)-block-poly (propylene glycol)-block-poly (ethylene glycol) (Pluronic L-81) and calcium chloride dihydrate ($CaCl_2$·$2H_2O$) from Sigma Aldrich. Multi-walled carbon nanotubes (MWCNTs) and modified silica nanoparticles (HDK H18) were kindly provided by Arkema (Lacq, France) and Wacker Chemie AG (Germany), respectively. All chemicals were used as received.

2.2. Preparation of emulsion templates and poly(epoxide)MIPEs

Emulsions were prepared in a reaction vessel with a three-neck flat flange lid, which was fitted with a dropping funnel and an anchor-shaped glass paddle rod driven by an overhead stirrer (Phoenix Instruments RSO-20D). MWCNTs were homogenised in the epoxy resin for 5 min at a stirring speed of 10,000 rpm. The mixture of resin and MWCNTs, hardener and surfactant was then transferred into the reaction vessel. The aqueous internal phase, containing 10 g/l $CaCl_2$·$2H_2O$ as electrolyte, was added dropwise to the organic phase under stirring at a speed of 400 rpm, until an internal phase ratio of 60 or 70 vol% was reached. Once the addition of the aqueous phase was finished, the stirring speed was increased to 1000 rpm for 2 min to homogenise the emulsion. The MIPEs were transferred into free standing polypropylene centrifuge (Falcon®) tubes and cured at 23 °C or 50 °C for 24 h. Afterwards, the polyMIPEs were washed with distilled water and dried at 50 °C until constant weight. The compositions and curing conditions of the MIPEs used to produce epoxide foams S1–S6 are listed in Table 1.

2.3. Characterisation of the polyMIPEs

Pore morphology of the polyMIPEs was investigated using scanning electron microscopy (SEM, JCM-6000 Neoscope, JEOL Ltd., Eching, Germany). The polyMIPEs were mounted on a SEM stub using a conductive carbon sticker. Prior to observation, the facture surface of the polyMIPEs were gold-coated using a fine coater (JFC-1200, JEOL Ltd., Eching, Germany) to achieve sufficient electrical conductivity. The SEM was operated in secondary electron mode at an acceleration voltage of 15 kV. SEM images were further analysed using the software ImageJ. At least 150 pores and pore throats were measured to determine the average pore and pore throat diameters, d_p and d_{pt}, respectively.

The ***foam densities*** ρ_f of the polyMIPEs were determined on cuboids with a dimension of 10 mm × 15 mm x 15 mm. After calculating their volumes from the measured dimensions and weighing the foams, their foam densities were calculated from weight over volume. ***Skeletal densities*** ρ_s were determined by helium displacement pycnometry (AccuPyc II 1340, Micromeritics Ltd., Aachen, Germany). About 0.1 g of the polyMIPE fragments were measured. The percentage porosity P of the monolithic polyMIPEs was calculated by:

$$P\left(1\frac{\rho_f}{\rho_s}\right).100\% \quad (1)$$

Mechanical properties of the macroporous foams were tested under compression using a universal mechanical testing frame (Instron Series 5969, Instron Ltd., Buckinghamshire, UK) equipped with a 1 kN load cell. The polyMIPEs were cut into cuboids of dimensions 10 mm × 15 mm x 15 mm. Tests were carried out at room temperature with a compression speed of 1 mm/min. The specimens were compressed by 70% of their initial height. The elastic modulus E_c was determined from the slope of the initial linear region of the stress-strain curves. The crush strength σ_c, which is the maximum strength at the end of the initial linear elastic section, was obtained from the interception point of the extensions of linear regressions to the initial and second (plateau) linear regions. For each polyMIPE at least five specimens were tested.

Durability and reversibility of the polyMIPEs were investigated by means of cyclic compression tests, which were carried out using the same equipment. The specimens were of same size and shape as for the compression tests. In each compression cycle, the specimens were compressed by a desired strain (10%, 20%, 50% and 70% of their original height, respectively) at a loading rate of 5 mm/min; the cross-head of the testing machine unloaded at the same rate to zero point to allow for the recovery of the specimens. The polyMIPEs were cyclically compressed for 200 cycles. The stress-strain curves of each loading and unloading cycle were recorded. The area enclosed by the loading and unloading curves S_{load} and S_{unload}, respectively, was obtained by integrating the curves using software (OriginPro 2019b). The energy loss coefficient ELC [36], sometimes also referred to as loss ratio [37] or hysteresis ratio [28], was calculated as follows:

$$ELC = \frac{S_{load} - S_{unload}}{S_{load}} \quad (2)$$

Residual strains were determined as the strains of the unloading curves when the stresses reached zero.

3. Results and discussion

S1 was produced from emulsion templates containing epoxy resin, hardener and surfactant in the continuous phase. It had been noted that the emulsion template was stable even without surfactant, due to the amphiphilic nature of the hardener (**ESI S1**) and the high viscosity of the epoxy formulation, which kinetically stabilised the emulsions during the curing at 23 °C. However, curing such surfactant-free emulsions led to predominantly closed-cell polyMIPEs, which did not dry completely. Curing the emulsion template with surfactant, e.g. emulsion template of S1, resulted in an open porous polyMIPE (Fig. 2a and b), with pore diameters of 6 ± 1 μm and pore throat sizes of 3 ± 1 μm (Table 2). S1 possessed a skeletal density of 1.11 g/cm^3 and a foam density of 0.44 g/cm^3, resulting in a porosity of 60%. This was as expected as the polyMIPE was synthesised using a MIPE template with an internal phase ratio of 60% (Table 1).

To shorten the curing time of the epoxy foams, we attempted to cure the MIPEs at 50 °C. However, the surfactant stabilised MIPEs were not stable enough to endure the curing step; phase separation occurred prior to solidification of the epoxy foams. To improve the stability of the MIPEs, MWCNTs were added to the organic phase of the emulsion. Emulsion templates with 0.4 wt% MWCNTs (of S2) were also cured at 23 °C. S2 had within errors identical density and porosity, but increased average pore and pore throat sizes as compared to S1 (Fig. 2c and d,

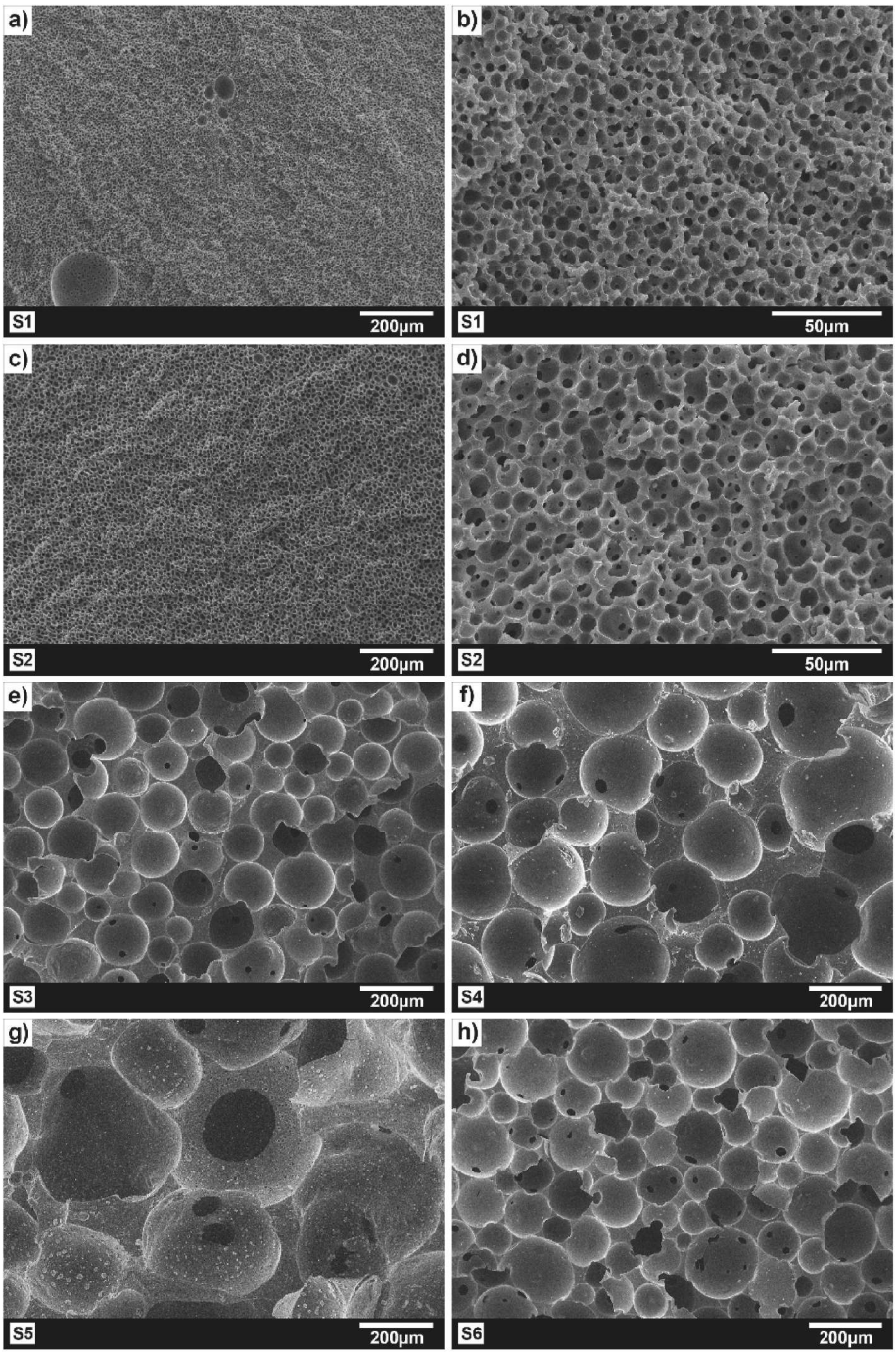

Fig. 2. Characteristic SEM images of poly(epoxide)MIPEs S1–S6. S1–S5 were produced from MIPEs with internal phase ratio of 60%. S1 and S2 were produced from MIPEs without and in presence of MWCNTs, respectively, and cured at 23 °C. S3–S5 were produced from MIPEs with 0.4 wt%, 0.8 wt% and 1.2 wt% MWCNTs and cured at 50 °C. S6 was produced from MIPEs with 70% internal phase volume ratio.

Table 2). This could be due to the increased viscosity of the continuous phase in the emulsions of S2. The identical mixing energy was insufficient to break the droplets down to the size in the MIPEs of S1 (e.g. approximately 6 µm). S3 was produced by curing an epoxy-based emulsion template containing surfactant and 0.4 wt% MWCNTs at 50 °C. The resulting foam exhibited a slightly higher foam density and decreased porosity than expected (Table 2). This could be due to loss of internal phase from the emulsion template during curing. S3 possessed a pore structure with spherical pores interconnected by pore throats; however, the pore and pore sizes (112 ± 26 µm and 21 ± 14 µm, respectively, Table 2) were much larger than those of S1 and S2 (Fig. 2e). PolyMIPE S2 of identical composition as polyMIPE S3 did not possess such large pores, which does indicate that the emulsion template of S3 underwent droplet coalescence during curing at 50 °C, resulting in much larger droplets than present in its initial MIPE template. When cured at 50 °C, the droplet coalescence of the emulsion templates was accelerated due to the decreased viscosity of the liquid mixture of epoxy resin, hardener and surfactant. However, the presence of MWCNTs in the continuous phase of the emulsion resulted in an increased viscosity and, consequently, arrested droplet coalescence. Therefore, the MIPEs did not undergo phase separation but contained large droplets, resulting after curing in polyMIPEs with large pores. In this manuscript, we

Table 2
Morphological and mechanical properties of the prepared epoxy foams.

	ρ_s [g/cm^3]	ρ_f [g/cm^3]	P [%]	d_p [μm]	d_{pt} [μm]	E_c [MPa]	σ_c [MPa]
S1	1.11 ± 0.01	0.44 ± 0.02	60 ± 1	6 ± 1	3 ± 1	0.25 ± 0.01	0.034 ± 0.003
S2	1.11 ± 0.01	0.42 ± 0.03	63 ± 2	14 ± 4	5 ± 1	0.32 ± 0.02	0.039 ± 0.005
S3	1.10 ± 0.01	0.48 ± 0.05	56 ± 5	112 ± 26	21 ± 14	0.30 ± 0.02	0.038 ± 0.003
S4	1.14 ± 0.01	0.41 ± 0.01	64 ± 2	170 ± 50	40 ± 30	0.21 ± 0.01	0.028 ± 0.001
S5	1.15 ± 0.01	0.39 ± 0.01	67 ± 2	400 ± 100	90 ± 50	0.19 ± 0.01	0.030 ± 0.002
S6	1.11 ± 0.01	0.32 ± 0.01	71 ± 1	118 ± 35	23 ± 13	0.20 ± 0.03	0.026 ± 0.010

utilised CNTs as the rheology modifier in the emulsion templates due to the 2D shape of CNTs; other functioning thickening agents, e.g. modified silica nanoparticles, were also good candidates for this purpose (**ESI S2**).

MWCNT loading in the MIPEs was increased to 0.8 wt% and 1.2 wt% (for S4 and S5, respectively). The MIPEs were stable and could be cured at 50 °C. The resulting polyMIPEs S4 and S5 possessed open porous structures with larger pores and pore throats up to 400 μm as compared to S3. An explanation for the large pores was, as mentioned for the MIPEs of S1 and S2, the larger droplets in the as-prepared MIPEs of S4 and S5 caused by the highly viscous continuous phase containing an increased amount of MWCNTs. Furthermore, the dispersion of MWCNTs in the epoxy formulations was poor due to the high MWCNT loading (as indicated by the distribution of the MWCNTs in S5, Fig. 3) and low energy input during mixing. As a result, during the curing, the MWCNTs still arrested the coalescence of the droplets but may not be as efficient as in the MIPEs with 0.4 wt% MWCNTs (of S3), resulting in polyMIPEs with larger pores after curing.

Emulsion templates of S6 containing epoxy formulation, 0.4 wt% MWCNT and surfactant in the continuous phase and an internal phase volume ratio of 70% were successfully produced. However, due to the viscosity of the continuous phase, it was impossible to increase the internal phase volume further. S6 had a porosity of 70%. The polyMIPE S6 exhibited an open-porous structure with large average pore and pore throat sizes, which were identical within error to those of S3 (Table 2). If no Pluronic L81 was used it was still possible to produce macroporous epoxy foams with 60% and 70% porosity by emulsion templating. The emulsions had to contain CNTs and be cured at 50 °C. The resulting foams had an open-celled, interconnected pore structure comparable to that of S3 and S6 (**ESI, S3**).

The polyMIPEs were compressed by a strain of 70% of their original height. The stress-strain curves of the polyMIPEs (Fig. 4) had initial linear elastic regions, extending up to 10% strain, representing the elastic deformation of the polyMIPEs. The curves then levelled off and entered a plateau region. The absence of a clear inflection point is tantamount to a rather indistinct transition from the linear elastic to the plateau region. The latter ended at a strain of 45–50%. In the last section of the stress-strain curves, stress increased rapidly as function of strain because of densification of the polyMIPEs. Until the end of the tests at 70% compression, no visible failure (e.g. breaking, cracking or tearing) was observed and after unloading the polyMIPEs could recover to their original height. The elastic moduli of the prepared polyMIPEs S1–S6 ranged from 0.2 MPa to 0.3 MPa and crush strengths from 0.02 MPa to 0.04 MPa, with foam densities between 0.3 g/cm^3 and 0.5 g/cm^3 (Table 2). Both, moduli and strengths, increased with increasing foam densities and thus followed the well-established Gibson-Ashby correlation (Fig. 5) [38,39].

The relationship between the stiffness and pore sizes of foam materials have been investigated in several studies [40–44]. It is anticipated that for elastomeric foam materials, the pore sizes and interconnectivity play an important role, as they affect the gas release from the foam, [45] while the mechanical properties of rigid foam materials are dominated by the stiffness of the pore walls. S1 and S2, cured at room temperature, showed the characteristic polyMIPE morphology with small pores and pore throats; yet the diameters of the pore throats were as large as 50% of those of the pores, resulting in "channels" in the foam structure. On the other hand, S3–S6 were characterised by large pores and pore throats. However, the distribution of pore throats per pore was random, leading to a number of closed pores. The normalised modulus (elastic

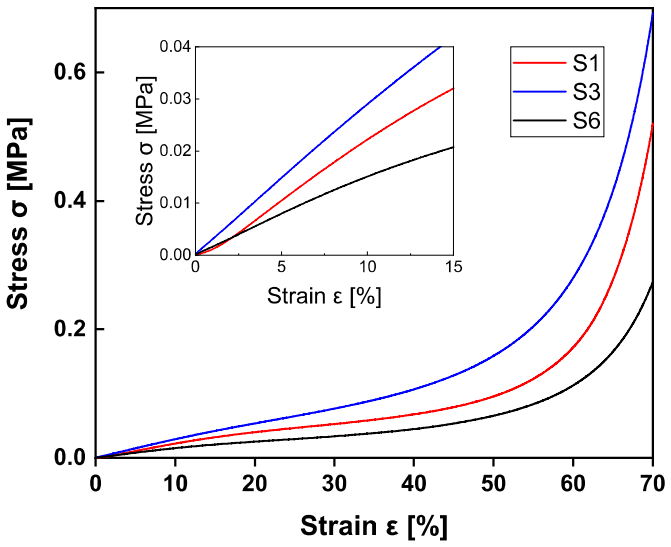

Fig. 4. Characteristic compression stress-strain curves of three representative epoxy foams.

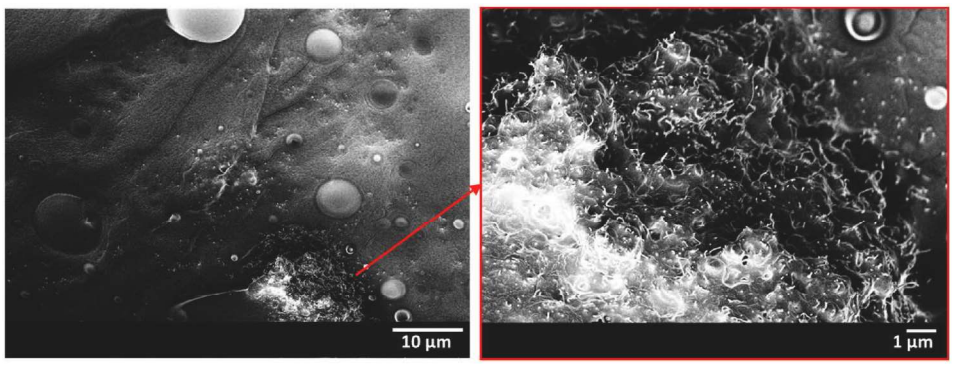

Fig. 3. Distribution of 1.2 wt% MWCNTs in epoxy based polyMIPEs S5.

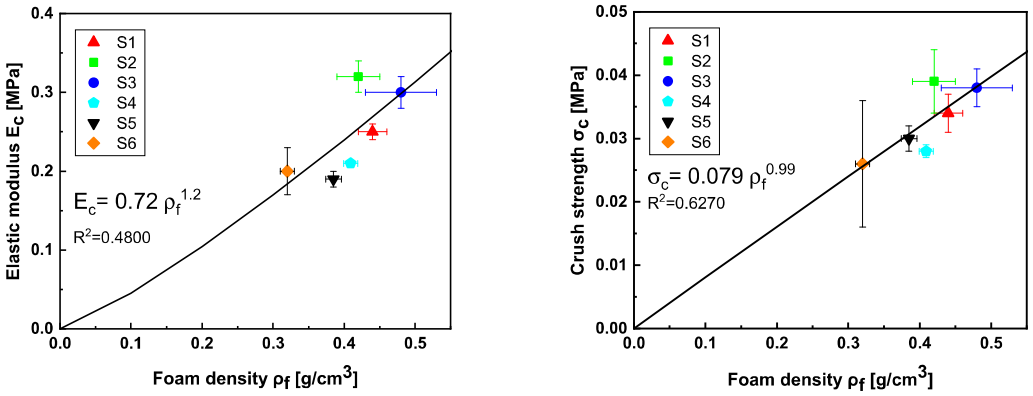

Fig. 5. Elastic moduli E_c (left) and crush strengths σ_c (right) of polyMIPEs as function of their foam density ρ_f.

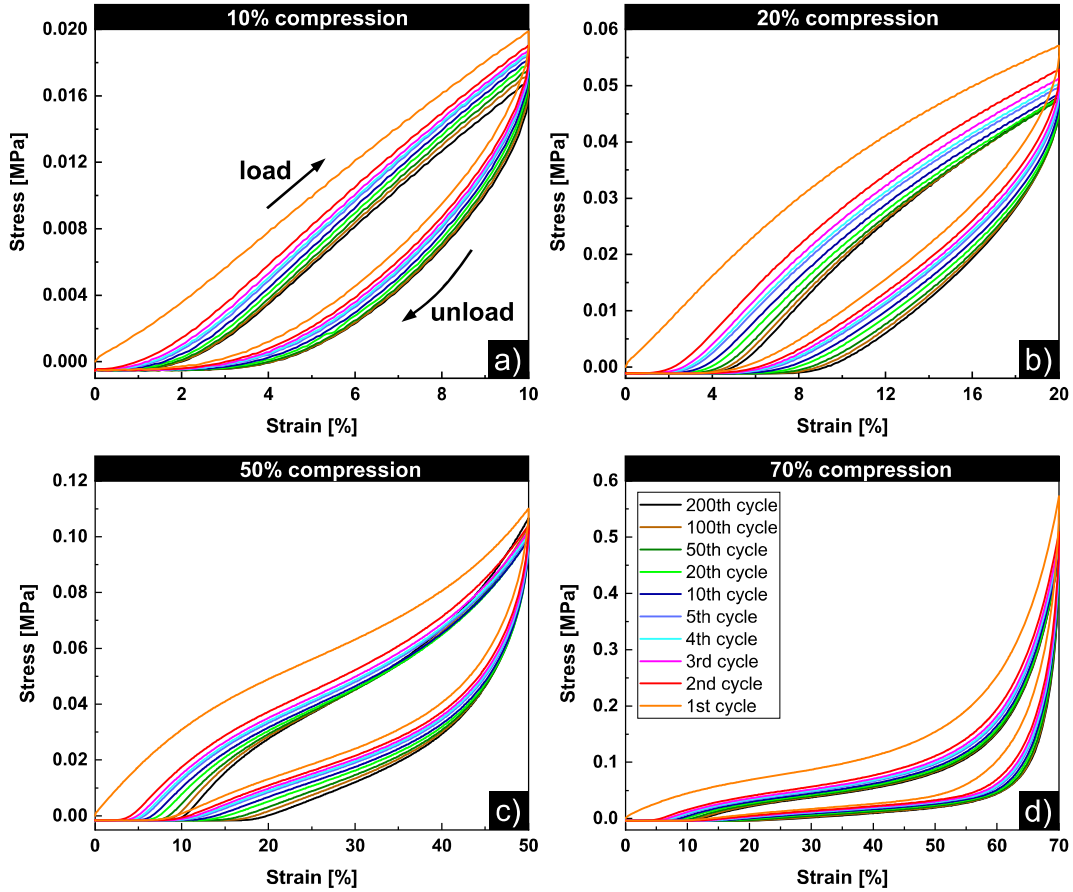

Fig. 6. Cyclic stress-strain curves of S6, representative for all samples. Tests were performed to compression amplitudes of (a) 10%, (b) 20%, (c) 50% and (d) 70%.

modulus over foam density) of S1 was 0.57 MPa/(g/cm^3), while that of S2 was 0.76 MPa/(g/cm^3) probably due to the presence of CNTs. The normalised modulus of S3, however, was only 0.63 MPa/(g/cm^3), despite its identical composition as S2. This indicated that the larger pores with randomly distributed yet large pore throats did assist the air release from the foam during compression, while small pores and pore throats hindered the gas release from the foam, resulting in a small increase of the stiffness. A further increase in pore and pore throat sizes of S4 and S5 resulted in normalised moduli of 0.51 MPa/(g/cm^3) and 0.49 MPa/(g/cm^3), respectively. Although the CNTs loadings in S4 and S5 were different from those in S2 and S3, the decreased normalised moduli could also partially attributed to the increased pore and pore throat sizes as discussed.

The epoxy foams S1–S3 and S6 were subjected to cyclic compression tests at predefined strain amplitudes of 10%, 20%, 50% and 70% for 200 cycles. These strains were selected because they represented the poly-MIPEs' mechanical behaviour at the end of the first linear region, beginning of the linear plateau region, the end of the plateau region and the densification (Fig. 4). Within each loading cycle, the unloading curve shifted downwards as compared to the loading curve. The lower stress of an unloading curve as compared to that at corresponding strain of the loading curve was because of the viscoelastic behaviour of the poly(epoxide)MIPEs [45,46]. During compression the polymer chains were deformed elastically, while slippage of polymer chains occurred simultaneously. The elastic deformation of the polymer chains recovered and responded (in stress) instantly during unloading, while the

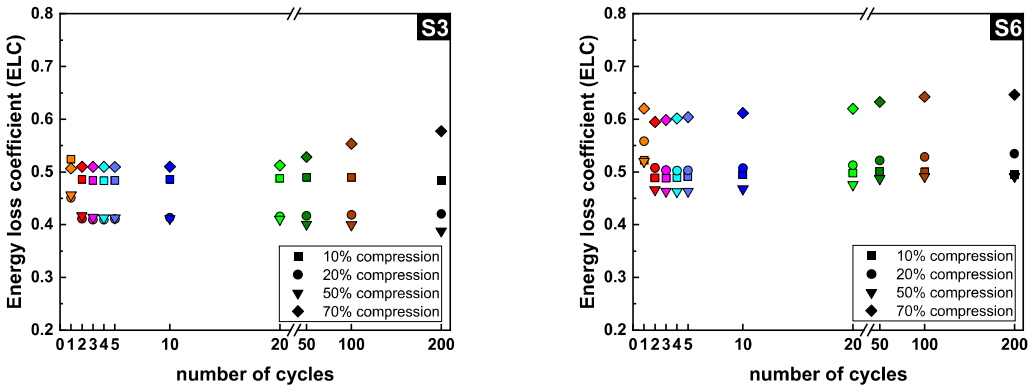

Fig. 7. Characteristic energy loss coefficients as function of cycle numbers (the plot of S3 and S6, the plots of the other polyMIPEs are included in ESI).

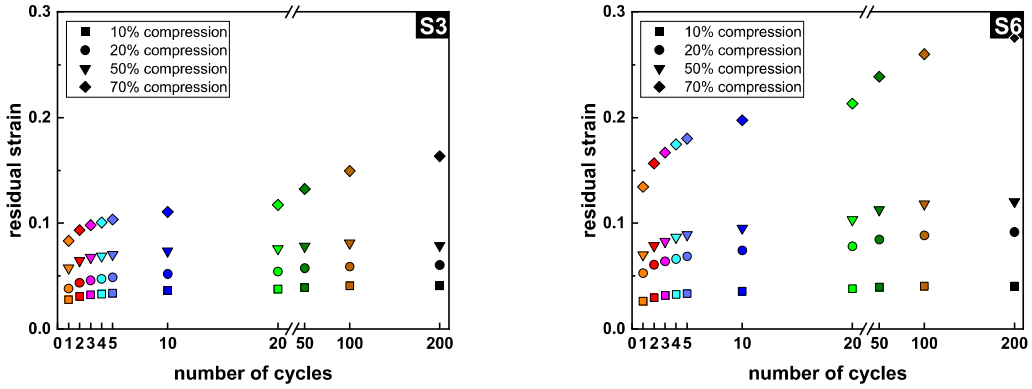

Fig. 8. Characteristic residual strains as function of cycle numbers for poly (epoxide)MIPEs S3 and S6. (the plots of the other polyMIPEs are included in ESI) The residual strain increases significantly within the first loading-unloading cycles. The lower the strain level, the faster the approach of a steady state.

slippage (viscous deformation) of the polymer chains did not recover simultaneously, leading to a lower stress. With increasing cycle numbers, the loading and unloading curves shifted downwards (Fig. 6). This softening effect, due to the relaxation of the polymer chains or networks, has been reported in work on rubbery materials [47–54]. The softening effect was most significant in the first cycle, represented by a large drop of the loading and unloading curve in the second cycle. The softening effect then became marginal as shown by gradually overlapping loading and unloading curves in the following cycles (Fig. 6). These phenomena are consistent with many previous findings [28,37, 53–57].

The percentage of the adsorbed energy was determined by the ratio of the area between the loading and unloading curve and the area beneath the loading curve in each cycle (Eq.(2), ESI Fig. S6). All polyMIPEs had ELCs ranging from 0.4 to 0.6, indicating an energy absorption of 40%–60% by the foams, within the 200 loading cycles (Fig. 7). This was because of the viscoelasticity of the polyMIPEs. In the first and second loading cycles, the ELC experienced a reduction, corresponding to the pronounced softening effect in these two cycles. Afterwards, the ELC of most of the polyMIPEs reached constant values; this phenomenon was also observed in our previous work on flexible polyHIPEs [23,28]. However, in some cyclic loading tests, e.g. S3 and S6 loaded to a strain of 70%, the ELC increased slightly after 20 cycles (Fig. 7, ESI Figure S6). Our hypothesis is that the cyclic loading could cause some pore walls to stick to each other and closure of pore throats. With increasing loading cycles, the closure of pore throats became more influential and hindered the recovery of the polyMIPEs by impeding air flowing back into the pore structure during unloading.

The polyMIPEs do not recover their shape fully when unloaded, i.e. no stress applied. Fig. 6 shows this residual strain. The residual strains were higher when the polyMIPEs were compressed by higher strains (Fig. 8, Fig. S7). Again, the residual strain increased within the first couple of loading cycles and then reached a constant value. For some of the foams, the residual strains increased from 20 loading cycles, which was corresponding to the increased energy adsorption after 20 loading cycles. It is noted that S3 and S6, which had identical polymer phase formulation and average pore and pore throat size but different porosities (Table 2), had residual strains of 0.16 and 0.29, respectively, when being compressed by 70% (Fig. 8). With a higher porosity, S6 did require more air to flow back into the polyMIPE to assist the recovery of the foams during unloading.

4. Conclusions

Emulsion templates containing epoxy resin, hardener, surfactant and carbon nanotubes in the continuous phase and an aqueous internal phase with a volume ratio up to 70% were cured to produce flexible macroporous polyepoxides. Emulsion templated epoxy foams cured at 23 °C possessed an open-porous structure with an average pore size of about 10 μm. Curing of the emulsion templates at 50 °C required the presence of MWCNTs (or hydrophobized silica particles) in the continuous phase in order to raise the viscosity of the resin phase to arrest droplet coalescence. However, the emulsion templates still underwent some droplet coalescence and the polyMIPEs cured at 50 °C had pore sizes of about 110 μm. Increasing the MWCNT loading in the MIPEs resulted in increased pore sizes up to 400 μm of the cured epoxy foams. The polyMIPEs were compressed by 70% of their original height without showing visible failure and characterised by elastic moduli of up to 0.3 MPa and crush strengths of up to 0.04 MPa. The polyMIPEs endured the loading and unloading of at least 200 cycles; they had energy loss coefficients, representing their energy adsorption during cyclic loading, ranging from 40% to 60%, indicating their potential application as

cushioning and packaging materials.

Declaration of competing interest

The authors declare that they have no known competing financial interests or personal relationships that could have appeared to influence the work reported in this paper.

Acknowledgements

The authors acknowledge the support of the Austrian Science Fund (FWF) through the project I1800 for funding PS and the EU for FP7-NMP project MATFLEXEND (grant #: 604093) for funding QJ.

Appendix A. Supplementary data

Supplementary data to this article can be found online at https://doi.org/10.1016/j.polymer.2021.123380.

References

[1] H. Zhang, Y. Lu, A. Ghaffarinejad, P. Basset, Progressive contact-separate triboelectric nanogenerator based on conductive polyurethane foam regulated with a Bennet doubler conditioning circuit, Nanomater. Energy 51 (2018) 10–18, https://doi.org/10.1016/j.nanoen.2018.06.038.

[2] S. Evlashin, P. Dyakonov, M. Tarkhov, S. Dagesyan, S. Rodionov, A. Shpichka, M. Kostenko, S. Konev, I. Sergeichev, P. Timashev, I. Akhatov, Flexible polycaprolactone and polycaprolactone/graphene scaffolds for tissue engineering, Materials 12 (18) (2019) 2991, https://doi.org/10.3390/ma12182991.

[3] J. Kim, S. Kwon, S. Seo, K. Park, in: Highly Wearable Galvanic Skin Response Sensor Using Flexible and Conductive Polymer Foam, 2014, pp. 6631–6634, https://doi.org/10.1109/EMBC.2014.6945148, 2014 36th Annual International Conference of the IEEE Engineering in Medicine and Biology Society, 26-30 Aug. 2014.

[4] M. Pruvost, W.J. Smit, C. Monteux, P. Poulin, A. Colin, Polymeric foams for flexible and highly sensitive low-pressure capacitive sensors, npj Flexible Electronics 3 (1) (2019) 7, https://doi.org/10.1038/s41528-019-0052-6.

[5] G.M. Nisola, L.A. Limjuco, E.L. Vivas, C.P. Lawagon, M.J. Park, H.K. Shon, N. Mittal, I.W. Nah, H. Kim, W.-J. Chung, Macroporous flexible polyvinyl alcohol lithium adsorbent foam composite prepared via surfactant blending and cryo-desiccation, Chem. Eng. J. 280 (2015) 536–548, https://doi.org/10.1016/j.cej.2015.05.107.

[6] A. Mohammadi, M.M. Lakouraj, M. Barikani, Preparation and characterization of p-tert-butyl thiacalix[4]arene imbedded flexible polyurethane foam: an efficient novel cationic dye adsorbent, React. Funct. Polym. 83 (2014) 14–23, https://doi.org/10.1016/j.reactfunctpolym.2014.07.003.

[7] D. Danninger, F. Hartmann, W. Paschinger, R. Pruckner, R. Schwödiauer, S. Demchyshyn, A. Bismarck, S. Bauer, M. Kaltenbrunner, Stretchable polymerized high internal phase emulsion separators for high performance soft batteries, Advanced Energy Materials 10 (19) (2020), https://doi.org/10.1002/aenm.202000467, 2000467.

[8] N.T.P. Phong, N.V.K. Thanh, P.H. Phuong, Fabrication of antibacterial water filter by coating silver nanoparticles on flexible polyurethane foams, J. Phys. Conf. 187 (2009), 012079, https://doi.org/10.1088/1742-6596/187/1/012079.

[9] Q. Chai, Y. Huang, T.L. Kirley, N. Ayres, Shape memory polymer foams prepared from a heparin-inspired polyurethane/urea, Polym. Chem. 8 (34) (2017) 5039–5048, https://doi.org/10.1039/C7PY00204A.

[10] L. Liu, L. Bai, A. Tripathi, J. Yu, Z. Wang, M. Borghei, Y. Fan, O.J. Rojas, High axial ratio nanochitins for ultrastrong and shape-recoverable hydrogels and cryogels via ice templating, ACS Nano 13 (3) (2019) 2927–2935, https://doi.org/10.1021/acsnano.8b07235.

[11] G. Wang, H. Uyama, Facile synthesis of flexible macroporous polypropylene sponges for separation of oil and water, Sci. Rep. 6 (1) (2016) 21265, https://doi.org/10.1038/srep21265.

[12] C. Schugens, V. Maquet, C. Grandfils, R. Jerome, P. Teyssie, Polylactide macroporous biodegradable implants for cell transplantation. II. Preparation of polylactide foams by liquid-liquid phase separation, J. Biomed. Mater. Res. 30 (4) (1996) 449–461. https://dx.doi.org/10.1002/(sici)1097-4636(199604)30:4<449::Aid-jbm3>3.0.Co;2-p.

[13] A.S. Alex, D. Thomas, S.K. Manu, N. Sreenivas, V. Sekkar, C. Gouri, Addition-cure, room temperature vulcanizing silicone elastomer based syntactic foams with glass and ceramic microballoons, Polym. Bull. 75 (2) (2018) 747–767, https://doi.org/10.1007/s00289-017-2052-9.

[14] V.H. Bartl, W. Von Bonin, Über die Polymerisation in umgekehrter Emulsion, Makromol. Chem. 57 (1) (1962) 74–95, https://doi.org/10.1002/macp.1962.020570105.

[15] N.R. Cameron, High internal phase emulsion templating as a route to well-defined porous polymers, Polymer 46 (5) (2005) 1439–1449, https://doi.org/10.1016/j.polymer.2004.11.097.

[16] B.A. Dikici, F. Claeyssens, Basic principles of emulsion templating and its use as an emerging manufacturing method of tissue engineering scaffolds, Frontiers in Bioengineering and Biotechnology 8 (875) (2020), https://doi.org/10.3389/fbioe.2020.00875.

[17] T. Zhang, R.A. Sanguramath, S. Israel, M.S. Silverstein, Emulsion templating: porous polymers and beyond, Macromolecules 52 (15) (2019) 5445–5479, https://doi.org/10.1021/acs.macromol.8b02576.

[18] M.S. Silverstein, Emulsion-templated porous polymers: a retrospective perspective, Polymer 55 (1) (2014) 304–320, https://doi.org/10.1016/j.polymer.2013.08.068.

[19] C. Sherborne, R. Owen, G.C. Reilly, F. Claeyssens, Light-based additive manufacturing of PolyHIPEs: controlling the surface porosity for 3D cell culture applications, Mater. Des. 156 (2018) 494–503, https://doi.org/10.1016/j.matdes.2018.06.061.

[20] Y. Tunc, N. Hasirci, K. Ulubayram, Synthesis of emulsion-templated acrylic-based porous polymers: from brittle to elastomeric, Soft Mater. 10 (4) (2012) 449–461, https://doi.org/10.1080/1539445X.2010.532848.

[21] C.L. McGann, B.C. Streifel, J.G. Lundin, J.H. Wynne, Multifunctional polyHIPE wound dressings for the treatment of severe limb trauma, Polymer 126 (2017) 408–418, https://doi.org/10.1016/j.polymer.2017.05.067.

[22] B. Aldemir Dikici, C. Sherborne, G.C. Reilly, F. Claeyssens, Emulsion templated scaffolds manufactured from photocurable polycaprolactone, Polymer 175 (2019) 243–254, https://doi.org/10.1016/j.polymer.2019.05.023.

[23] Q. Jiang, H. Barkan, A. Menner, A. Bismarck, Micropatterned, macroporous polymer springs for capacitive energy harvesters, Polymer 126 (2017) 419–424, https://doi.org/10.1016/j.polymer.2017.04.018.

[24] D. David, M.S. Silverstein, Porous polyurethanes synthesized within high internal phase emulsions, J. Polym. Sci. Polym. Chem. 47 (21) (2009) 5806–5814, https://doi.org/10.1002/pola.23624.

[25] H. Gui, G. Guan, T. Zhang, Q. Guo, Microphase-separated, hierarchical macroporous polyurethane from a nonaqueous emulsion-templated reactive block copolymer, Chem. Eng. J. 365 (2019) 369–377, https://doi.org/10.1016/j.cej.2019.02.015.

[26] M. Tebboth, Q. Jiang, A. Kogelbauer, A. Bismarck, Inflatable elastomeric macroporous polymers synthesized from medium internal phase emulsion templates, ACS Appl. Mater. Interfaces 7 (34) (2015) 19243–19250, https://doi.org/10.1021/acsami.5b05123.

[27] D.B. Mahadik, K.-Y. Lee, R.V. Ghorpade, H.-H. Park, Superhydrophobic and compressible silica-polyHIPE covalently bonded porous networks via emulsion templating for oil spill cleanup and recovery, Sci. Rep. 8 (1) (2018) 16783, https://doi.org/10.1038/s41598-018-34997-1.

[28] Q. Jiang, A. Morand, A. Menner, A. Bismarck, Emulsion templated resilient macroporous elastomers, Polymer 186 (2020), 122023, https://doi.org/10.1016/j.polymer.2019.122023.

A.-M. Garnault, M.-F. Brouttier, Multi-layer metal sandwich materials comprising epoxy-based adhesive systems, US patent US20040058181A1 (2001).

[30] E.M. Russick, P.B. Rand, Epoxy Foams Using Multiple Resins and Curing Agents, 2000, US6110982A.

[31] W.-T. Wang, L. Watkins, *Flexible Epoxy Syntactic Foam Thermal Insulation For High Temperature Deepsea Reelable Pipelay Installations*, ASME 2010 29th International Conference on Ocean, Offshore and Arctic Engineering, 2010, pp. 269–273, https://doi.org/10.1115/omae2010-21014.

[32] N. Khundamri, C. Aouf, H. Fulcrand, E. Dubreucq, V. Tanrattanakul, Bio-based flexible epoxy foam synthesized from epoxidized soybean oil and epoxidized mangosteen tannin, Ind. Crop. Prod. 128 (2019) 556–565, https://doi.org/10.1016/j.indcrop.2018.11.062.

[33] R. Gu, M. Sain, S. Konar, Development and characterization of flexible epoxy foam with reactive liquid rubber and starch, J. Mater. Sci. 49 (8) (2014) 3125–3134, https://doi.org/10.1007/s10853-014-8013-x.

[34] J. Wang, Z. Du, H. Li, A. Xiang, C. Zhang, Interconnected porous epoxy monoliths prepared by concentrated emulsion templating, J. Colloid Interface Sci. 338 (1) (2009) 145–150, https://doi.org/10.1016/j.jcis.2009.06.013.

[35] J. Wang, C. Zhang, Z. Du, A. Xiang, H. Li, Formation of porous epoxy monolith via concentrated emulsion polymerization, J. Colloid Interface Sci. 325 (2) (2008) 453–458, https://doi.org/10.1016/j.jcis.2008.06.012.

[36] J. Bhinder, P.K. Agnihotri, Synthesis and characterization of poly-urethane foam doped with different nano-fillers, Mater. Today: Proceedings 18 (2019) 1479–1488, https://doi.org/10.1016/j.matpr.2019.06.617.

[37] H.A. Kharbas, J.D. McNulty, T. Ellingham, C. Thompson, M. Manitiu, G. Scholz, L.-S. Turng, Comparative study of chemical and physical foaming methods for injection-molded thermoplastic polyurethane, J. Cell. Plast. 53 (4) (2016) 373–388, https://doi.org/10.1177/0021955x16652107.

[38] M.F. Ashby, The properties of foams and lattices, Philos Trans A Math Phys Eng Sci 364 (1838) (2006) 15–30, https://doi.org/10.1098/rsta.2005.1678.

[39] M. Jalalian, Q. Jiang, A. Bismarck, Air templated macroporous epoxy foams with silica particles as property-defining additive, ACS Applied Polymer Materials 1 (3) (2019) 335–343, https://doi.org/10.1021/acsapm.8b00084.

[40] G. Ceglia, L. Mahéo, P. Viot, D. Bernard, A. Chirazi, I. Ly, O. Mondain-Monval, V. Schmitt, Formulation and mechanical properties of emulsion-based model polymer foams, The European Physical Journal E 35 (4) (2012) 31, https://doi.org/10.1140/epje/i2012-12031-0.

[41] G. Ceglia, A. Merlin, P. Viot, V. Schmitt, O. Mondain-Monval, Porous materials with tunable mechanical properties, J. Porous Mater. 21 (6) (2014) 903–912, https://doi.org/10.1007/s10934-014-9831-6.

[42] L. Maheo, P. Viot, D. Bernard, A. Chirazi, G. Ceglia, V. Schmitt, O. Mondain-Monval, Elastic behavior of multi-scale, open-cell foams, Compos. B Eng. 44 (1) (2013) 172–183, https://doi.org/10.1016/j.compositesb.2012.06.006.

[43] A. Quell, S. Heitkam, W. Drenckhan, C. Stubenrauch, Creating honeycomb structures in porous polymers by osmotic transport, ChemPhysChem 18 (5) (2017) 451–454, https://doi.org/10.1002/cphc.201600834.
[44] H. Iba, Y. Nishikawa, K. Urayama, Nonlinear stress-strain behavior of elastomer foams investigated by various types of deformation, Polymer 83 (2016) 190–198, https://doi.org/10.1016/j.polymer.2015.12.021.
[45] W. Brostow, S.H. Goodman, J. Wahrmund, Epoxies, in: H. Dodiuk, S.H. Goodman (Eds.), Handbook of Thermoset Plastics, third ed., William Andrew Publishing, Boston, 2014, pp. 191–252, https://doi.org/10.1016/B978-1-4557-3107-7.00008-7.
[46] C. Manas, Plastics properties and testing, in: Plastics Technology Handbook, CRC Press, 2017, https://doi.org/10.1201/9781315155876-3.
[47] S. Cantournet, R. Desmorat, J. Besson, Mullins effect and cyclic stress softening of filled elastomers by internal sliding and friction thermodynamics model, Int. J. Solid Struct. 46 (11) (2009) 2255–2264, https://doi.org/10.1016/j.ijsolstr.2008.12.025.
[48] H. Wan, K. Gao, S. Li, L. Zhang, X. Wu, X. Wang, J. Liu, Chemical bond scission and physical slippage in the mullins effect and fatigue behavior of elastomers, Macromolecules 52 (11) (2019) 4209–4221, https://doi.org/10.1021/acs.macromol.9b00128.
[49] J. Plagge, M. Klüppel, Mullins effect revisited: relaxation, recovery and high-strain damage, Materials Today Communications 20 (2019), 100588, https://doi.org/10.1016/j.mtcomm.2019.100588.
[50] Y. Miao, Mechanism analysis on the increased stress softening of Mullins effect for rubber matrix composites, Plastics, Rubber and Composites 48 (5) (2019) 226–233, https://doi.org/10.1080/14658011.2019.1596395.
[51] Z. Yousaf, M. Smith, P. Potluri, W. Parnell, Compression properties of polymeric syntactic foam composites under cyclic loading, Compos. B Eng. 186 (2020) 107764, https://doi.org/10.1016/j.compositesb.2020.107764.
[52] L.-C. Tang, L. Zhao, F. Qiang, Q. Wu, L.-X. Gong, J.-P. Peng, Mechanical properties of rubber nanocomposites containing carbon nanofillers. Carbon-Based Nanofillers and Their Rubber Nanocomposites, 2019, pp. 398–410, https://doi.org/10.1016/b978-0-12-817342-8.00012-3.
[53] J. Bhinder, P.K. Agnihotri, Effect of carbon nanotube doping on the energy dissipation and rate dependent deformation behavior of polyurethane foams, J. Cell. Plast. (2020), https://doi.org/10.1177/0021955x20917280.
[54] L. Mullins, Softening of rubber by deformation, Rubber Chemistry and Technology 42 (1) (1969) 339–362, https://doi.org/10.5254/1.3539210.
[55] C. Zhu, T.Y. Han, E.B. Duoss, A.M. Golobic, J.D. Kuntz, C.M. Spadaccini, M. A. Worsley, Highly compressible 3D periodic graphene aerogel microlattices, Nat. Commun. 6 (2015) 6962, https://doi.org/10.1038/ncomms7962.
[56] W. Zhao, Y. Li, S. Wang, X. He, Y. Shang, Q. Peng, C. Wang, S. Du, X. Gui, Y. Yang, Q. Yuan, E. Shi, S. Wu, W. Xu, A. Cao, Elastic improvement of carbon nanotube sponges by depositing amorphous carbon coating, Carbon 76 (2014) 19–26, https://doi.org/10.1016/j.carbon.2014.04.032.
[57] J. Bhinder, P.K. Agnihotri, Poly(vinyl alcohol) foams reinforced with carbon nanotubes for stapedial annular ligament applications, J. Appl. Polym. Sci. 137 (33) (2019), https://doi.org/10.1002/app.48736.

Supplementary information for

Emulsion-templated flexible epoxy foams

Patrick Steindl[a], Helena Decker[a], Bernhard Retzl[a], Qixiang Jiang[a,*] Angelika Menner[a], and Alexander Bismarck[a,b,*]

[a]Polymer and Composite Engineering (PaCE) Group, Institute of Materials Chemistry and Research, University of Vienna, Währinger Strasse 42, 1090 Vienna, Austria

[b]Department of Chemical Engineering, Imperial College London, South Kensington Campus, London, SW7 2AZ, UK.

[*]Corresponding author email: qixiang.jiang@univie.ac.at, alexander.bismarck@univie.ac.at

S1 - Migration of resin/hardener into the aqueous internal phase

1 ml epoxy resin was dropped into 10 ml DI water and the internal phase of the emulsion (e.g. aqueous solution of 10 g/L $CaCl_2$), respectively; the epoxy resin was, as expected, insoluble in the aqueous phase (**Figure S1**). 1 ml hardener was also dropped into 10 ml water and the $CaCl_2$ solution, respectively. After hand-shaking for 30 s, an emulsion formed. The emulsion settled to the bottom of the exceed water or $CaCl_2$ solution in 72 h. Given the structure of the epoxy resin and hardener components (Figure 1), it is unlikely that significant partitioning of monomers into the water phase will occur. However, we noted that upon addition of the hardener to water phase, resulted after shaking in the formation of an emulsion because of the amphiphilic nature of the hardener molecules. The partitioning of the hardener to the w/o interface of our water-in-epoxy emulsions could have affected the curing reaction. However, we noted the glass transition temperatures (T_g) of EF80 (cured epoxy polymer), EF80S (cured epoxy polymer with surfactant) and epoxy polyMIPE S1, determined by differential scanning calorimetry (DSC) (Discovery DSC, TA Instruments, Eschborn, Germany), were not dramatically different. For DSC measurements, about 0.3 g samples were heated/cooled/heated/cooled between -50°C to 110°C at a rate of 10°C / min. The heat flow curves of EF80, EF80S and S1 did not show pronounced glass transitions (**Figure S2**). The T_g of EF80 and EF80S were estimated to be 14°C, indicating that the presence of surfactant did not significantly plasticize the polymer network. S1 had an approximate T_g of 9°C, which was only slightly lower than the pure epoxy polymer.

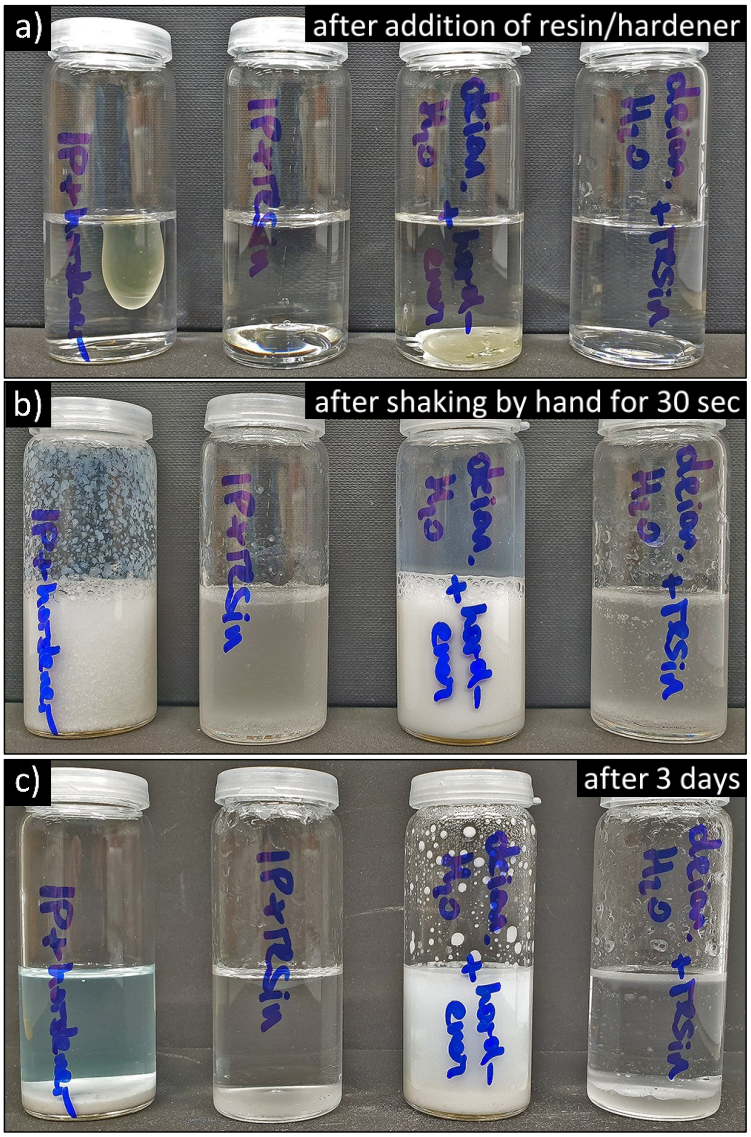

Figure S1: A small amount of resin/hardener was added to a large excess of internal phase (IP) and DI water, respectively, in order to investigate eventual migration tendencies (from the left: IP + hardener, IP + resin, DI water + hardener, DI water + resin). The images illustrate the interactions between aqueous and organic components at three different stages: a) right after the addition of resin/hardener; b) immediately after shaking; c) after three days.

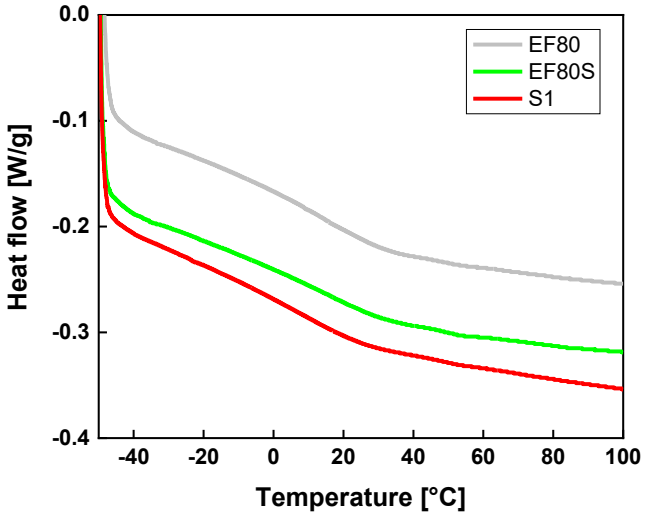

Figure S2: 2nd heat flow curves of cured epoxy polymer (EF80), cured epoxy polymer with surfactant (EF80S) and cured epoxy polyMIPE (S1). The reduced heat flow during heating of the samples from -40°C to 20°C indicated the glass transition of the epoxy. The glass transition temperatures (middle point of the glass transition) of the EF80 and EF80S were 14°C, while the glass transition temperature of S1 was 9°C.

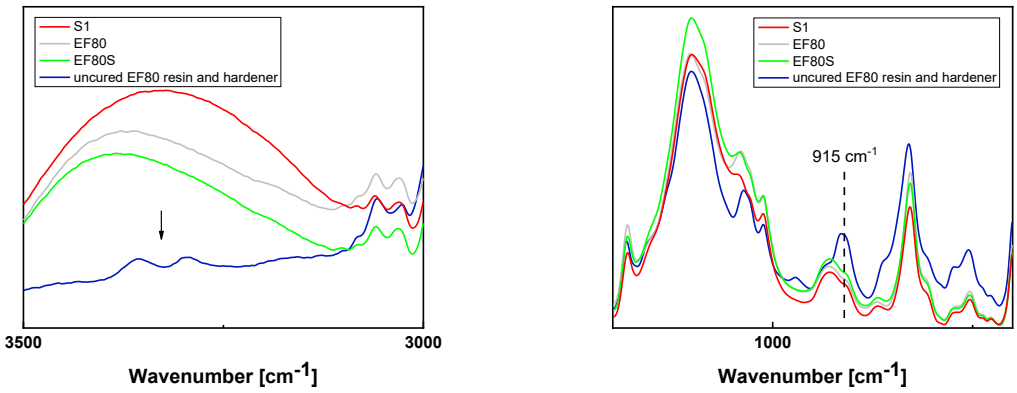

Figure S3: FTIR of uncured EF80 resin and hardener, cured EF80, cured EF80 with surfactant (EF80S) and cured epoxy polyMIPE (S1).

The curing of the epoxy was also confirmed by FTIR (Tensor II, Bruker, Vienna, Austria). The presence of primary amines in the uncured EF80 resin and hardener was shown by the two bands in the range of 3200 – 3400 cm^{-1} (**Figure S3).** However, after curing, the bands of primary amines overlapped with the broad adsorption band of –OH and, therefore, cannot be used to determine the presence of unreacted primary amines in the cured epoxy polyMIPEs. The band at 915 cm^{-1} indicated the presence of glycidyl groups in the uncured epoxy resin. After curing, the bands at 915 cm^{-1} reduced in EF80, EF80S and S1, caused by the

consumption of glycidyl groups. The resemblance of the band intensity at 915 cm^{-1} in the three samples indicated their similar curing degrees. Thus, even if hardener components adsorbed to the w/o interface with amine groups in the water phase, this would have an insignificant influence on the curing of the epoxy foams in emulsion templates.

S2 – Emulsion templated epoxy foams with modified silica nanoparticles

Hydrophobic silica nanoparticles HDK H18 (Wacker Chemie AG, Germany) were dispersed within the epoxy resin and hardener in a glass vessel equipped with overhead stirrer. The internal phase was added drop by drop into the continuous phase at a stirring speed of 400 rpm. After the addition of the internal phase, the emulsions were further stirred at 1000 rpm for 2 min to homogenise the emulsions. The emulsions were placed into an oven at 50°C for curing the continuous resin phase.

Table S1: Composition and curing temperature of emulsion templates with modified SiO_2 (Wacker HDK H18).

	continuous phase				**internal phase**	
	resin	**hardener**	**surfactant**		**ratio (IPR)**	**curing-temperature**
	EF80	EF80	Pluronic L-81	**SiO_2**	H_2O+$CaCl_2$·2H_2O	
sample ID	[vol%][a]	[vol%][a]	[vol%][a]	[wt%][b]	[%][c]	[°C]
S9	36.4	54.6	9	0.4	60	50
S10	36.4	54.6	9	1.2	60	50

Table S2: Density and mechanical properties of epoxy foams with silica nanoparticles.

	ρ_f	**P^a**	**d_p**	**E_c**	**σ_c**
	[g/cm^3]	[%]	[µm]	[MPa]	[MPa]
S9	0.44 ± 0.01	61 ± 1	145 ± 37	0.40 ± 0.02	0.061 ± 0.003
S10	0.46 ± 0.01	59 ± 1	215 ± 79	0.45 ± 0.06	0.054 ± 0.010

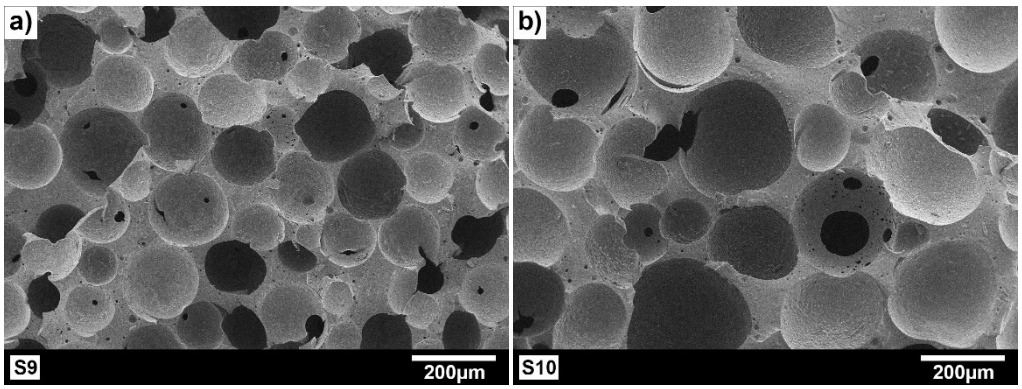

Figure S4: SEM images of epoxy polyMIPEs S9 (a) and S10 (b), prepared from emulsion templates with 0.4 and 1.2 wt% silica nanoparticles, respectively.

The epoxy based emulsions containing silica nanoparticles in the continuous phase could be successfully cured at 50°C, resulting in flexible macroporous epoxy foams. The epoxy foams with silica nanoparticles had densities of 0.44 and 0.46 g/cm^3, resulting in porosities of approximately 60%, which was as expected from emulsion templates containing 60% internal phase by volume. The polyMIPE S9 with 0.4% silica nanoparticles had a higher elastic modulus as compared to those with corresponding loadings of CNTs. This could be explained by a more homogeneous distribution of the hydrophobised silica particles throughout the continuous phase of the emulsions, after curing the silica particles reinforced the epoxy polymer. In contrast, CNTs tend to form large agglomerates, which have to be broken up by applying high shear forces, which are not easily applied in liquid resin formulations. Nevertheless, the pore sizes of the epoxy foams with 0.4% silica particles were slightly larger than those (112 ± 26 µm) with 0.4% CNTs. This indicated that during the curing of the emulsions at elevated temperature, the silica nanoparticles, even when homogeneously distributed, did not act as a better thickening agent as compared to CNTs, which, due to their 2D shape, are more effective to increase the viscosity of the continuous phase. Increasing the silica nanoparticle loading to 1.2% in the epoxy based emulsion templates resulted after curing in epoxy foam with larger pore sizes. Yet, the increase of the pore sizes was not as pronounced as that of epoxy foams with CNTs. This indicated that the increased loading did not affect the dispersion of the silica. As such, the stiffness of the epoxy foams with 1.2% silica nanoparticles were identical within error to that of the epoxy foams with 0.4% silica particles.

S3 - Producing polyMIPEs without surfactant

Table S3: Composition and curing temperature of emulsion templates without surfactant (for S7 and S8). The compositions were compared with the MIPEs (of S3 and S6, respectively) with surfactant.

continuous phase				internal phase	
resin	**hardener**	**surfactant**	**MWCNTs**	**ratio (IPR)**	**curing-temperature**
EF80	EF80	Pluronic L-81		$H_2O+CaCl_2 \cdot 2H_2O$	

sample ID	[vol%][a]	[vol%][a]	[vol%][a]	[wt%][b]	[%][c]	[°C]
S3	36.4	54.6	9	0.4	60	50
S7	40	60	-	0.4	60	50
S6	36.4	54.6	9	0.4	70	50
S8	40	60	-	0.4	70	50

[a] with respect to the volume of the continuous phase

[b] wt% CNT relative to the monomers

[c] relative to the total emulsion volume

Table S4: Morphological and mechanical properties of S3 and S6 - S8.

	ρ_s [g/cm^3]	ρ_f [g/cm^3]	P [%]	d_p [µm]	d_{pt} [µm]	E_c [MPa]	σ_c [MPa]
S3	1.10 ± 0.01	0.48 ± 0.05	56 ± 5	112 ± 26	21 ± 14	0.30 ± 0.02	0.038 ± 0.003
S7	1.12 ± 0.01	0.40 ± 0.04	64 ± 4	108 ± 12	26 ± 16	0.32 ± 0.06	0.038 ± 0.009
S6	1.11 ± 0.01	0.32 ± 0.01	71 ± 1	118 ± 35	23 ± 13	0.20 ± 0.03	0.026 ± 0.010
S8	1.17 ± 0.01	0.32 ± 0.01	72 ± 1	100 ± 40	17 ± 9	0.18 ± 0.01	0.023 ± 0.002

The preliminary experiment in producing polyMIPEs from MIPEs without surfactant indicated that the viscosity of the formulation had a significant impact on the stability of the emulsions and the morphology of the subsequent polyMIPEs, while the surfactant played a minor role in the properties of the emulsions and epoxy foams. Therefore, S7 and S8 were cured from emulsion templates with MWCNTs but no surfactant. S7 and S8 showed both analogic pore morphology and mechanical properties to their corresponding polyMIPEs (S3 and S6, respectively) (**Table S2** and **Figure S5**). This provided a method to produce epoxy foams without the presence of surfactant.

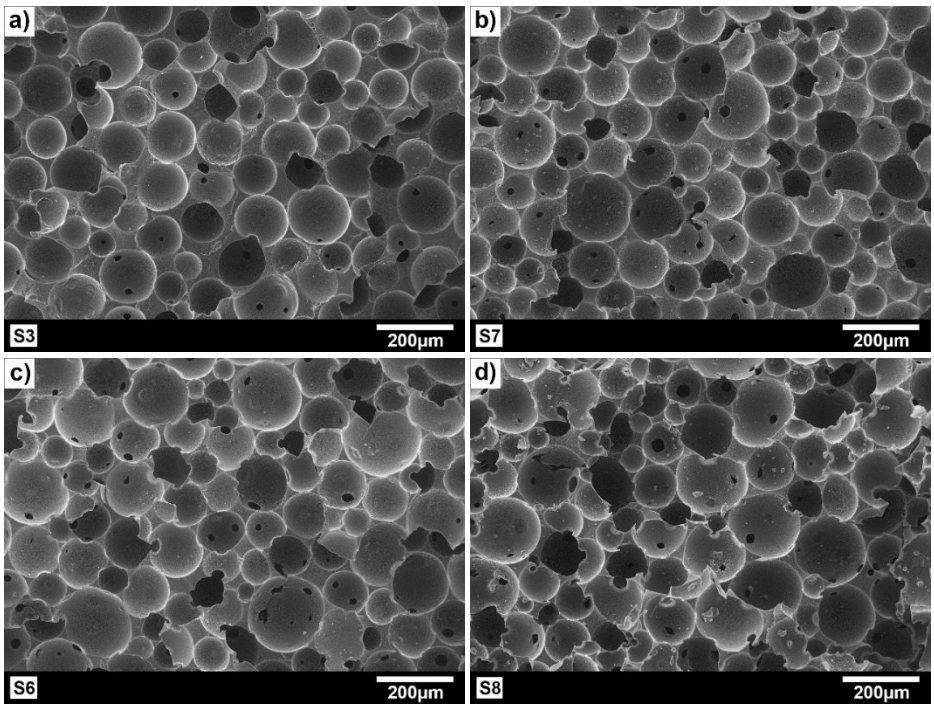

Figure S5: SEM images of epoxy polyMIPEs S3, S6, S7 and S8, prepared from emulsion templates with 60% IPR (a,b) and 70% IPR (c,d). The MWCNT content was 0.4 wt% for all four samples. A small amount of surfactant (9 vol%) was employed in S3 and S6.

S4 - ELC and residual strains as function of cycle numbers of epoxy-based polyMIPEs

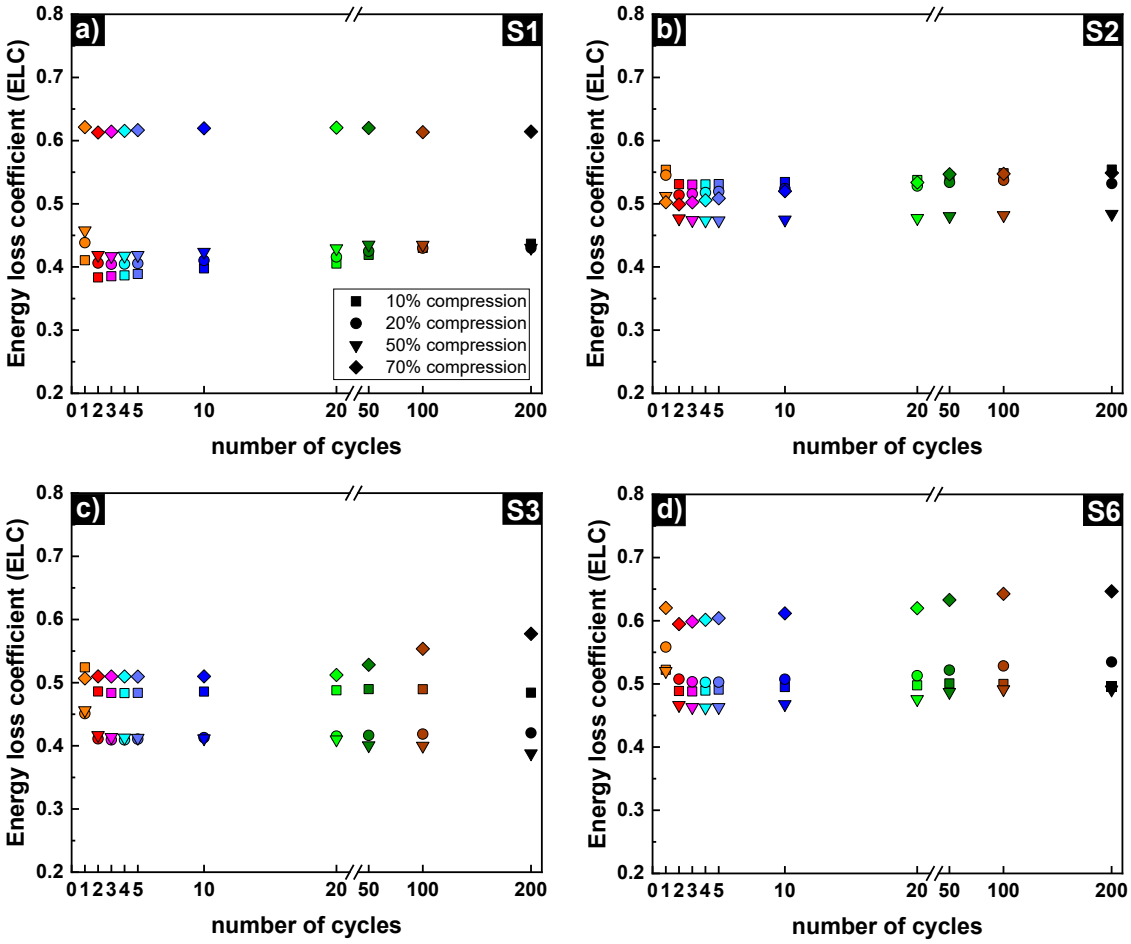

Figure S6: Development of the ELC with increasing cycle number for S1-S3 & S6

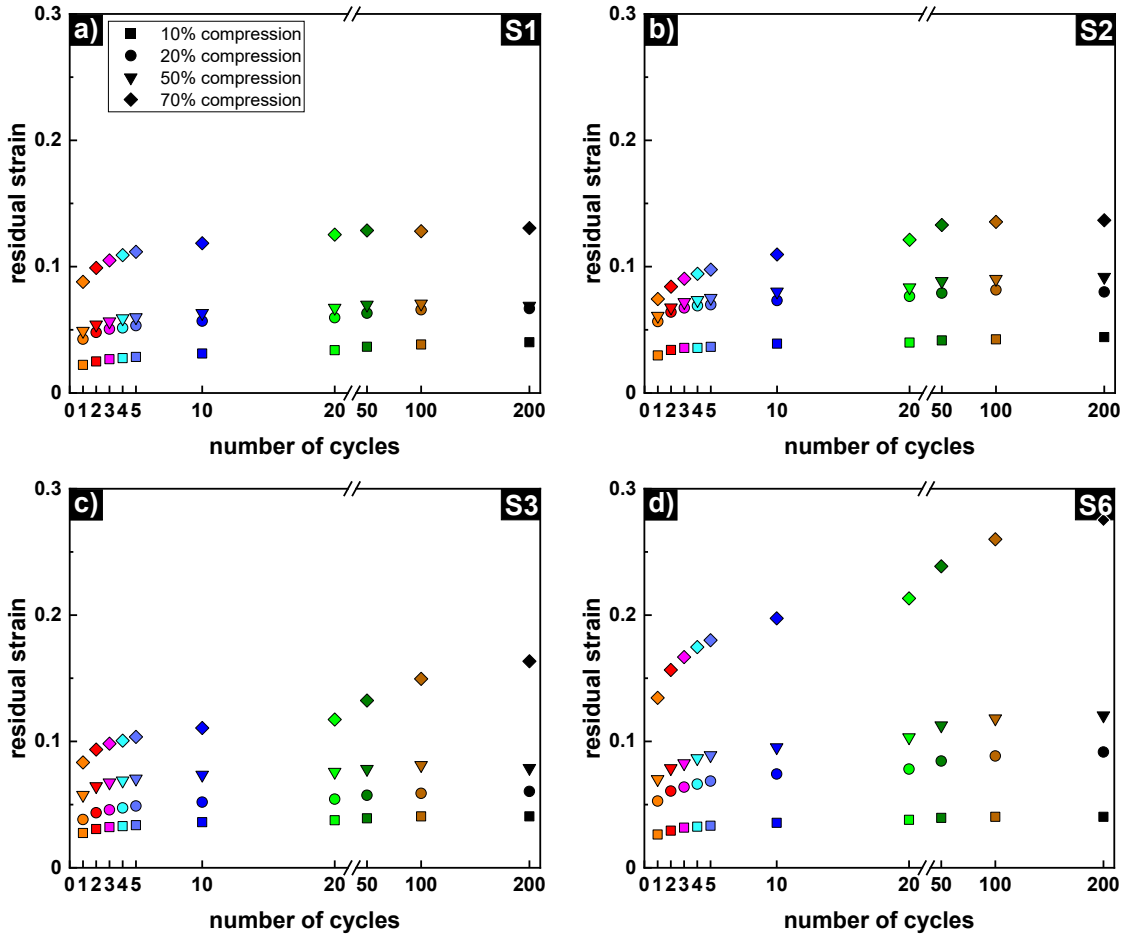

Figure S7: Course of the residual strain with increasing number of cycles